THE JOURNAL OF

PHYSICAL CHEMISTRY

THE JOURNAL OF
PHYSICAL CHEMISTRY

∎ Supplementary material for this paper is available separately, in photocopy or micro-
fiche form. Ordering information is given in the paper.

* In papers with more than one author, the asterisk indicates the name of the author to
whom inquiries about the paper should be addressed.

AUTHOR INDEX

Picosecond Pulse Radiolysis. I. Time or Concentration Dependent Rate Constants[1]

C. D. Jonah, J. R. Miller, E. J. Hart, and Max S. Matheson*

Chemistry Division, Argonne National Laboratory, Argonne, Illinois 60439 (Received June 25, 1975)

Publication costs assisted by Argonne National Laboratory

Rate constants for the reaction of the hydrated electron with reactive solutes at high concentrations have been measured, using our single fine-structure pulse stroboscopic apparatus. The accessible time region is 50–3500 psec. A time-dependent rate constant in accord with theory was found for the neutral reactant, nitromethane, whereas acetone reacting one-third as fast showed no time dependence. For $e_{aq}^- + NO_3^-$ the rate constant increases with concentration (i.e., at short times), owing both to the ionic strength effect and the time dependence effect. Only time-dependent effects seem to be present in our concentration range for the reactions of the hydrated electron with IO_4^- and CrO_4^{2-}. Ionic strength effects seem to be absent, probably because tunneling extends the reaction radii to about 10 Å where coulomb forces between the reactants are small. Cd^{2+} reacts with e_{aq}^- at nearly the diffusion-limited rate so that no Cd^{2+} ion atmosphere can form about surviving e_{aq}^-. Thus, reacting Cd^{2+} has an anion atmosphere but e_{aq}^- reacts without a cation sheath in pure $Cd(ClO_4)_2$ solution, and this decreases the effect of ionic strength on the rate constant. The effect is estimated from experimental data. Cu^{2+} reacts at half the diffusion-limited rate so a partial Cu^{2+} atmosphere can build up about e_{aq}^-.

Introduction

For reactions of the hydrated electron with reactive solutes many rate constants have been measured in dilute solutions using microsecond pulse radiolysis.[2,3] In concentrated solutions several factors may cause the rate constant values to differ from those observed in dilute solution. For the diffusion-controlled reaction of a neutral solute with the hydrated electron the rate constant is expected to be time dependent, since, if the initial distributions of hydrated electron and solute are random, the fraction of surviving e_{aq}^- having close solute neighbors will decrease with time until a steady state is reached.[4,5] Recently, this time dependence of the rate constant has been examined and shown to fit the Noyes' equation within experimental error.[6-8] Further, if the solute is charged the Coulombic interaction with the hydrated electron will decrease as the solute concentration is increased. Also reaction may occur before the ionic atmosphere can attain equilibrium around the newly formed e_{aq}^-.[9,10]

To examine these factors we have studied the reactions of the hydrated electron with reactive solutes, both neutral and charged. Hunt and co-workers have already reported the rate constants for a number of such reactions at high

solute concentrations,[11-13] measured using their stroboscopic pulse radiolysis apparatus. Except for the reactions with cadmium chloride, which is known to form complexes, and with H_3O^+, which does not react with e_{aq}^- at a diffusion-controlled rate, all rate constants were constant over the concentration range accessible with their 20–350-psec time window. They also compared the rate constants in concentrated solutions with those for dilute solutions and found no change for neutral molecules, an increase for anions, and a decrease for cations. The time range of our modification of Hunt's apparatus[14] is 50–3500 psec, which enables measurements at intermediate concentrations where the rate constant is changing from the dilute to the concentrated solution value. Further, the more intense fine structure pulse from our linac yields higher e_{aq}^- concentrations and should therefore yield higher precision. As reported in this paper, we have observed changes in rate constants over the accessible concentration range: changes explicable in terms of the factors mentioned above.

Experimental Section

Stroboscopic Pulse Radiolysis System. A schematic diagram of the pulse radiolysis apparatus is shown in Figure

1. This is an adaptation of the brilliant concept of Hunt and co-workers,[15] and is described in detail elsewhere.[14] In essence a portion of the beam is delayed a fixed time by passage around the 270° magnet and then irradiates the reaction cell. Another portion of the beam is intercepted by the Cerenkov generator, where Cerenkov light is generated in xenon gas at 1 atm and then delayed a variable amount by delay mirrors moving at a fixed speed. The accelerator is pulsed 60 times per second and as the mirrors move the Cerenkov light pulse scans the absorption in the cell before, during, and after the time the corresponding electron pulse strikes it. For all the experiments described in this paper, the hydrated electron absorption was monitored at 600 nm. The Cerenkov pulse has the same time width as the electron pulse, so the time resolution is determined by the pulse width. There are three advantages in our modification. First, only one fine structure pulse is used, so that a reaction can be followed from ~40 psec to 3.5 nsec after irradiation. This enables reaction rates to be measured with greater accuracy and over a wider range of solute concentrations. Second, the single pulse ensures that the age of the primary species such as e_{aq}^- and OH varies only by the pulse duration. This is important in studying spur kinetics. Third, the fine structure pulse from our linac is several fold more intense, enabling the direct observation of weakly absorbing species such as OH. The single fine structure pulse was isolated by subharmonic bunching[16] and its full-width at half-maximum has been measured as ~25 psec.[17] The optical transmission data are stored in the Chemistry Division Sigma 5 computer,[18] where it can be subsequently manipulated in various calculations.

Irradiation Cell and Flow System. Since the solution is repetitively irradiated, a flow system to minimize product buildup is used.[14]

Materials. All aqueous solutions were made either with once-distilled water or with water purified by deionization and filter equipment supplied by Continental Water Co. Although, with the high concentrations of reactive solutes used, water purity is not a problem. The conductivity of the deionized and filtered water was comparable to that of triply-distilled water. All solutes used were reagent grade chemicals, although again, trace impurities would not affect any rate constant measurements on the experimental time scale.

Rate Constants. The rate constant k, for a given solute concentration [s], was determined by a non-linear least-squares fitting of the raw experimental data. The errors for each point are equally weighted. Rate constant measurements at the lower solute concentrations were corrected for the small amount of hydrated electron decay in the "spurs" observed in the period 40–4000 psec after the pulse.[19]

Results and Discussion

Neutral Reactants. Noyes[5] has considered the time dependence of the rate constant for reaction of two types of molecules, A and B, where each type of molecule exerts no long-range forces and each "is distributed completely at random the way it would be if the other type were not present". His eq 2.16[20] can be recast as

$$k_t = k_\infty \left[1 + \frac{k_\infty}{4\pi r_{AB} D_{AB}(N/10^3)} \frac{r_{AB}}{(\pi D_{AB} t)^{1/2}} \right] \quad (1)$$

where k_t is the rate constant at time t, k_∞ is the rate constant at long times, r_{AB} is the reaction radius, D_{AB} is the diffusion coefficient for relative diffusion of A and B, and
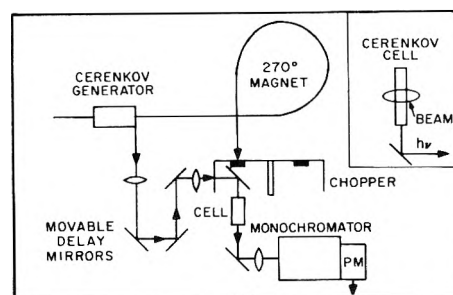
Figure 1. Stroboscopic picosecond pulse radiolysis apparatus using Cerenkov analyzing light: PM = photomultiplier. Chopper enables correction of signal for Cerenkov generated in reaction cell. View parallel to beam shows beam is spread horizontally and the center of the beam is intercepted by the Cerenkov cell. The outer portions of the electron beam are focussed together before entry into the reaction cell.

N is Avogadro's number. $4\pi r_{AB} D_{AB} N/10^3$ is the diffusion-controlled encounter rate in units, M^{-1} sec^{-1}. We assume that the electron is hydrated in probably less than 1 psec,[12] and that, although the hydrated electron is not homogeneously distributed in the solution, it is randomly distributed with respect to e_{aq}^-–solute separation distances. High local concentrations of e_{aq}^- in a spur could cause local depletion of solute. Naleway[21] has considered an average spur containing 2.7 e_{aq}^- (radius 18.75 Å) and 2.7 each of H_3O^+ and OH (radii 6.25 Å). If a solute, which reacts at a diffusion-controlled rate, is present in 0.01 M concentration, he finds the maximum effect of depletion on the rate occurs at 900 psec and is less than 2%. The depletion is less with higher concentrations of scavenger and with less reactive solutes. The choice of a small number of radicals per average spur is supported by the estimate of Mozumder and Magee[22] that ~80% of the energy for fast electrons (10 MeV) is deposited in spurs of less than 100 eV containing mostly one and two radical pairs (one and two hydrated electrons). Thus, the depletion effect in spurs is small under our conditions, and was neglected. Finally, immediate reaction of electrons solvated next to a solute as postulated by Czapski and Peled[23] would not affect distributions at 50 psec and longer after energy deposition.

We have compared our experimental rate constants (for reaction of e_{aq}^- with a number of solutes) with the theoretical results predicted by eq 1. The dilute solution value of k (sometimes measured, sometimes taken from the literature) was taken as k_∞. Where radii were estimated from physical volumes, $r_{e_{aq}^-}$ was taken as 3.0 Å. $D_{e_{aq}^-}$, 4.96 × 10^{-5} cm^2 sec^{-1},[24] is several fold larger than the diffusion constants of the solutes used so that errors in estimates of these diffusion constants contributed only a small error to D_{AB}. The time, t, corresponding to each solute concentration was taken as the half-life calculated from the experimental rate constant observed for that particular concentration plus 25 psec. As noted earlier the pulse width of the electron pulse is 25 psec fwhm, and it is also ~50 psec at the base. For rate constant determinations only the experimental points after the light pulse and the electron pulse cease to overlap are used. This means that the peak light intensity is initially sampling the transmission 25 psec after the end of the electron pulse. Further, while the age distribution of hydrated electrons formed by the electron pulse will be skewed and slightly narrowed by reaction of the first-formed e_{aq}^-, the distribution still has a finite width. The added 25 psec probably undercorrects a little.

In Figure 2 $k(e_{aq}^- +$ acetone) is plotted against concentration (time). For acetone $k_\infty/(4\pi r_{AB}D_{AB}N/10^3)$ is 0.35, i.e., the long time rate constant is only one-third the encounter rate and the time-dependent effect is reduced proportionately. In agreement with the small effect predicted theoretically we find that $k(e_{aq}^- +$ acetone) shows no dependence on time or acetone concentration within our small experimental error. Aldrich et al.[12] also found no dependence with $k = 9.5 \times 10^9$ M^{-1} sec^{-1} over the acetone concentration range 0.2–1.75 M. Schwarz[25] recognized that $k_\infty/(4\pi r_{AB}D_{AB}N/10^3)$ was less than 1, but omitted this term and overestimated the time-dependent effect for acetone in his discussion of the results of Hunt and co-workers.

Nitromethane which reacts threefold faster than acetone with e_{aq}^- is expected to show a measurable time dependence for $k(e_{aq}^- + CH_3NO_2)$ since k_∞ is approximately equal to the encounter rate, $4\pi r_{AB}D_{AB}N/10^3$. Quite satisfactory agreement is obtained between experiment and theory in Figure 3.

Charged Reactants. In a solution of electrolyte the concentration of a positive ion about e_{aq}^- will be enhanced and the concentration of a negative ion reduced relative to average solution concentrations by the Coulombic interaction between e_{aq}^- and the ions. Debye[26] has included the Coulombic interaction and derived eq 2 for k_{diff}, the rate constant of a diffusion-controlled reaction between ions A and B in dilute solution.

$$k_{diff} = \frac{4\pi r_{AB}D_{AB}N}{10^3} \left\{ \frac{Z_A Z_B r_0}{r_{AB}} \bigg/ \left(\exp\left[\frac{Z_A Z_B r_0}{r_{AB}}\right] - 1 \right) \right\} \quad (2)$$

r_{AB}, D_{AB}, and N have the same significance as in eq 1; Z_A and Z_B are the units of electronic charge on ions A and B; and $r_0 = e^2/\mathbf{D}\mathbf{k}T = 7.1 \times 10^{-8}$ cm in water at 25°C, where e = charge on the electron, $\mathbf{D}$ = dielectric constant, $\mathbf{k}$ = Boltzmann constant, and T = K. The term in braces gives the effect of the Coulombic interaction on the diffusion-controlled rate. If A reacts with B in a solution containing an excess of inert salt, the ionic atmospheres around A and B will reduce the Coulombic interaction. The Brønsted–Bjerrum, Debye–Hückel treatment of this effect in dilute solutions leads to eq 3 for the variation of the rate constant with ionic strength μ in water at 25°C

$$\log \frac{k_2}{k_0} = 1.02 Z_A Z_B \frac{\mu^{1/2}}{1 + 0.329 a \mu^{1/2}} \quad (3)$$

where k_2 is the rate constant at ionic strength μ (both A and B having equilibrium ionic atmospheres), k_0 is the rate constant at zero ionic strength, a is the distance of closest approach of the ions in ångströms (assumed the same for both ions).

In a solution of a pure reactive salt another effect is possible; the hydrated electron may react before an equilibrium ionic atmosphere is formed about it. Coyle, Dainton, and Logan[9] have considered the situation in which an ion A (i.e., e_{aq}^-) is suddenly produced in a solution of a salt, one of whose constituents is ion B, and A reacts with B before an ionic atmosphere can be established about A. In this case the activated complex, $(AB)^-$, will have a charge $Z_A + Z_B$, while the ionic atmosphere initially corresponds to that of ion B with charge Z_B. In reactions in which e_{aq}^- reacts rapidly with ion B, $(AB)^\ddagger$ is an excited ion B with charge $Z_B - 1$, and if, as is probable, the excitation is lost before the ionic atmosphere relaxes, the electrical potential exerted at $(AB)^\ddagger$ will be proportional to Z_B and not $Z_A + Z_B$.
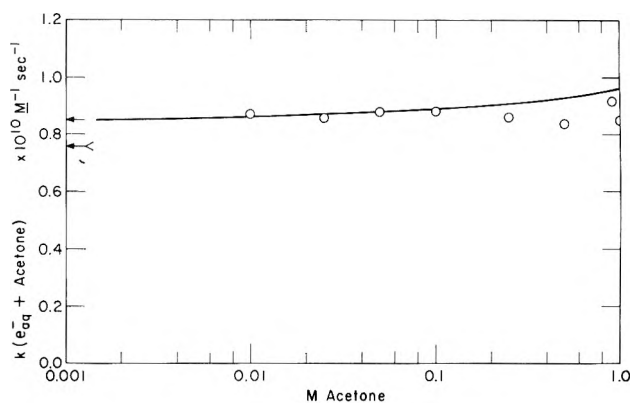
Figure 2. Variation of $k(e_{aq}^- +$ acetone) as a function of acetone concentration. Line shows the theoretical dependence from eq 1 with $r_{AB} = 5 \times 10^{-8}$ cm, $D_{AB} = 6.5 \times 10^{-5}$ cm^2 sec^{-1}, and $k_\infty = 0.85 \times 10^{10}$ M^{-1} sec^{-1}. Aldrich et al.[12] find an average k of 0.96×10^{10} M^{-1} sec^{-1} between $M = 0.20$ and 1.75, and a dilute solution k of 0.76×10^{10} (lower arrow).
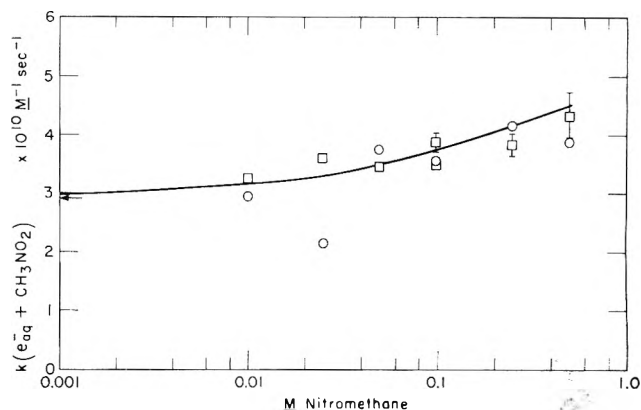
Figure 3. Variation of $k(e_{aq}^- + CH_3NO_2)$ as a function of nitromethane concentration. Line shows theoretical dependence according to eq 1 with $r_{AB} = 6.0 \times 10^{-8}$ cm, $D_{AB} = 6.5 \times 10^{-5}$ cm^2 sec^{-1}, and $k_\infty = 2.9 \times 10^{10}$ M^{-1} sec^{-1}.

For the reaction described above the activity coefficients to be used in Brønsted–Bjerrum treatment are $f_A = 1$, $-\log f_B = 0.51 Z_B^2 \mu^{1/2}/(1 + 0.329 a \mu^{1/2})$, and $-\log f_{AB}^\ddagger = 0.51(Z_A + Z_B)Z_B\mu^{1/2}/(1 + 0.329 a \mu^{1/2})$. Consequently, the effect of ionic strength on the reaction of A + B when A does not have an ionic atmosphere is that in

$$\log \frac{k_1}{k_0} = 0.51 Z_A Z_B \mu^{1/2}/(1 + 0.329 a \mu^{1/2}) \quad (4)$$

k_1 is the rate constant at ionic strength μ. It is apparent that, in dilute solutions where the Debye–Hückel treatment is valid, k_1 is the geometric mean of k_0 and k_2 for a given value of μ. Further considerations (see Appendix) indicate that this relation may be valid at higher concentrations, if k_0 is then defined as the rate constant for reaction between A and B when neither has an ionic atmosphere.

Reactions with Negative Ions. The rate constants for reaction of e_{aq}^- with three negative ions (NO_3^-, IO_4^-, and CrO_4^{2-}) have been measured at high concentrations. The results for $k(e_{aq}^- + NO_3^-)$ are given in Figure 4. The dashed line is the average of the results obtained by Peled and Czapski[27] and at this laboratory[28] for dilute $NaNO_3$ with 0, 0.1, and 1.0 M $NaClO_4$ added. The physical contact
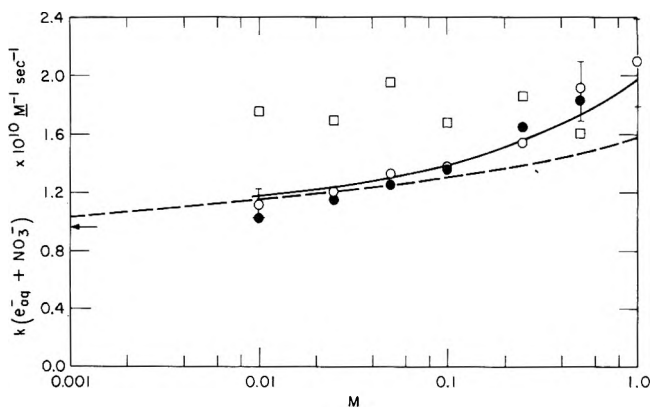
Figure 4. (Dashed line) $k(e_{aq}^- + NO_3^-)$ for dilute nitrate vs. total salt ($NaClO_4$ added); (solid line) eq 1 (O,●) experimental k for pure $NaNO_3$; (□) k at constant ionic strength ($NaNO_3 + NaClO_4 = 0.5$ M) vs. NO_3^- concentration. 2σ determined only for experiment O, where not shown for O $2\sigma < 0.1$. Aldrich et al.[12] find an average k = 2.1 × 10^{10} over the range 0.125–0.75 M $NaNO_3$.

radius, r_{AB}, of e_{aq}^- and NO_3^- is 5.0 × 10^{-8} cm using $r_{NO_3^-}$ = 2.0 × 10^{-8} cm,[29] and $D_{NO_3^-}$ = 2.02 × 10^{-5} cm^2 sec^{-1} from the ionic mobility. These values in eq 2 yield k_{diff} = 1.20 × 10^{10} M^{-1} sec^{-1}, while $4\pi r_{AB}D_{AB}N/10^3$ = 2.65 × 10^{10} M^{-1} sec^{-1} which would be the diffusion-controlled rate constant in the absence of Coulombic repulsion. The observed rate constant at zero ionic strength is 0.81 of the diffusion-controlled value calculated from eq 2.

To estimate τ_R, the time of formation of the Na$^+$ ion atmosphere around the hydrated electron in 1 M $NaNO_3$, we use eq 5 given by Falkenhagen[30]

$$\tau_R = \frac{6.92 \times 10^{-9}}{c \, \Lambda_\infty} \text{sec} \tag{5}$$

where c is the molar concentration and Λ_∞ is the molar conductance at infinite dilution. With limiting equivalent conductances of 175 and 50 cm^2 ohm^{-1} equiv^{-1} for e_{aq}^- and Na$^+$, respectively, τ_R is 31 psec, while the half-life of reaction calculated from the observed rate constant at 1 M is 34 psec. However, $\frac{1}{2}\tau_R$ is more nearly the time in which half the ionic atmosphere density relaxes. Because of Coulombic attraction the diffusion-controlled encounter rate between e_{aq}^- and Na$^+$ is about 3.5 × 10^{10} M^{-1} sec^{-1}, while even at 1 M $NaNO_3$ $k(e_{aq}^- + NO_3^-)$ is only 2 × 10^{10}, therefore it is not surprising that the ionic atmosphere forms somewhat faster than e_{aq}^- reacts in this case. Further, as noted earlier the peak of our Cerenkov pulse samples e_{aq}^- absorption 25 psec after the end of the electron pulse with surviving e_{aq}^- having an age distribution half-width less than 25 psec. We conclude that over the course of our observations most of the hydrated electrons have ionic atmospheres. We therefore assume that for $e_{aq}^- + NO_3^-$ the time-dependent effect operates on species with ionic atmospheres.

From the foregoing we conclude that eq 1 may be applied to $e_{aq}^- + NO_3^-$, if k_∞ for a given $NaNO_3$ concentration is taken from the dashed line in Figure 4. Further, we replace r_{AB} by ρ^* where ρ^* is r_{AB} times the term in braces in eq 2, so that $4\pi\rho^*D_{AB}N/10^3$ corresponds to the expected diffusion-controlled rate constant. The magnitude of ρ^* is expected to increase with ionic strength, but this variation is unimportant since ρ^* effectively cancels out in eq 1. This procedure yields the solid line in Figure 4 for the combined effect of ionic strength and time dependence. It should also

be noted in Figure 4 that within experimental error $k(e_{aq}^- + NO_3^-)$ is independent of NO_3^- concentration if the ionic strength is maintained constant. On the basis of the previous discussion one expects $k \sim 1.46 \times 10^{10}$ (the value on the dashed line at 0.5 M) at 0.01 M NO_3^-, and increasing values due to the time-dependent effect so as to intersect the solid line at 0.5 M $NaNO_3$.

We conclude that the reaction of $e_{aq}^- + NO_3^-$ occurs when the two are in physical contact, at an approximately diffusion-controlled rate, and that a small time-dependent effect seems to exist which can be accounted for by eq 1. The physical contact reaction radius is in agreement with the results of Miller,[31] who finds that quantum-mechanical tunneling of electrons trapped in low temperature glasses to nitrate ions is relatively slow.

Trapped electrons in low temperature glasses do tunnel rapidly to chromate or periodate ions,[31] and this fact suggested that the reactions of e_{aq}^- with high concentrations of these ions should be of interest. The results for $k(e_{aq}^- + CrO_4^{2-})$ are presented in Figure 5 and those for $k(e_{aq}^- + IO_4^-)$ in Figure 6. Peled and Czapski[27] found for dilute Na_2CrO_4 in 0, 0.1, and 1.0 M Na_2SO_4, k = 1.8 × 10^{10}, 2.7 × 10^{10}, and 2.6 × 10^{10} M^{-1} sec^{-1}, respectively. These results show that the reaction is very fast and that at high salt concentrations the rate constant is independent of ionic strength. We have confirmed this latter point in that for 0.01 M Na_2CrO_4 in 0, 0.1, 0.25, and 0.5 M Na_2SO_4 $k(e_{aq}^- + CrO_4^{2-})$ was measured respectively as 2.95 × 10^{10}, 3.15 × 10^{10}, 3.10 × 10^{10}, and 2.97 × 10^{10} M^{-1} sec^{-1}. Note also in Figure 5 that the rate constant with added Na_2SO_4 (total salt equals 0.25 M) to give constant ionic strength, or with Na_2CrO_4 alone, shows the same dependence on $[CrO_4^{2-}]$. Using k_{diff} = 1.8 × 10^{10} M^{-1} sec^{-1} and D_{AB} = 5.5 × 10^{-5} cm^2 sec^{-1} in eq 2 yields r_{AB} = 9.8 × 10^{-8} cm, from which we conclude in agreement with Hart and Anbar[32] that electron tunneling is also occurring in water at 25°C. This large radius can also explain the lack of ionic strength effect at high salt concentrations, since at high concentration the distance at which the Coulombic interaction equals kT will decrease from 14.2 Å to a value less than the reaction radius of 9.8 Å. Thus the time-dependent effect alone should be largely adequate to explain our results. Using k_∞ as 3 × 10^{10} M^{-1} sec^{-1}, D_{AB} and r_{AB} as above, and $4\pi N r_{AB}D_{AB}/10^3$ = 4.08 × 10^{10} M^{-1} sec^{-1} reduces the effective r_{AB} from 9.8 to 7.2 Å in eq 1. As seen in Figure 5, the variation of $k(e_{aq}^- + CrO_4^{2-})$ with concentration between 0.005 and 0.25 M CrO_4^{2-} is largely accounted for by the time-dependent effect.

The values of $k(e_{aq}^- + IO_4^-)$ in concentrated solutions were found to be even higher than those for the chromate reaction. However, the literature value for the rate constant in dilute solution was only 1.1 × 10^{10} M^{-1} sec^{-1}. We redetermined the dilute solution rate constant as 3.7 × 10^{10}, 4.2 × 10^{10}, and 4.0 × 10^{10} M^{-1} sec^{-1} in the presence of 0, 0.1, and 1.0 M $NaClO_4$, respectively. The effect of ionic strength is seen to be small. Setting k_{diff} = 3.7 × 10^{10} M^{-1} sec^{-1} and D_{AB} = 6.5 × 10^{-5} cm^2 sec^{-1} in eq 2 yields r_{AB} = 10.6 Å. This value is larger than the distance, 7.1 Å, at which the Coulombic interaction equals kT, and the small ionic strength effect is not surprising. Further 0.005 M $NaIO_4$ plus 0, 0.1, 0.25, and 0.5 M $NaClO_4$ gave $k(e_{aq}^- + IO_4^-)$ = 4.7, 5.0, 5.1, and 6.8 × 10^{10} M^{-1} sec^{-1}, respectively. k_∞ was taken as 5.2 × 10^{10}, and value of $4\pi N r_{AB}D_{AB}/10^3$ with r_{AB} and D_{AB} as above, for use in eq 1. We conclude that with both IO_4^- and CrO_4^{2-} the hydrated electron
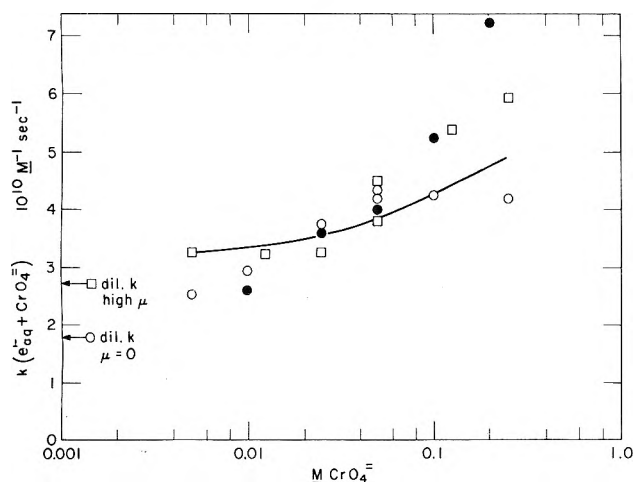
Figure 5. $k(e_{aq}^- + CrO_4^{2-})$ vs. CrO_4^{2-} concentration: (●,○) pure Na_2CrO_4; (□) k vs. $[CrO_4^{2-}]$ with $Na_2CrO_4 + Na_2SO_4 = 0.25\ M$, i.e., μ = constant. Solid line from eq 1.
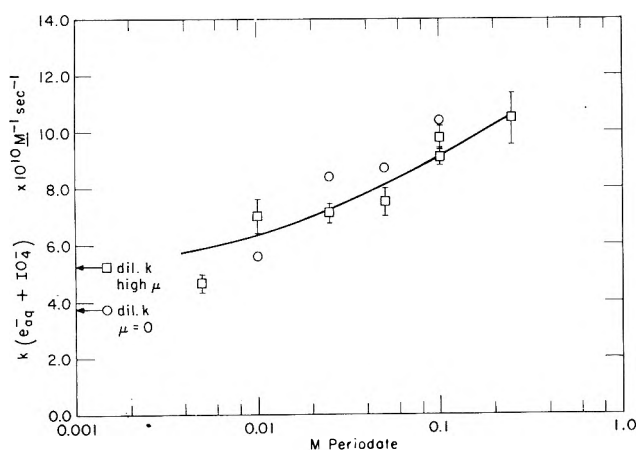
Figure 6. $k(e_{aq}^- + IO_4^-)$ vs. $[IO_4^-]$: (○,□) experimental points. 2σ determined only for experiment □. Line from eq 1.

Figure 7. $k(e_{aq}^- + Cd^{2+})$ vs. total salt concentration: (upper solid line) k_0; (lower solid line) k_2 for dilute Cd^{2+} in $Ca(ClO_4)_2$; (dashed line) $k_1 = (k_2k_0)^{1/2}$. See text for k_0, k_1, k_2: (●) from Wolff et al.;[13] (□) experiments using pure $Cd(ClO_4)_2$; (◐) 0.01 $M\ Cd^{2+}$ plus $Ca(ClO_4)_2$; (◑) 0.05 $M\ Cd^{2+}$ plus $Ca(ClO_4)_2$; (◒) 0.1 $M\ Cd^{2+}$ plus $Ca(ClO_4)_2$; (○) 0.2 $M\ Cd^{2+}$ plus $Ca(ClO_4)_2$. $2\sigma \le 0.1 \times 10^{10}\ M^{-1}\ sec^{-1}$. The dotted lines connect the points showing the changes in the rate constants as $Ca(ClO_4)_2$ is added to 0.01, 0.05, 0.1, and 0.2 $M\ Cd^{2+}$.
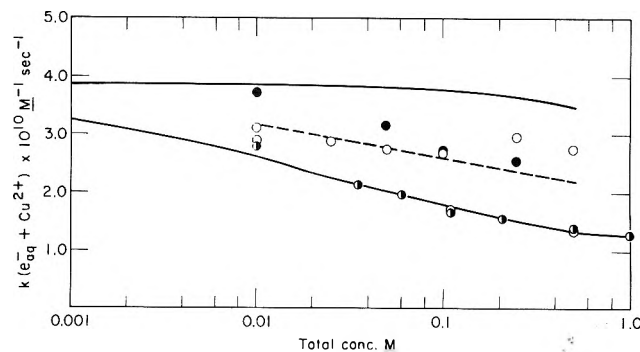
Figure 8. $k(e_{aq}^- + Cu^{2+})$ vs. total salt concentration: (upper solid line) k_0; (lower solid line) k_2; (dashed line) $k_1 = (k_2k_0)^{1/2}$. See text for k_0, k_1, k_2: (○,●) experiments using pure $Cu(ClO_4)_2$; (◐) 0.01 M Cu^{2+} plus $Ca(ClO_4)_2$. $2\sigma \le 0.1 \times 10^{10}\ M^{-1}\ sec^{-1}$.

reacts by tunneling 10 Å (center-to-center distance) in dilute solutions, that the ionic strength effect saturates for salt concentrations of about 0.01 M and above, and that $k(e_{aq}^- + IO_4^-)$ or $k(e_{aq}^- + CrO_4^{2-})$ vary at high concentrations in accord with the time-dependent effect.

Buxton et al.[7] have also found time dependence on the time scale of tens of nanoseconds for the rate constants of reaction of e_{aq}^- with NO_3^-, CrO_4^{2-}, and even with acetone at low temperatures (190–260 K) in about 10 M solutions of LiCl and NaOH + KOH. Owing to the strong electrolyte concentrations, both NO_3^- and CrO_4^{2-} behave as neutral species. In their work the radius of reaction for $e_{aq}^- + CrO_4^{2-}$ is ~20 Å. This large value is to be expected, since in these viscous fluids tunneling competes more favorably with diffusion. It is also to be expected that $e_{aq}^- +$ acetone can be diffusion controlled in these solutions, but not in water at 25°C, since Buxton et al. tentatively conclude that most of the activation energy of reaction is in the diffusion process.

Reactions with Positive Ions. The rate constants for the reactions of $e_{aq}^- + Cd^{2+}$ and $e_{aq}^- + Cu^{2+}$ have been measured in concentrated solutions of the perchlorate salts. The results are shown in Figures 7 and 8. The rate constants for dilute Cd^{2+} and Cu^{2+} as a function of added

$Ca(ClO_4)_2$ have also been measured.[28] It was found that for a given concentration of $Ca(ClO_4)_2 \gtrsim 0.04\ M$, the rate constants for dilute (~1–5 × 10$^{-4}\ M$) and for 0.01 $M\ Cd^{2+}$ are the same. This was also true for Cu^{2+}.

Using eq 5 we calculate τ_R = 61 psec at 0.25 $M\ Cd(ClO_4)_2$ whereas the observed half-life for reaction is 78 psec. By the same arguments used in considering the relaxation of Na$^+$ around e_{aq}^- in the NO_3^- reaction, we conclude that the time required for relaxation of the ionic atmosphere is less than the age of the e_{aq}^- we observe in the rate constant measurement. However, in this case the Cd^{2+} ions react at a nearly diffusion-controlled rate with e_{aq}^-, since the rate constant at zero ionic strength is 5.44 × 10$^{10}\ M^{-1}\ sec^{-1}$ (Peled and Czapski[27] report 6.4 × 10^{10}) or 0.76 of the diffusion-controlled k calculated from eq 2 (7.13 × 10$^{10}\ M^{-1}\ sec^{-1}$). Thus, our rate constant measurement corresponds to a time period in which a steady-state concentration around surviving e_{aq}^- has essentially been achieved. Further, this concentration gradient corresponds to a depletion of Cd^{2+} around the remaining e_{aq}^-, so that the e_{aq}^- we observe lack an ionic atmosphere of positive ions.

In view of the foregoing we apply the treatment of Coyle, Dainton, and Logan to the reaction of e_{aq}^- in pure

$Cd(ClO_4)_2$ solution as discussed in the Appendix so that $k_1(e_{aq}^- + Cd^{2+}) = (k_2k_0)^{1/2}$. We take k_2 as the rate constant for dilute Cd^{2+} in a concentration of $Ca(ClO_4)_2$ equal to the $Cd(ClO_4)_2$ concentration of k_1. We cannot measure k_0 directly as a function of $Cd(ClO_4)_2$ concentration. However, we have measured $k(e_{aq}^- + CH_3NO_2)$ as a function of $Ca(ClO_4)_2$ concentration using 0.05 and 0.5 M CH_3NO_2. We assume that k_0 (= 5.44×10^{10} at zero salt) varies proportionately with added salt as does $k(e_{aq}^- + 0.5 M CH_3NO_2)$, an assumption which yields the upper solid line in Figure 7. The Coulombic interaction for charged species without ionic atmosphere should not vary strongly with ionic strength, and, if the principal effect of the added salt is on the diffusion constants, then the above procedure should give a reasonable approximation to k_0. The mean of k_2 and k_0 is plotted (dashed line) in Figure 7. In view of the inadequacies of the treatment we cannot say whether the deviation between k_1 and experiment is significant. Any time-dependent effect appears to be small on our time scale.

Experiments with 0.01, 0.05, 0.1, and 0.2 M $Cd(ClO_4)_2$ were carried out, adding to each varying amounts of $Ca(ClO_4)_2$. The rate constant variations measured for these solutions are also plotted in Figure 7. If the rate constants on each of the curves for the four concentrations of $Cd(ClO_4)_2$ are normalized to 1.0 for the pure Cd^{2+} solutions and the resulting relative rate constants are plotted against $[Ca(ClO_4)_2]/[Cd(ClO_4)_2]$ all points fall on a single curve. This suggests that at each Cd^{2+} concentration the rate constant is affected in the same manner by the competition between Cd^{2+} and Ca^{2+} diffusing toward e_{aq}^-. Again from Figure 7 $k(e_{aq}^- + Cd^{2+})$ for 0.05 M $Cd(ClO_4)_2$ + 0.05 M $Ca(ClO_4)_2$ is found to be close to the mean of the k's for 0.1 M $Cd(ClO_4)_2$ and for dilute Cd^{2+} in 0.1 M $Ca(ClO_4)_2$, and similarly k for 0.1 M $Cd(ClO_4)_2$ + 0.1 M $Ca(ClO_4)_2$ is the mean of the k's for 0.2 M $Cd(ClO_4)_2$ and dilute Cd^{2+} in 0.2 M $Ca(ClO_4)_2$. This is consistent with the idea that the ionic strength due to the Cd^{2+} has little or no influence on the reaction rate. Thus, for pure cadmium perchlorate solutions, only the ionic strength effect due to the ClO_4^- sheath around the Cd^{2+} is effective in reducing the reaction rate, and the hydrated electron reacts almost without an ionic atmosphere.

We have measured $k(e_{aq}^- + Cu^{2+})$ as 3.88×10^{10} M^{-1} sec^{-1} (Peled and Czapski[27] give 4.5×10^{10}) or 0.54 of the diffusion-controlled value. Therefore, there will be more tendency to build up ionic atmospheres about e_{aq}^-. Nevertheless, the mean of k_2 and k_0 was again determined as for Cd^{2+}. In Figure 8 the experimental points at higher concentrations are again somewhat above the dashed line corresponding to the mean.

We tentatively conclude that in a diffusion-controlled reaction with a positive ion the hydrated electron reacts without an ionic atmosphere, and that any significant time-dependent effects precede our measurements (≥ 50 psec).

Conclusion

Time-dependent rate constants in accord with the theory of Noyes[5] were observed in the time range of 100 psec to 3.0 nsec for the reactions of the hydrated electron with high concentrations of highly reactive solutes. Several other factors may also affect the rate constants at high concentration.

Neutral Solutes. The reaction of e_{aq}^- + nitromethane is diffusion controlled and its rate constant varies with concentration (or time) as predicted by eq 1. Acetone reacts

with e_{aq}^- at only one-third the diffusion-limited rate and little variation of $k(e_{aq}^- + $ acetone) is expected or found.

Negatively Charged Reactants. The reaction of e_{aq}^- + NO_3^- occurs when the two are in physical contact, at a nearly diffusion-controlled rate. At higher ionic strength the repulsion between the like charged e_{aq}^- and NO_3^- is reduced, and thus the rate constant increases with increasing salt concentration. In our experiments e_{aq}^- acquires its ionic atmosphere before we observe its reaction. The observed variation of $k(e_{aq}^- + NO_3^-)$ with $[NaNO_3]$ is the product of the ionic strength effect and the time-dependent rate constant effect of eq 1. For both IO_4^- and CrO_4^{2-} the hydrated electron reacts by tunneling 10 Å, and the ionic strength effect disappears above 0.01 M salt, since the tunneling distance becomes greater than the distance at which the energy of Coulombic repulsion equals kT. For these two negative ions the variation in rate constant is accounted for entirely by the time-dependent effect.

Positively Charged Reactants. Cd^{2+} and e_{aq}^- react on almost every encounter. This means that in $Cd(ClO_4)_2$ solution the hydrated electron cannot build up a positive ion atmosphere and reacts without one. The rate constant is expected to be the mean of k_2 (dilute Cd^{2+} in $Ca(ClO_4)_2$, i.e., both e_{aq}^- and Cd^{2+} have ionic atmospheres) and k_0 (neither reactant has an ionic atmosphere). There may also be a small time-dependent effect. $k(e_{aq}^- + Cu^{2+})$ is half the diffusion-controlled rate. Thus a partial atmosphere of Cu^{2+} may be built up around unreacted e_{aq}^-. However, the mean rate constant equals $(k_2k_0)^{1/2}$ was calculated as for Cd^{2+}, and falls a little below the experimental values for higher concentrations of pure $Cu(ClO_4)_2$.

Appendix

Robinson and Stokes[33] give the derivation of a one parameter relation for mean activity coefficients

$$\log f_{\pm} = \frac{-0.51|Z_1Z_2|\mu^{1/2}}{1 + 0.329a\mu^{1/2}} - \frac{h}{n}\log a_W - $$
$$\log[1 - 0.018(h-n)m] \quad (6)$$

when n is the total number of ions from the salt (1 molecule of salt gives $n_1 + n_2 = n$ ions), h is the number of water molecules bound to n molecules of ions, a_W is the activity of the water, and m is the molality of the salt. The constant a, or mean distance of closest approach of ions, is given by, $a = r_1' + r_2 - \Delta$, where r_1' is the radius of the hydrated cation in ångströms, r_2 is the crystal radius of the anion, and Δ is the distance the hydration layer is penetrated when the ions approach each other. Δ is 0.7 Å for 1:1 salts and 1.3 Å for 2:1 salts. The value of r_1' is found from $\frac{4}{3}r_1'^3 = 30h + V_1$ where V_1 is the apparent molal volume of cation, and the value estimated for 1 M may be used at all concentrations since V_1 is small compared to $30h$. Thus only the parameter h needs to be fixed. Equation 6 is valid up to about $hm \approx 12$, when about one quarter of the water molecules are bound to the ions, i.e., up to 0.5 M or more depending on the salt. Equation 6 may be modified to give eq 7, since $f_{\pm}^n = f_1^{n_1}f_2^{n_2}$ and $|Z_1Z_2|$

$$\log f_1{}^{n_1} f_2{}^{n_2} a w^h [1 - 0.018(h - n)m]^n =$$

$$\frac{-0.51(n_1 Z_1{}^2 + n_2 Z_2{}^2)\mu^{1/2}}{1 + 0.329 a\mu^{1/2}} \quad (7)$$

was derived from $n_1 Z_1{}^2 + N_2 Z_2{}^2$ using the relation $n_1 Z_1 = -n_2 Z_2$. According to eq 7 we may write

$$f_1{}^{n_1} f_2{}^{n_2} K_m = (10^{-0.51 Z_1{}^2 K_L})^{n_1}(10^{-0.51 Z_2{}^2 K_\mu})^{n_2} \quad (8)$$

where K_m and K_μ are constants for a given molality, m. From this we write for the ith ion $-\log f_i(K_{im})^{1/n_i} = 0.51 Z_i{}^2 \mu^{1/2}/(1 + 0.329 a\mu^{1/2})$, noting that K_m or K_{im} involves ion–solvent interactions and therefore will be little affected by whether the ionic atmosphere is established around an ion or not. This suggests that the treatment of Coyle, Dainton, and Logan[9] can be extended to higher concentrations, with $k_1 = (k_2 k_0)^{1/2}$ if k_0 is defined as the rate constant where neither $e_{aq}{}^-$ nor the ion it reacts has an ionic atmosphere.

References and Notes

(1) Work performed under the auspices of the U.S. Energy Research and Development Administration.
(2) M. Anbar, M. Bambenek, and A. B. Ross, Natl. Stand. Ref. Data Ser., Natl. Bur. Stand., No. 43 (1973).
(3) Supplement 1 to ref 2, A. Ross, AEC Document C00-38-905, submitted 1973.
(4) F. C. Collins and G. E. Kimball, J. Colloid Sci., 4, 425 (1949).
(5) R. M. Noyes, Prog. React. Kinet., 1, 129 (1961).
(6) M. S. Matheson, E. J. Hart, J. R. Miller, and C. D. Jonah, Radiat. Res., 59, 110 (1974); Abstract B-20-4.
(7) G. V. Buxton, F. C. R. Cattell, and F. S. Dainton, J. Chem. Soc., Faraday Trans. 1, 71, 115 (1975).
(8) T. J. Chuang and K. B. Eisenthal, J. Chem. Phys., 62, 2213 (1975).
(9) P. J. Coyle, F. S. Dainton, and S. R. Logan, Proc. Chem. Soc., 219 (1964).
(10) S. R. Logan, Trans. Faraday Soc., 63, 3004 (1967).
(11) M. J. Bronskill, R. K. Wolff, and J. W. Hunt, J. Chem. Phys., 53, 4201 (1970).
(12) J. E. Aldrich, M. J. Bronskill, R. K. Wolff, and J. W. Hunt, J. Chem. Phys., 55, 530 (1971).
(13) R. K. Wolff, J. E. Aldrich, T. L. Penner, and J. W. Hunt, J. Phys. Chem., 79, 210 (1975).
(14) C. D. Jonah, Rev. Sci. Instrum., 46, 62 (1975).
(15) M. J. Bronskill and J. W. Hunt, J. Phys. Chem., 72, 3762 (1968); M. J. Bronskill, W. B. Taylor, R. K. Wolff, and J. W. Hunt, Rev. Sci. Instrum., 41, 333 (1970).
(16) G. Mavrogenes, W. J. Ramier, W. A. Wesolowski, K. Johnson, and G. Clifft, presented at the International Accelerator Conference, March 5-7, 1973, San Francisco Calif.
(17) G. Mavrogenes, G. Tripp, L. Coleman, C. Jonah, K. H. Schmidt, and S. Gordon, to be submitted for publication.
(18) P. Day and J. Hines, Oper. Systems Rev., 7, No. 4, 28 (1973).
(19) C. D. Jonah, M. S. Matheson, J. R. Miller, and E. J. Hart, J. Phys. Chem., submitted for publication.
(20) Equation 2.16 was obtained as an approximation[5] replacing e^{x^2} erfc x by $1/x\pi^{1/2}$, the first term of a series expansion, where $x = (D_{AB}t)^{1/2}(1 + k/4\pi r_{AB}D_{AB})/r_{AB}$. We have calculated the errors involved in this approximation with respect to the systems we have investigated. The approximation is high at the shortest times for Cu^{2+} by 17%, for Cd^{2+} by 10%, for acetone by 10%, for $NO_3{}^-$ by less than 2%; while for nitromethane, $CrO_4{}^{2-}$, and $IO_4{}^-$ the error is quite small.
(21) C. Naleway, results to be published.
(22) A. Mozumder and J. L. Magee, Radiat. Res., 28, 203-215 (1966).
(23) G. Czapski and E. Peled, J. Phys. Chem., 77, 893 (1973).
(24) K. H. Schmidt, Int. J. Radiat. Phys. Chem., 4, 439 (1972).
(25) H. A. Schwarz, J. Chem. Phys., 55, 3647 (1971).
(26) P. Debye, Trans. Electrochem. Soc., 82, 265 (1942).
(27) E. Peled and G. Czapski, J. Phys. Chem., 74, 2903 (1970).
(28) B. B. Saunders, W. A. Mulac, and M. S. Matheson, unpublished results.
(29) W. L. Masterton, D. Bolccofsky, and T. P. Lee, J. Phys. Chem., 75, 2809 (1971).
(30) H. Falkenhagen, "Theorie der Elektrolyte", S. Hirzel, Verlag, Stuttgart, 1971, p 120.
(31) J. R. Miller, to be published.
(32) E. J. Hart and M. Anbar, "The Hydrated Electron", Wiley-Interscience, New York, N.Y., 1970, p 188.
(33) R. A. Robinson and R. H. Stokes, "Electrolyte Solutions", 2nd ed, Academic Press, New York, N.Y., 1959, p 248.

Laser Flash Photolysis of Aqueous Tryptophan[1]

F. Dudley Bryant, R. Santus,[2] and L. I. Grossweiner*

Biophysics Laboratory, Physics Department, Illinois Institute of Technology, Chicago, Illinois 60616   (Received June 4, 1975)

Publication costs assisted by the Illinois Institute of Technology

Laser flash photolysis of aqueous tryptophan at 265 nm generates the neutral radical product of indole ring N–H bond photolysis (λ_{max} 510 nm, 1800 M^{-1} cm^{-1}; 330 nm, 3100 M^{-1} cm^{-1}), the triplet state (λ_{max} 460 nm), and the hydrated electron as initial products. The photoionization quantum yields for tryptophan, 1-methyltryptophan, tyrosine, and glycine–tryptophan peptides have been determined using ferrocyanide as the reference system. The electron and aromatic radical decay by a previously unreported first-order back reaction of 0.80-μsec half-time, leading to residual yields of the separated products after several microseconds significantly smaller than the photoionization yield. The kinetics results are consistent with the formation of a loose complex between the hydrated electron and the radical in which recombination competes with separation. The implications of this process for tryptophyl residue destruction in proteins are considered. A comparable first-order electron decay stage was observed with tryptophan derivatives, tyrosine, I$^-$, and Fe(CN)$_6{}^{4-}$.

Introduction

The mechanism of tryptophan (Trp) photolysis is of interest in connection with the photochemistry of indole derivatives and the role of Trp as a major chromophore in many proteins. Early flash photolysis studies showed that irradiation of aqueous Trp in the longest wavelength absorption band generates the hydrated electron ($e_{aq}{}^-$) and a radical coproduct absorbing near 500 nm.[3-6] Santus and Grossweiner identified this product with the neutral species (Trp) by showing that the radical cation absorbing

near 580 nm is formed by irradiating Trp in acidic conditions (Trp^+) or 1-methyltryptophan ($1\text{-}MeTrp^+$) in acidic or alkaline solutions.[7] The same workers identified the triplet states of Trp and 1-MeTrp with a 460-nm band of about 10^{-5} sec lifetime. The 5-μsec time response of the xenon flash lamp measurements was not adequate to establish the photoionization kinetics or the role of the triplet state in the electron ejection process. In a recent laser flash photolysis investigation of indole derivatives, Bent and Hayon[8] confirmed the identification of these Trp radicals and triplet state absorptions. They observed also a very short lived species at 450 nm (<10 nsec) suggested to be another triplet state associated with the presence of the terminal NH_3^+ group. Based on the dependence of the electron yield on the 3.6-nsec laser flash intensity it was concluded that neither the triplet states or the fluorescent state are involved in the photoionization process.

The work in this paper emphasizes the fate of the ejected electron. The usual e_{aq}^- reactions of water radiolysis do not explain the fast, exponential disappearance of the electron in the period from 100 nsec to about 1 μsec after the laser pulse. Similar decay kinetics were observed with Trp, 1-MeTrp, tyrosine, and several inorganic anions, indicative of a general phenomenon which does not appear to have been observed previously. New results are reported for the photoionization quantum yields obtained by comparison with ferrocyanide ion and the extinction coefficient of the Trp radical.

Experimental Section

The experiments were carried out with a 150-MW Nd: glass laser system (Holobeam Model 631) with Pockel's cell Q-switching providing a 17-nsec pulse at 265 nm after doubling with CDA and quadrupling with ADP crystals. The typical pulse energy at 265 nm was 60 mJ as measured with a calibrated photodiode and confirmed by estimating the electron yield obtained by photolyzing $Fe(CN)_6^{4-}$ as described in the Results. The transient absorptions were measured in a 1-cm quartz cuvette perpendicular to the laser flash using an ILC Type 4L2 xenon flash lamp as the monitoring beam. This lamp was energized by a 200-mF capacitor charged to 0.8 kV to provide a 300-μsec flash. A timing circuit applied the laser pulse during the peak flat output of 20-μsec duration. The laser beam was limited to a horizontal area 0.95-cm long by 3-mm high perpendicular to the monitoring beam. Spatial uniformity of the laser beam was monitored on each run by observing the "burn pattern" on a developed polaroid print. The beam was confined to a 2-mm depth from the front face of the cell so that the optical path length was 0.95 ± 0.05 cm through an irradiated volume of known dimensions. The transient spectra were measured with a Jarrell-Ash 0.25-mm grating monochromator with Hamamatsu HTV R-136 photomultiplier at the exit slit. A Tektronix Type 7704A oscilloscope with Tektronix Type C-51 camera made it possible to obtain usable single-sweep traces at 20 nsec/cm. The 1-methyltryptophan was prepared and purified by M. Bazin at Museum National d'Histoire Naturelle, Paris; other chemicals were the best available commercial grade, and were used as received.

Results

1. Transient Product Spectra and Yields. The transient spectra from 400 μM 1-MeTrp in Figure 1 show bands near 330 and 580 nm, not quenched by air, previously identified
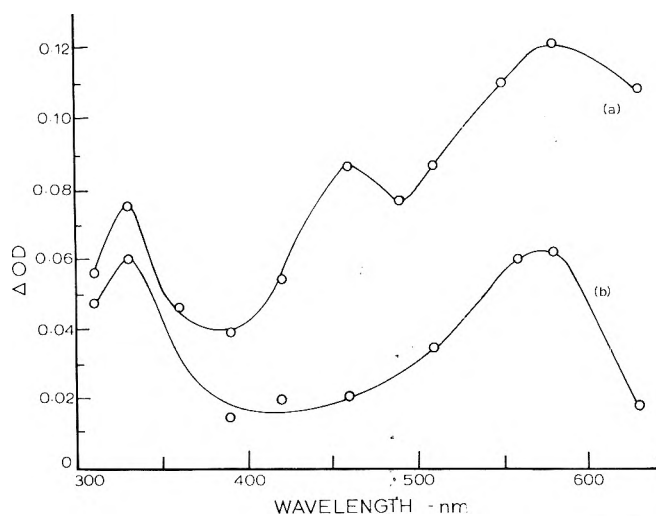
Figure 1. Transient spectrum from laser photolysis of 400 μM 1-methyltryptophan (aq): (a) nitrogen saturated, 0.7-μsec delay; (b) oxygen saturated, 0.7-μsec delay.
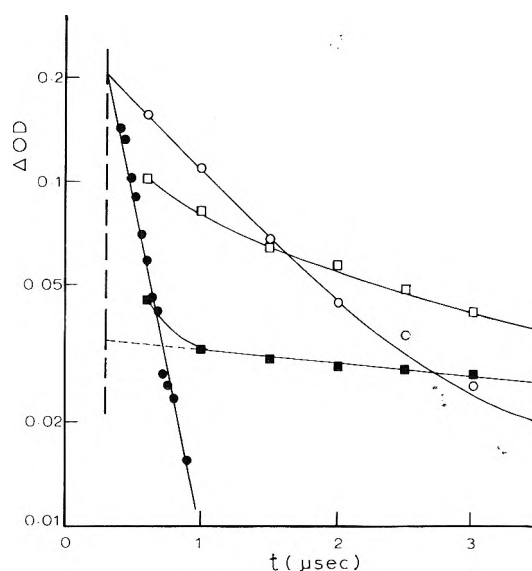
Figure 2. Transient decays from 400 μM tryptophan: (O) 630 nm, nitrogen saturated; (●) 630 nm, air saturated; (□) 510 nm, nitrogen saturated; (■) 510 nm, air saturated.

with the $1\text{-}MeTrp^+$ radical.[7] The 460-nm absorption evident in the deaerated solution has been attributed to the triplet state. Laser photolysis of Trp gave similar results with $1\text{-}MeTrp^+$ replaced by the 330- and 510-nm bands of neutral Trp. No precursors could be detected within the 50-nsec solution of our system indicating that deprotonation must be very fast. Typical decay results at 630 nm in Figure 2 show that the initial electron decay is exponential. The corresponding 510-nm decay represents a superposition of the electron, ^3Trp, and Trp. The radical extinction coefficient was determined by comparing the initial 630-nm optical density to the extrapolation of the "long-time" radical decay curve obtained in air-saturated solutions back to the time of the laser pulse. This method assumes that the radical and electron are 1:1 coproducts and the overlapping electron and triplet absorptions are negligible after about 1 μsec. The results in Table I are in satisfactory agreement with independent pulse radiolysis determinations, in which Trp and $1\text{-}MeTrp^+$ were produced by allow-

TABLE I: Optical Spectra of Aromatic Amino Acid Radicals

Solute	Radical	Spectra[a]		Ref
Tryptophan pH 7–12	Trp·	510 nm 1800 ± 200	330 nm 3100 ± 300	This work
pH 7		510 nm 1750(±20%)	320 nm 2800(±20%)	9a
pH 7		520 nm 1840	320 nm 2860	9b
Tyrosine pH 7	Tyr·	410 nm 2600 ± 500		This work
pH 7		410 nm 2750 ± 200		10
1-Methyltryptophan pH 7	1-MeTrp+	570 nm 2600(±20%)	340 nm 3900(±20%)	9a
pH 7		580 nm 2900 ± 600		This work

[a] Absorption maxima and molar absorbance (M^{-1} cm^{-1}).

TABLE II: Photochemical Electron Quantum Yields Based on Ferrocyanide Ion Reference System

Solute	pH[a]	$\Delta OD/(\Delta OD)_{ref}$[b]	ϕ_e[c]
400 μM tryptophan	aq (7)	0.48 ± 0.07	0.25
	9 (11)	0.70 ± 0.08	0.36
	11.8 (3)	0.82 ± 0.14	0.43
400 μM 1-methyltryptophan	aq (2)	0.69 ± 0.12	0.36
	11.8 (1)	0.81	0.42
1.5 mM tyrosine	aq(2)	0.55 ± 0.07	0.29[d]
	9 (2)	0.60 ± 0.02	0.31[d]
0.16 M KI	aq (3)	0.69 ± 0.05	0.36

[a] Number of runs in parentheses; 25 ± 1°C. [b] Initial ΔOD (630 nm) divided by ΔOD (630 nm) with $Fe(CN)_6^{4-}$ at same initial OD (265 nm). [c] Based on ϕ_e = 0.52 at 265 nm for $Fe(CN)_6^{4-}$.[12] [d] Proposed as a biphotonic process in ref 8.

ing Br_2^- or $(CNS)_2^-$ to react with the ground state molecules.[9] The same approach applied to tyrosine gives results in fair agreement with an earlier flash photolysis determination, notwithstanding the evidence in that work that about 20% of the phenoxyl radical results from O–H bond splitting and not photoionization.[10]

Previous measurements of the aqueous Trp photoionization electron quantum yield were based on actinometric techniques. The results reported for broad-band flash lamp irradiation were 0.09 (pH 11.8)[11] and 0.008 (pH 10–12),[6] while laser flash photolysis at 265 nm led to 0.08 at pH 6 and 0.21 at pH 11.[8] The low values obtained with conventional flash techniques must be discounted because of the electron–radical back-reaction discussed below. Although the laser data should be accurate in principle, pulsed laser outputs are variable and difficult to measure accurately. A comparison method has been employed in the present work based on measuring the electron yield from $Fe(CN)_6^{4-}$ solutions of the same initial absorbance. The photochemistry of $Fe(CN)_6^{4-}$ has been investigated extensively. While there has been controversy about the photoionization mechanism between Stein[12,13] and Dainton,[14] the electron yields obtained with several scavenging systems are in good agreement. The present results have been normalized to ϕ_e = 0.52 at 265 nm (no buffer) reported by Shirom and Stein[12] where N_2O was employed as the electron scavenger. The same work reports ϕ_e = 0.66 at 254 nm, in exact agreement with Airey and Dainton[14] for N_2O solutions from pH 4 to 12. The results in Table II were obtained by extrapo-

lating the optical density at 630 nm back to the time of the laser flash. The "initial" yields as reported here exclude any components that decay within 50 nsec and do not consider possible nonlinear absorption effects at laser intensities. Bent and Hayon[8] observed a slightly higher yield of e_{aq}^- with <10-nsec decay which could not be observed with our system.

The effect of peptide bonding on the electron yield is relevant to the photoionization of tryptophyl residues in proteins. The results for three time periods are summarized in Table III, normalized in each case to Trp as unity. The <50 nsec period should include any very fast electron decay processes that could not be resolved with our apparatus. The 100 nsec results are the linear extrapolation of the present laser data to the time of the laser flash. The 5 μsec data are new results of Baugher[15] obtained with a xenon flash lamp system, representing the approximate radical yields at the completion of the exponential decay period. The three independent sets of measurements show that peptide bonding decreases the actual electron yield at each stage of the decay process.

2. Electron Decay. At a typical electron concentration of 20 μM at 100 nsec one would expect a second-order decay of about 3-μsec half-time based on $k(e_{aq}^- + e_{aq}^-) = 6 \times 10^9$ M^{-1} sec^{-1}.[16] Instead, we observed consistently that the disappearance of the electron was exponential during the time period where about 80% of the initial yield disappears. Check experiments were done with several sources of distilled water and chemicals, with and without buffers, sever-

TABLE III: Relative Electron Yields at Three Time Stages

Solute	< 50 nsec[a]	100 nsec[b]	5 μsec[c]
Trp	(1.0)	(1.0)	(1.0)
Trp-Gly	0.6	0.8	0.6
Gly-Trp	0.4	0.6	0.5
Gly-Trp-Gly	0.5		0.4

[a] Reference 8. [b] This work. [c] Reference 15; based on Trp yields.
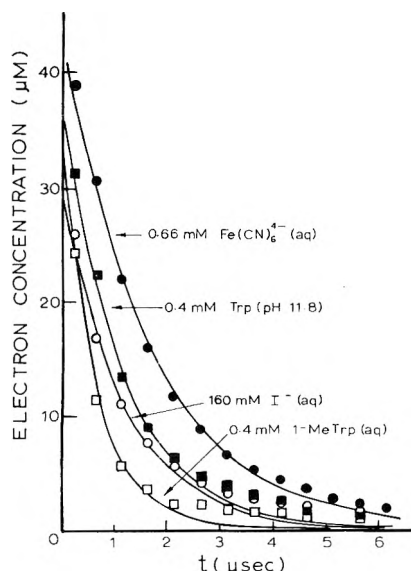
Figure 3. Analog computer fitting of observed electron decays to first-order kinetics.

Figure 4. Electron decay from laser photolysis of 0.66 mM ferrocyanide (points): (a) theoretical decay for bimolecular process with 10:1 initial electron distribution in two compartments across cell (see text); (b) theoretical decay for bimolecular process with uniform initial electron distribution.

al sources of saturating nitrogen and evacuation, and different irradiation cells, with no indications that the results are an experimental artifact. Figure 3 shows the analog computer fit of exponential decay to the data obtained with several solutes. The average first-order electron decay lifetime for Trp photolysis was 0.80 ± 0.04 μsec for 18 runs from pH 6.4 to 11.8 and with Trp concentrations ranging from 100 to 800 μM. Since the initial OD (265 nm) varied from 0.4 to 3.2 (1 cm path) the possibility of an error due to concentration gradients across the monitoring field was considered using the analysis of Boag.[17] Figure 4 shows the measured electron decay obtained from photolysis of 0.66 mM Fe(CN)$_6^{4-}$ (points) and the expected second-order decay if the same initial electron concentration were uniformly distributed (Figure 4b). The apparent second-order decay if the electrons are divided into two compartments across the cell with 10 times higher initial concentration in one than the other is shown in Figure 4a. Although this high nonuniformity leads to a small error in the magnitude of the measured optical density, the predicted decay curve does not approach the experimental data. The actual electron concentration change across the 2-mm measuring window was 2.1 with 400 μM Trp, so that the case of Figure 4a is an extreme overestimate. It can be concluded that nonuniform light absorption in the direction of the laser beam cannot lead to a concentration gradient across the cell such that the usual bimolecular electron decay reaction has the appearance of an exponential process of the correct lifetime.

In view of the e_{aq}^- extinction coefficients of 14400 at 630
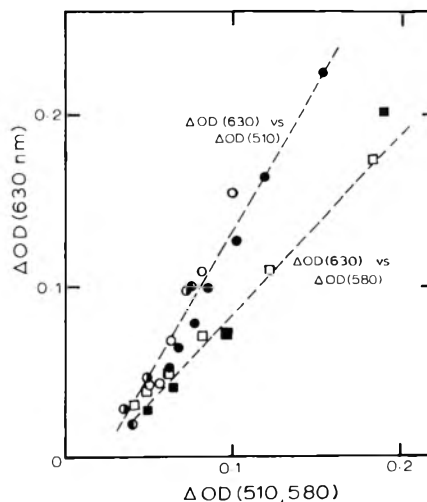
Figure 5. Relationship of electron absorption to radical absorption after laser photolysis: (O) tryptophan (aq); (◑) tryptophan (pH 9.0); (◐) tryptophan (pH 10.0); (●) tryptophan (pH 11.8); (■) 1-methyltryptophan (aq); (□) 1-methyltryptophan (aq). Each set of points represents an independent run; all 400 μM, nitrogen-saturated solutions. The *dashed lines* indicate the slope that should be observed if the electrons and radicals react together (see text).

nm, 11000 at 580 nm, and 6400 at 510 nm (M^{-1} cm^{-1})[18,19] it is apparent that the electron when present makes a major contribution to the total absorbance in the radical bands. However, if the radicals and e_{aq}^- maintain a constant concentration ratio during the exponential decay process, then ΔOD (630 nm) is proportional to ΔOD (510 nm) for Trp photolysis and to ΔOD (580 nm) for 1-MeTrp photolysis (see Discussion). The proportionality constant in each case should be approximately the corresponding value of $\epsilon_e^{630}/(\epsilon_e^{510} + \epsilon_R^{510})$ or $\epsilon_e^{630}/(\epsilon_e^{580} + \epsilon_R^{580})$. Figure 5 shows experimental data for several runs where ΔOD (630 nm) is plotted against ΔOD(510 nm) or ΔOD(580 nm) at different

TABLE IV: Dependence of Electron Decay Half-Time on Temperature after Laser Photolysis of Aqueous Tryptophan

t, °C	$\tau_{1/2}$, μsec	η^b	$10^5 \tau_{1/2}/\eta$
27.0	0.86 ± 0.08	0.851	1.01
40.0	0.65 ± 0.06	0.653	1.00
50.0	0.54 ± 0.10	0.547	0.99
60.0	0.49 ± 0.10	0.467	1.05

[a] Electron decay half-time; average of three runs; 400 μM Trp at pH 9. [b] Water viscosity, centipoise.

times during the exponential decay period. The dashed lines are drawn with the slope specified by the appropriate extinction coefficient values (Table I) and fit quite well. It is concluded that a back reaction of the electron and radical takes place during the exponential decay stage, so that the products previously measured with conventional flash photolysis are residual yields after substantial recombination. The rate of the exponential decay process increases with increasing temperature closely following the same temperature dependence as the viscosity of water (Table IV), suggesting that solvent reorganization is involved in the back reaction. In air-saturated solutions the electron decay half-time for Trp was reduced to 0.13 ± 0.02 μsec (15 runs). This value corresponds with the expected halftime for the superposition of an anaerobic process of 0.80-μsec half-time and scavenging by oxygen with $k(e_{aq}^- + O_2) = 2 \times 10^{10} \ M^{-1} \ \text{sec}^{-1}$.[16] However, a series of runs with added H_2O_2 led to an effective rate constant of $k(e^- + H_2O_2) = 7 \times 10^9 \ M^{-1} \ \text{sec}^{-1}$ compared with the radiolysis value of $k(e_{aq}^- + H_2O_2) = 1.2 \times 10^{10} \ M^{-1} \ \text{sec}^{-1}$,[16] suggesting that the electron may be less accessible than free e_{aq}^-. A mechanism that explains the experimental observations is based on the assumption that the electron and radical form a loosely bound complex in which the first-order back-reaction competes with separation into free products. The implications of this process for the photochemistry of Trp are considered below.

Discussion

The photoionization pathway of an aromatic molecule in aqueous solution depends critically upon the specific structure and dissociation state. Recent work indicates that the photoionization of phenylalanine is biphotonic in neutral and alkaline solutions[8] while the tyrosine photolysis mechanism changes from biphotonic to monophotonic when the phenolic group is dissociated.[8,20e] The triplet state was postulated as the intermediary in those cases. It does not appear that either the Trp triplet state or fluorescent state are involved in the photoionization of Trp. Bent and Hayon[8] suggest that the electron is released from a higher excited-singlet state or a vibrationally excited, lowest excited-singlet state. Their work indicating that the electron release intermediary has a lifetime <3.6 nsec is consistent with the earlier conclusion of Grossweiner and Usui[11] that photoionization, followed by rapid deprotonation in neutral and alkaline solutions, competes with the formation of the Trp fluorescent state. It now appears quite certain that within several nanoseconds after excitation of aqueous Trp in the longest wavelength absorption band, initial products are formed with absorptions similar to e_{aq}^- and the same Trp radicals as observed after 5 μsec in water or stabilized in rigid media.[7] The present work indicates that these ini-

tial products remain coupled and interact via a first-order back-reaction with 0.80-μsec half-time. This mechanism is supported by recent flash photolysis studies on N-acetyltryptophanamide by Evans et al.[20b] indicating that the absorption maximum of the electron at 5 μsec delay is blueshifted about 20 nm from the radiolysis e_{aq}^- absorption as attained in their work after about 20 μsec. This effect was not observed with aniline.

To a first approximation the exponential stage may be considered as the competition between the back-reaction and separation of the complex:

$$(\text{Trp} \ldots \text{e}^-) \quad \begin{array}{c} \xrightarrow{\text{H}^+} \text{Trp} \\ \longrightarrow \text{Trp} + \text{e}_{aq}^- \end{array} \quad \begin{array}{c} (1) \\ (2) \end{array}$$
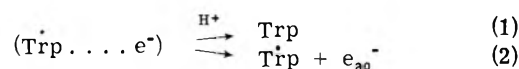
leading to the kinetics solution:

$$[\text{e}^-]_{tot} = \frac{[\text{e}^-]_0}{k_1 + k_2} (k_2 + k_1 e^{-(k_1+k_2)t}) \tag{I}$$

where $[\text{e}^-]_{tot}$ is the sum of the electron concentrations in the complex and present as free e_{aq}^-. The good fit of the decay data to pure exponential indicates that reaction 1 dominates. A certain fraction of the original electrons and radicals survive the recombination stage and subsequently react as free species. The residual fraction can be estimated by comparing the "initial" yields as measured with xenon lamp flash photolysis with Table II. Pailthorpe et al.[6] reported electron quantum yields of 0.008 ± 0.002 for Trp and 0.006 ± 0.002 for 1-MeTrp (pH 10–12) by extrapolating the e_{aq}^- absorbance at 250 μsec to zero time leading to $k_1 \simeq 50k_2$. The "long-time" tail of the data in Figure 3 which deviates from the line is attributed to residual electrons which react via the slower bimolecular processes.

The linear dependence in Figure 5 can be strictly true only for complete recombination of electrons and radicals. The assumption that the free and complexed electrons and radicals present at any time have the same extinction coefficients leads to

$$\Delta OD(510)/\Delta OD(630) = \frac{\epsilon_e^{510}}{\epsilon_e^{630}} + \frac{\epsilon_R^{510}[\text{R}]_c + \epsilon_R^{510}[\text{R}]_f}{\epsilon_e^{630}[\text{e}^-]_c + \epsilon_e^{630}[\text{e}^-]_f} \tag{II}$$

where f and c denote free and complexed species, respectively. Assuming that $[\text{e}^-]_c \gg [\text{e}^-]_f$ during the initial decay stage leads to

$$\Delta OD(510)/\Delta OD(630) \simeq \frac{\epsilon_e^{510} + \epsilon_R^{510}}{\epsilon_e^{630}} + (\epsilon_R^{510}/\epsilon_e^{630})\frac{[\text{R}]_f}{[\text{e}^-]_c} \tag{III}$$

In the case of the Trp radical, the first term on the right side equals 0.57 while the coefficient of the second term on the right is 0.125. Furthermore, $[\text{R}]_f \ll [\text{e}^-]_c$ so that the second term is negligible during the exponential decay stage, when the concentrations of free electrons and radicals are low, in agreement with the good fit in Figure 5. (The corresponding values for 1-MeTrp⁺ are 0.95 and 0.18.) Although the exact solution of kinetic system in which a second-order decay follows a first-order decay cannot be found, the above considerations show that the proposed model is in approximate agreement with the experimental data.

The electron back-reaction should lead to photooxidation quantum yields significantly lower than the laser flash

initial yields. The average of four published values cited by Vladimirov et al.[21] is 0.0065 ± 0.0012 for irradiation of aqueous Trp at 254 to 280 nm, i.e., about 50 times smaller than 0.25 in Table II. (Pailthorpe et al.[6] report permanent destruction quantum yields about a factor of 10 higher than the earlier determinations but there is no obvious explanation for the discrepancy.) The quantum yields for Trp destruction in proteins are considerably higher than aqueous Trp when based on light absorbed by tryptophyl residues, e.g., lysozyme 0.040;[22] trypsin 0.047;[22] papain 0.06;[23] myosin 0.013;[24] ovalbumin 0.015.[24] Flash photolysis spectra for a number of proteins have shown that the Trp radical and e_{aq}^- are initial products (e.g., lysozyme,[11] trypsin,[25] papain,[26] carbonic anhydrase,[27] human serum albumin[27]) so that the higher Trp destruction yields can be explained by the suppression of the back-reaction promoted by rapid reaction of the electron at nearby electrophilic sites. The actual photolysis quantum yields per residue are almost certainly several times higher than the above average values because the exposed Trp residues should be much more photolabile than the buried residues. The lower electron yields in the small Trp peptides (Table III) may be a result of competitive photolysis pathways in which the electron is not a product, which might contribute also to the higher photolysis yield of Trp in proteins. Laser photolysis experiments on proteins should help clarify this key point.

In view of the more rapid disappearance of the electron during the exponential decay stage when oxygen is present, it might be expected that the radical yield after about 1 μsec would be considerably higher than in deaerated solutions. However, the flash spectra indicate that the radical yields are actually somewhat lower at this time period (e.g., Figure 1 and ref 7). The only possible explanation we can suggest for this surprising result is that molecular oxygen diffuses into the complex and replaces the electron, leading to the apparent disappearance of the e_{aq}^- absorption, while the back-reaction between O_2^- and the radical continues. The electron decay half-time for Trp derivatives is constant within the statistical variation. The average value for Trp (18 runs) 1-MeTrp (3 runs), Gly-Try (3 runs), and Trp-Gly (4 runs) was 0.78 ± 0.03 μsec at pH 6.4 to 11.8. Corresponding values for other solutes are: tyrosine 0.67 ± 0.07 μsec (4 runs; pH 7), I^- 0.80 ± 0.05 μsec (2 runs; pH 7), and $Fe(CN)_6^{4-}$ 1.01 ± 0.03 μsec (21 runs; pH 9.5). The relatively small effect of the radical charge on the decay rate suggest that the interacting species are separated by several water layers, which is consistent also with the rate of electron scavenging by oxygen and excellent correlation between the effect of temperature on the decay rate and the viscosity of water. Although e_{aq}^- complexes have not been

postulated previously, there is no reason why they should not be formed with the observed properties. This type of intermediate can be stabilized only after hydration of the ejected electron and does not involve the postulated "solvent cage". While the present work was undertaken to study the photolysis of aqueous Trp, the observation of the exponential electron decay with I^- and $Fe(CN)_6^{4-}$ indicates that previously proposed mechanisms for inorganic anion photolysis cannot be correct and should be reexamined.

References and Notes

(1) Work supported by ERDA Contract No. AT(11-1)-2217. This is COO-2217-11.
(2) Laboratoire de Biophysique, Museum National d'Histoire Naturelle, Paris.
(3) L. I. Grossweiner, G. W. Swenson, and E. F. Zwicker, *Science,* **141,** 805 (1963).
(4) L. I. Grossweiner and H. I. Joschek, *Adv. Chem. Ser.,* **No. 50,** 279 (1965).
(5) H. I. Joschek and L. I. Grossweiner, *J. Am. Chem., Soc.,* **88,** 3261 (1966).
(6) M. T. Pailthorpe, J. P. Bonjour, and C. H. Nicholls, *Photochem. Photobiol.,* **17,** 209 (1973).
(7) R. Santus and L. I. Grossweiner, *Photochem. Photobiol.,* **15,** 101 (1972).
(8) D. V. Bent and E. Hayon, *J. Am. Chem. Soc.,* **97,** 2599, 2606, 2612 (1975).
(9) (a) J. L. Redpath, R. Santus, J. Ovadia, and L. I. Grossweiner, *Int. J. Radiat. Biol.,* **27,** 201–204 (1975); (b) M. L. Posner, G. E. Adams, P. Wardman, and R. B. Cundall, *J. Chem. Soc., Faraday Trans. 2,* submitted for publication.
(10) J. Feitelson and E. Hayon, *J. Phys. Chem.,* **77,** 10 (1973).
(11) L. I. Grossweiner and Y. Usui, *Photochem. Photobiol.,* **13,** 195 (1971).
(12) M. Shirom and G. Stein, *J. Chem. Phys.,* **55,** 3372, 3379 (1971).
(13) G. Stein, "Actions Chimiques et Biologiques des Radiation", Vol. 13, M. Haissinsky, Ed., Masson, Paris, 1969, pp 119–144.
(14) P. L. Airey and F. S. Dainton, *Proc. R. Soc. London, Ser. A,* **291,** 340, 478 (1966).
(15) J. F. Baugher, unreported results.
(16) M. Anbar, M. Bamenek, and A. B. Ross, *Natl. Stand. Ref. Data Ser., Natl. Bur. Stand.,* **No. 43** (1973).
(17) J. W. Boag, *Trans. Faraday Soc.,* **64,** 677 (1968).
(18) E. M. Fielden and E. J. Hart, *Trans. Faraday Soc.,* **63,** 2975 (1967).
(19) B. D. Michael, E. J. Hart, and K. H. Schmidt, *J. Phys. Chem.,* **75,** 2798 (1971).
(20) (a) J. Feitelson, E. Hayon, and A. Treinin, *J. Am. Chem. Soc.,* **95,** 1025 (1973); (b) R. F. Evans, W. A. Volkert, and C. A. Ghiron, private communication.
(21) Yu. A. Vladimirov, D. I. Roshchupkin, and E. E. Fesenko, *Photochem. Photobiol.,* **11,** 227 (1970).
(22) S. Risi, K. Dose, T. K. Rathinasamy, and L. Augenstein, *Photochem. Photobiol.,* **6,** 423 (1967).
(23) K. Dose and S. Risi, *Photochem. Photobiol.,* **15,** 43 (1972).
(24) Yu. A. Vladimirov and N. I. Perrase, *Biofizika,* **13,** 988 (1968).
(25) A. G. Kaluskar and L. I. Grossweiner, *Photochem. Photobiol.,* **20,** 329 (1974).
(26) J. F. Baugher and L. I. Grossweiner, *Photochem. Photobiol.,* in press.
(27) A. G. Kaluskar, Ph.D. Thesis, Illinois Institute of Technology, 1973.

Radiolysis of Compounds in Solution. Model Calculations on the Effects of Concentration, Impurity, and Dose Rate

Robert N. Rice, George Gorin, and L. M. Raff*

Chemistry Department, Oklahoma State University, Stillwater, Oklahoma 74074 (Received March 26, 1975)

Publication costs assisted by the National Science Foundation

The kinetic behavior of compounds subjected to radiolysis in solution has been investigated for a generalized mechanism that comprises an infinite number of consecutive reactions between the radiolysis products and radicals (Z·) derived from the solvent. When steady-state conditions for these primary radicals exist, it is rigorously shown that the dose, D_x, required to convert any desired fraction x of the original solute A_1 into products varies linearly with the initial A_1 concentration, A_0, regardless of the number of steps in the process and independently of whether or not A_1 decreases exponentially with dose. Furthermore, it is demonstrated that the slope of the linear plot measures the reactivity of A_1 and all products derived therefrom with (Z·), while the intercept measures the reactivity of (Z·) with solute-independent impurities that may be present. The kinetic behavior of the system is independent of dose rate when only consecutive steps are involved in the radiolysis mechanism. The characteristics of radiolysis mechanisms that involve reaction of the solute with secondary products of the radiolysis have also been investigated. Such mechanisms do not, in general, yield linear plots of D_x vs. A_0. The deviation from linearity are, in fact, a measure of the reactions of solute with secondary products. Model calculations also show that the kinetic behavior of such systems depends on the dose rate. This dependence can, under the proper conditions, become manifest at much lower dose rates than that due to reactions of primary and secondary intermediates with one another.

Introduction

Ionizing radiations are, unfortunately, extraordinarily harmful to living organisms. Many of them, including man, are killed by exposures to 300–3000 rads, even though the amount of energy absorbed is minute, 3–30 (J kg^{-1}).[1] If adequately controlled, radiation can, however, be put to important and humane uses, notably in cancer therapy.[2]

A great deal of attention has accordingly been devoted to investigating the effects of radiation upon the substances of which living organisms are composed. For the most part, these substances have complex, polymeric chemical structures, with molecular weights in the range of 10^4–10^9. When exposed to radiation, the molecules of these substances can undergo a myriad of chemical changes. A large volume of experimental data has been obtained, but the interpretation of this data has proven to be a very difficult and laborious task.

A number of models have been proposed to interpret the kinetics of radiolysis in aqueous solutions[3–9] (additional references, published before 1959, may be found in the cited papers). In these models, however, one or more of the following restrictions have been imposed: (1) that inactivation or decomposition of the substrate vary exponentially with the dose; (2) that the substrate be inactivated only by reaction with radicals derived directly from the solvent, thus excluding inactivation by secondary products derived from further reaction of said radicals; and (3) that impurities be negligible.

In the present paper we present a phenomenological treatment for some model systems in which we have relaxed the above restrictions. The characteristics of consecutive and parallel radiation processes are derived, and the effects of dose rate examined for each case. It is recognized that the models examined are much simpler than the systems which have been investigated experimentally. The results of the model calculations nevertheless shed some light on how properly to interpret existing phenomenological kinetic data. They also suggest types of experiments that might be carried out in the future to elucidate aspects of the problem that are currently still in doubt.

Theoretical Formulation

In the model systems we shall be considering, the concentration of biologically active substance will be denoted by A_1. We shall assume that its concentration is directly proportional to some property, Φ, that is measured experimentally, i.e., $A_1 = \phi\Phi$.[10]

It is assumed that the mass fraction of water is much greater than that of A_1, so that the energy absorbed "directly" by A_1, and its consequences, can be neglected. The water is decomposed by the radiation into radicals (Z·):

$$H_2O \rightsquigarrow (Z\cdot)$$
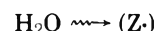
where (Z·) represents (OH·), (H$_2$O·$^-$), (H·), etc. If the "yield" of radicals is G, we may write for the rate of production of (Z·), $d(Z\cdot)/dt = G\rho(dD/dt)$, where ρ is a proportionality constant that has the dimensions of density (= energy absorbed × dose^{-1} × volume^{-1}).

It is further assumed that the chemical processes following the absorption of radiation can be described by specific rate coefficients, $k_1 \ldots k_i$, which have the significance usually attributed to them in chemical kinetics, i.e., they represent the reactivity of thermally equilibrated species and are constant throughout the solution.

The initial concentration of A_1 is denoted by A_0. It is postulated that successive reactions with (Z·) converts A_1 into products $A_2 \ldots A_i$, and no restriction is placed, except as specified, on the number of such reactions that may take

place until a product I is formed which is impervious to further reaction with (Z·). It is furthermore stipulated that the products $A_2 \ldots A_i$ have no biological activity, i.e., A_1 at any point is measured by the value of Φ.

Since it is never possible, in any real system, to eliminate all the impurities, it is appropriate to have a formulation that permits their influence to be evaluated. Accordingly, the model allows the presence of one or more impurities, $C_1 \ldots C_i$, in the solvent medium.

Finally, the models do not permit the reaction of one (Z·) with another or with the products of such reactions. In point of fact, such processes must inevitably come into play as A_i and C_i approach zero, since at that point there would be nothing else left with which (Z·) might react. However, such processes are expected to become important only at very low concentrations, far below those actually utilized in most laboratory experiments, or at extremely high dose rates.[11-15]

The models are analyzed within the framework of the "steady-state" approximation, i.e., in the condition that the concentration of (Z·) radicals remain essentially constant:

$$d(Z\cdot)/dt \approx 0$$

Since the concentrations of (Z·) to be expected at "moderate" dose rates (1–100 rads sec^{-1}) is on the order of 10^{-9} M, steady-state conditions can generally be expected to be present.

The list of symbols to be employed in the paper is as follows: G = yield of radicals (Z·) per unit energy absorbed; D = radiation dose; ρ = proportionality constant; t = time; (Z·) = primary radical product from radiolysis of water; A_0 = initial concentration of biologically active substance A_1; k_j = thermal reaction rate coefficient for reaction of (Z·) with A_j; A_j = product formed by the reaction of A_{j-1} with (Z·); I = concentration of product impervious to reaction with (Z·); C_0 = initial concentration of impurity C_1 in the solvent; $C_i (i \neq 1)$ = concentration of impurity formed by reaction of C_{i-1} with (Z·); K_n = thermal reaction rate coefficient for reaction of (Z·) with C_n.

A. Consecutive Processes. We begin by investigating the kinetics to be expected if the radiolysis mechanism consists of a series of consecutive reactions with (Z·). The mechanism to be considered then is

$$H_2O \xrightarrow{G\rho(dD/dt)} (Z\cdot)$$

$$A_1 + Z\cdot \xrightarrow{k_1} A_2$$

$$A_2 + Z\cdot \xrightarrow{k_2} A_3$$

$$\cdots$$

$$A_j + Z\cdot \xrightarrow{k_j} I$$

$$C_1 + Z\cdot \xrightarrow{K_1} C_2$$

$$C_2 + Z\cdot \xrightarrow{K_2} C_3$$

$$\cdots$$

$$C_n + Z\cdot \xrightarrow{K_n} I$$
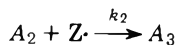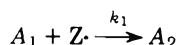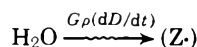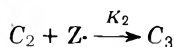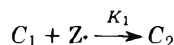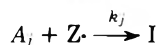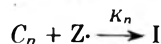
For arbitrary j and n, we have

$$dA_1/dt = -k_1 A_1 (Z\cdot) \tag{1}$$

$$dA_i/dt = [k_{n-1}A_{n-1} - k_n A_n](Z\cdot) \tag{2}$$

for $1 < i \leq j$

$$dC_1/dt = -K_1 C_1 (Z\cdot) \tag{3}$$

and

$$dC_m/dt = [K_{m-1}C_{m-1} - K_m C_m](Z\cdot) \tag{4}$$

for $(1 < m \leq n)$.

The steady-state concentration of (Z·) is now given by

$$(Z\cdot) = G\rho(dD/dt)\left[\sum_{i=1}^{j} k_i A_i + \sum_{m=1}^{n} K_m C_m\right]^{-1} \tag{5}$$

Integration of the above equations is most conveniently done in terms of the transformed variable

$$x = A_1/A_0 \tag{6}$$

Substitution of eq 5 into eq 2 followed by use of eq 6 yields, after integration

$$D_x = -\frac{1}{G\rho}\left[A_0(x-1) + \sum_{i=2}^{j}\frac{k_i}{k_1}\int_1^x \frac{A_i\,dx}{x} + \sum_{m=1}^{n}\frac{K_m}{K_1}\int_1^x \frac{C_m\,dx}{x}\right] \tag{7}$$

It may be shown that the second term in eq 7 is proportional to A_0:

$$\left[\sum_{i=2}^{j}\frac{k_i}{k_1}\int_1^x \frac{A_i\,dx}{x}\right] \propto A_0 \tag{8}$$

The proof is as follows. Division of eq 1 by eq 2 followed by integration between corresponding limits yields

$$A_i = -\frac{k_{i-1}}{k_1}x^{k_i/k_1}\int_1^x \frac{A_{i-1}\,dx}{x^{(k_i/k_1+1)}} \tag{9}$$

For $i = 2$, this gives

$$A_2 = -x^{k_2/k_1}A_0 \int_1^x x^{-(k_2/k_1)}\,dx \tag{10}$$

We now define

$$f_2(x) \equiv -x^{k_2/k_1}\int_1^x x^{-(k_2/k_1)}\,dx \tag{11}$$

which makes $A_2 = A_0 f_2(x)$. In a straightforward manner, eq 9 now yields with $i = 3$

$$A_3 = \frac{-k_2}{k_1}x^{k_3/k_1}A_0 \int_1^x \frac{f_2(x)\,dx}{x^{(k_3/k_1+1)}} \tag{12}$$

We now define for general i

$$f_i(x) \equiv \frac{-k_{i-1}}{k_1}x^{k_i/k_1}\int_1^x \frac{f_{i-1}(x)\,dx}{x^{(k_i/k_1+1)}} \tag{13}$$

With this definition we have $A_3 = f_3(x)A_0$.

A simple induction proof now demonstrates that

$$A_n = f_n(x)A_0 \tag{14}$$

and consequently

$$\sum_{i=2}^{j}\frac{k_i}{k_1}\int_1^x \frac{A_i\,dx}{x} = A_0 \sum_{i=2}^{j}\frac{k_i}{k_1}\int_1^x \frac{f_i(x)\,dx}{x} \tag{15}$$

which is the required proof.

By a similar derivation, we can show that

$$C_m = h_m(x)C_0 \tag{16}$$

where

$$h_m(x) = -\frac{K_{m-1}}{K_1} x^{K_m/K_1} \int_1^x \frac{h_{m-1}(x)\,dx}{x^{(K_m/K_1+1)}} \qquad (17)$$

for $m > 1$, and

$$h_1(x) = x^{K_1/k_1} \qquad (18)$$

The above results indicate that eq 7 may be written in the form

$$D_x = -\frac{1}{G\rho}\left[A_0\left\{(x-1) + \sum_{i=2}^{j} \frac{k_i}{k_1} \int_1^x \frac{f_i(x)\,dx}{x}\right\} + C_0 \sum_{m=1}^{n} \frac{K_m}{K_-} \int_1^x \frac{h_m(x)\,dx}{x}\right] \qquad (19)$$

Equation 19 may be applied to the case in which diverse impurities are present. In that case, C_0 is the sum of all initial impurities, and the K_i are effective rate coefficients that measure the rate of subsequent reactions of these impurities.

Equation 19 clearly indicates that the dose required to reduce the activity of substance A_1 to a fraction x of its original value increases linearly with the initial concentration A_0. From eq 19 we see that the slope of the line is given by

$$\text{slope} = \frac{-1}{G\rho}\left[(x-1) + \sum_{i=2}^{j} \frac{k_i}{k_1} \int_1^x \frac{f_i(x)\,dx}{x}\right] \qquad (20)$$

i.e., it is proportional to the capacity of solute A_1 and all derived products A_j to react with (Z·). From eq 19, it can also be seen that the intercept is

$$\text{intercept} = C_0 \sum_{m=1}^{n} \frac{K_m}{K_1} \int_1^x \frac{h_m(x)\,dx}{x} \qquad (21)$$

i.e., it is a measure of the radical scavenging ability of the solute-independent impurity and of all products derived from it.

Similar equations have been previously derived by Augenstine[4] and by Hutchinson and Ross.[5] However in both cases the derivations assumed that the decomposition or inactivation of A_1 was exponential with dose. The above results demonstrate that such restriction is not necessary. Any consecutive mechanism will exhibit such behavior. Conversely, if a linear D_x vs. A_0 plot is found empirically, this may be taken as evidence for a consecutive radiolysis mechanism.

It is instructive to note in this connection what conditions would give rise to an exponential relationship between A_1 and D. From eq 1 and 5 it may be seen that exponential concentration–dose curves will result if and only if

$$\sum_{i=1}^{j} k_i A_i + \sum_{m=1}^{n} K_m C_m = \text{constant} \qquad (22)$$

That is, the total radical scavenging ability of the system must remain constant throughout the radiolysis. Although this condition is not likely to be fulfilled, it will be approximated if the original solute reacts with (Z·) to form diverse products, whose combined reactivity toward (Z·) is close to that of the initial compound. This is likely to be realized in the case of enzymes because they typically contain many amino acid residues (ten to a hundred or more) that react rapidly with the radicals from water.

Hutchinson and Ross[5] have reported on the radiolytic decomposition of methylene blue, coenzyme A, and sulfanilamide, both alone and in the presence of added "impurity". Their data are reproduced in Figures 1–3. The empiri-
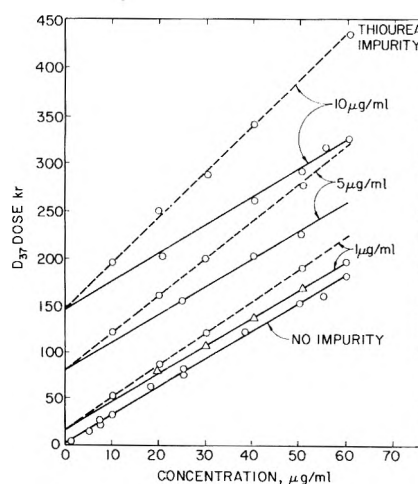
Figure 1. Methylene blue, $D_{0.37}$ against A_0: (———) in O_2; (– – – –) in N_2.
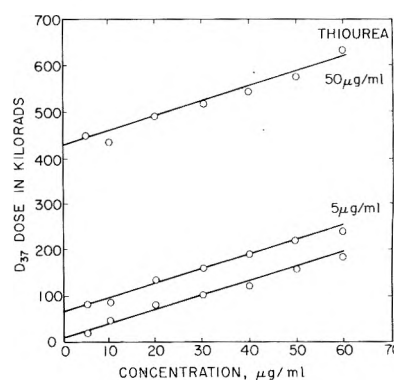
Figure 2. Coenzyme A, $D_{0.37}$ against A_0. Thiourea impurity added.
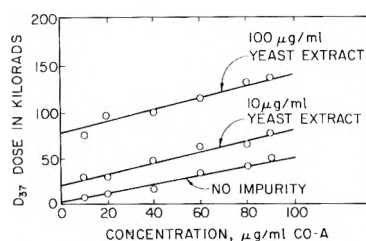
Figure 3. Sulfanilamide, $D_{0.37}$ against A_0. Yeast extract impurity added.

cal data are in agreement with the behavior to be expected for a consecutive mechanism. In the absence of an added impurity, plots of $D_{0.37}$ vs. A_0 are linear and extrapolate nearly to the origin. In the presence of added impurity, thiourea in the first two cases, yeast extract in the third case, plots of $D_{0.37}$ vs. A_0 are still linear but the intercept at $A_0 = 0$ is shifted in proportion to the impurity, as required by eq 19.

Augenstine[4] has reported data for some enzymes. His treatment of the data involves plotting the reciprocal of the yield G for the solute A_1 vs. $1/A_0$. This procedure can easily be shown to be equivalent to that of plotting D_x vs. A_0: eq 19 may be written in the form

$$D_x = aA_0 + b \qquad (23)$$

where a and b are constants at a given x. G is the amount of A_1 decomposed per unit dose; i.e.
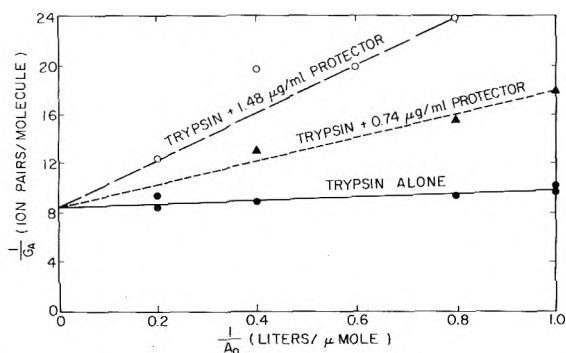
Figure 4. Trypsin, $1/G_A$ against $1/A_0$.
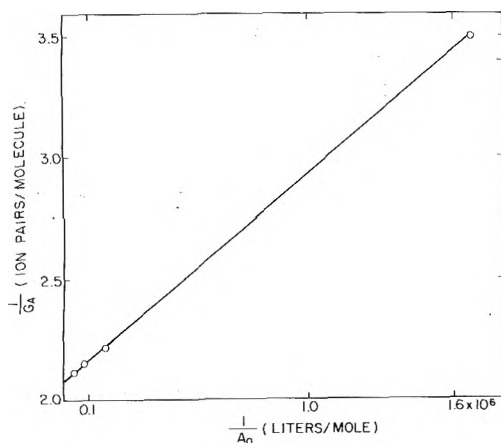
Figure 5. D-Amino acid oxidase, $1/G_A$ against $1/A_0$

$$G_{A_1} = (1 - x)A_0/\rho D_x \qquad (24)$$

Combination of eq 23 and 24 yields

$$G_{A_1} = \frac{(1 - x)A_0}{aA_0 + b} \qquad (25)$$

which may be written in the form

$$1/G_{A_1} = b/(1 - x)A_0 + a/(1 - x) = b'/A_0 + a' \qquad (26)$$

where a' and b' are constants.

The data on trypsin, reproduced in Figure 4, are in accordance with the consecutive mechanism, i.e., in absence or presence of appreciable impurity, the reciprocal of the inactivation yield for trypsin varies linearly with $1/A_0$ in the concentration range examined. Similar conclusions may be reached for D amino acid oxidase, whose radiolysis is shown in Figure 5. Augenstine[4] reports, in addition, two cases which are not in agreement with the consecutive mechanism, the data for chymotrypsin and ribonuclease, shown in Figures 6 and 7. In these cases, it may be seen that the $|G_{A_1}|$ value increases at high concentrations of enzyme. One possibility is that the enzyme in these cases is appreciably inactivated by secondary products. This possibility, that has been excluded from the mechanisms discussed above, is considered in the next section.

It is pertinent to note, at this point, that eq 19 is independent of dose rate. Therefore, if measurements taken at different dose rates yield identical plots of D_x vs. A_0, one may infer that the radiolysis mechanism is, to a large extent, consecutive in nature. Conversely, if a variation is noted for different dose rates, this may be taken as evidence that the mechanism is not consecutive.
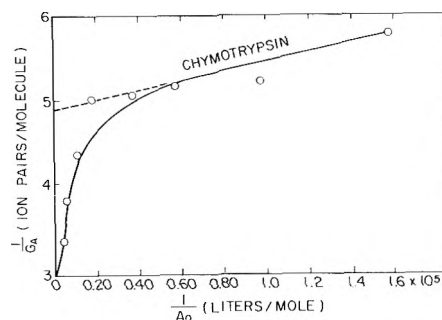
Figure 6. Chymotrypsin, $1/G_A$ against $1/A_0$.
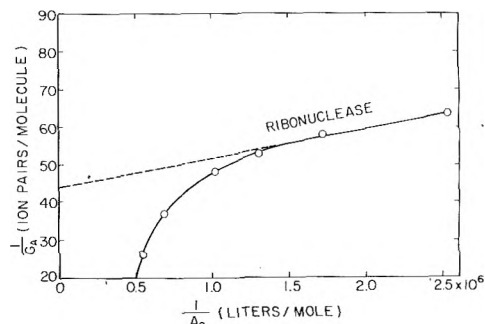
Figure 7. Ribonuclease, $1/G_A$ against $1/A_0$.

It should also be noted that eq 19 involves ratios of the rate constants that may be expected to vary with temperature. Determining D_x vs. A_0 at different temperatures therefore provides a means of monitoring the temperature dependence of the k_i.

B. Parallel Processes. If the radiolysis mechanism involves the inactivation of substrate A_1 by secondary radicals A_i ($i > 1$), the linear dependence of D_x upon A_0 is removed. Furthermore, the inactivation process becomes dose-rate dependent. This dependence is markedly different from that which develops at high dose rates because of the onset of second-order reactions between primary radicals (Z·).[11-14] The onset of the latter effects has been observed to occur at dose rates approaching 10^8 rads/sec.[15] In the present case, on the other hand, it is possible, under the right conditions, to observe such effects at much lower dose rates, between 10–50 rads/sec.

One may easily see how such effects result from the reaction of secondary radicals with A_1 by consideration of the following simple parallel mechanism:

$$H_2O \xrightarrow{G(dD/dt)} Z\cdot$$

$$A_1 + Z\cdot \xrightarrow{k_0} A_1 \qquad (R0)$$

$$A_1 + Z\cdot \xrightarrow{k_1} A_2 \qquad (R1)$$

$$A_2 + Z\cdot \xrightarrow{k_2} A_3 \qquad (R2)$$

$$A_3 + Z\cdot \xrightarrow{k_3} I \qquad (R3)$$

$$A_2 + A_2 \xrightarrow{k_4} A_3 + A_3 \qquad (R4)$$

$$A_2 + A_1 \xrightarrow{k_5} A_2 + A_3 \qquad (R5)$$

$$A_2 + Z\cdot \xrightarrow{k_6} I \qquad (R6)$$
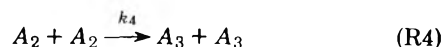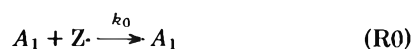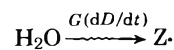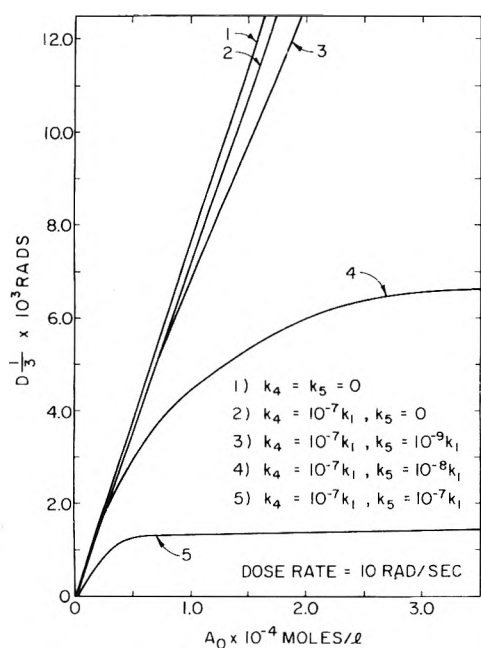
Figure 8. Results of numerical integration of parallel mechanism.

TABLE I: Parameters for Numerical Integration of Parallel Mechanisms

Parameter	Value
k_0	1.0×10^9 M^{-1} sec^{-1}
k_1	1.5×10^9
k_2	1.8×10^9
k_3	1.0×10^9
k_4	Varied (see Figures 8 and 9)
k_5	Varied (see Figures 8 and 9)
k_6	1.0×10^9
G	3×10^{-9} mol of radicals/rad
A_0	0.5×10^{-5} to 5.0×10^{-4} in increments of 0.5×10^{-3}
C_0	0.0
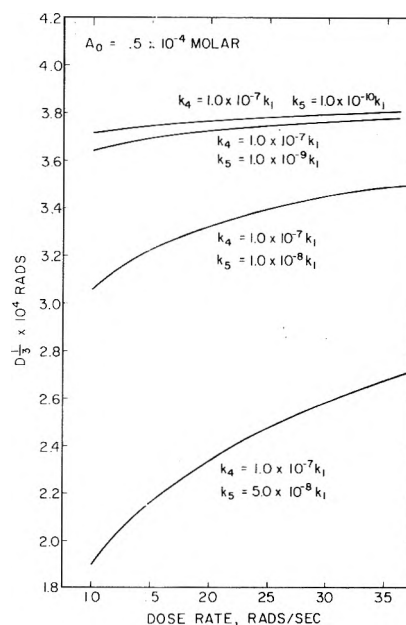
Figure 9. Dose rate effects.

Reaction R0 represents the possibility of primary solvent radical attack upon solute A_1 without change in the assayable property Φ. Reactions R1, R2, and R3 constitute a sequence of consecutive processes analogous to those in the previous section. Reactions R4, R5, and R6 allow product A_2 to react in several modes concurrently; reaction R5 explicitly admits reaction of solute A_1 with A_2 product, and furthermore forms a product which can react with A_1.

From the steady-state expression for (Z·), the variation of A_1 with dose may be shown to be

$$dA_1/dD = -k_1 G\rho A_1/[A_1(k_0 + k_1) + A_2(k_2 + k_6) + k_3 A_3] - k_5 A_1 A_2/(dD/dt) \quad (27)$$

$$dA_2/dD = \frac{G\rho(k_1 A_1 - k_2 A_2)}{[A_1(k_0 + k_1) + A_2(k_2 + k_6) + k_3 A_3]} - \frac{k_4 A_2^2}{(dD/dt)} \quad (28)$$

and

$$dA_3/dD = \frac{G\rho(k_2 A_2 - k_3 A_3)}{[A_1(k_0 + k_1) + A_2(k_2 + k_6) + k_3 A_3]} + \frac{2k_4 A_2^2 + k_5 A_1 A_2}{(dD/dt)} \quad (29)$$

Since the dose rate appears explicitly in eq 27–29, we would expect to see a variation of the observed results as (dD/dt) changes. Moreover, it should also be noted that the magnitude of the term containing the dose rate in eq 27 and 29 depends upon the product $A_1 A_2$ rather than upon the product of two primary or secondary radical concentrations. Since A_1 may often be some 10^4–10^6 times larger than the concentration of reaction intermediates like (Z·), A_2, etc., the effect of dose rate should be observable at much lower dose rates than those due to the interaction between intermediates or primary radicals.

As an illustrative numerical example of the above observations, we have examined the kinetic behavior of the above system by Runga–Kutta numerical integration on a 360/65 digital computer. It was assumed that the reaction of primary radicals (Z·) with A_1 proceeds with a typical

specific rate constant of 10^9 mol dm^{-3} sec^{-1}. The importance of secondary radical recombination and the inactivation of A_1 by secondary radicals was then investigated by systematically varying the relative magnitude of k_4 and k_5.

Figure 8 shows the results of calculations for the parameter values listed in Table I. If $k_4 = k_5 = 0$, the mechanistic scheme reduces to a special case of the generalized consecutive mechanism already discussed, and a plot of $D_{1/3}$ vs. A_0 is linear, as expected. If k_4 is made small, but nonzero, only a slight deviation from linearity (see curve 2, Figure 8) is observed. However, a very marked curvature develops whenever secondary products A_2 react mainly to inactivate the substrate A_1 (see curves 3 and 4, Figure 8).

The dose–rate effect induced by the inactivation of substrate by secondary radicals, reaction R5, is clearly illustrated by the results shown in Figure 9 where the calculated value of $D_{1/3}$ is plotted against dose rate for varying values of the k_4/k_5 ratio. It is obvious that there is a significant effect, even for rather small values of k_5. It should also be noted that this effect is computed to occur at dose rates between 10 to 40 rads/sec, a range that is readily attained in most experimental radiolysis laboratories. Measurement of this dependence might therefore be utilized as a diag-
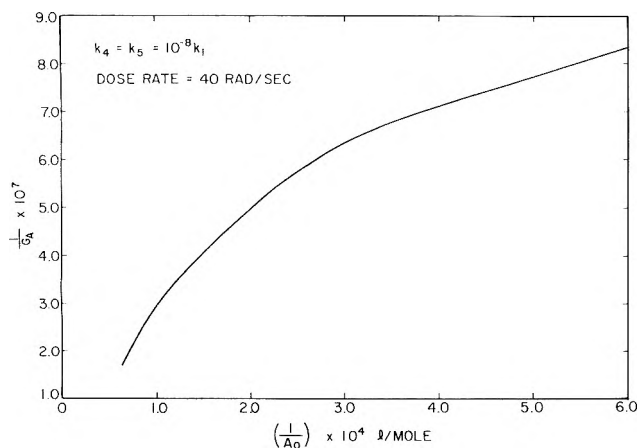
Figure 10. Simulated nonlinear $1/G_A$ against $1/A_0$.

nostic tool to assess in a semiquantitative manner the relative importance of inactivation by secondary radicals.

In Figure 10 we illustrate that by making appropriate choices for the values of the pertinent constants one can generate curves of D_x vs. A_0 which resemble the nonlinear data reported by Augenstine[4] for chymotrypsin and ribonuclease. From this one may infer that inactivation of the enzymes in question by secondary products may be an explanation of the observed results.

Conclusions and Summary

We have shown that if a solute is decomposed by a series of consecutive reactions with primary solvent radicals, a plot of D_x vs. A_0 will be linear. The intercept of the line is a measure of the concentration of solute-independent impurity, and the slope measures the capacity of the solute, and of all products derived from the solute, to react with the primary products formed by radiolysis of the solvent. For any species in the consecutive mechanism, its rate of change with dose will be independent of dose rate; therefore, no dose rate effect should be observed if the mechanism is of this general type.

With "parallel" mechanisms, i.e., involving reaction of

A_1 with secondary products derived from A_1 and (Z·), plots of D_x vs. A_0 may be nonlinear, depending on the rate constants of the reactions that are taking place concurrently. Deviations from linearity become more pronounced as the secondary products come to make an increasing contribution to the inactivation of the original solute. Reactions between intermediate radicals, A_2, A_3, ..., are important only if these reactions produce a significant change in the steady-state concentration of primary radicals Z·.

If inactivation of A_1 by secondary radicals plays an important role in the radiolysis mechanism, a dose–rate effect with a readily accessible onset should be observed.

References and Notes

(1) A. P. Casarett, "Radiation Biology", Prentice-Hall, Englewood Cliffs, N.J., 1968.
(2) W. T. Moss, W. N. Brand, and H. Battifora, "Radiation Oncology: Rationale, Technique, Results", 4th ed, C. V. Mosby, St. Louis, Mo., 1973.
(3) L. G. Augenstine. *Adv. Enzymol.,* **24**, 359–412 (1962).
(4) L. G. Augenstine, *Radiat. Res.,* **10**, 89–111 (1959).
(5) F. Hutchinson and D. A. Ross, *Radiat. Res.,* **10**, 477–489 (1959).
(6) J. A. V. Butler, A. B. Robins, and J. Rotblat, *Proc. R. Soc. (London), Ser. A,* **256**, 1–14 (1960).
(7) T. Sanner and A. Pihl, *Radiat. Res.,* **19**, 12–26 (1963).
(8) N. Arley, *Radiat. Res.,* **29**, 1–17 (1966).
(9) A. Kuppermann in "Radiation Research", G. Silini, Ed., North-Holland Publishing Co., Amsterdam, 1967, pp 212–234.
(10) Proportionality between the catalytic activity and the enzyme concentration should not be assumed to obtain in all circumstances; considerable study may be required to establish "assay" conditions in which the condition is fulfilled. For other substances, the quantitative relationship between mass and biological effect may be even more complicated.
(11) J. P. Keene, *Radiat. Res.,* **6**, 424 (1957).
(12) J. Rotblat and H. C. Sutton, *Proc. R. Soc. (London), Ser. A,* **255**, 490 (1960).
(13) A. R. Anderson, *J. Phys. Chem.,* **66**, 180 (1962).
(14) J. K. Thomas and E. J. Hart, *Radiat. Res.,* **17**, 408 (1962).
(15) H. Fricke and E. J. Hart in "Radiation Dosimetry", Vol. 2, F. H. Attix and W. C. Roesh, Ed., Academic Press, New York, N.Y., 1966, pp 224–229.

Pulsed Photoconductivity of Chlorophyll-a Films in Contact with a Nonpolar Solution[1]

C. W. Tang, F. Douglas, and A. C. Albrecht*

Department of Chemistry, Cornell University, Ithaca, New York 14853 (Received July 11, 1975)

Publication costs assisted by the National Institutes of Health

Pulsed photoconductivity of a chlorophyll-a (Chl-a) system consisting of an electrodeposited film of Chl-a microcrystals on an electrode surface in contact with a solution of Chl-a monomers in a nonpolar solvent has been investigated. Dual electric current signals are observed. A fast photocurrent signal appearing on the time scale of the microsecond light pulse is followed by a dark current signal which appears on a much slower time scale on the order of hundreds of milliseconds. The dual signals originate from an initial fast photogeneration of charge with electronic conduction in the Chl-a film, followed by a slow process of charge injection from the Chl-a film into the solution and subsequent ionic transport across the cell. The action spectrum of each kind of signal follows the absorption spectrum of the film when the Chl-a microcrystals are coated on the front (directly, illuminated) electrode. However, when the Chl-a film is coated on the back (indirectly illuminated) electrode the action spectra reveal a slight "inverse" type response indicating that there is a progressively increasing photoelectric efficiency in the Chl-a film as the light traverses it toward the metallic electrode. The time profile of the slow signal depends on the external applied field and in a manner which suggests that ionic conduction in the nonpolar solvent is responsible for this dark slow signal. The total coulombs carried in the slow signal can be considerably increased simply by increasing the concentration of Chl-a monomers in the nonpolar solvent suggesting that Chl-a monomers can serve to enhance the yield of charge injection and/or act as ionic carriers. The lower limit to the quantum yield of charge generation in the Chl-a film exceeds 1%.

I. Introduction

In a previous paper on the photoconductivity of chlorophyll-a (Chl-a) microcrystals in a nonpolar solvent such as 3-methylpentane (3MP), dual photoelectric signals have been seen.[2] These two signals appear on entirely different time scales. The fast photocurrent is on the time scale of the pulse of the exciting light (~20 μsec) and is followed by a slow current pulse on the scale of tens or hundreds of milliseconds, well after the light pulse is over. Studies were carried out both at room temperature and at 77 K where the microcrystals are suspended in the rigid organic solvent. At the low temperature the slow component of the dual current signals is entirely absent, whereas persistent internal polarization is seen to develop on the fast time scale upon successive flashing. At room temperature it was found that the magnitude of the slow component of the conductivity pulse apparently depends on the concentration of monomeric Chl-a in the solvent. These two signals have been attributed, respectively, to the light-induced polarization current within the Chl-a microcrystal followed by the slow ejection of charge from the Chl-a microcrystal (in the polarized state) into the solvent medium. Further experiments have been performed on this system and it has been shown that the Chl-a microcrystals suspended in a nonpolar solvent actually behave like positively charged particles.[3] Thus under the influence of an external applied electric field, these positively charged Chl-a microcrystals migrate and adhere to the cathode to form a film on its surface. The photoeffects seen at room temperature presumably originate from the photosensitization of the Chl-a microcrystals located on the electrode surface rather than from suspension of them as at 77 K.

In this investigation, we have explored the photoelectric effects of this electrodeposited Chl-a film in considerably more detail. The configuration of the photoconductivity cell consists of a Chl-a coated electrode as a cathode in a solution of Chl-a monomers (and other small Chl-a aggregates such as dimers). The separation between the planar cathode and the anode is large compared with the thickness of the Chl-a film (which is on the order of 10^3 Å). The dual photoelectric signals have been studied with respect to their dependence on the monochromatic light, the applied field strength, and the concentration of the monomers. A more quantitative estimate of the efficiency of the photogeneration of charge carriers also has been carried out. It will be shown that the dual photoelectric effects observed in the system of Chl-a reflect a primary process of photoionization in the Chl-a film on the cathode surface, followed by a secondary act of charge transfer from the Chl-a film into the surrounding fluid.

Very recently[4] detailed experiments and kinetic analysis have been reported for the photogenerated charge transfer from a photoconductor (metal free phthalocyanine or amorphous selenium) into insulating liquids. The configuration used is not unlike that found in the present work except here pulsed high voltages are not employed. The current work is more qualitative in nature (particularly as regards to kinetic details) nevertheless the phenomenological results of the two investigations are quite similar. This probably implies a generality to the physical basis of the photoelectric behavior seen in such systems.

II. Experimental Section

The preparation of Chl-a and the method of preparing a Chl-a film on an electrode surface by electrodeposition have been described in a previous paper.[3]

Figure 1 shows the configuration of the photoconductivity cell used in this work. The front electrode, which directly receives the incident light, is a semitransparent Cr coated quartz disk (2 in. diameter). The back electrode is a
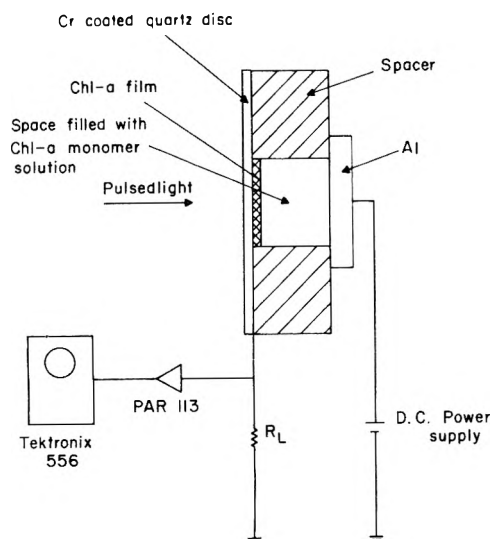
Figure 1. Cell configuration.

Figure 2. Dual photoelectric signals. Exciting light is 740 nm: (upper trace) "slow" signal, 0.1 sec/horizontal division; (middle trace) "fast" signal, 10 μsec/division; (lower trace) light pulse, 10 μsec/division.

piece of flat and polished Al. The separation from 25 μ to 0.5 cm is achieved by using spacer rings made of either Mylar or Teflon. The Chl-a film can be coated on either the front or the back electrode in the process of electrodeposition. The space between the electrodes (within the spacer ring) is filled with a solution of Chl-a monomer in 3MP or isooctane. This monomeric solution is obtained by heating a suspension/solution of Chl-a (containing both monomers and microcrystals) to 50°C for a few minutes. Chl-a microcrystals irreversibly dissolve to give a true solution of monomers (and other small aggregates such as dimers). Alternatively, by the act of electrodeposition, the Chl-a microcrystals in a suspension/solution of Chl-a can be driven to the cathode and are thus removed from the solution which then only contains monomers (and small aggregates). In fact, in most experiments, the electrodeposition and photoelectric measurement were performed in a photoconductivity cell without interruption.

The dc high voltage (50–3000 V) applied to the back electrode was supplied by a Power Design high voltage source (Model 2K-10). The other electrode was connected to ground via a load resistor. A 10^6-Ω resistor was used for the measurement of the "slow" signal, while a 10^4-Ω resistor was used for the "fast" signal. The time constant of the circuit (load resistor × capacitance of the cell) is on the order of 1 μsec with a load resistance of $\sim 10^4$ Ω.

The pulsed light source was an EG+G flash lamp (FX-42-C3). The lamp was triggered when a 40-μF capacitor was charged to 2500 V. Monochromatic light was provided by a B+L high intensity monochromator with a grating blazed at 500 nm. An EG+G SGD 100 A silicon photodiode was used to monitor the shape and the relative intensity of the light pulse. Absolute intensity of the light pulse was estimated to within a factor of 2 by a TRG ballistic thermopile.

The electrical measuring system was a Tektronix 556 dual channel oscilloscope which simultaneously traced both the dual signals, or one component of the dual signal and the light pulse. The signal was preamplified by a PAR 113 preamplifier.

III. Results and Discussion

A. *Cell Configuration.* In Figure 1, the Chl-a film is seen to be coated on the semitransparent Cr electrode, which
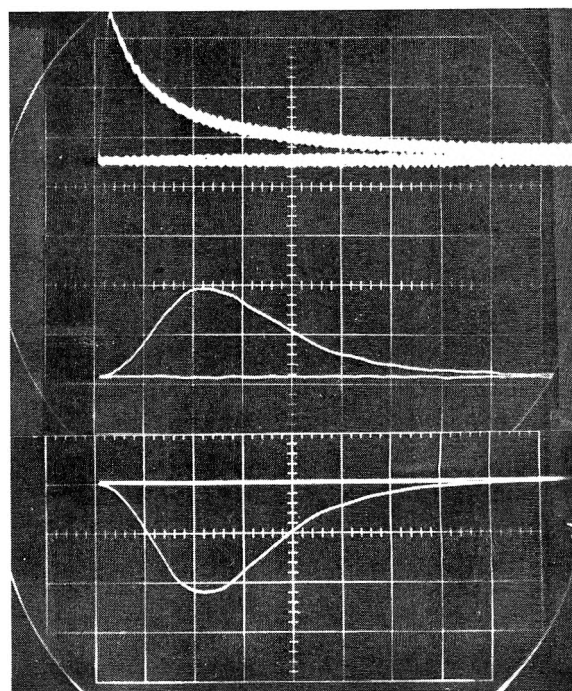
has a negative polarity. It is important that the polarity of this Chl-a coated electrode remains negative in all photoelectric experiments to be performed with this cell. Reversing this Chl-a coated electrode to a positive polarity usually results in the ejection of some of the Chl-a microcrystals from the electrode surface followed by the migration of these microcrystals to the new cathode, the back (Al) electrode. Perhaps those Chl-a microcrystals that have been electrodeposited but are in contact with the monomer solution still retain some of their positive charges, thus when the applied field is reversed, these positive charged microcrystals migrate. An alternate possibility is that positive charges are injected into the Chl-a microcrystal upon switching the Chl-a coated electrode to a positive polarity. In any case such switching of polarity usually results in having Chl-a deposited on both electrodes. Analysis of the photoelectric effects of such a system is more complicated. To avoid these difficulties, a single Chl-a film on either the front or the back electrode is used in all cell configurations. Thus, when the back, Al, electrode is initially coated with Chl-a, a negative polarity on this electrode is maintained throughout the subsequent photoelectric experiments performed with this cell.

B. *"Fast" and "Slow" Signals.* A typical measurement from a Chl-a system (represented in Figure 1) is shown in the two oscillographs in Figure 2. These signals are like those previously reported.[2] The Chl-a film on the Cr electrode is about 1000 Å thick and the space between the two electrodes is 76 μ (3 mil). The concentration of the monomeric Chl-a solution is about 10^{-4} M. The lower oscillograph shows the shape of the exciting light pulse. The wavelength of this exciting light is 740 nm centering at the peak of the Chl-a microcrystal absorption in this region. The upper oscillograph shows the dual photoelectric signals seen when the Chl-a system is exposed to a single exciting light pulse. In this oscillograph, the lower trace rep-

resents the "fast" photocurrent signal. It is seen that the shape of this signal matches very well that of the light pulse. The upper trace shows the "slow" current signal. The signal appears on the time scale of several hundreds of milliseconds, well after the light pulse is over. Thus, it actually represents a dark current flow in the Chl-a cell. A similar measurement from this Chl-a system but with the exciting light in the Soret band of Chl-a at 440 nm was carried out. The xenon light pulse is of shorter duration in this region, and correspondingly, the "fast" signal induced by this light is shorter too. In fact, when using a nanosecond pulsed dye laser, the response of this "fast" photoconductivity continues to follow the light pulse.[5] The charge separation responsible for the true photocurrent possesses a subnanosecond response time at room temperature. As mentioned above, the dual signal seen in Chl-a at room temperature was attributed previously[2] to the initial polarization of suspended Chl-a microcrystals followed by a subsequent ejection of the charges from the polarized Chl-a microcrystals into the solvent medium. It appears that such a description is at least qualitatively correct, although in fact the Chl-a microcrystals turn out to be attached to the cathode. Since in the earlier work only very thin samples were exposed to applied fields, it may be inappropriate to regard the electrodeposited Chl-a as a film in those cases. In the present work electrodeposition is from an abundant supply of microcrystals and distinctly uniform films are obtained.[3] In the present studies, the "fast" signal can be attributed to the rapid electrical polarization within the Chl-a film at the cathode surface, and the "slow" signal to the transport in the dark of negative charges from the Chl-a film at the cathode to the anode under the external applied field. The sign of the charges responsible for the slow signal is deduced from the fact that the film is, necessarily, of negative polarity and the assumption that the current essentially reflects the transport of space charge.

Whatever the detailed mechanism of primary charge formation in the Chl-a film, it must reflect the fact that the action spectrum matches the spectrum of the Chl-a microcrystal itself (see below). Possibilities other than direct ionization could include exciton formation followed by ionization at appropriate sites. To account for the "fast" signal from the electrical point of view, however, it is only necessary to propose that the interface between the Chl-a film and the solution, or between the Chl-a and the electrode, is blocking to charge transport on the short time scale of the light pulse. Thus, charge flow across or within the film momentarily acts as an electrical polarization. It may even be that the interfaces between the individual microcrystals within the film are sufficiently blocking to charge transport on this time scale. The polarization seen[2] at 77 K is almost certainly due to the blocking interface between individual microcrystals and the glassy matrix. As will be seen, if there are blocking regions within the film they do not seem to seriously inhibit the efficiency of charge production on the long time scale.

C. Intensity Dependence. The "fast" and "slow" photocurrents are seen to be linearly dependent on the light intensity of the exciting light at low levels (Figure 3). At higher light levels, the dependence becomes sublinear. The light exponent in the photocurrent is quite independent of the wavelength of the exciting light, but shows variation among different cells, ranging from 0.6 to unity.

D. Action Spectra. The action spectra of the dual photocurrents are shown in Figures 4 and 5, which correspond re-
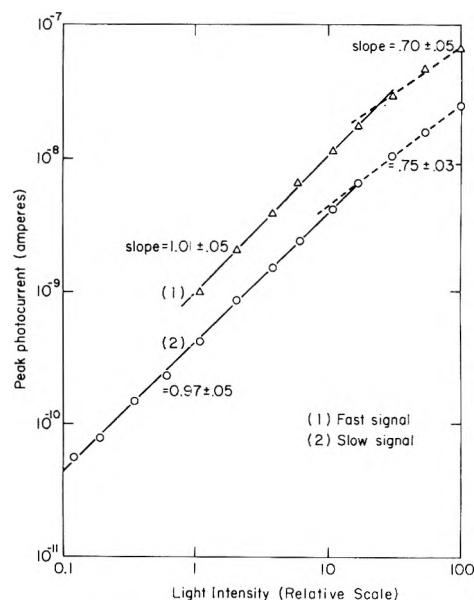
Figure 3. Light intensity dependence of the "fast" and the "slow" signal.
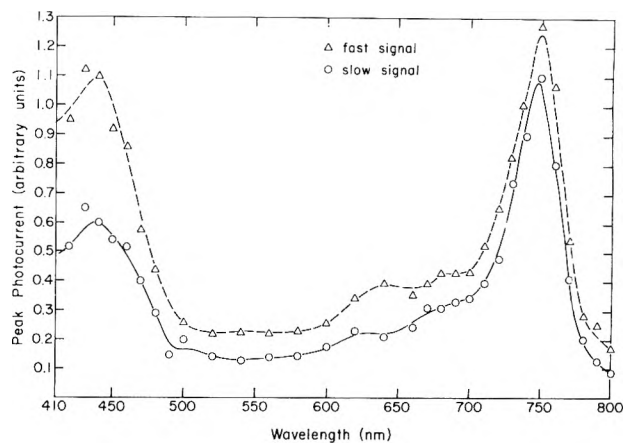
Figure 4. Action spectra, Chl-a on front electrode: (- - -) fast signal; (—) slow signal.
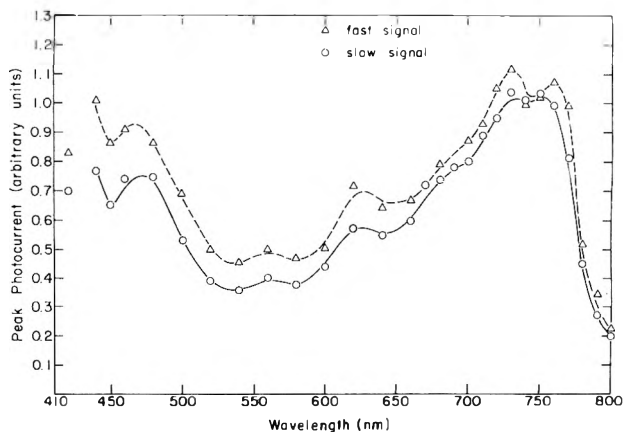
Figure 5. Action spectra, Chl-a on back electrode: (- - -) fast signal; (—) slow signal.

spectively to cells with Chl-a films coated at the front, Cr, electrode and at the back, Al, electrode. In both cells, the separation between the front and back electrode is 76 μ (3

mil) and the concentration of the Chl-a monomeric solution is about 10^{-4} M. The thickness of the Chl-a film is about 1000 Å, corresponding to an optical density of about 1 at 740 nm. It can be seen from Figure 4 that the spectral responses of the "fast" and "slow" current show a good match with the absorption spectrum of Chl-a film. The response of the "fast" photocurrent appears to be stronger in the blue spectral region than what would be indicated by the absorption spectrum. The response of the "slow" signal appears to be normal. However, it must be noted that the uncertainty in determining the response in the blue region is relatively larger than in the red region because of a greater fluctuation of the more intense xenon light level as well as the lower sensitivity of the monitoring silicon photodiode.

The spectral response of these dual photocurrents in a cell with the Chl-a film at the *back,* Al, electrode is seen to match the Chl-a absorption less perfectly (Figure 5). Though here the spectral response of both the "fast" and the "slow" signal still reveals maxima in the strongly absorbing region of Chl-a, small dips in the response corresponding to the absorption maxima of the Chl-a film are also seen in the action spectra.

The match between the spectral response of the dual photoelectric signal (at least that seen in the front surface) and the absorption spectrum of the Chl-a film indicates that the Chl-a film on the electrode surface is essentially responsible for the photoactivity. It is not immediately apparent, however, why the fast signal seems to have an enhanced response at the blue spectral region whereas the "slow" signal shows a normal behavior. It is conceivable that the more energetic photons of the blue region can be responsible for increased charge flow per photon absorbed provided this flow is somehow coupled with the energy in excess of the ionization energy, which cannot exceed that of the near-infrared photon. If the distance traveled were greater, but the number of charges produced per photon were unchanged, then no parallel effect would be seen for the "slow" signal.

The slight but definite mismatch of the absorption spectrum of the Chl-a film and the spectral response of the dual photoelectric signals seen in the cell having the Chl-a film coated at the *back* electrode implies that an inner filter effect is present in the film (the optical density of the 3-mil path of the solution of monomers is negligible). That is, photoelectric activity is more efficient in regions within the film *nearer to the electrode.* When studying a metal–Chl-a–metal sandwich cell in the photovoltaic mode,[6] dramatic inverse type action spectra are seen when the photoactive region is located at the back electrode and the light must traverse more than 10^3 Å of solid Chl-a to reach the photoactive region. In the present work, the "inverse" effect is only slight. This may simply mean that the first several hundred ångströms of film (on the solution side) are photoelectrically less efficient. For example, the film near the Chl-a–solution interface may be less "perfect" than the portion first reaching the cathode during electrodeposition, and charge separation within it may therefore be less efficient.

E. Effect of Applied Field. The effect of the applied field on the dual signal is seen in Figure 6. At low applied fields the peak photocurrent signals are seen to increase with the applied field. Saturation of both signals is seen at higher field strengths.

The shape of the fast signal is found to be independent
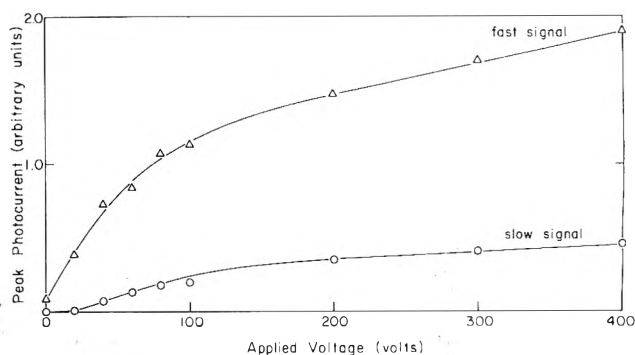
Figure 6. Field dependence of the dual signals.
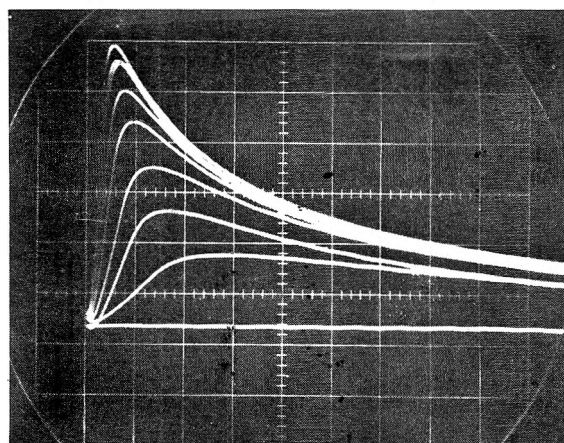
Figure 7. Time profile of the "slow" current signals at different field strengths, separation of electrodes in this cell is 7.6×10^{-3} cm (3 mil). From the top trace, the applied voltage is 400, 300, 200, 150, 100, 80, 50 V (20 msec/horizontal division).

of the applied field. Its shape appears to be fully determined by the shape of the light pulse. The time profile of the "slow" signal is, however, strongly dependent on the field. In Figure 7, the traces in the oscillograph represent the "slow" signal pulses at different applied field strengths. The thickness of the spacer is again 76 μ (3 mil) in this cell. It can be seen that the peak of the current pulse moves to a longer time as the field strength decreases.

The origin of the features of the time profile of the "slow" signal can be sought in several complicating factors. The slow signal originates from the ejection of the photoproduced negative charges from the Chl-a film and the subsequent ionic transport to the anode. However, the nature of the negatively charged species is not clear. The Chl-a microcrystal is known to contain water.[7] Thus, the solution of Chl-a monomers in the space between the electrodes most likely also contains water as well as dissolved gases such as O_2. All these species when charged may act as carriers and may have different mobilities. Another factor is that the rate of charge injection from the photosensitized Chl-a film into the solution can depend on the applied voltage.[4] If the process of charge injection is rate determining (most likely at small electrode spacing), the time profile of the slow signal will primarily reflect this event. If ionic transport is rate determining, then space charge effects may make their appearance in the initial portion of the signal. At high fields but at large spacings the transport ought to be the principal determinant of signal shape. If under these conditions we use LeBlanc's time of flight method[8] the transit

time for the carrier to traverse the distance between the electrodes is taken to be the time for the peak photocurrent to appear. In a thin sample ($\sim 10^{-1}$ mm, see Figure 7) such a calculation gives an apparent mobility of 2×10^{-5} cm^2 V^{-1} sec^{-1}, but here the current pulse is very likely convoluted with the injection pulse and such a figure cannot represent the true mobility. As the sample becomes thicker (several millimeters) the mobility, thus measured, becomes greater and exceeds 10^{-4} cm^2 V^{-1} sec^{-1}, a typical value for ionic mobility. For any given thickness the mobility is relatively independent of the applied field.

F. Effect of Concentration of the Monomeric Solution. The Chl-a monomer solution in the cell is seen to alter only slightly the "fast" signal, but changes the "slow" signal to a much stronger extent. Figure 8, shows the dependence of the "slow" signal on the concentration of the Chl-a monomer solution. It can be seen how an increase of more than a factor of 10 in the "slow" signal is achieved when raising the concentration of monomer from 10^{-5} to 10^{-4} M. As mentioned earlier, the solution of Chl-a monomers (and dimers) is obtained by heating a suspension/solution of Chl-a in isooctane (containing both monomers and microcrystals). If the Chl-a microcrystal is indeed an aggregate of Chl-a–H$_2$O in a 1:1 ratio, as suggested by Katz and Ballschmitter,[7] then its dissolution by heating will give an equivalent amount of monomeric Chl-a and water. Water alone does not seem to play a significant role in enhancing the "slow" signal. When a water-saturated solution of either 3-methylpentane or isooctane (obtained by purging the solvent with a stream of wet N$_2$) is used in place of the monomer solution in the photoconductivity cell, the "slow" signal is weak compared with that in the cell containing the monomeric Chl-a solution. In fact, the strength of the slow signal in the cell with wet solvent is comparable to that seen in the cell containing dry 3-methylpentane or isooctane (stored over molecular sieves). This fact alone does not suggest that the Chl-a monomers act as primary acceptors of the negative charges ejected from the Chl-a into the solution, because dissolved gaseous species may also play a role. The estimate made for the mobility of the major carrier is typical for ordinary ions and would seem to be too large for a molecule as large as the Chl-a monomer. Direct ejection of negative Chl-a ions from the Chl-a film may occur. Ion desorption from the photoconducting film was deduced as the rate-controlling step in the phthalocyanine example.[4] The role of the neutral monomer in such a case could be to suppress the readsorption process by inviting ion–neutral electron transfer away from the surface. That is, the monomers act as available trapping sites away from the surface in the solution and thereby suppress the surface readsorption step.

G. Quantum Efficiency of Charge Generation. The minimum number of charges produced by a single light pulse can be obtained by integrating over time the "slow" current pulse. All electric signals seen of course represent charges flowing through the external measuring circuit. If we take the "slow" signal to represent the charges which have completely traversed the cell, than a count of the coulombs in the "slow" pulse is a count of charges in our cell which have been photoproduced in the Chl-a film (fast signal) and transported across the cell. The ratio of the time integrated "slow" current (coulombs) to the integrated light pulse (photons), all of which is absorbed, is measured as 0.04 for an optimal cell configuration (monomer concentration about 10^{-4} M, field 10^4 V/cm). This ratio should represent
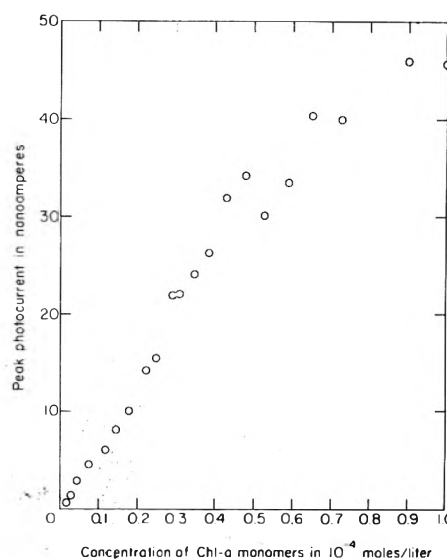
Figure 8. The dependence of the "slow" signal on the concentration of Chl-a monomers in solution.

the minimum quantum yield of charge production and ejection of charges from the Chl-a film into the solution. The accuracy of the thermopile (an uncertainty of a factor of 2 in measured power), nevertheless, permits one to say that the lower limit of the quantum yield for charge generation exceeds 1% under these conditions. This figure is much higher than that found for phthalocyanine and approaches within an order of magnitude the value accepted for amorphous selenium.[4] The yield, thus calculated, would be higher if all charges in the "slow" signal were not fully transported across the cell (bulk recombination). The quantum yield of primary charge generation within the film (an act prior to ejection) must be equal to this or greater. It is interesting to note that the number of coulombs contained within the "fast" signal is found to be typically a factor of 10^{-3} less than that seen in the slow signal; (the coulombs seen in the external circuit reflect the number of charges responsible for the signal multiplied by the ratio of the distance they travel to the cell spacing). Since the number of charges responsible for the "fast" signal must be equal to or greater than the number responsible for the slow signal, the distance traversed by the "fast" charges must be equal to or less than a factor of 10^{-3} of the distance traveled by the "slow" charges. The upper limit traveled by the "slow" charges is just the cell spacing. It then turns out that the upper limit of the distance traveled by the "fast" charges is very close to the film thickness. A minimum distance of 150 Å has been inferred elsewhere.[5]

IV. Summary

These pulsed photoelectric studies of biased Chl-a film–Chl-a solution cells have revealed several interesting properties. The fast–slow dual photoelectric response seems to clearly represent instantaneous charge separation within the Chl-a film (the fast signal) followed by charge injection from the film into the solution layer and transport across it (the slow signal). The spectral response of both the fast and slow signals essentially matches the spectrum of the Chl-a film (and not that of the Chl-a solution) but with sufficient variation to indicate that the region of principal charge generation within the film lies nearest to the metallic electrode. A minimum to the quantum yield of charge produc-

tion in the film is found to be 0.04. This is conservatively based on the number of coulombs carried in the slow signal per photons absorbed in the Chl-a film. An estimate of the maximum distance of charge separation within the Chl-a film, following ionization, turns out to be close to the film thickness itself.

The yield of mobile charges within the solution (produced by charge injection from the Chl-a film) can be dramatically increased by raising the level of Chl-a monomer in the solution. On the other hand the estimates of mobility indicate that the principal charge carriers are ions of ordinary size and very likely not charged Chl-a molecules. We therefore suspect that the main role of the Chl-a monomer is to mediate the transfer of charge across the Chl-a film–Chl-a solution interface. The charge carriers themselves remain unidentified, but ions from water, impurities, or dissolved gases are possible candidates. The Chl-a monomer

in solution may provide a resonance charge-transfer path for the transport of the charge away from the film–solution interface. Careful mobility measurements in thin cells as a function of Chl-a monomer concentration ought to provide a test for a resonance charge transfer mechanism of transport in the solution.

References and Notes

(1) This work has been supported in part by a PHS Grant (No. 10865) and the Materials Science Center of Cornell.
(2) F. Douglas and A. C. Albrecht, *Chem. Phys. Lett.*, **14**, 150 (1972).
(3) C. W. Tang and A. C. Albrecht, *Mol. Cryst. Liq. Cryst.*, **25**, 53 (1974).
(4) G. C. Hartmann and F. W. Schmidlin, *J. Appl. Phys.*, **46**, 266 (1975).
(5) A. Bromberg, C. W. Tang, and A. C. Albrecht, *J. Chem. Phys.*, **60**, 4058 (1974).
(6) C. W. Tang and A. C. Albrecht, *J. Chem. Phys.*, **62**, 2139 (1975).
(7) K. Ballschmitter and J. J. Katz, *Nature (London)*, **220**, 1231 (1968).
(8) O. H. LeBlanc, *J. Chem. Phys.*, **30**, 1443 (1959).

Radiative Lifetimes of the Benzyl, Deuterated Benzyl, and Methyl-Substituted Benzyl Radicals

Tadashi Okamura* and Ikuzo Tanaka

Department of Chemistry, Tokyo Institute of Technology, Ohokayama, Meguro-ku, Tokyo, Japan   (Received January 3, 1975; Revised Manuscript Received May 27, 1975)

Radiative lifetimes of the benzyl, deuterated benzyl, and some methyl-substituted benzyl radicals trapped in EPA matrices have been determined by measurements of fluorescence lifetimes and quantum yields. It is found that the radiative lifetimes of these radicals are very long, on the order of 10^{-6} sec, and the nonradiative decay processes of the lowest excited doublet states are competing with the radiative processes. Small oscillator strengths (10^{-3} to 10^{-4}) derived from the radiative lifetimes indicate that the first electronic transitions of the radicals are forbidden.

Introduction

The electronic spectra of the benzyl radical have been the subject of much experimental and theoretical work as a representative of the aromatic free radicals. It is known that the first electronic transition of this radical is in the visible region, and very weak and structured.[1,2] In the language of a C_{2v} point group, this transition was assigned to be $^2A_2 \leftarrow ^2B_2$ by recent experimental works.[3,4] The oscillator strength of this transition has been estimated theoretically by several authors[5–10] and, as a result, it has been proposed that the transition is forbidden contrary to the selection rule. Previously we measured fluorescence lifetimes of the benzyl and methyl-substituted benzyl radicals and showed that the lifetimes of these radicals are very long on the order of 10^{-7} to 10^{-6} sec.[11,12] Also the very long fluorescence lifetimes of the deuterated benzyl radicals were reported.[13] These results seemed to indicate the forbidden character mentioned above.

However, the radiative lifetimes of these radicals remained unknown because of the absence of the data of flu-

orescence quantum yields. Since it is very difficult to obtain reliable values of the intrinsic lifetime of the radicals from the absorption data, we have measured the fluorescence quantum yields and lifetimes of the radicals including deuterated benzyl radical trapped in the EPA matrices to obtain the radiative and nonradiative lifetimes and oscillator strength of the first electronic transitions. In present paper, we report the results of these experiments.

Experimental Section

Parent molecules of the benzyl radicals are given in Table I. Materials for the parent molecules used in this work were the same as reported in the previous papers[11,12] except for toluene-d_8, which was 99% D (Merck Sharp and Dohme). Benzophenone used as a reference for the measurement of the quantum yield was refined by recrystallization. EPA (5:5:2 volume mixture of ether, isopentane, and ethyl alcohol) used as the solvent was purified by treating with charcoal.

The radicals were prepared by the photolysis of the par-

TABLE I: Lifetimes and Quantum Yields of the Benzyl Radical and Its Derivatives[a]

Parent molecule	τ_0, nsec[b]	Radical	τ_f, μsec	Φ_f	τ_r, μsec	τ_{nr}, μsec	f
Toluene	173.8	Benzyl	1.28 ± 0.08	0.39	3.3	2.1	0.00098
Toluene-d_8	192.3	Benzyl-d_7	2.97 ± 0.20	0.47	6.3	5.6	0.00050
p-Xylene	92.5	p-Methylbenzyl	1.21 ± 0.09	0.18	6.7	1.5	0.00049
m-Xylene	167	m-Methylbenzyl	0.75 ± 0.04	0.38	2.0	1.2	0.0017
o-Xylene	153.4	o-Methylbenzyl	0.79 ± 0.07	0.59	1.3	1.9	0.0026
Mesitylene	192.3	3,5-Dimethylbenzyl	0.56 ± 0.02	0.64	0.88	1.6	0.0040
Durene		2,4,5-Trimethylbenzyl	0.52 ± 0.02	0.42	1.2	0.90	0.0030

[a] The Φ_f data include a 20% (maximum) deviation, and those of τ_r, τ_{nr}, and f include a $\pm 30\%$ (maximum) deviation. [b] Data presented in ref 19; solvent cyclohexane.

ent molecules dissolved in EPA at 77 K, after degassing. The concentration of the solution was about 5×10^{-3} M. The light sources used for the photolysis were a low-pressure mercury lamp and a high-pressure one of 1-kW power, respectively, for the measurements of fluorescence lifetime and fluorescence quantum yield. A typical irradiation time was 0.5 hr. On the photolysis using a high-pressure mercury lamp, the efficiency of radical formation was found to be about 10% for toluene, from the absorption data (refer to the next section of the text).

Fluorescence lifetimes were measured using a N_2 laser pumped dye laser (BBO dye) which emitted pulses with a duration of 3 nsec at 410 nm (half-width, 10 nm). The Blumlein type N_2 laser emitted pulses with a duration of 3 nsec and maximum peak power of 500 kW. The radicals trapped in EPA matrix at 77 K were excited by the pulses of the dye laser. The fluorescence was observed with a Hamamatsu TV R-106UH photomultiplier through a filter, Toshiba V-Y45, which transmitted visible light with a wavelength longer than 450 nm. The fluorescence decay curve was displayed on an Iwatsu 212 oscilloscope.

The fluorescence quantum yields were measured by the apparatus shown in Figure 1. Samples of the radicals which were contained in a quartz cell of 1-cm pathlength kept at 77 K in an optical dewar were irradiated by the 313-nm light of a high-pressure mercury lamp equipped on a monochromator Hitachi 139 through an aperture. Transmitted light by the sample was reduced by passing through an attenuator made of metal meshes and apertures, and detected by the photomultiplier Hamamatsu TV 1P21. Light emitted by the sample at 90° to the incident beam passed through a Corning O-52 filter and an aperture was projected on a quantum counter, which consisted of an ethylene glycol solution of Rhodamine B (8 g/l.) within a 5-mm cell. The red light emitted by the quantum counter was detected by a photomultiplier Hamamatsu TV R376. The quantum counter used has the spectral response from 250 to 600 nm (yield is constant to within $\pm 4\%$),[14] while the emission spectra of the benzyl radical and its derivatives studied in this work are all within the wavelength region of 450–580 nm.[15]

Excitation spectra of the radical were observed by a Hitachi MPF-2A fluorescence spectrometer.

Results and Discussion

The excitation spectrum of the benzyl radical in an EPA matrix is shown in Figure 2. The spectrum was obtained by monitoring the emission at 500 nm, and was corrected for the intensity of the excitation light by using a quantum counter. The result corresponds well with the absorption
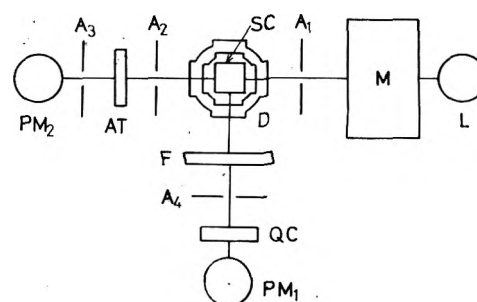
Figure 1. A schematic diagram of the apparatus for the quantum yield measurements. L, M, A, D, SC, QC, AT, and PM represent the high-pressure mercury lamp, monochromator, aperture, dewar, sample cell, quantum counter, attenuater, and photomultiplier, respectively.
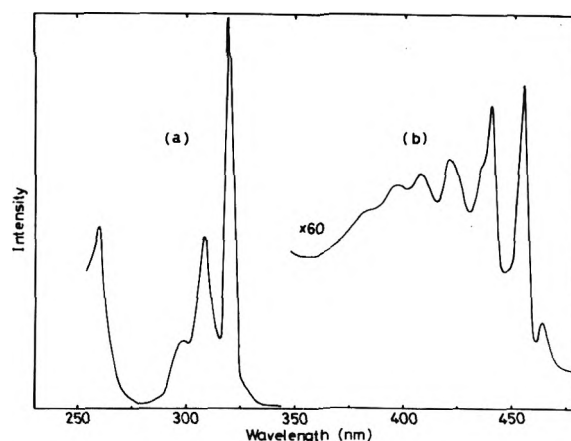
Figure 2. The excitation spectrum of the benzyl radical in EPA at 77 K. The monitor wavelength is 500 nm. Intensity in (b) is magnified by a factor of 60 with respect to (a).

spectra established already.[1,2] If the fluorescence quantum yield does not change in the excitation region from visible to near-ultraviolet, the intensity ratios of the two bands, i.e., a very weak one in the visible region and a strong one in the near-ultraviolet region, are the same both for the absorption and the excitation spectra. We found this ratio to be about 60. Besides, Land and Porter[16] estimated the values of the extinction coefficients to be ~ 30 at 453 nm and 1100 at 318 nm in hydrocarbon glass, and the ratio should be given about 40. The above comparison of the ratios probably suggests that the fluorescence quantum yield keeps a nearly constant value in the region from visible to near-ultraviolet. This suggestion may be also supported by the following reason. Any quartet states have not been ob-
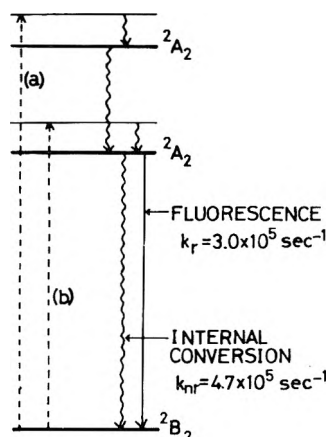
Figure 3. Energy level diagram of the benzyl radical showing the decay processes. Dashed lines (a and b) represent two kinds of excitations for the measurements of Φ_f and τ_f, respectively. k_r and k_{nr} are the rate constants of radiative and nonradiative decays, respectively.

served yet, and theoretical studies estimated the energy values of the lowest quartet state to be higher than the upper excited doublet state,[6,8,17] and therefore intersystem crossing should not exist in such a energy region.

The radicals were excited into the upper excited doublet states in the near-ultraviolet region for measurements of the fluorescence quantum yields (see Figure 3). The extinction coefficient of the absorption of the benzyl radical at 310 nm was estimated to be about 300, referring to the data mentioned above, and the optical density of the radical was found to be 0.1 at the same wavelength. Therefore, the concentration of the radical was 3×10^{-4} M. The optical densities of the other radicals were within 0.1–0.4, and the parts of the samples penetrated by the exciting beam emitted fluorescence evenly. The fluorescence quantum yields were derived from the intensity ratios of absorbed light to emitted light by the radicals and EPA matrix of benzophenone $(2.5 \times 10^{-3}$ $M)$ at 77 K as the reference, assuming that the phosphorescence quantum yield of benzophenone in EPA matrix is 0.84.[18] The fluorescence quantum yields Φ_f obtained in this work are listed in Table I. All Φ_f's of the benzyl and its related radicals are on the order of 10^{-1}.

For the measurements of the fluorescence lifetimes, the radicals were excited into the lowest doublet states by the visible laser pulse. The fluorescence lifetimes τ_f obtained in this work are listed in Table I, which are somewhat shorter than those previously reported.[11,12] The differences may be caused by the solvent effect. On the assumption that the fluorescence quantum yields obtained are almost the same as those obtained by the excitation into the lowest excited states, radiative lifetimes τ_r and nonradiative lifetimes τ_{nr} were estimated from the data of the fluorescence lifetimes and quantum yields by the relationships

$$\tau_r = \tau_f/\Phi_f$$

and

$$\tau_{nr} = \tau_f/(1 - \Phi_f)$$

Such an assumption may be proper as mentioned above, and the results of these estimations are listed in Table I, together with the data of the natural lifetimes τ_0 of the parent molecules. The oscillator strengths f of the lowest doublet states were estimated from the data of the radiative lifetimes by a relationship $f = mc/8\pi^2 e^2 \nu^2 \tau_r$.[20] The ob-

tained values of the oscillator strength are also listed in Table I.

The radiative lifetimes and oscillator strengths obtained are in the order of 10^{-6} sec and 10^{-3} to 10^{-4}, respectively. In comparison with the stable aromatic molecules, these radiative lifetimes are remarkably long. From the value of the extinction coefficient of the first absorption band mentioned above,[16] the intrinsic lifetime of 10^{-6} sec can be estimated. Small value of the oscillator strength of the benzyl radical was already calculated theoretically by several authors,[8-10] and also an experimental value in vapor phase (3 $\times$ 10^{-5}) was estimated using microsecond pulse discharge.[21] These small values of the oscillator strength indicate that the first doublet–doublet electronic transitions of the benzyl radical and its derivatives are eventually forbidden, though the transition $^2A_2 \rightarrow {}^2B_2$ is allowed by the selection rule. It is interesting that the oscillator strength of the p-methylbenzyl radical is remarkably smaller than that of the benzyl radical. It is presumed that a methyl group in the para position has the particular effect of enhancing the forbiddenness of the benzyl radical. In cases of other methyl-substituted benzyl radicals, the methyl substitutions have an effect of increasing the oscillator strength.

Deuteration of the radical has the noticeable effect of increasing the radiative lifetime, while generally such effect is not so noticeable in cases of the $S_1 \rightarrow S_0$ transitions of the aromatic molecules (parent molecules). Recently the remarkable isotope effect was also found in $T_1 \rightarrow S_0$ transitions of the aromatic molecules such as pyrene and naphthalene.[22] These phenomena were explained by the breakdown of the adiabatic Born–Oppenheimer approximation and/or the quadratic terms in the Herzberg–Teller expansion of the transition moment and/or nuclear hyperfine interaction. It should be important that the relatively strong forbiddenness of the transition is one of the necessary conditions of the appearance of such an effect, and that is common in the $D_1 \rightarrow D_0$ $(^2A_2 \rightarrow {}^2B_2)$ transition of the benzyl and the $T_1 \rightarrow S_0$ transitions of the aromatic compounds.

The nonradiative lifetimes obtained are all in the same order as the radiative lifetimes. The nonradiative lifetime remains nearly constant in the monomethylbenzyl and dimethylbenzyl radicals. The nonradiative decay processes of these radicals are little influenced by methyl substitution, while the lifetime is dramatically effected by deuteration. Such a drastic isotope effect was also found in the $^1B_{2u} \rightarrow {}^1A_{1g}$ transition of benzene[23] and the $T_1 \rightarrow S_0$ transitions of some aromatic molecules.[21] It was suggested that the accepting modes which correspond to the C–D stretching modes play an important role in the isotope effect of increasing the rate of the radiationless decay process.[24] Changes of the Franck–Condon factors of the stretching modes caused by deuteration may be the main origin of this effect.

An energy level diagram of the benzyl radical with the decay rates is shown in Figure 3. It is clear that the two kinds of decay processes, radiative and nonradiative (internal conversion) ones, are competing with each other in the benzyl radical and its derivatives.

References and Notes

(1) G. Porter and B. Ward, J. Chim. Phys., **61**, 1517 (1964).
(2) G. Porter and E. Strachan, Spectrochim. Acta, **12**, 299 (1958).
(3) D. M. Friedrich and A. C. Albrecht, J. Chem. Phys., **58**, 4766 (1973).
(4) C. Cossart-Magos and S. Leach, J. Chem. Phys., **56**, 1534 (1972).
(5) W. Bingel, Z. Naturforsch. A, **10**, 462 (1955).
(6) H. C. Longuet-Higgins and J. A. Pople, Proc. Phys. Soc. (London), Sect.

A, **68**, 591 (1955).

(7) A. Hinchliffe, R. E. Stainbank, and M. A. Ali, *Theor. Chim. Acta*, **5**, 95 (1966).

(8) Y. Mori, *Bull. Chem. Soc. Jpn.*, **34**, 103 (1961).

(9) J. Baudet and M. Suard, *J. Chim. Phys.*, **67**, 1088 (1970).

(10) H. M. Chang and H. H. Jaffé, *Chem. Phys. Lett.*, **23**, 146 (1973).

(11) T. Okamura, K. Obi, and I. Tanaka, *Chem. Phys. Lett.*, **20**, 90 (1973).

(12) T. Okamura, K. Obi, and I. Tanaka, *Chim. Phys. Lett.*, **26**, 218 (1974).

(13) J. D. Laposa and V. Morrison, *Chem. Phys. Lett.*, **28**, 270 (1974).

(14) J. Yguerabide, *Rev. Sci. Instrum.*, **39**, 1048 (1968).

(15) T. Okamura, Sc.D. Thesis, Tokyo Institute of Technology, 1975.

(16) E. J. Land and G. Porter, *Trans. Faraday Soc.*, **59**, 2027 (1963).

(17) C. Bertheuil, *C. R. Acad. Sci.*, **256**, 5097 (1963).

(18) E. H. Gilmore, G. E. Gibson, and D. S. McClure, *J. Chem. Phys.*, **20**, 829 (1952); **23**, 399 (1955).

(19) I. B. Berlman, "Handbook of Fluorescence Spectra of Aromatic Molecules", 1st ed, Academic Press, New York, N.Y., 1951.

(20) R. Ladenburg, *Z. Phys.*, **4**, 451 (1921).

(21) M. Kempfle and M. Stockburger, *Z. Naturforsch. A*, **21**, 1394 (1966).

(22) N. Kanamaru, H. R. Buhattacharjee, and E. C. Lim, *Chem. Phys. Lett.*, **26**, 174 (1974).

(23) A. S. Abramson, K. G. Spears, and S. A. Rice, *J. Chem. Phys.*, **56**, 2291 (1972).

(24) S. H. Lin and R. Bersohn, *J. Chem. Phys.*, **48**, 2732 (1968).

A Rapid Radiationless Decay Process Competing with the Intramolecular Proton Transfer in the Excited State

H. Shizuka,* K. Matsui,

Department of Chemistry, Gunma University, Kiryu, Gunma 376, Japan

T. Okamura, and I. Tanaka

Department of Chemistry, Tokyo Institute of Technology, Meguro-ku, Tokyo, Japan (Received June 19, 1975)

It has been shown that a rapid radiationless deactivation competes with the intramolecular proton transfer in the lowest excited singlet of TH [2,4-bis(dimethylamino)-6-(2-hydroxy-5-methylphenyl)-s-triazine] at temperatures higher than 230 K. The decay process with an activation energy of $2.5 + E_{PT}$ kcal/mol has been discussed.

1. Introduction

The intramolecular proton transfer in the excited state of salicylic acid has been originally studied by Weller[1] in 1956. He has shown that the fluorescence with a large Stokes shift, besides the normal fluorescence, corresponds to that from the proton transferred species. Schulman and Gershon[2] have pointed out that the intramolecular proton transfer in the excited state is mediated by intramolecular hydrogen bonding in the ground and the Franck–Condon excited states of the molecule. Murrill and Bennett[3] have demonstrated that the quantum yields for fluorescence and chemical reaction of the intramolecular hydrogen-bonded ortho isomer [2-(aminophenyl)-2,1,3-benzotriazole] are much lower than those of the nonhydrogen-bonded meta and para isomers; these phenomena are explained by the fact that the internal conversion in the excited state of the ortho isomer is a 100-fold more rapid than that in the para or meta isomer. Similarly, the photostability in the intramolecular hydrogen-bonded molecules has been recently displayed by Otterstedt.[4]

The enol–keto isomerization caused by the proton transfer in the excited state is a very simple photochemical process. In order to elucidate further the photochemical and photophysical behaviors in the excited state of intramolecular hydrogen-bonded species, we have made measurements on the fluorescence quantum yields from proton transferred excited TH and their fluorescence decay times in the temperature range 230–330 K.

2. Experimental Section

The preparation and purification of materials were described in previous papers.[5] The deuterium isomer TD was prepared by treating TH with the mixed solution of D_2O and acetone in the presence of a trace NaOH, whose isotope purity was greater than 90% by the NMR method.

The fluorescence quantum yields Φ_f' were measured by comparison with quinine bisulfate 0.1 N H_2SO_4. The absolute Φ_f' was determined to be 0.54 by Melhuish.[6] The concentration of the solutions used was adjusted so that the optical density was 0.75 at 337 nm. All samples were degassed by the freeze–pump–thaw method.

The fluorescence decay was measured by the detection equipment consisting of a coaxial type nitrogen laser (7 nsec, 40-kW peak power) or a Blumlein type nitrogen laser (3 nsec, 500-kW peak power), a Hamamatsu R-106 (UH) photomultiplier with a Toshiba VG 52-filter (transmission maximum 520 nm), and an Iwatsu SS-212 (200 MHz) oscilloscope. The decay times were determined by the convolution method.[7]

3. Results and Discussion

Absorption and fluorescence spectra of TH and TD in some solvents at 298 K are shown in Figure 1 and Table I. The normal fluorescence could not be observed, but only the green emission with a maximum at ca. 500 nm. The latter fluorescence was assigned to that of the corresponding proton transferred excited species of TH or TD.[8] The lack

TABLE I: Fluorescence Quantum Yields Φ_f' at 298 K and 337 nm[a]

Substance	Solvent	Fluoscn max, kK (nm)	Φ_f'	$\Delta\bar{\nu}$, kK
TH	CH	19.9(502)	0.38 ± 0.03	10.1
	MP	19.9(502)	0.38 ± 0.03	10.1
	EtOH	20.6(486)	0.19 ± 0.02	10.3
	AN	20.3(492)	0.18 ± 0.02	10.6
TD	CH	19.9(502)	0.38 ± 0.03	10.1
	MP	19.9(502)	0.38 ± 0.03	10.1

[a] A 150-W Xe lamp with a diffraction grating was used as the radiation source. CH, cyclohexane; MP, methylcyclohexane; isopentane = 3:1; EtOH, ethanol; AN, acetonitrile; $\Delta\bar{\nu}$, Stokes shift.
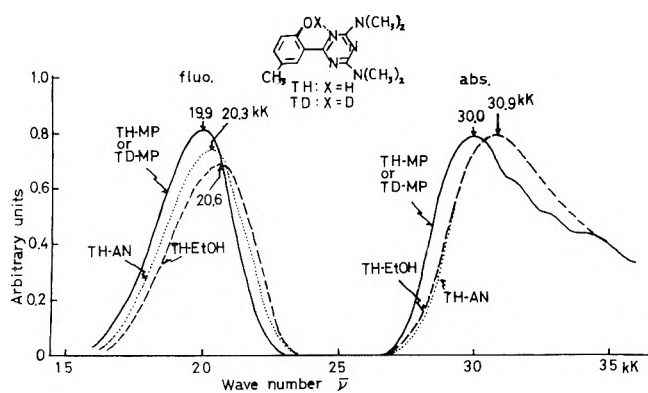
Figure 1. Absorption and corrected fluorescence spectra of TH and TD.

Figure 2. The temperature dependence of the fluorescence quantum yields Φ_f'.

Figure 3. The temperature effect on the fluorescence lifetimes τ_f'.

of normal fluorescence indicates that (1) the lifetime of the fluorescent state of TH (S_1, see below) is very short, which seems to be $\leq 10^{-11}$ sec judging from the Einstein transition theory and the sensitivity of fluorimeter used; (2) the enthalpy change ΔH^* between the S_1 (enol form) and S_1' (keto form) states was large in comparison with that of salicylic acid[1] or 2-(aminophenyl)-2,1,3-benzotriazole.[3] Therefore, the reverse proton transfer $S_1 \leftarrow S_1'$ is negligibly small in the present case. Spectral change was scarcely observed in the temperature range 230–330 K. The excitation spectra of TH and TD at the fluorescence maximum were close to the absorption spectra. The absence of excitation wavelength effects on the fluorescence quantum yields Φ_f' (excitation 280–360 nm) shows that the intramolecular proton transfer originates from the thermally relaxed excited state, and $k_{PT} < k_{VR}$ (see eq 0' and 1) in the condensed media.

Measurements of the quantum yields Φ_f' and the lifetimes τ_f' for the fluorescence originated from the S_1' state as a function of temperature have been carried out. The results of Φ_f' and τ_f' are shown in Figures 2 and 3. The Φ_f' values increased with decreasing temperature in each solvents. No temperature effect on τ_f' was observed in nonpolar solvents (MP and CH), although the τ_f' values in polar solvents (EtOH and AN) decreased with increasing temperature.

The photostability of TH and TD was similar to those of hydrogen-bonded molecules studied by Otterstedt.[4] Of course, the ground state of TH has an intramolecular hydrogen bond (OH···N) on the bases of the large pK_a value of 12.23 and the NMR data ($\tau_{OH} = -3.13$).[9]

These results can be accounted for by the following scheme:
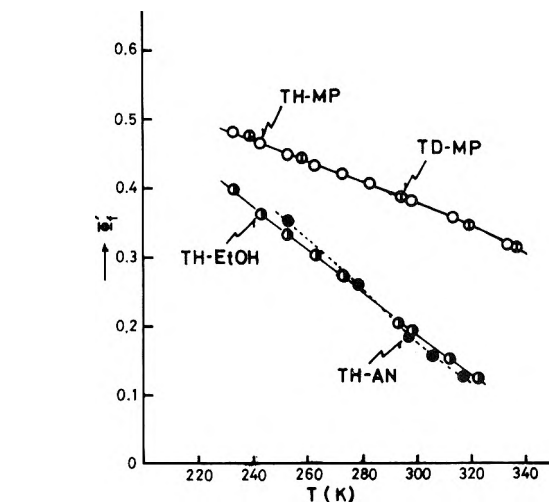
$S_0 + h\nu \longrightarrow S_1^\dagger$		absorption	(0)
$S_1^\dagger \longrightarrow S_1$	k_{VR}	vibrational relaxation	(0')
$S_1 \longrightarrow S_1'$	k_{PT}	intramolecular proton transfer	(1)
$S_1 \longrightarrow S_0$	k_{rd}	rapid deactivation	(2)
$S_1 \longrightarrow S_0 + h\nu'$	k_f	normal fluorescence	(3)
$S_1 \longrightarrow T$	k_{isc}	intersystem crossing	(4)
$S_1 \longrightarrow S_0$	k_{ic}	internal conversion	(5)
$S_1' \longrightarrow S_0' + h\nu''$	k_f'	green fluorescence	(6)
$S_1' \longrightarrow S_0'$	k_d'	radiationless deactivation in S_1'	(7)
$S_0' \longrightarrow S_0$	k_{-PT}	back proton transfer	(8)
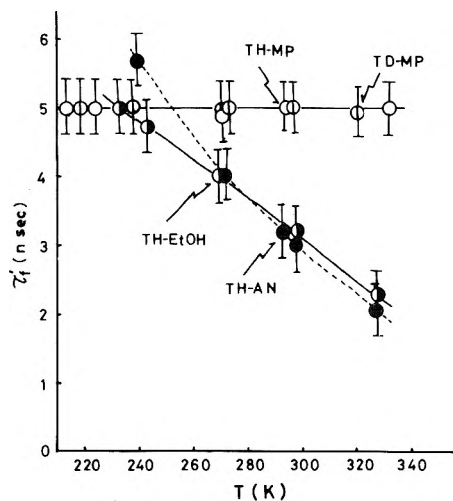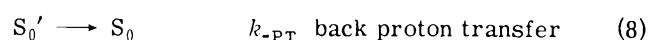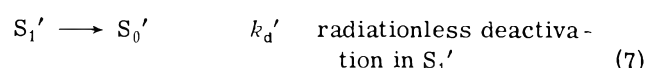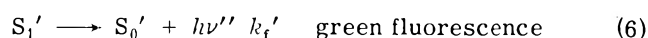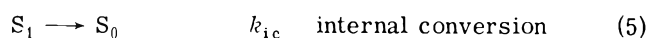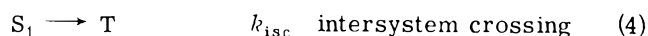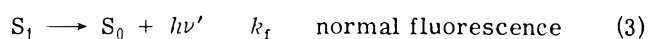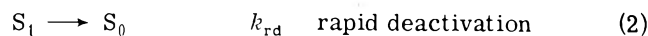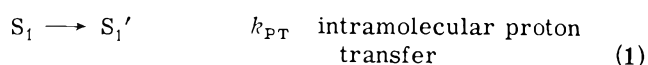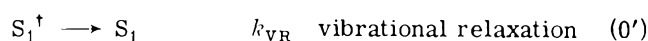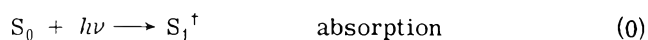
where S_0, $S_1^\dagger$, S_1, and T are the ground state, the excited Franck–Condon state, the vibrationally relaxed excited state, and the triplet state of enol form, respectively, and S_0' and S_1' are the ground state and the proton transferred excited state of keto form, respectively.

From the steady-state approximation, Φ_f' is given by

$$\Phi_f' = \frac{k_{PT}}{k_{PT} + k_d} \frac{k_f'}{k_f' + k_d'} = \frac{k_{PT}}{k_{PT} + k_d} k_f' \tau_f' \quad (9)$$

where $k_d = k_{rd} + k_f + k_{isc} + k_{ic}$ and $\tau_f' = (k_f' + k_d')^{-1}$. If the activation energies E_{PT} and E_d and the frequency factors A_{PT} and A_d exist in the processes 1 and 2 respectively, eq 10 is derived from eq 9.

$$\log [(\alpha - \Phi_f')/\Phi_f'] = \log \frac{A_d}{A_{PT}} - \frac{E_d - E_{PT}}{2.303RT} \quad (10)$$

where $\alpha = k_f'\tau_f'$. The α value is $0.5 \leq \alpha \leq 1$ in MP. The plot of $\log [(\alpha - \Phi_f')/\Phi_f']$ vs. T^{-1} at the several values of α is shown in Figure 4. The activation energy E_d can be obtained from the slope of the linear plot which is given at $\alpha = 0.55$.

$$E_d = 2.5 + E_{PT} \text{ kcal/mol} \quad (11)$$

Weller[1] has estimated the E_{PT} value to be less than 2.6 kcal/mol. Recently, Ingham and El-Bayoumi[11] have determined the activation barrier of 1.4 kcal/mol in the double proton transfer process of the excited dimer of 7-azaindole. From the above data of E_{PT}, the E_d value was estimated to be ca. 4 kcal/mol.

The value of frequency factor ratio was obtained from eq 10 and Figure 4.

$$A_d/A_{PT} \simeq 34 \quad (12)$$

The value of E_d is close to the activation energy for the viscous flow of solvent. However, the deactivation process is different from diffusional quenching by an unspecified quenching species, since the k_d value at higher temperatures ($T > 230$ K) is large enough to compete with the proton transfer. Considering the lack of normal fluorescence, the rate constant of k_{rd} is approximately given by

$$k_{rd} \simeq k_d \quad (13)$$

where $T > 230$ K.

The reasons why the temperature-dependent deactivation of internal quenching occurs have been explained as follows: (1) rotational deactivation[12-14] (The radiationless process from the excited state of some dyes such as Auramine O and Crystal Violet is enhanced by rotational motions.); (2) intersystem crossing to a higher triplet state[15-17] (In higher condensed aromatic hydrocarbons the temperature-dependent component is attributed to intersystem crossing from S_1 to a higher triplet state.); (3) deactivation via an isomeric state[18] (In cases of benzene and its derivatives, thermally activated $S_1 \rightarrow S_0$ internal conversion takes place via an isomeric state.).

Taking into these account, one will discuss the rapid deactivation process in the present work. If the process would occur due to rotational deactivation, hydrogen-bond breaking in excited TH should take place to deform its planar structure. This case is unlikely because the hydrogen bond OH···N in excited TH may be stronger than that in the ground state on the basis of theoretical calculation.[19]

The rate constant for intersystem crossing from S_1 to a higher triplet state of TH may be less than 10^{11} sec^{-1}, since the rate constant for intersystem crossing from the lowest vibronic level of benzophenone is 2×10^{11} sec^{-1},[20] whose value may be the most fastest rate constant for intersystem crossing. Therefore, the possibility for the deactivation due to the second case becomes small.

Mataga et al.[21] have demonstrated that hydrogen bonding in the carbazole–pyridine system enhances internal conversion but not intersystem crossing. On theoretical
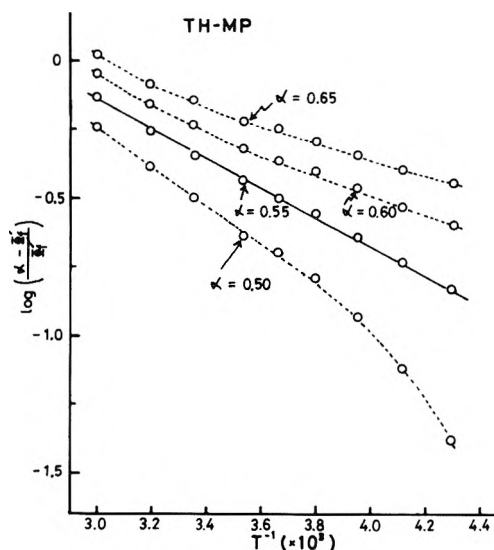
Figure 4. Plots of $\{(\alpha - \Phi_f')/\Phi_f'\}$ vs. T^{-1} (see text).
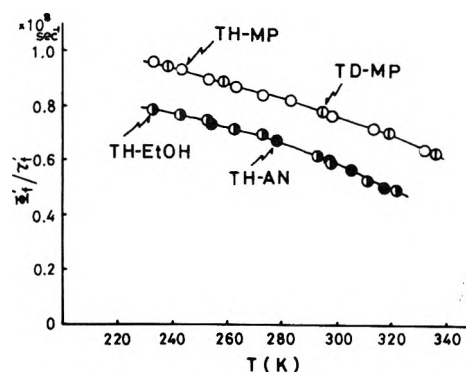
Figure 5. Plots of Φ_f'/τ_f' vs. T.

grounds, Rehm and Weller[22] have proposed that fluorescence quenching is caused by a transient hydrogen transfer. Recently, Kikuchi et al.[23] have shown that singlet excited β-naphthol in the presence of 10^{-4} to 10^{-1} M pridine undergoes collisional deactivation and this deactivation is mainly attributed to the transient hydrogen atom transfer via hydrogen bonding. If rapid deactivation in excited TH is caused by transient hydrogen atom transfer, the S_0 state is repopulated to a great extent and the S_0' state is directly produced to a small extent. No transient neutral radical could be observed in the intramolecular system. Although we had no information of the photochemical isomerization of TH except for the proton transfer, the third case described above seems likely.

On the other hand, the possibility of the decrease in Φ_f' due to hydrogen-bond breaking in the S_0 state may be excluded, since the enthalpy change in the breaking process is 4.7 kcal/mol[24] and the population of TH free from the hydrogen bond is less than 0.001 at 300 K.

Figure 5 shows plots of Φ_f'/τ_f' vs. T, indicating that the rapid deactivation process in S_1 should be also involved in polar solvents. The values of Φ_f'/τ_f' in polar solvents are smaller than those in nonpolar solvents. Complicating features may arise in polar solvents, where the ground and excited species of TH interact with solvent molecules resulting in a decrease in Φ_f'.

No deuterium isotope effect on the intermolecular proton transfer is known at higher temperatures.[11] A similar

result was obtained in the intramolecular proton transfer process.

Although no decisive answer as to the mechanism of rapid deactivation can be given at this time, the deactivation competing with the proton transfer exists in the excited TH at higher temperatures (>230 K).

References and Notes

(1) A. Weller, *Z. Elektrochem.*, **60**, 1144 (1956).
(2) S. G. Schulman and H. Gershon, *J. Phys. Chem.*, **72**, 3297 (1968).
(3) J. R. Murrill and R. G. Bennett, *J. Chem. Phys.*, **43**, 1410 (1965).
(4) J.-E. A. Otterstedt, *J. Chem. Phys.*, **58**, 5716 (1973).
(5) H. Shizuka, T. Kanai, T. Morita, Y. Ohto, and K. Matsui, *Tetrahedron*, **27**, 4021 (1971); Y. Ohto, H. Shizuka, S. Sekiguchi, and K. Matsui, *Bull. Chem. Soc. Jpn.*, **47**, 1209 (1974).
(6) W. H. Melhuish, *J. Phys. Chem.*, **65**, 229 (1961).
(7) R. A. Kashow and J. A. Sousa, *J. Appl. Phys.*, **42**, 2128 (1971).
(8) H. Shizuka, K. Matsui, T. Okamura, and I. Tanaka, presented at the 30th Annual Meeting of the Chemical Society of Japan, Osaka, April, 1974.
(9) Y. Ohto, Y. Hashida, S. Sekiguchi, and K. Matsui, *Bull. Chem. Soc. Jpn.*, **47**, 1301 (1974).
(10) Unfortunately, the precipitation of the starting material took place in MP at low temperatures (≤220 K).
(11) K. C. Ingham and M. A. El-Bayoumi, *J. Am. Chem. Soc.*, **96**, 1674 (1974).
(12) G. Oster and Y. Nishijima, *J. Am. Chem. Soc.*, **78**, 1581 (1956).
(13) Th. Forster and G. Hoffmann, *Z. Phys. Chem.* (*Frankfurt am Main*), **75**, 63 (1971).
(14) D. Magde and M. W. Windsor, *Chem. Phys. Lett.*, **24**, 144 (1974).
(15) As for kinetic data of internal quenching of aromatic molecules, see J. B. Birks, "Photophysis of Aromatic Molecules", Interscience, New York, N.Y., 1970, p 180, and the many references therein.
(16) R. G. Bennett and P. J. McCartin, *J. Chem. Phys.*, **44**, 1969 (1966).
(17) B. Stevens, M. F. Thomatz, and J. Jones, *J. Chem. Phys.*, **46**, 405 (1967).
(18) See ref 15, p 240.
(19) The π-formal charges calculated by a semiempirical SCF–MO–CI method were as follows:

Proper atoms	S_0	S_1	S_0'	S_1'
O	+0.1423	+0.2668	−0.5888	−0.3930
N	−0.3800	−0.4084	+0.3929	+0.3590

It is clear that the hydrogen bond OH⋯N in S_1 is stronger than that in S_0 judging from the π-formal charges. The above data also show that the proton transfer originates from S_1 or S_0'.
(20) P. M. Rentzepis and G. E. Bush, *Mol. Photochem.*, **4**, 353 (1972).
(21) N. Mataga, F. Tanaka, and M. Kato, *Acta Phys. Polon.*, **34**, 733 (1968).
(22) D. Rehm and A. Weller, *Isr. J. Chem.*, **8**, 259 (1970).
(23) K. Kikuchi, H. Watarai, and M. Koizumi, *Bull. Chem. Soc. Jpn.*, **46**, 749 (1973).
(24) E. M. Eyring and D. L. Cole in "Fast Reactions and Primary Processes in Chemical Kinetics", S. Claesson, Ed., Interscience, London, 1967, p 255.

Thermodynamic Theory of the Solvent-Jump Relaxation Method[1]

D. Y. Chao and Z. A. Schelly*

Department of Chemistry, University of Georgia, Athens, Georgia 30602 (Received June 9, 1975)

The thermodynamic parameters governing the chemical relaxation in solvent-jump experiments are discussed. The expression for the relaxation amplitude $\Delta\xi$ is derived as a function of the dilution ratio, the equilibrium constants in the initial and final media of given dielectric constants, as well as the stoichiometric coefficients, activity coefficients, mole numbers, and charges of the species present in a single step equilibrium.

Introduction

Chemical equilibria can be disturbed by changing external or internal thermodynamic variables of the system in question. If the perturbation is sufficiently small and significantly faster than the rate of adjustment of the system to the new conditions, the relaxation times τ_j can be interpreted in terms of rate constants and concentration variables in a relatively simple fashion. This represents the basis of relaxation method studies of fast reactions.[2]

The external parameters usually altered are the temperature T, the pressure P, or the electric field strength $\bar{E}$ and the internal ones are the concentration of solutes and/or the composition of the solvent. A perturbation of the total solute concentration can be achieved by sudden dilution (concentration-jump) of the equilibrium system using rapid mixing devices.[3] Similarly, the composition of the solvent can be abruptly changed by fast mixing of two equilibrium solutions of different solvents, or one equilibrium solution with another solvent. Since the total concentration of the solute is not necessarily changed in the experiment, the name solvent-jump is more generally descriptive of the method than concentration-jump. This type of relaxation experiment was first suggested by Ljunggren and Lamm[4] and has been applied to slow[5] as well as to fast reactions, using transient and also nontransient[8] observation in stopped- and continuous flow systems, respectively.

The direct information obtained from relaxation experiments is usually the spectrum of relaxation times and the relaxation amplitudes. The latter represent the net signal changes observed, which are measures of equilibrium shifts and can be used to determine thermodynamic functions (ΔH, ΔV, etc.) for elementary reaction steps.

For perturbations by changing *external* variables, the general thermodynamic relations governing chemical relaxation have been developed by Eigen and DeMaeyer,[2] and the calculation of relaxation amplitudes was further discussed by Czerlinski[9] and Thusius.[10]

In the present paper we focus on the thermodynamic aspects of *internal* perturbation relaxation methods, and on

the calculation of relaxation amplitudes in solvent-jump studies of single step equilibria.

Definition of System and Conditions

Consider the chemical equilibrium

$$\nu_1 A_1 + \nu_2 A_2 + \ldots \underset{k_r}{\overset{k_f}{\rightleftharpoons}} \nu_i A_i + \nu_{i+1} A_{i+1} + \ldots \quad (1)$$
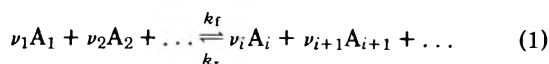
for which the equilibrium constant is given by $K = \Pi a_i{}^{\nu_i}$, where the a_i are the activities of A_i, and the stoichiometric coefficients ν_i's are positive for products and negative for reactants. Since $a_i = c_i \gamma_i$, we can write

$$\ln K = \Sigma \nu_i \ln a_i = \Sigma \nu_i \ln c_i + \Sigma \nu_i \ln \gamma_i \quad (2)$$

If the temperature and pressure are kept constant, dilution of the equilibrium solution with the same solvent has no effect on K, but it changes the concentrations c_i and the activity coefficients γ_i, which are functions of the volume V. Mixing with another solvent results in a new medium, and all variables K, c_i, and γ_i in (2) may be affected. If the instantaneous (immediately after dilution) values of c_i and γ_i do not satisfy the equilibrium condition

$$-\mathcal{C} \equiv \Delta G \equiv \Sigma \nu_i \mu_i = \Sigma \nu_i \mu_i{}^\circ + \\ RT(\Sigma \nu_i \ln c_i + \Sigma \nu_i \ln \gamma_i) = 0 \quad (3)$$

the system will relax to zero affinity, $\mathcal{C} = 0$. The $\mu_i{}^\circ$ and μ_i are the chemical potentials of A_i in the standard state ($a_i = 1$, but with properties like at infinite dilution) and under experimental conditions, respectively.

In order to facilitate the analysis, the overall dilution-relaxation process will be subdivided as a transition from state 1 to state 3 over a distinct intermediate state 2:

$$\text{state 1} \rightarrow \text{state 2} \rightarrow \text{state 3} \quad (4)$$

State 1 is the initial equilibrium state ($\Delta G_1 = \Sigma \nu_i \mu_{i1} = 0$) at T and P, in a volume V. All parameters, such as concentrations, activity coefficients, etc., in this state are identified by a subscript 1. We restrict our considerations to a range of ionic strength $I = \frac{1}{2}\Sigma c_i z_i{}^2 < 10^{-2}\ M$, where the Debye–Hückel limiting law[11] is adequate for the calculation of γ_i from

$$\ln \gamma_i = -B\epsilon^{-3/2} z_i{}^2 I^{1/2} \quad (5)$$

B in eq 5 is a function of T only, ϵ is the dielectric constant of the medium, and z_i is the charge of the ith ion.

State 2 arises shortly after the sudden n-fold ($n > 1$) dilution with the original or with another pure solvent. The homogeneous mixing can be achieved in about 1 msec, which time constant is limited essentially only by cavitation.[12] At this point all fast physical processes (i.e., the redistribution of the solvent and ionic atmospheres) have been completed and the system is ready for the much slower chemical relaxation. The solvent-jump methods are usually limited to studying chemical equilibria with relaxation times longer than a few milliseconds. The temperature and pressure are kept constant at their values of state 1, but the new volume is nV. Since equilibrium 1 has not yet shifted, the extent of reaction ξ is the same as in state 1, given by

$$n_{i2} = n_{i1} = n_i{}^0 + \nu_i \xi \quad (6)$$

where n_{i1}'s are the numbers of moles A_i present at equilibrium, and $n_i{}^0$'s are the initial numbers of moles of A_i at the time when the equilibrium mixture was prepared. Thus, $n_i{}^0 = 0$ are typical for the products in (1). Due to the dilution,

the concentrations $c_{i1} = n_{i1}/V$ decreased to $c_{i2} = n_{i1}/nV$, and the equilibrium constant also has a new value K_2, unless the original solvent was used for dilution, in which case K_1 is valid throughout the whole process. The activity coefficients in this state are given by

$$\ln \gamma_{i2} = -B\epsilon_2{}^{-3/2} z_i{}^2 (\tfrac{1}{2}\Sigma n_{i1} z_i{}^2 / nV)^{1/2} \quad (7)$$

where ϵ_2 is replaced by ϵ_1 in case of dilution with the original solvent.

Although the perturbation was kept small enough for the linearization of the rate equations, state 2 is a nonequilibrium state with $\Delta G_2 = \Sigma \nu_i \mu_{i2} \neq 0$.

State 3 is the final equilibrium state reached after completion of the chemical relaxation. In step $2 \rightarrow 3$ all variables stay constant and only n_{i1} change to n_{i3}, and of course also those parameters (c_i and γ_i) which depend on n_i. Thus, $c_{i3} = n_{i3}/nV$, and $\ln \gamma_{i3}$ have the form of eq 7 but with n_{i3} substituted for n_{i1}. The extent of the reaction in this step changes by $\Delta\xi$, that we define as the relaxation amplitude. The relaxation *signal* amplitude can easily be obtained from $\Delta\xi$, using the function which relates concentrations to the physical property measured. The final equilibrium mole numbers are given by

$$n_{i3} = n_i{}^0 + \nu_i(\xi + \Delta\xi) \quad (8)$$

that with eq 6 yields

$$n_{i3} = n_{i1} + \nu_i \Delta\xi \quad (9)$$

Since $\Delta G_3 = \Sigma \nu_i \mu_{i3} = 0$, the driving force of the chemical relaxation is $\mathcal{C}_{23} = \Delta G_3 - \Delta G_2 = -\Delta G_2$.

Calculation of the Relaxation Amplitude

Since the chemical relaxation takes place in step $2 \rightarrow 3$, $\Delta\xi$ has to be calculated from the change of the Gibbs free enthalpy $\Delta G_{23} = -\mathcal{C}_{23}$ of this step:

$$\Delta G_{23} = \Sigma \nu_i \mu_{i3} - \Sigma \nu_i \mu_{i2} = \Sigma \nu_i \Delta\mu_i \quad (10)$$

The change in chemical potential $\Delta\mu_i = \mu_{i3} - \mu_{i2}$ of species A_i is given by

$$\Delta\mu_i = \mu_i{}^\circ + RT(\ln c_{i3} + \ln \gamma_{i3}) - \\ \mu_i{}^\circ - RT(\ln c_{i2} + \ln \gamma_{i2}) \quad (11)$$

or in an abbreviated form by

$$\Delta\mu_i = RT(\Delta \ln c_i + \Delta \ln \gamma_i) \quad (12)$$

By substituting the proper values for c_{i3}, c_{i2}, γ_{i3}, and γ_{i2} in eq 12 using (7) we have in general for dilution with any solvent

$$\Delta\mu_i / RT = \ln (n_{i3}/nV) - \\ \ln (n_{i1}/nV) - B'\epsilon_2{}^{-3/2} z_i{}^2 [(\Sigma n_{i3} z_i{}^2/nV)^{1/2} - \\ (\Sigma n_{i1} z_i{}^2/nV)^{1/2}] \quad (13)$$

with $B' = B(\tfrac{1}{2})^{1/2}$. The first two terms on the right side of eq 13 can be evaluated by using (6) and (8)

$$\ln \frac{n_{i3}}{n_{i1}} = \ln \frac{n_i{}^0 + \nu_i(\xi + \Delta\xi)}{n_i{}^0 + \nu_i \xi} = \ln \left(1 + \frac{\nu_i \Delta\xi}{n_{i1}}\right) \simeq \frac{\nu_i \Delta\xi}{n_{i1}} \quad (14)$$

Similarly, using (9), the expression between the brackets in (13) becomes

$$(1/nV)^{1/2}\{[\Sigma(n_{i1} z_i{}^2 + \nu_i z_i{}^2 \Delta\xi)]^{1/2} - [\Sigma n_{i1} z_{i1}{}^2]^{1/2}\} \quad (15)$$

The first square-root term between the braces in (15), using binomial expansion, becomes

$$[\Sigma n_{i1}z_i{}^2 + \Delta\xi\Sigma\nu_i z_i{}^2]^{1/2} \simeq$$

$$(\Sigma n_{i1}z_i{}^2)^{1/2}(1 + \tfrac{1}{2}\Delta\xi\frac{\Sigma\nu_i z_i{}^2}{\Sigma n_{i1}z_i{}^2} - \dots) \quad (16)$$

Substituting (14) through (16) into (13) we obtain

$$\Delta\mu_i/RT = \frac{\nu_i\Delta\xi}{n_{i1}} -$$

$$B'\epsilon_2{}^{-3/2}z_i{}^2(1/nV)^{1/2}\frac{\Delta\xi\Sigma\nu_i z_i{}^2}{2\Sigma n_{i1}z_i{}^2}(\Sigma n_{i1}z_i{}^2)^{1/2} \quad (17)$$

which can be rearranged to

$$\Delta\mu_i/RT = \Delta\xi\left(\frac{\nu_i}{n_{i1}} - \ln\gamma_{i2}\frac{\Sigma\nu_i z_i{}^2}{2\Sigma n_{i1}z_i{}^2}\right) \quad (18)$$

Substitution of (18) into (10) yields ΔG_{23}, which however is

$$\Delta G_{23} = -RT\ln K_3 + RT\ln Q_2 \quad (19)$$

where $K_3 = K_2$ is the equilibrium constant in the final medium that prevails already in state 2 and $Q_2 = \Pi a_{i2}{}^{\nu_i}$, with the nonequilibrium values of a_{i2} in state 2. Q_2 can be expressed in terms of the equilibrium constant K_1 in the original solution in state 1, minus difference terms:

$$\ln Q_2 = \ln K_1 - \ln n\Sigma\nu_i - BI_1{}^{1/2}(\epsilon_2{}^{-3/2}n^{1/2} -$$

$$\epsilon_1{}^{-3/2})\Sigma\nu_i z_i{}^2 \quad (20)$$

Equation 20 results from the subtraction of $\ln K_1$ from $\ln Q_2$. The expression used for $\ln K_1$ is obtained through substitution of (5) into (2), specified for state 1, and the function for $\ln Q_2$ is obtained by substituting (7) into $\ln Q_2 = \Sigma\nu_i[\ln(n_{i1}/nV) + \ln\gamma_{i2}]$.

Finally, with (18) through (20) substituted into (10) we obtain the relaxation amplitude $\Delta\xi$ as a function of the initial K_1 and final K_3 equilibrium constants, the dilution factor n, the ionic strengths I_1 and I_2, and the dielectric constants of the original ϵ_1 and final medium ϵ_2

$$\Delta\xi =$$

$$\left[\ln\frac{K_1}{K_3} - \ln n\Sigma\nu_i - BI_1{}^{1/2}(\epsilon_2{}^{-3/2}n^{-1/2} - \epsilon_1{}^{-3/2})\Sigma\nu_i z_i{}^2\right]\Big/$$

$$\left[\Sigma\nu_i{}^2/n_{i1} - \Sigma\ln\gamma_{i2}\frac{\Sigma\nu_i{}^2 z_i{}^2}{2\Sigma n_{i1}z_i{}^2}\right] \quad (21)$$

For nonionic species $(z_i = 0)$ in equilibrium diluted with the original solvent $(K_1 = K_3)$ eq 21 simplifies to

$$\Delta\xi = \frac{-\ln n\Sigma\nu_i}{\Sigma\nu_i{}^2/n_{i1}} = \frac{-V\ln n\Sigma\nu_i}{\Sigma\nu_i{}^2/c_{i1}} \quad (22)$$

In such a case $\Sigma\nu_i \neq 0$ is the necessary requirement for the applicability of solvent-jump perturbation, and the dilution ratio n that results in a certain relaxation amplitude can be estimated from eq 22. Typically, $\Delta\xi$ should be kept around $0.05\,n_{i1}$ (for that species i which is present in limiting amount), so that the relaxation rate equation can be linearized. E.g., for a monomer–dimer equilibrium $2A \rightleftharpoons A_2$ $n = 1.28$ is needed if all $n_{i1} = 10^{-3}$ m.

The value of B in (21) is a function of the temperature only

$$B = e^3(2N)^{1/2}/8\pi(\epsilon_0 kT)^{3/2} \quad (23)$$

which is kept constant during the experiment. By substituting the physical constants $\epsilon_0 = 8.859 \times 10^{-14}$ A sec V^{-1} cm^{-1}, $e = 1.602 \times 10^{-19}$ A sec, $k = 1.389 \times 10^{-16}$ erg K^{-1}, and $N = 6.023 \times 10^{23}$ mol^{-1} into (23) we obtain

$$B = 4.204 \times 10^6 \text{ K}^{3/2} M^{-1/2} T^{-3/2} \quad (24)$$

For the common case of dilution of an aqueous ionic equilibrium $(z_i \neq 0)$ with water $(\epsilon = 78.56)$ at 25°C, the numerator in eq 21 becomes

$$-\ln n\Sigma\nu_i - 1.17(n^{-1/2} - 1)I_1{}^{1/2}\Sigma\nu_i z_i{}^2 \quad (25)$$

Applying eq 21 to an aqueous ionic dimerization equilibrium $2A^- \rightleftharpoons A_2{}^{2-}$ (with counterion M^+) at 25°C, $\Delta\xi = 0.025\,n_{i1}$ is predicted for a 1.28-fold dilution with water, if $n_{i1} = 10^{-3}$ m in an initial volume of 1 l. A tenfold dilution would represent a large perturbation with $\Delta\xi = 0.53\,n_{i1}$. In experiments with large perturbation the observation has to be restricted to the end of the relaxation process. Using dioxane for dilution $(\epsilon_{diox} = 2.209, \epsilon_2 = 6.1)$,[13] $n = 10$ would result in $\Delta\xi = 0.19\,n_{i1}$ if $K_1/K_3 = 10^2$.

An interesting situation arises in mixing two solutions of the same equilibrium but of different concentrations. Here the concentration of one of the two original subsystems is jumped downward and the other upward. In such a case eq 21 has to be applied separately to the subsystems and the experimental conditions have to be chosen such that the difference of the opposing amplitudes $\Delta\xi = \Delta\xi_1 - \Delta\xi_2 \neq 0$. Otherwise, the final equilibrium concentrations would immediately be reached upon mixing and no kinetics could be observed.[14]

In certain cases, where the temperature change caused by the heats of mixing and/or dilution is not negligible, values of all parameters in (21) have to be taken at the final temperature. The resulting $\Delta\xi$ represents only the solvent-jump part of the total relaxation amplitude, and the temperature-jump part must be calculated separately[1,9,10] and added to it.

In general, depending on the system in question, the relative magnitude of the terms in (21) dictates the proper dilution ratio and the choice of the diluting solvent for achieving the maximum tolerable $\Delta\xi$. Alternatively, from the experimentally measured *signal* amplitude one can calculate $\Delta\xi$, which in turn can be used to estimate thermodynamic quantities associated with the reaction. The present treatment does not include the activity coefficients of nonelectrolytes. This will be considered in a latter communication.

References and Notes

(1) Abstracted in part from D. Y. Chao's dissertation, to be submitted to the University of Georgia.
(2) M. Eigen and L. DeMaeyer in "Techniques of Organic Chemistry", Vol. 8, 2nd ed, Part 2, S. L. Friess, E. S. Lewis, and A. Weissberger, Ed., Wiley, New York, N.Y., 1963, p 895.
(3) B. Chance, Q. H. Gibson, R. H. Eisenhardt, and K. K. Lonberg-Holm, Ed., "Rapid Mixing and Sampling Techniques in Biochemistry", Academic Press, New York, N.Y., 1964.
(4) S. Ljunggren and O. Lamm, *Acta Chem. Scand.*, **12**, 1834 (1958).
(5) J. H. Swinehart and G. W. Castellan, *Inorg. Chem.*, **3**, 278 (1964).
(6) Z. A. Schelly, R. D. Farina, and E. M. Eyring, *J. Phys. Chem.*, **74**, 617 (1970).
(7) M. M. Wong and Z. A. Schelly, *J. Phys. Chem.*, **78**, 1891 (1974).
(8) Z. A. Schelly and M. M. Wong, *Int. J. Chem. Kinet.*, **6**, 687 (1974).
(9) G. H. Czerlinski, "Chemical Relaxation", Marcel Decker, New York, N.Y., 1966.
(10) D. Thusius, *J. Am. Chem. Soc.*, **94**, 356 (1972).
(11) S. Glasstone, "Textbook of Physical Chemistry", 2nd ed, Van Nostrand, New York, N.Y., 1959, p 959.
(12) M. M. Wong and Z. A. Schelly, *Rev. Sci. Instrum.*, **44**, 1226 (1973).
(13) R. A. Robinson and R. H. Stokes, "Electrolyte Solutions", 2nd ed, Butterworths, London, 1970, p 401.
(14) G. H. Czerlinski in "Techniques of Electrochemistry", Vol. 2, E. Yeager and A. J. Salkind, Ed., Wiley-Interscience, New York, N.Y., 1973, p 378.

Apparent Specific Heat of Tetrapentylammonium Bromide in Aqueous Solution

Julian M. Sturtevant

Departments of Chemistry and Molecular Biophysics and Biochemistry, Yale University, New Haven, Connecticut 06520 (Received November 15, 1974; Revised Manuscript Received September 15, 1975)

Scanning calorimetry has been employed to evaluate the apparent specific heat of tetra-n-pentylammonium bromide in aqueous solution over the temperature range from 10 to 80° and the concentration range from 5×10^{-4} to 8×10^{-2} M. Variations with temperature not exceeding 20% are observed, as contrasted with variations exceeding 50% reported by Mohanty, Sunder and Ahluwalia for the excess partial specific heat of this solute.

Introduction

In a paper published in 1972, Mohanty, Sunder, and Ahluwalia[1] reported the results of calorimetric measurements of the heat of solution of tetra-n-pentylammonium bromide (TPAB) in water in the temperature range 5–85°C. The excess molal heat capacity of the solute was calculated from the temperature variation of the heat of solution. Since the solute concentrations were very low, ranging from 10^{-4} to 10^{-3} m, it was concluded that the experiments yielded the partial rather than the apparent excess heat capacity.

The results obtained by Mohanty et al. are shown in Figure 1, curve A, expressed as excess specific heats rather than excess molal heat capacities. It is seen that the excess specific heat undergoes remarkable variations, including a drop by a factor of 1/2.5 between 50 and 60°. Mohanty et al. presented a tentative interpretation of the temperature dependence of the excess specific heat in terms of the influence of the hydrophobic alkyl groups on the structure of the solvent.

In view of the importance of hydrophobic interactions in a wide variety of chemical and biochemical systems, it seemed important to reinvestigate this system by direct solution heat capacity calorimetry, to free the results from any dependence on possible changes in the heat capacity of the crystalline form of the solute species. To this end I have determined the apparent specific heat of TPAB solutions using two different scanning microcalorimeters, with results which show much smaller variations with temperature than reported by Mohanty et al. for the excess specific heat.

Experimental Section

Eastman White Label TPAB was recrystallized from benzene and dried to constant weight at 40–50° in vacuo.

The differential scanning calorimeter used for solutions of concentration greater than 0.02 M has been previously described.[2,3] For more dilute solutions the calorimeter developed by Privalov[4] and available from Mashpriborintorg, Moscow, USSR, was employed. In what follows these calorimeters are designated A and B, respectively. Differential scanning calorimetry provides the most convenient means for evaluating specific heats over a wide range of temperatures, and it can be applied to very dilute solutions provided adequate sensitivity and an adequately stable baseline are available. The apparent specific heat of the solute, s_{app},

in a solution containing c grams of solute per milliliter of solution, is given by the expression

$$s_{app} = s_0 + \frac{d}{c}(s - s_0) \qquad (1)$$

where s and s_0 are respectively the specific heats of the solution and the solvent, and d is the density of the solution. The advantage of differential operation is evident from the occurrence of the difference $s - s_0$ in eq 1. The occurrence of the factor $1/c$ shows that uncertainty in s_{app} is approximately inversely proportional to the concentration. A conservative statement of the capability of calorimeter A is that the uncertainty in a_{app} for a 1% solution in water is ± 0.04 over the temperature range 5–80°. Calorimeter B gives this level of accuracy down to a concentration of 0.1%.

In both instruments the calorimeter cells are completely filled and are open to the atmosphere through filling tubes of small internal diameter. Since any expansion or contraction of solvent or solution during scanning changes the amount of material contained in the effective volumes of the cells, it is essential to have accurate density data for materials studied in these calorimeters. These data were obtained as a function of both concentration and temperature, using a vibrating tube densimeter, manufactured by Sodev, Inc., Sherbrooke, Quebec, Canada. This instrument, which requires only a few tenths of a milliliter of liquid, has a resonant frequency of about 300 Hz. The average period, averaged over 10^3 cycles, was determined by means of a Model 700 counter manufactured by Newport Laboratories, Inc., Santa Ana, Calif. Although the frequency of the densimeter tube varies strongly with temperature, and is dependent on the immediate past thermal history of the instrument, the difference between the square of the period observed with water, τ_0^2, and that observed with solution, τ^2, could be determined with a reproducibility corresponding to an uncertainty of approximately 20 nsec in each period.

The densimeter was thermostated by water pumped from a bath regulated to $\pm 0.03°$, the temperature of which was measured with a Hewlett-Packard quartz thermometer. The densimeter was contained in an insulated air bath maintained at a temperature within a few degrees of that of the water bath.

In all cases, 20 or more readings of the period of the densimeter filled with N_2 and then with solution were sandwiched between an equal number of readings with two fill-
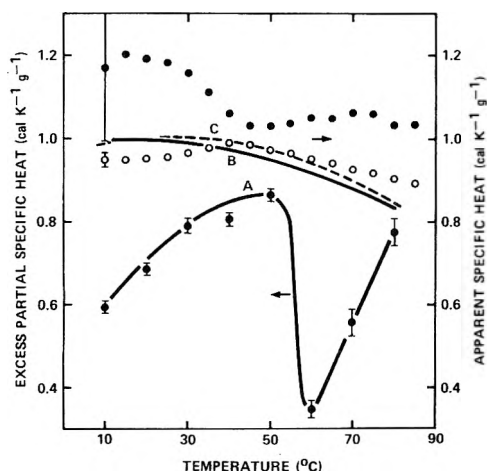
Figure 1. The specific heat of tetra-n-pentylammonium bromide (TPAB) as a function of temperature: (curve A, left-hand ordinate) the excess partial specific heat of TPAB in aqueous solution as reported by Mohanty et al., ref 1; (curves B and C, right-hand ordinate) the apparent specific heat of TPAB in 0.0797 and 0.0273 M solutions, respectively, as determined in calorimeter A; (O, ●) the apparent specific heat of TPAB in 0.0555 and 0.00050 M solutions, respectively, as determined in calorimeter B.

ings of water. The liquids were partially degassed at room temperature under aspirator vacuum.

The square of the period of the densimeter varies linearly with the density of the material it contains. Therefore the density, d, is given by the expression

$$d = a + b\tau^2 \tag{2}$$

The calibration constants, which vary with temperature, although much less strongly than the period, were evaluated from the N_2 and water fillings. When τ is expressed in microseconds, a was found to be approximately -5.3 g ml^{-1} and b approximately $+7.2 \times 10^{-7}$ g ml^{-1} μsec^{-2}.

The apparent specific volume of the solute, v_{app}, is given by the expression

$$v_{app} = \frac{1}{d_0} + \frac{1}{c}\left(1 - \frac{d}{d_0}\right) \tag{3}$$

where d_0 and d are respectively the densities of the solvent and the solution. From this it follows that

$$v_{app} = \frac{1}{d_0} + \frac{b}{cd_0}(\tau_0^2 - \tau^2) \tag{4}$$

Values of d_0, in grams per milliliters, were calculated from the equation[5]

$$d_0 =$$

$$\frac{0.9998 + 18.225t - 7.9222t^2 - 55.45t^3 + 149.8t^4 - 393t^5}{1 + 18.1597t} \tag{5}$$

where $t = {}^\circ C/1000$.

In the present experiments, the uncertainty in $\tau_0^2 - \tau^2$ appeared to be about 5%. This corresponds to an uncertainty of ± 0.002 in v_{app}. In two series of experiments in which the temperature was varied, the standard deviations encountered were about twice this size. Although it is probable that considerably more precise results could be obtained at the expense of much more careful attention to thermostating the densimeter and "ageing" it at each tem-
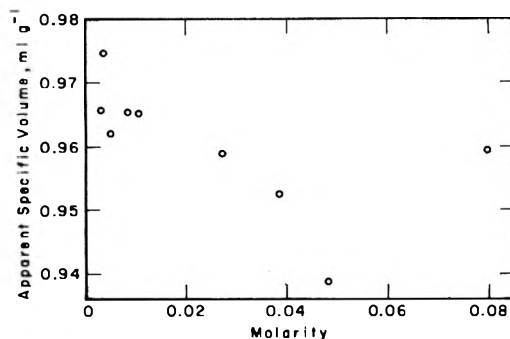
Figure 2. The apparent specific volume of TPAB in aqueous solution as a function of concentration at 25.01°C.
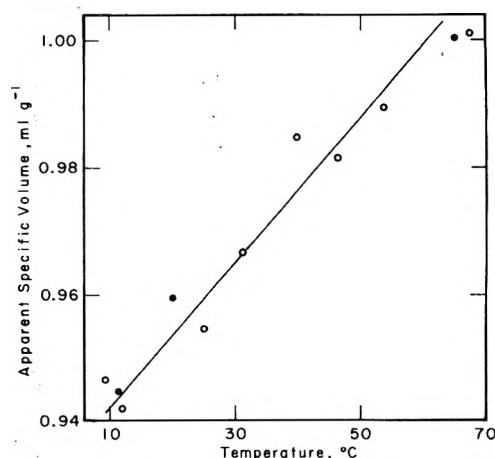
Figure 3. The apparent specific volume of TPAB in aqueous solution as a function of temperature at concentrations of 0.0273 (O) and 0.0797 M (●).

perature, the present results are more than adequate for the purpose of correcting the calorimetric data.

Results and Discussion

Apparent Specific Volumes. The variation of v_{app} with concentration at 25.01° is indicated in Figure 2. Although insufficient concentrations were studied to permit accurate delineation of the v_{app}–molarity curve, there is no doubt about the existence of a minimum in the curve at approximately 0.05 M.

The temperature variation of v_{app} at 0.0273 and 0.0797 M was studied in the range 10–65°, with the results shown in Figure 3. The specific volume increases linearly with the temperature, with the same dependence on temperature at each concentration. The least-squared line in the figure is

$$v_{app} = 0.9304 + 0.001145T \tag{6}$$

with T expressed in °C.

At 0.0797 M, the specific gravity of the solution varies from 1.0017 at 10° to 1.0003 at 70°.

Apparent Specific Heats. Solutions of concentration 0.0273 and 0.0797 M were scanned in calorimeter A over the temperature range from 10 to 70°C. The data were corrected for the expansion of the solution and the solvent, and were least squared to quadratic expressions in the temperature. The results at 0.0273 M are fit by the equation

$$s_{app} = 0.964 + 0.002915T - 0.0000549T^2 \tag{7}$$

(curve C, Figure 1), with a standard deviation of ±0.018, and those at 0.0797 M by the equation

$$s_{\text{app}} = 0.989 + 0.001197T - 0.0000390T^2 \qquad (8)$$

(curve B, Figure 1), with a standard deviation of ±0.009, in units of cal K^{-1} g^{-1}.

Solutions of concentration 0.00050 and 0.0555 M were scanned in calorimeter B over the temperature range from 10 to 85°, with results, corrected for expansion, plotted at 5° intervals in Figure 1 as closed and open circles, respectively. Error bars indicate the estimated uncertainty in the results. The apparent minimum at about 45° in the specific heat of TPAB in the most dilute solution is not statistically significant.

It is evident that there is no very remarkable variation of the apparent specific heat within the temperature range studied.

The large apparent specific heat of TPAB, approximately 1 cal K^{-1} g^{-1} is in striking contrast with the negative value of approximately −0.25 cal K^{-1} g^{-1} for ammonium bromide.[6] The effect of the ionic charges in decreasing the specific heat of neighboring water molecules is completely overwhelmed by the opposite effect of the hydrophobic alkyl groups. The decrease in the apparent specific heat of the solute at higher temperatures reflects a decreasing tendency of water to form structured clusters around the aklyl groups.

From the temperature variation of heats of solution, as measured by Mohanty et al., one can calculate the differ-

ence in specific heat between the pure solid solute and the solute in solution. It is this quantity, after multiplication by the molecular weight, 378.5, which is designated as the excess partial molal heat capacity by Mohanty et al. From their data and my values for the specific heat in very dilute solution, one can in principle calculate the specific heat of crystalline TPAB. This calculation results in a curve having a shape similar to that of curve A rotated 180° about a horizontal axis. This very unusual temperature dependence for the specific heat of a crystalline solid certainly needs confirmation by direct measurements.

References and Notes

(1) R. K. Mohanty, S. Sunder, and J. C. Ahluwalia, *J. Phys. Chem.*, **76**, 2577 (1972).
(2) R. Danforth, H. Krakauer, and J. M. Sturtevant, *Rev. Sci. Instrum.*, **38**, 484 (1967).
(3) T. Y. Tsong, R. P. Hearn, D. P. Wrathall, and J. M. Sturtevant, *Biochemistry*, **9**, 2666 (1970).
(4) P. L. Privalov, V. V. Plotnikov, and V. V. Filimonov, *J. Chem. Thermodyn.*, **7**, 41 (1975).
(5) G. S. Kell, *J. Chem. Eng. Data*, **12**, 66 (1967).
(6) E. D. Washburn, Ed., "International Critical Tables", Vol. III, McGraw-Hill, New York, N.Y., 1928, p 60 (densities); Vol. V, 1929, p 122 (specific heats).

Interactions of Aqueous Poly(N-vinylpyrrolidone) with Sodium Dodecyl Sulfate. II. Correlation of Electric Conductance and Viscosity Measurements with Equilibrium Dialysis Measurements

M. L. Fishman* and F. R. Eirich

Department of Chemistry, Polytechnic Institute of New York, Brooklyn, New York 11201 (Received October 7, 1974; Revised Manuscript Received June 11, 1975)

The interaction of sodium dodecyl sulfate (SDS) and aqueous poly(N-vinylpyrrolidone) (PVP) was studied over a large range of SDS concentrations and several polymer concentrations by conductivity and viscosity measurements at 25°C. The data tend to confirm earlier equilibrium dialysis measurements which indicated three regions of behavior. Correlation of the conductivity–dialysis data prove that the PVP detergent complex and associated counterions could supply up to 20% of the total conductivity due to SDS. Remarkably, it was found that equivalent conductance of the interacted detergent was higher than that of the pure micelles. This suggests that the detergent forms submicellar clusters stabilized with the aid of poly(vinylpyrrolidone). At higher concentrations, the aggregates, although of the nature of mixed micelles, mimic true micelles in that the ratio of charge to hydrodynamic volume remains constant with increasing SDS concentration. Viscosity measurements confirmed the presence of three regions of behavior: no change of the polymer coil shape in region I, a rapid expansion of the polymer coils in region II, and a further, but less rapid, expansion in region III. Since the higher polymer concentrations exhibit a more rapid expansion in region III than the lower polymer concentrations, this substantiates a previous conclusion, i.e., that increasing the polymer concentration at constant detergent increases the degree of counterion dissociation.

Introduction

Over the last 15 years, numerous studies[2-24,32-39] concerning the interaction of ionic detergents with nonionic polymers in aqueous media have indicated a continuing interest in these systems. Three of these studies[2,19,20] have attempted to determine the nature of these interactions by equilibrium dialysis measurements in the absence of salt, which may be added to eliminate Donnan effects.[3] The presence of salt simultaneously lowers the cmc and increases the micellar weight of the detergent.[16,20,21,35,37,38] In two of these studies,[2,19] the authors considered detergent solutions to behave like uni-univalent salts; in both cases the binding isotherms exhibited maxima. For the system poly(N-vinylpyrrolidone) (PVP)–sodium dodecyl sulfate (SDS), we have shown subsequently[20] that the maxima are artifacts which disappear if one accounts for the aggregation, or micelle formation, of SDS itself in equilibrium with the SDS–PVP complex. Modification of the Donnan equation, which describes the distribution of unbound SDS across the semipermeable membrane in the dialysis cell, allowed us to correct for this aggregation.

In the following, we will attempt to show that conductivity and viscosity data from PVP–SDS studies in conjunction with our previous binding data on the same system under closely similar conditions of temperature and composition[2] (a) give the contribution of each species present (unbound sodium and detergent ions, and polymer–detergent complex) to the total solution conductivity; (b) provide information on the hydrodynamic behavior of the polymer and detergent in each others presence; (c) lend support to our treatment of dialysis data by showing that the information obtained is consistent with other measure-

ments; and, finally, (d) allow us to propose a fairly detailed model for PVP–SDS interaction.

Experimental Section

A. Materials. Synthesis and purification of poly(N-vinylpyrrolidone) (PVP) of $\bar{M}_w = 400000$ and of SDS have been described in the previous paper.[20] The description of the dialysis, apparatus, and procedures will also be found there.

B. Conductometry. Two Jones[22] conductivity bridges were used during the course of the experiments. One, made by the Klett Mfg. Co., was modified to detect the balance point by a cathode ray oscilloscope rather than headphones. The other bridge, Industrial Instruments Inc., Model RC-18, already had the oscilloscope built in and operated on the same principle.

Both bridges were checked against high-precision (±0.001%) General Radio Co. resistors in the range 500–10000 ohms, and reproduced resistance readings to within ±1%. The resistances of the solutions were measured at two frequencies (1 and 3 kHz) and agreed within the precision of the bridges. Deionized distilled water of average conductivity 1.52 μmho cm was used. The calibration of the conductivity cells was carried out with KCl purified according to the procedure of Dagget.[23] Values of the specific conductance, κ, as a function of KCl concentration, were obtained from the literature.[24] A series of resistances was measured and the "best" cell constant obtained from the least-squares slope of the function κ against $(1/R)$.

The four conductivity cells used were: cell no. 1 (Jones type); cell no. 2 (flask type); cells no. 3 and 4 (Kraus type).[22] All conductivity measurements were made in a thermostated oil bath (±0.02°C).

Special procedures in cell preparation and platinization as well as for the conductance measurements themselves

* Address correspondence to this author at the Richard B. Russell Agricultural Research Center, P.O. Box 5677, Athens, Ga. 30604.

were required to obtain stable and reproducible data in the presence of surfactants; see ref 1. The cell constants ranged from 0.172 to 0.8508.

C. Viscometry. The measurements were carried out with Cannon–Ubbelohde capillary viscometers, No. 75, thermostated to within (±0.05°C). Flow times in excess of 120 sec made kinetic energy corrections unnecessary.

All solutions were filtered immediately before use through millipore "cellotate" (cellulose acetate) circular membrane filters of pore size 0.5 ± 0.05 μ.

Solution foaming was avoided by applying a positive N_2 pressure at the filling end of the viscometer, thus forcing the solution through the capillary into the upper reservoir without bubbles.

The first flow time of a series of solutions was made on the most concentrated solution. Subsequent measurements were made by pipet dilutions within the viscometers. Only measurements whose three consecutive flow times agreed within 0.06 sec were recorded. Reduced viscosities are given in grams per cubic centimeter.

Results and Discussion

A. Calculation of the Free Ion Contribution to the Overall Conductance. The results obtained from equilibrium dialysis measurements enabled us to calculate the binding of sodium dodecyl sulfate (SDS) onto aqueous poly(vinylpyrrolidone) by assuming that all ions are present in either a bound, or the free, state.[20]

Three further assumptions are necessary to evaluate the conductances of each species at any concentration: (1) the equivalent conductances of the free ions are independent of any polyelectrolyte present; (2) all free ions have the same equivalent conductance as an SDS solution isoionic in uni-univalent ions; (3) the transference number of each ion is independent of concentration over the pertinent range. The first two assumptions have been justified experimentally and theoretically.[25] Transference experiments on pure SDS solutions give results which are virtually independent of the singly charged ion concentration.[26]

Acceptance of all three assumptions permits us to derive for the specific conductivity of the free sodium, κ_{Na}, and dodecyl ions, κ_{DS}, respectively

$$\kappa_{Na} = l^0{}_{Na}(Na_f)\lambda_{SDS}/\lambda^0{}_{SDS} \qquad (1)$$

$$\kappa_{DS} = (\lambda^0{}_{SDS} - l^0{}_{Na})(DS_f)\lambda_{SDS}/\lambda^0{}_{SDS} \qquad (2)$$

where λ_{SDS} is the equivalent conductance of pure aqueous SDS at the same free ionic strength, and (DS_f), (Na_f) are the free concentrations of the appropriate unbound ions, $l^0{}_{Na}$ is the ionic conductance of sodium, a value available in the literature.[28] $\lambda^0{}_{SDS}$ is the value at infinite dilution, for the equivalent conductance of SDS.[20]

In Figure 1, we plotted the ionic strength of the free ions, I_f,

$$I_f = [(Na_f) + (DS_f)]/2 \qquad (3)$$

calculated from the previously reported[20] equilibrium data according to eq 3 against the total detergent concentration $[S_I]$. Figure 2 shows the course of the calculated specific conductivity (the sum of eq 1 and 2) of the free ions also against $[S_I]$, again based on the same dialysis data. Conductivity data taken under similar conditions are reproduced in Figure 3 (tabulated in ref 1).

For pure detergent, curve 1, Figure 1, we assumed complete dissociation of detergent for the section of curve 1
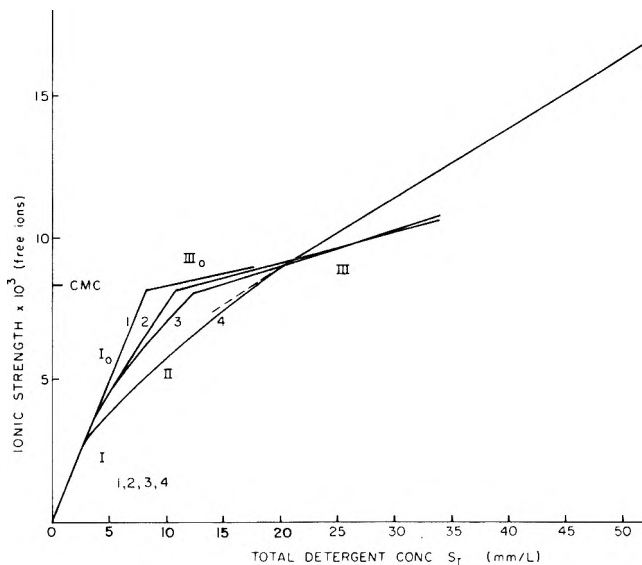
Figure 1. The course of ionic strength of sodium dodecyl sulfate ions against total detergent concentration in the absence and presence of PVP (data from membrane equilibrium measurements, ref 20): curve 1, pure SDS; curve 2, with 9.92–8.15 in millimolar PVP; curve 3, with 18.1–17.2 in millimolar PVP; curve 4, with 78.8–65.9 in millimolar PVP; all data at 25°C. Curve 2a at 30°C is practically indistinguishable from curve 2 and therefore omitted. Roman numerals indicate aggregation states: I_0, I, unassociated; II, clusters, at low-order micelles; III_0, III, true, pure, or mixed micelles.
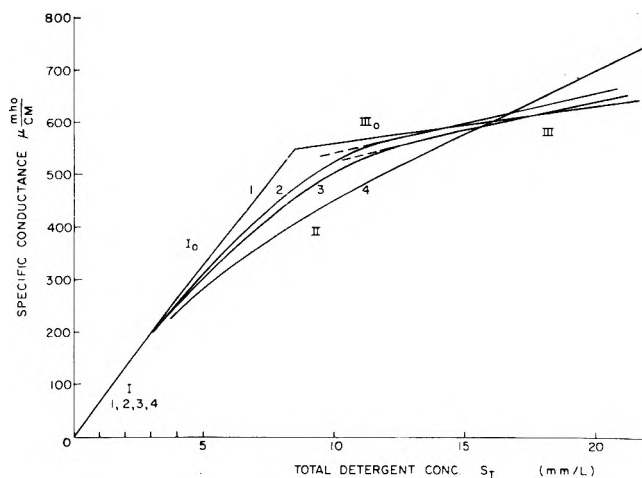
Figure 2. Dependence of specific conductance of the free sodium dodecyl sulfate ions, calculated from dialysis data (ref 20), on the total detergent concentration: (a) in pure detergent solution, curve 1; (b) in equilibrium with PVP as cosolute, curves 2, 3, 4; for remaining information, see Figure 1.

below the break, with the ionic strength identical with that of Na_f, DS_f, or S_I. The break of curve 1 occurs at the cmc of SDS. Above this break (the cmc), we assumed no increase in DS_f, but a linear fractional increase of Na_f of 18% (see, in particular, ref 27) for each additional mole of S_I.

In the presence of PVP, Figure 1, curves 2, 2a, 3, and 4 are at first identical with curve 1. This first, lower region ends in a break in the curves 2 to 4 at the detergent concentration ($\approx$3 mmol) at which an interaction between the detergent to PVP becomes noticeable. Through this region II up to the main, second break of curves 2–4, the free ion concentrations rise more slowly with the increase in total SDS in both chambers of the dialysis cell indicating an inactivation or "binding", of SDS; i.e., $[S_I]$ no longer equals
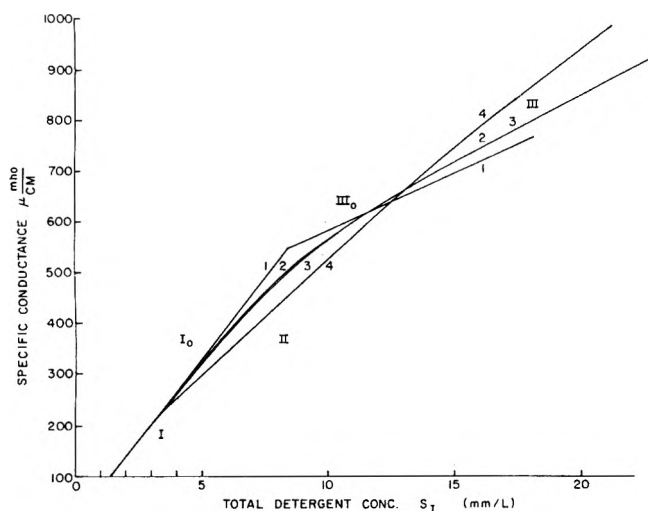
Figure 3. Dependence of specific conductance of sodium dodecyl sulfate ions on total SDS concentration, determined by measurement in pure detergent and in detergent-PVP solutions, for comparison with Figure 2: (a) pure detergent solution, curve 1; (b) detergent-PVP cosolutions, curves 2, 3, 4. For other information, see Figures 1 and 2.

$[DS_f]$. The detailed course of these curves depends on the relationship between the concentration of free sodium, S_I, and free dodecyl sulfate ions. Dialysis indicated a linear increase in bound sulfate with total SDS over this region which means that its complementary quantity, DS_f, should also increase linearly. Therefore, the curvature in the ionic strength function with S_I must be caused by a decreasing contribution by (i.e., by a binding of) Na^+. The curvature is seen, however, to increase also with the polymer concentration (from curve 2–4), a further indication of the perturbation of associated detergent structure by polymer. At the highest polymer concentration, curve 4, region II is no longer delineated from III by a break in slope. Thus, in the presence of PVP, SDS exhibits features of aggregation which, though not of the regular micellar kind, include increasing SDS^- clustering accompanied by some Na^+ binding.

In region III, i.e., above the cmc for regular micelles (the second break of Figure 1), the increase in free SDS ion concentration is as fully suppressed as in pure micelle formation (see Figure 4, ref 20). The $[Na_f^+]$ in the presence of polymer increases again linearly with total SDS, but with slopes larger than 18%; i.e., of 20, 25, and 56%, at our polymer concentrations of 9, 18, and 79 mmol, respectively.

In this context, looking at curves 1–4, Figure 1, the discontinuities, i.e., the cmc's, occur at the same ionic activity in the outside, and therefore also on the inside, of the dialysis chamber. Thus, the shifts of the cmc's along the abscissa to higher total SDS, represent the amounts of SDS inactivation (binding) by PVP at the instant of micelle formation.

The similarity between Figures 1 and 2 arises from the practically linear (experimental) relation between the ionic strength of the pure detergent and its specific conductivity below the cmc; see our first assumption. Figure 3, by comparison, shows the measured specific conductances against $[S_I]$, for the same three polymer concentrations and pure detergent. If all ions bound to the PVP lost their ability to conduct the electrical current, Figure 3 would be identical with Figure 2. Instead, except for the nonbinding section I and I_0, sections II and III of curves 2–4 in Figure 3 include

the contributions of the micellized and complexed detergent to the conductivity and therefore lie above the corresponding curves of Figure 2. The upper limiting slopes in Figure 3 are steeper than in Figure 2, so that the separation between the curves is more pronounced. These differences are again due to the contribution of the complexed and micellized detergent to the specific conductance. Thus, the data from dialysis alone (Figure 1), the combined dialysis and conductance data (Figure 2), and the conductivity data (Figure 3) are all consistent, confirm the existence of three different interaction regimes, and show that, as also reported in the literature,[14,15] the free ions determine the overall conductance to an extent which makes it difficult to derive quantitative relations for the polymer–soap complex from conductivity data alone. Nonetheless, contributions to the conductivity by the bound and micellar species are significant as will now be calculated.

B. *Calculation of the Conductivity of Polyion and Neutral Polysalt.* If the specific conductance of the free ions and the corresponding values of the total specific conductance, κ_T, are known, the specific conductances, κ_p, of the polyion and of the polysalt, κ_{NPS}, can be calculated by

$$\kappa_P = \kappa_T - \kappa_{Na} - \kappa_{DS} \tag{4}$$

$$\kappa_{NPS} = \kappa_T - \lambda_{SDS}[DS_f] \tag{5}$$

By dividing κ_P, or κ_{NPS}, by $[S_I-DS_f]$, derived from dialysis measurements,[20a] the equivalent conductances of the sulfate in the polyion, λ_p, or of the neutral salt, λ_{NPS}, are obtained. In Figure 4 we plotted these values against bound sulfate, $[S_I-DS_f]$. The λ_{NPS} data for clusters and micelles with their counterions, are given by the three upper curves 1, 2, and 3, while the lower three curves show the equivalent conductances λ_p for clusters and micelles, as well as for the polysalt, minus the contribution counterion. The curves 1 and 1a are those of pure SDS in the micellar region III.

All curves of Figure 4 exhibit linear sections, III, above critical values of $[S_I-DS_f]$. These represent the regions of true micellization throughout which the sizes, shapes, and charges of the polymer–detergent complexes are likely to remain constant, independent of SDS concentration. Increase in polymer concentration, per given total SDS, increases the quantities of "bound" detergent, yet causes the equivalent conductance of the polysalt to rise from curve 1 to 3, in accord with the conclusions drawn from the dialysis data alone, namely that for bound SDS the degree of Na ion dissociation increases with polymer concentration.

Below the cmc, through section II, the conductance of the polysalts, curves 2 and 3, drop increasingly, while κ_P passes through a shallow minimum (curves 2a and 3a, Figure 4) to a level above curve 1a for the normal cmc. We attribute the decrease in conductivity in the two ranges not only to the submicellar complex, or cluster formation of the SDS ions, but also to the fractional decrease of dissociated counterions. The rise in κ_P of curves 2a and 3a, Figure 4, above the conductance values for pure SDS micelles, we attribute to a higher exchange rate of dodecyl sulfate anions between the free and the micellar state when PVP is present.

C. *Viscosity Data.* The curves of Figure 5 show graphically the viscosities of the PVP–detergent solutions as a function of increasing total detergent concentration. Since viscosity changes attributable to the detergent alone are negligible, the viscosities reflect the conformational
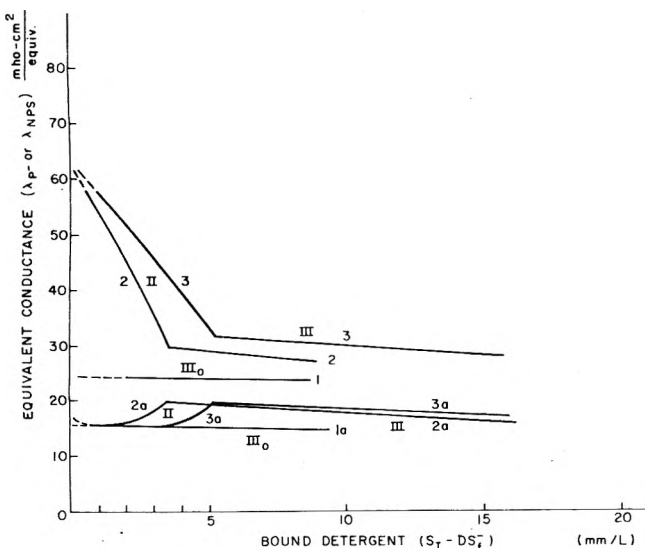
Figure 4. Equivalent conductances of sodium dodecyl sulfate and of the (single and complex) anions vs. the concentration of bound detergent in region II and III, where binding to PVP and cluster and micelle formation occur. The data are derived from those of Figure 3, with the aid of eq 4 and 5. Curves 1 and 1a are those of pure detergent; curves 2,3 and 2a,3a represent the detergent–PVP cosolutions. For all other information, see Figures 1–3.
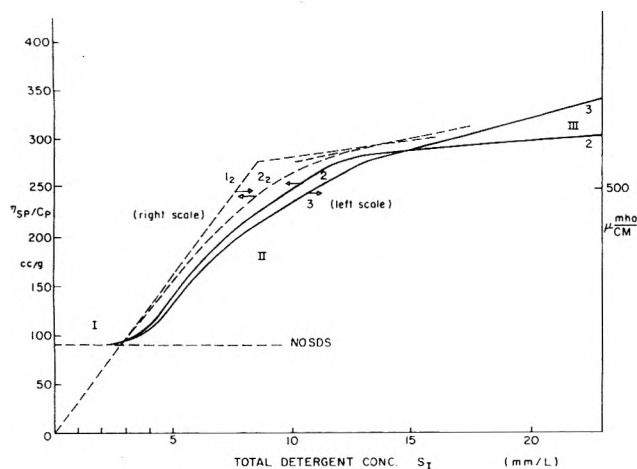
Figure 5. The course of the reduced viscosity (specific viscosity divided by polymer concentration) of PVP in mixed PVP–SDS solutions, vs. total SDS concentration, curves 2 and 3 (same numbering as in the four other figures). Curves 1_2 and 2_2 are repeated from Figure 2, for comparison. For all other information see again the legend of Figure 1.

changes of the polymer, presumably due to increasing detergent binding.[20,32] A plot of reduced viscosity, based on polymer concentration $[C_P]$, against $[S_I]$ for the two polymer concentrations shows the same three regions of behavior, i.e., two breaks at $[S_I] \approx 3$ mM and at $[S_I] \approx 12$–13 mM. More clearly than on any of the other plots, a change in slope occurs at $[S_I] \approx 8$ mM.

Figure 5 confirms that in region I, the polymer behaves as if it were uncomplexed. In region II, the viscosity rises sharply with the detergent concentration. In conjunction with other data,[2,12,30,36–38] this rise stems most likely from an increased repulsion between segments of the polymer chains which carry adsorbed detergent molecules, ions, and their clusters. About halfway through region II, the drop of Na$^+$ ion conductance, Figure 4, curves 2 and 3, concurs

with the decreasing slope of the viscosity curves, suggesting that the adsorbed clusters become more micelle like. The higher slope of curve 3 in region III of Figure 5, compared with curve 2, indicates a greater degree of coil expansion at higher polymer concentration, as a consequence of the fact that, for a given total detergent concentration, the polymer causes a drop in the ionic strength of the detergent (free monomer and/or micelles), but an increase in the fraction of dissociated sodium ions.

Conclusions

The conduction and viscosity data presented here, together with the earlier results on equilibrium dialysis[20] and other pertinent data in the literature,[13,16,26,32–39] permit one to sketch the following picture of the interaction of SDS with PVP.

In region I, of very dilute SDS solutions, there is little indication of SDS adsorption on polymer coils, though some minor hydrophobic binding is possible. At a critical product of concentrations, tentatively written as $[SDS]^n \cdot [PVP]^{1/m}$ (n = number of SDS/clusters, $1/m$ = fraction of the polymer chain (or number of monomer units) which induces the cluster), a cooperative inactivation of SDS occurs, as shown by the ongoing lowering of the SDS activity. The sharpness of the onset of region II indicates a change in state, from a homogeneous SDS–PVP solution to a dispersion of SDS–PVP clusters in equilibrium with monomeric SDS. An aggregate state for SDS is also supported by the work of Lange[16] who finds that dye solubilization by SDS begins exactly with the onset of region II, at which point also the curves of surface tension vs. SDS concentration in PVP–SDS solutions show a halt.

Our data permit only estimates of n, and $1/m$. In view of our values for the dissociation constant, α, for the Na$^+$ ions (see also ref 16), n must fall within the limits $1 \ll n < N_{cmc}$, where $N_{cmc} \approx 60$, the number of SDS molecules and ions in regular micelles. The quantity $1/m$ must be smaller than unity and may approximate the binding ratios, $r = $ mol of bound SDS/mol of monomer units which we found earlier[20] to lie between 0.01 and 0.3 under our conditions. The strong drop of the equivalent conductances, and the rapid declining of α, further show that through region II the clusters become larger and better ordered as the SDS concentration increases.

An aggregation of PVP, according to Rudd and Jennings, is not likely,[39] but the following evidence from our viscosity data indicates that the clusters, or premicelles, of SDS in region II encompass portions of the PVP chains (see also again ref 16), while the specific and intrinsic[1,2,35–38] viscosities in region I may go through a shallow minimum or, in some cases, a maximum, most likely as the result of SDS anion adsorption[31] counteracting incipient desolvation of the polymer, the final, very rapid and then slowing, rise in viscosity in region II can only stem from double layer effects and/or coil expansion. Electrical double layers have never been found to cause large viscosity increases. If the clusters in region II were unattached to the polymer, the latter would contract and fold around these large negative SDS multiions.[33] Since the polymer expands, several clusters must be affixed to the individual chains along their length, like spaced pearls on a string, stretching the chains by their electrostatic repulsion. The PVP is thus converted into a complex polyelectrolyte.[2,3,17,32,38] The altered absorption spectrum of dyes[16,3] solubilized in region II also speaks for a participation of PVP segments in the clusters.

The fact that n and $1/m$ change throughout region II[1,20] shows that the SDS aggregation is not of true micellar character and deserves the designation of "clusters formation."

Region II ends when the activities of the free SDS reach the cmc, marking the second discontinuity and the onset of region III, the formation of true micelles. These appear to be of mixed character, containing SDS and PVP. Firstly, the cmc's marking the onset of region III are higher than those for PVP-free SDS, and are the higher, the greater the PVP concentration. Secondly, all conductances in region III are higher (see Figures 3 and 4) than those of PVP-free SDS solutions in the micellar region, indicating "abnormal" micelles. Thirdly, the specific viscosities rise throughout III. The reduced rate of this rise can be explained by the formation of additional, free, SDS micelles which act as multivalent electrolytes. In view of the continual thermal collisions, and of the continuous equilibration between all types of aggregates, any distinction between them might be considered nominal were it not for the nature of the differences found in the conductances and viscosities in regions II and III in PVP-containing vs. pure SDS solutions. Thus we postulate in region III the existence of mixed micelles along segments of the polymer coils, in equilibrium with free micelles and monomeric SDS, with activities somewhat larger than those of pure SDS micelles at a given concentration.

With increasing polymer concentrations, the polymer coils fill eventually the whole solution volume and any distinction between intra- and intercoil micellization must disappear. This phenomenon is noticeable for our highest polymer concentration (see Figures 1 and 3) for which the delineations of regions II and III are not very distinct. In line with this, the equivalent conductance of the SDS rises with PVP concentration, a sign of SDS ion exchanges in the direction of the current which shorten the electrolytic migration path by a relay effect across the cluster, or micelle, diameters.

One might object to our postulate of mixed PVP-SDS micelles in view of Rudd and Jennings[39] findings. Their interpretation is that the decay of the Kerr effect after a high-voltage-pulse application, depending little on SDS concentration, speaks against conformational changes of the PVP as a result of SDS adsorption, or cluster formation. However, their decay data are far too inaccurate, their Kerr constant dependence on SDS concentration is observed at such high polymer concentration (at which coil compression and interpretation must dampen any coil rotation), and the Kerr effect of the pure PVP is so small that their results will only to a small degree be affected by polymer-segmental orientation, but overwhelmingly so by the polarization of the electrical double layer of the micelles. Their data then simply reflect the occurrence of increasingly micelle-like aggregations through range II, and do not allow conclusions on their effects on the PVP coils.

In summary, we believe that the interaction mechanism between PVP and SDS is likely to obtain with some varia-

tion for a wide range of polymers and detergents, with many cases already reported in the literature.[2-4,29,32-39] The mechanism of association which we here propose should provide a basis for a better understanding of such processes as polymer enhanced detergency, latex stabilization and solubilization, lipid-protein complexes and membranes, and the formation of polyelectrolyte associations.

References and Notes

(1) M. L. Fishman, Ph.D. Thesis, Polytechnic Institute of Brooklyn, 1969. A copy of this is obtainable from University Microfilms, 313 First St., Ann Arbor, Mich., Order No. 69-17, 790.
(2) S. Barkin, Ph.D. Thesis, Polytechnic Institute of Brooklyn, 1957.
(3) S. Saito, *Kolloid-Z.*, **137**, 98 (1954); **154**, 19 (1957).
(4) S. Saito, *Kolloid-Z.*, **158**, 120 (1958).
(5) I. Isemura and A. Imanishi, *J. Polym. Sci.*, **33**, 337 (1958).
(6) S. Saito, *Kolloid-Z.*, **165**, 162 (1959).
(7) S. Saito, *Kolloid-Z.*, **168**, 128 (1960).
(8) S. Saito, *J. Colloid Sci.*, **15**, 283 (1960).
(9) I. Maruta, *J. Chem. Soc. Jpn.*, **83**, 782 (1962).
(10) M. Nakagaki and Y. Ninomiya, *Bull. Chem. Soc. Jpn.*, **37**, 817 (1964).
(11) C. Botre, F. De Martiis, and M. Solinas, *J. Phys. Chem.*, **68**, 3624 (1964).
(12) S. Saito, *Kolloid-Z.*, **215**, 16 (1967).
(13) S. Saito, *J. Colloid Sci.*, **24**, 227 (1967).
(14) M. N. Jones, *J. Colloid Sci.*, **23**, 36 (1967).
(15) S. Gravsholt, L.T.D. Thesis, Fysisk-Kemisk Institut, Technical University of Denmark, Feb. 1969.
(16) H. Lange, *Kolloid-Z.*, **243**, 101 (1971).
(17) H. Arai and S. Horin, *J. Colloid Sci.*, **30**, 372 (1969).
(18) S. Horin and H. Arai, *J. Colloid Sci.*, **32**, 547 (1970).
(19) K. E. Lewis and C. P. Robinson, *J. Colloid Sci.*, **32**, 539 (1970).
(20) M. L. Fishman and F. R. Eirich, *J. Phys. Chem.*, **75**, 3135 (1971).
(21) K. Shinoda, "Colloidal Surfactants", Academic Press, New York, N.Y., 1963, p 23.
(22) R. A. Robinson and R. H. Stokes, "Electrolyte Solutions", Butterworths, London, 1968, Chapter 5.
(23) H. M. Dagget, E. J. Bair, and C. A. Kraus, *J. Am. Chem. Soc.*, **73**, 799 (1951).
(24) J. E. Lind, Jr., J. J. Zwolenik, and R. M. Fuoss, *J. Am. Chem. Soc.*, **81**, 1557 (1959).
(25) H. Morawetz, "Macromolecules in Solution", Interscience, New York, N.Y., 1965, p 361.
(26) A. P. Brady and D. J. Salley, *J. Phys. Chem.*, **70**, 914 (1948).
(27) R. J. Williams, J. N. Phillips, and K. J. Mysels, *Trans. Faraday Soc.*, **51**, 728 (1955).
(28) D. MacInnes, "The Principles of Electrochemistry", Dover Publications, New York, N.Y., 1961, p 342.
(29) W. Scholtan, *Makromol. Chem.*, **11**, 131 (1954).
(30) S. Barkin, H. P. Frank, and F. R. Eirich, *J. Phys. Chem.*, **61**, 1357 (1957).
(31) J. Eliassaf, F. Erikson, and F. R. Eirich, *J. Polym. Sci.*, **47**, 193 (1960).
(32) M. Nakagaki and S. Shimabyashi, *J. Jpn. Soc.*, No. 6, p 1174 (1973).
(33) S. Barkin, H. P. Frank, and F. R. Eirich, Simp. Intern. Chim. Macro., Cons. Nazipn. Delle Ricerche, 1955.
(34) S. Scarlatti, Master's Thesis, Polytechnic Institute of Brooklyn, 1971.
(35) G. Popesku, M. Radu, and D. Anghel, *Kolloid Z. Z. Polym.*, **250**, 303 (1972).
(36) M. Radu, G. Popesku, and D. Anghel, *Kolloid Z. Z. Polym.*, **250**, 875 (1972).
(37) M. Radu, G. Popesku, and D. Anghel, *Kolloid Z. Z. Polym.*, **251**, 1039 (1973).
(38) S. Saito, *Kolloid Z. Z. Polym.*, **249**, 1096 (1971).
(39) P. J. Rudd and B. R. Jennings, *J. Colloid Interface Sci.*, **48**, 302 (1974).

Mixing of Ionic and Covalent Configurations for NaH, KH, and MgH⁺. Potential Energy Curves and Couplings between Molecular States[1a]

Robert W. Numrich and Donald G. Truhlar*[1b]

Department of Chemistry, University of Minnesota, Minneapolis, Minnesota 55455 (Received June 12, 1975)

Configuration mixing between ionic and covalent configurations in the hydrides NaH, KH, and MgH⁺ has been studied using a two-electron valence bond model in which the valence electrons are assumed to interact with the metal core through a Hellmann-type pseudopotential. Adiabatic potential energy curves are reported for the $X^1\Sigma^+$, $A^1\Sigma^+$, $B^1\Sigma^+$, $a^3\Sigma^+$, $b^3\Sigma^+$, $c^3\Sigma^+$, $^1\Pi$, and $^3\Pi$ states arising from the ns, np, and $(n + 1)s$ atomic states of the metal atoms. For each hydride a polarization potential was added to the diabatic ionic potential curve and this potential was adjusted in such a way that the binding energy of the $A^1\Sigma^+$ adiabatic state is in good agreement with the experimental value. The $A^1\Sigma^+$ potential energy curves are also in good agreement with RKR curves determined from experiment although they are shifted slightly to larger values of the internuclear distance. For each diatomic system, coupling matrix elements between electronic states were calculated in a nonorthogonal diabatic representation, in a symmetrically orthogonalized diabatic representation, and in the adiabatic representation. The elements of the nonorthogonal diabatic Hamiltonian matrix and the overlap matrix were used to calculate the Landau–Zener–Stueckelberg parameter ΔW which is the separation between adiabatic potential energy curves at the position of an avoided crossing in a two-state approximation. Comparison with values of ΔW obtained earlier by Bates and Boyd and by Grice and Herschbach shows fair agreement between the values obtained here and those obtained by Bates and Boyd while the values obtained by Grice and Herschbach are two to three times larger. The elements of the nonorthogonal diabatic Hamiltonian matrix and the elements of the inverse square root of the overlap matrix were fit to analytic forms as functions of the internuclear distance. These forms were used to evaluate the part of the coupling matrices between adiabatic states which arises from the R dependence of the transformation matrices between the three electronic representations. The results show that coupling between adiabatic states in these molecules is important over intervals as large as 10 bohrs and serious questions are raised concerning the Landau–Zener–Stueckelberg model for treating the problem of avoided crossings in scattering calculations involving these systems.

I. Introduction

Interest in the electronically inelastic scattering of alkali atoms and alkali-like ions has been strong in recent years due to improved experimental techniques for measuring such processes and the fact that electronically excited states of these atoms and ions are amenable to quantum theoretical treatment.

In the work reported in this paper the valence bond configuration mixing method was combined with the use of model atomic pseudopotentials in calculations of the potential energy curves and the matrix elements which couple different electronic states of NaH, KH, and MgH⁺ in both adiabatic and diabatic representations. Since the coupling terms have not been well studied, this work seeks to determine their general features as functions of internuclear distance.

This work was carried out as the initial stage of scattering calculations for electronically inelastic collisions of Na, K, and Mg⁺ with H and H₂. The calculations are also of intrinsic value, especially for illustrating the nature of the coupling terms and the diabatic potential energy curves and for showing the level of accuracy which can be achieved for adiabatic potential energy curves using this method.

The Landau–Zener–Stueckelberg (LZS) model[2] for electronically inelastic collisions has been applied to two of the avoided crossings in each of the systems NaH and KH by Bates and Boyd[3] and the treatment has been repeated in modified fashion for one of the avoided crossings in each

system by Grice and Herschbach.[4] This model requires the energy separation ΔW between adiabatic potential energy curves at an avoided crossing. Although the primary purpose of this work is not to apply the LZS model, we are able to calculate ΔW within our treatment and we shall compare our results for this quantity with the results reported in the references cited.

II. Electronic Representations

For a fixed value of the internuclear distance R we consider the electronic Hamiltonian

$$H_{el}(R) = \frac{1}{2\mu_e} \sum_{i=1}^{n} p_{x_i}^2 + V(\vec{x}, R) \tag{1}$$

where

$$\frac{1}{\mu_e} = \frac{1}{(M_A + M_B)} + \frac{1}{m} \tag{1a}$$

m is the electronic mass, p_{x_i} is the operator for linear momentum of electron i, x_i is the coordinate of electron i in a molecule-fixed coordinate system with origin at the center-of-mass of the nuclei, $\vec{x}$ represents the entire set of electronic coordinates, and V is the total potential energy consisting of electron–nucleus attractions, electron–electron repulsions, and nucleus–nucleus repulsions. We also consider the eigenvalue problem

$$H_{el}(R)\phi_k(\vec{x}, R) = W_k(R)\phi_k(\vec{x}, R) \tag{2}$$

with eigenvalues $W_k(R)$ and electronic eigenfunctions $\phi_k(\vec{x}, R)$ which are taken to be orthonormal as follows

$$(\phi_i \mid \phi_j) = \int \phi_i^*(\vec{x}, R)\phi_j(\vec{x}, R)\,\mathrm{d}\vec{x} \qquad (3a)$$

$$= \delta_{ij} \qquad (3b)$$

The inner product notation introduced in eq 3a refers to integration over electronic coordinates only and δ_{ij} is the kronecker delta. The total wave function is expanded in terms of these electronic eigenfunctions as

$$\Psi(\vec{x}, \vec{R}) = \sum_{l=1}^{\infty} \phi_l(\vec{x}, R)\chi_l(\vec{R}) \qquad (4)$$

where the nuclear motion wave functions $\chi_k(\vec{R})$ are to be determined. We substitute expansion (4) into the Schroedinger equation

$$H\Psi = W\Psi \qquad (5)$$

where H is the Hamiltonian in the barycentric coordinate system given by

$$H = \frac{1}{2\mu}p^2 + \left(\frac{1}{M_A + M_B}\right)\sum_{i<j}\vec{p}_{x_i} \cdot \vec{p}_{x_j} + H_{el} \qquad (6a)$$

where[5]

$$\vec{p} = -i\vec{\nabla}_R \qquad (6b)$$

and

$$\frac{1}{\mu} = \frac{1}{M_A} + \frac{1}{M_B} \qquad (6c)$$

We set the kinetic energy of the total center of mass equal to zero so W is the total energy. After multiplication on the left by $\phi_k^*(\vec{x}, R)$ and integration over electronic coordinates, we obtain the following coupled differential equations for the nuclear motion wavefunctions:[6]

$$\frac{1}{2\mu}p^2\chi_k(\vec{R}) + [W_k(R) - W]\chi_k(\vec{R}) + \sum_{l=1}^{\infty} [B_{kl}(R) +$$

$$G_{kl}(\vec{R})]\chi_l(\vec{R}) + 2\sum_{l=1}^{\infty} \vec{F}_{kl}(\vec{R}) \cdot \vec{p}\chi_l(\vec{R}) = 0 \qquad (7)$$

where

$$B_{kl} = \left(\frac{1}{M_A + M_B}\right)\left(\phi_k \Big| \sum_{i<j}\vec{p}_{x_i} \cdot \vec{p}_{x_j} \Big| \phi_l\right) \qquad (8)$$

$$\vec{F}_{kl} = \frac{1}{2\mu}(\phi_k | \vec{p} | \phi_l) \qquad (9)$$

$$G_{kl} = \frac{1}{2\mu}(\phi_k | p^2 | \phi_l) \qquad (10)$$

As seen from the above equations, the matrices **B**, **F**, and **G** couple nuclear motion in different electronic states. If we ignore all such coupling we obtain what is usually[6,7] referred to as the Born–Oppenheimer or Born–Oppenheimer adiabatic approximation.

In this article we shall ignore completely the coupling matrix **B**.

We assume next that expansion of the wave function may be terminated after N terms. We let $\phi^i(\vec{x}, R)$ represent an N-dimensional row vector of electronic basis functions of the ith electronic representation. Similarly $\chi^i(\vec{R})$ represents an N-dimensional column vector of nuclear motion wave functions in the ith electronic representation. The total wave function for the system may be written in matrix notation in terms of the ith electronic representation

$$\Psi(\vec{x}, \vec{R}) = \phi^i(\vec{x}, R)\chi^i(\vec{R}) \qquad (11)$$

Assume we pick a basis set ϕ^n which is linearly indepen-

dent but not necessarily orthogonal. The overlap matrix is defined by

$$\mathbf{S} = (\phi^n | \phi^n) \qquad (12)$$

where the inner product notation of eq 3a is implied along with conjugate transpose of the vector in the bra and the matrix multiplication. We substitute the total wave function in this nonorthogonal representation into the Schroedinger equation (5) and require the projection of $(H - W)$ onto the N-dimensional space of electronic wave functions be zero to obtain

$$\left(\phi^n \Big| \frac{1}{2\mu}\vec{p} \cdot \vec{p} + H_{el} - W \Big| \phi^n\chi^n\right) = 0 \qquad (13)$$

Applying the chain rule for differentiation and defining the matrices

$$\mathbf{H}^i = (\phi^i | H_{el} | \phi^i) \qquad (14)$$

$$\vec{\mathbf{F}}^i = \frac{1}{2\mu}(\phi^i | \vec{p} | \phi^i) \qquad (15)$$

$$\mathbf{G}^i = \frac{1}{2\mu}(\phi^i | p^2 | \phi^i) \qquad (16)$$

we obtain from eq 13 the following $N \times N$ matrix differential equation for the nuclear motion wave functions

$$\frac{1}{2\mu}\mathbf{S}(p^2\chi^n) + \mathbf{G}^n\chi^n + 2\vec{\mathbf{F}}^n \cdot (\vec{p}\chi^n) + \mathbf{H}^n\chi^n = W\mathbf{S}\chi^n \qquad (17)$$

Note that the differential operators are assumed to operate up to the next closing parentheses and no farther.

The presence of the overlap matrix **S** in eq 17 is troublesome. Let **A** be a matrix which transforms the nonorthogonal basis ϕ^n into the orthogonal basis ϕ^o. Then we have

$$\phi^o = \phi^n\mathbf{A} \qquad (18)$$

Since the total wave function is invariant to electronic representation we may write

$$\Psi = \phi^o\chi^o \qquad (19)$$

where

$$\chi^o = \mathbf{A}^{-1}\chi^n \qquad (20)$$

Following the same procedure which led to eq 17 we obtain

$$\frac{1}{2\mu}(p^2\chi^o) + \mathbf{G}^o\chi^o + 2\vec{\mathbf{F}}^o \cdot (\vec{p}\chi^o) + \mathbf{H}^o\chi^o = W\chi^o \qquad (21)$$

The method of orthogonalization used in this work corresponds to taking for the matrix **A** the product

$$\mathbf{A} = \mathbf{CU} \qquad (22)$$

where

$$\mathbf{C} = \mathbf{S}^{-1/2} \qquad (23)$$

and **U** is an arbitrary unitary matrix. In eq 23 the positive square root is implied as discussed by Löwdin.[8] If $\mathbf{U} = \mathbf{E}$ (the identity matrix) the method of orthogonalization is known as symmetric orthogonalization[8] or sometimes as Löwdin orthogonalization. When symmetric orthogonalization is used the superscript $i = o$ is replaced by $i = s$. The $i = n, o,$ and s representations will be collectively referred to as diabatic representations to distinguish them from the one to be considered next.

Another choice of **U** is that unitary matrix which diagonalizes the electronic Hamiltonian in the orthogonal basis set. That is we take **U** such that

$$\mathbf{H}^a = \mathbf{U}^\dagger\mathbf{H}^s\mathbf{U} \qquad (24)$$

is diagonal. This representation will be called the adiabatic representation.

Since one invariably begins a calculation with a nonorthogonal basis set, it is important to know the following relations

$$H^\circ = A^\dagger H^n A \tag{25}$$

$$\tilde{F}^\circ = A^\dagger \tilde{F}^n A + \frac{1}{2\mu} A^\dagger S(\tilde{p}A) \tag{26a}$$

$$= A^\dagger \tilde{F}^n A + \frac{1}{2\mu} U^\dagger C^{-1}(\tilde{p}A) \tag{26b}$$

$$G^\circ = A^\dagger G^n A + 2A^\dagger \tilde{F}^n A \cdot U^\dagger C^{-1}(\tilde{p}A) + \frac{1}{2\mu} U^\dagger C^{-1}(p^2 A) \tag{27}$$

In deriving eq 26a and 27 we took account of the fact that A is a function of R and is operated on by $\tilde{p}$. We see therefore that given the coupling matrices $\tilde{F}^n$ and G^n in the original nonorthogonal basis set, the coupling matrices in the orthogonal basis set are given in terms of transformed matrices $A^\dagger \tilde{F}^n A$ and $A^\dagger G^n A$ plus additional coupling terms which arise from the dependence of the transformation matrix A on the internuclear distance.

In this article we shall present calculations (as functions of the internuclear distance) of the matrices H^n, H^s, and H^a. In addition we have calculated the coupling matrices $(1/2\mu) U^\dagger C^{-1}(\tilde{p}A)$ and $(1/2\mu) U^\dagger C^{-1}(p^2 A)$. The matrices $\tilde{F}^n$ and G^n were not obtained.

III. Model Effective Potentials

We assume the hydrides under consideration may be treated as two-electron systems. The model Hamiltonian at internuclear distance R is assumed to be[5]

$$H_{el}(R) = \tfrac{1}{2} p_{x_1}^2 + \tfrac{1}{2} p_{x_2}^2 - \frac{1}{x_{1H}} - \frac{1}{x_{2H}} - \frac{Z_c}{x_{1M}} - \frac{Z_c}{x_{2M}} +$$
$$V_M(x_{1M}) + V_M(x_{2M}) + \frac{1}{|\vec{x}_1 - \vec{x}_2|} + \frac{Z_c}{R} \tag{28}$$

where x_{iH} and x_{iM} are the distances of electron i from the proton and the core M⁺ (M = Na, K, or Mg⁺; M⁺ = Na⁺, K⁺, or Mg²⁺), respectively, Z_c is the net charge on the core, and both electrons are assumed to interact with the core through the Coulomb potential and a model effective potential V_M. Both electrons, independent of their angular momenta about the core, are assumed to interact with the core through the same effective potential. This is an important simplification as compared to the ab initio effective potentials used elsewhere.[9] The effective potential chosen, in all cases, is the ground s-state effective potential. We shall see that, although this approximation in our model is certainly a source of inaccuracy, atomic energies calculated in this manner are in excellent agreement with the experimental values.

The concept of an effective potential is quite old and was developed independently by Hellmann[10] and Gombas.[11] Two recent review articles are available.[12] We approximate the effective potential V_M in eq 28 by the Hellmann potential

$$V_H(x_{iM}) = A x_{iM}^{-1} \exp(-\kappa x_{iM}) \tag{29}$$

where the parameters A and κ are to be determined empirically. The parameters have been determined in different ways by different workers. To compare how well some of

TABLE I: Experimental and Calculated Energies for Potassium Using Various Effective Potentials

State	E_{expt}, eV	E_H, eV	E_{HG}, eV	E_{SM}, eV	E_S, eV
4s	−4.431	−5.173	−4.776	−3.984	−4.343
5s	−1.734	−2.033	−1.949	−1.718	−1.765
6s	−0.937	−1.062	−1.032	−0.942	−0.953
7s	−0.587	−0.650	−0.635	−0.592	−0.596
8s	−0.402	−0.438	−0.430	−0.405	−0.407
4p	−2.726	−2.894	−2.775	−2.615	−2.848
5p	−1.276	−1.352	−1.317	−1.253	−1.327
6p	−0.744	−0.781	−0.766	−0.736	−0.768
7p	−0.488	−0.508	−0.500	−0.484	−0.501
8p	−0.345	−0.356	−0.351	−0.341	−0.351
Φ^a	0.000	0.697	0.182	0.213	0.027

[a] Sum of squares of the differences of experimental and calculated energies, eq 30.

these different effective potentials represent the actual energy levels of the valence electron, we have used a finite difference method[13] for numerical determination of eigenvalues to compute the first five s-state and p-state energies for potassium for four different effective potentials. We have used the s-state effective potential in each case and obtained the p-state energies by adding the appropriate centrifugal potential to the effective potential. The results are given in Table I. In that table E_H, E_{HG}, and E_S denote the energies obtained using the effective potentials of Hellmann as quoted by Szasz and McGinn,[14] of Hart and Goodfriend,[15] and of Schwarz,[16-18] respectively. For comparison, the table also includes experimental values[19] E_{expt} and energies E_{SM} obtained using the Philips–Kleinman effective potential[20] as calculated by Szasz and McGinn.[21]

As a measure of how well these effective potentials represent the actual states of the atom, we have calculated the sum of the squares of the differences of the experimental and calculated energies

$$\Phi = \Sigma (E_{expt} - E_{calcd})^2 \tag{30}$$

where the sum is extended over the ten states considered and we have entered the result in the last row of Table I. The effective potential due to Schwarz gives the best overall agreement with experiment in this case and we have adopted Schwarz's effective potentials for use in our model Hamiltonian, eq 28. The values of the parameters A and κ are listed in Table II. Note that in ref 16 an incorrect value is quoted for Mg⁺. The correct value listed in Table II is given in later references.[17,18]

Since the s-state effective potentials give good approximations for the p-state energies for potassium, the angular momentum dependence is in some sense weak, and our use of s-state potentials only is partly justified. Below we shall see that this statement is also true for the atomic states of interest for Na and Mg⁺.

The effective potential obtained by Callaway and Laghos[22] for Na by a different method is very similar to the effective potential of Schwarz for Na.

IV. Calculations

One-Electron Atomic Basis Set. All atomic basis functions in this work are linear combinations of Slater-type orbitals[23] (STO's) with principal quantum numbers n_k and orbital exponents ζ_k.

TABLE II: Pseudopotential Parameters in Hartree Atomic Units for the S State Pseudopotentials for Na, K, and Mg$^+$

Atom	Z_c	A	κ
Na	1.0	14.0	2.267
K	1.0	18.0	1.866
Mg$^+$	2.0	30.0	2.855

We have chosen for the H$^-$ wave function the GF function due to Goddard.[24] We have used the function involving four STO's as given in Table IV of ref 24.

For each covalent configuration, we use a hydrogen 1s orbital centered on the hydrogen atom and a pseudowave function centered on the alkali atom, in particular the pseudowave function for the atomic state which gives rise to the molecular state of interest. Three covalent configurations (corresponding to the two lowest s states and the lowest p state of the alkali) were included and the pseudowave functions for these states were obtained in the following way. To obtain a set of STO's in which to expand the pseudowave function, we first of all included the STO's given by Schwarz[17] for the ground and first excited s states and for the lowest p state. We also included the two most important STO's in the pseudowave functions given by Szasz and McGinn.[21] Using this set of STO's the secular equation was calculated using the effective Hamiltonian

$$H_M = \frac{1}{2}p_{x_1}^2 - \frac{Z_c}{x_{1M}} + V_M \qquad (31)$$

where V_M is approximated by eq 29 with the parameters given in Table II. The results are given in Table III where the calculated atomic energies are compared with the experimental values. The agreement between calculated and experimental atomic energies is especially good for neutral cases. We therefore have further verification that the effective potential is independent enough of angular momentum that one effective potential may be used for all the states.

Since the avoided crossings considered later in this article occur at rather large internuclear separation (e.g., as large as 23 a_0 in Na and 28 a_0 in K), it is important to check the behavior of our pseudowave functions at large distance from the nucleus. Comparison of numerical Hartree-Fock functions for potassium calculated with the program of Froese-Fischer[25] and coulomb approximation[26] functions indicates that in the regions of interest corresponding to the occurrence of avoided crossings (see below for the exact positions of these avoided crossings) the coulomb approximation functions give the correct behavior except possibly for normalization. Comparison of the logarithms of our wave functions with those of the coulomb approximation wave functions indicates that for Na and K, the wave functions are fairly good at distances less than about 14 or 15 a_0 while we may expect that the ground state wave functions are too large at larger distances. However, we will show below that the diabatic matrix elements $H_{2j}{}^n$ (j = 1, 3, 4) involving the nonorthogonal covalent configurations of NaH and KH which dissociate to ground atomic states are small for $x > 9$ a_0. Thus the wave functions do not need to be accurate to as large a distance for the ground state as for the excited states. For the excited states of Na and K, the wave functions appear to be more accurate at large distances but must eventually, at large

TABLE III: Experimental and Calculated Energies in Hartree Atomic Units at Infinite Internuclear Separation for the Four Atomic Configurations Used in Determining the Molecular Basis Set

State	$E_{expt}{}^a$	$E_{calcd}{}^a$	ΔE^b
Na(3s) + H(1s)	-0.68882	-0.68886	0.00004
Na(3p) + H(1s)	-0.61152	-0.61189	0.00037
Na(4s) + H(1s)	-0.57222	-0.57154	-0.00068
Na$^+$ + H$^-$	-0.52775	-0.51359	-0.01416
K(4s) + H(1s)	-0.65952	-0.65948	-0.00004
K(4p) + H(1s)	-0.60018	-0.60459	0.00442
K(5s) + H(1s)	-0.56371	-0.56483	0.00112
K$^+$ + H$^-$	-0.52775	-0.51359	-0.01416
Mg$^+$(3s) + H(1s)	-1.05254	-1.04963	-0.00291
Mg$^+$(3p) + H(1s)	-0.88974	-0.88529	-0.00445
Mg$^+$(4s) + H(1s)	-0.73448	-0.73563	0.00115
Mg^{2+} + H$^-$	-0.52775^c	-0.51359	-0.01416

^{a} The zero of energy is for M$^+$ + H$^+$ + 2e$^-$ where M is Na, K, or Mg$^+$. ^{b} The amount by which the calculated energy differs from the experimental one. ^{c} The energy of Mg(3s^2) + H$^+$ is -0.83346 hartree; although this is lower than Mg^{2+} + H$^-$, this state does not have a long-range coulomb attraction and may be less important for causing interactions among the covalent diabatic states.

enough distances, become too small. For Mg$^+$ the wave functions may be in serious error even for distances as small as 8 a_0. In this case, however, the important curve crossings occur at smaller distances [less than 6 a_0 for the covalent state which dissociates to Mg$^+$ (3p) and about 10 a_0 for the covalent state which dissociates to Mg$^+$ (4s)] and thus accuracy is not needed at distances as large as for the neutral cases. Nevertheless, we will show below that the coupling matrices in the MgH$^+$ system may have elements which are large at distances as great as about 14 a_0. Therefore, the quantitative results for MgH$^+$ may need to be reexamined and should not be treated with as much confidence as the results for NaH and KH.

Two-Electron Nonorthogonal Molecular Basis Set. Using the one-electron atomic basis functions ψ_i described above, we form two-electron valence bond wave functions as follows

$$\phi_m{}^n(\vec{x}_1, \vec{x}_2, R) = N_m(R)[\psi_i(1)\psi_j(2) \pm \psi_j(1)\psi_i(2)] \times$$
$$(1/\sqrt{2})[\alpha(1)\beta(2) \mp \beta(1)\alpha(2)] \quad (32)$$

where the normalization constant is

$$N_m(R) = [2(1 + s_{ij}{}^2)]^{-1/2} \qquad (33)$$

and the overlap between atomic functions is

$$s_{ij} = \langle \psi_i | \psi_j \rangle \qquad (34)$$

The numbers in parentheses indicate whether the ψ_i are to be taken as functions of the vector to electron 1 or electron 2 from the nucleus on which the atomic basis function is centered. The functions $\alpha(i)$ and $\beta(i)$ are the usual spin functions for electron i, and the upper and lower signs in eq 32 correspond to the singlet and triplet states, respectively.

For the ionic configuration, ψ_i and ψ_j are the GF orbitals for H$^-$ (see above). For the covalent configurations, ψ_j is always the 1s orbital of H while ψ_i is the orbital corresponding to the atomic valence state at infinite internu-

clear separation which gives rise to the molecular state of interest. From the ground and first excited atomic s states, we obtain $^1\Sigma^+$ and $^3\Sigma^+$ molecular states. From the first atomic p state, we obtain $^1\Sigma^+$ and $^3\Sigma^+$ molecular states with $m_l = 0$ STO's while $^1\Pi$ and $^3\Pi$ states are obtained with $m_l = \pm 1$ STO's. From the ionic configuration, we obtain only the $^1\Sigma^+$ state since the bound state of H^- is a singlet.

Since the diagonal matrix elements of the electronic Hamiltonian in the diabatic representations will cross each other as the internuclear distance changes, we need to adopt a numbering convention for the molecular states which shall be used at all values of the internuclear distance. Within the set of $^1\Sigma^+$ diabatic molecular states, we shall always assign the number 1 to the molecular state arising from the ionic configuration and label it $1\ ^1\Sigma^+$, the number 2 to the molecular state arising from the ground atomic state and label it $2\ ^1\Sigma^+$, the number 3 to the molecular state arising from the atomic p state and label it $3\ ^1\Sigma^+$, and the number 4 to the molecular state arising from the excited atomic s state and label it $4\ ^1\Sigma^+$. Within the set of $^3\Sigma^+$ molecular states, there is no molecular state arising from the ionic configuration, so we number the molecular states in the same order as the atomic states from which they originate. To emphasize the physical character of the covalent $^{1,3}\Sigma^+$ states we will also use the notation $ns\ ^{1,3}\Sigma^+$, $np\ ^{1,3}\Sigma^+$, and $n^*s\ ^{1,3}\Sigma^+$ where n is the principal quantum number of the valence electron in the ground state and $n^* = n + 1$. No numbering scheme is needed for the Π states since only one singlet and one triplet are considered for each value of m_l.

In the adiabatic representation, no crossing of curves occurs and we number them at each value of R in the order of their increasing energies. Following the usual spectroscopic notation, we may also refer to the adiabatic states as $X^1\Sigma^+$, $A^1\Sigma^+$, $B^1\Sigma^+$, and $C^1\Sigma^+$ for the singlets in order of increasing energy and $a^3\Sigma^+$, $b^3\Sigma^+$, and $c^3\Sigma^+$ for the triplets again in order of increasing energy. The Π states will be referred to as simply $^1\Pi$ and $^3\Pi$ since there is only one of each and they are the same in all representations.

Using the model electronic Hamiltonian (28) with the Hellmann effective potentials due to Schwarz and the molecular functions (32), we have calculated the electronic Hamiltonian matrix elements defined by eq 14 with $i = n$ as functions of the internuclear distance.

All the necessary molecular integrals were evaluated using a program due to Schaeffer.[27] This program has the advantage that integrals are computed directly over atomic orbitals rather than over atomic basis functions.

The experimental atomic energies of Table III represent the asymptotic limits which the diagonal elements of the electronic Hamiltonian should approach at infinite internuclear separation in each of the nonorthogonal diabatic, orthogonal diabatic, and adiabatic representations where the zero of energy is set at $M^+ + H^+ + 2e^-$ with $M = Na$, K, or Mg^+. The error involved in our calculation is given by the energy ΔE_k for each atomic state k and we see that this error is not the same for different atomic states. We could make one of the diagonal matrix elements approach the correct asymptotic value by a simple change in the zero of energy which in a nonorthogonal representation amounts to adding the quantity $\Delta E_k S_{ij}$ to each element H_{ij}^n of the Hamiltonian matrix where ΔE_k is the amount by which the zero is changed and S_{ij} is the overlap between the states i and j. Since the error ΔE_k is not the same for all states,

however, the other matrix elements would still have the wrong large R asymptotic values.

To make all the diagonal elements have the correct asymptotic energies, we have added to each diagonal element H_{kk}^n of the Hamiltonian matrix in the nonorthogonal diabatic representation the quantity ΔE_k listed in Table III. In making this correction, we have assumed that the error involved in our calculation is independent of internuclear distance in a given nonorthogonal diabatic valence-bond configuration, which is of course not true, but we believe that this method is a reasonable way of adjusting the curves to the correct asymptotic values especially since the corrections involved are small. One of the reasons we preferred the Schwarz effective potentials to other choices is that the ΔE_k are so small for this case.

The off-diagonal matrix elements in a nonorthogonal representation should also be adjusted whenever the diagonal matrix elements are altered as mentioned above. However, in this case we have not added the same value to all the diagonal matrix elements, and therefore there is no unique method for adjusting the off-diagonal matrix elements. Therefore no adjustment of the off-diagonal matrix elements has been made.

After addition of the quantities ΔE_k to the diagonal matrix elements, the zero of energy was adjusted to correspond to the ground state atomic configuration for each system by adding the quantity $|E_1| S_{ij}$ to each matrix element where $|E_1|$ is the absolute value of the experimental energy of the ground state of $M + H$ where $M = Na$, K, or Mg^+ as listed in Table III.

By adjusting the diagonal matrix elements before rather than after orthogonalization, we ensure that the final adiabatic potential energy curves obtained are independent of the method of orthogonalization.

Our four-state molecular valence-bond basis set for the $^1\Sigma^+$ states does not take into account the large polarization of H^- by the core M^+ as well as the smaller polarization of the core M^+ by H^-. We include this aspect of the system in our model by adding a polarization potential V_p to the calculated matrix element H_{11}^n corresponding to the ionic configuration. The polarization potential chosen is given by[5]

$$V_p = -\frac{\alpha_+ + \alpha_-}{2R^4}\left\{1 - \exp\left[-\left(\frac{R}{\gamma}\right)^6\right]\right\} \quad (35)$$

where α_+ is the dipole polarizability of the core M^+ and α_- is the dipole polarizability of H^-.

The parameter γ is adjustable. It was determined in such a way that after orthogonalization of the basis functions and diagonalization of the Hamiltonian matrix in the orthogonal basis, the adiabatic curves for the A states have dissociation energies as close as possible to the experimental values. This variation of γ could be carried out with little effect on the X and C state curves but with considerable effect on the A and B state curves. The polarization potential, of course, has no effect on the $^3\Sigma^+$, $^1\Pi$, or $^3\Pi$ states. We shall see below that the final A state curves obtained in this way give fairly good agreement with experimentally determined RKR curves although the curves for KH and MgH⁺ are displaced to larger values of R than the respective experimental ones. The final values of γ used in this work are $9.3\ a_0$ for NaH, $9.9\ a_0$ for KH, and $5.7\ a_0$ for MgH⁺. The dipole polarizabilities were taken from the tabulation of Dalgarno.[28]

For later computational purposes we have fit the ele-

ments of the electronic Hamiltonian matrix in the nonorthogonal diabatic basis to analytical forms containing three to five linear parameters and two or three nonlinear parameters adjusted to give the best fit in a least-squares sense to the calculated points. All curve fitting was done using the Marquardt non-linear least-squares method.[29] The analytic forms and curve fits are given elsewhere.[30]

Orthogonal Diabatic Basis. Using the orthogonalization procedure described above, we have transformed the electronic Hamiltonian matrix in the nonorthogonal diabatic basis to the symmetrically orthogonalized basis. In the case of the $^1\Sigma^+$ states we have included the correction of eq 35.

The matrix elements for the transformation $\mathbf{C} = \mathbf{S}^{-1/2}$ from the nonorthogonal to the orthogonal diabatic basis were also fit to an analytic form for later computational purposes. The form used and the parameters of the fits are given elsewhere.[30]

The fits for $\mathbf{C}(R)$ and $\mathbf{H}^n(R)$ will also be used below to determine the values of R_e and D_e for the adiabatic potential curves, to determine the crossing points in both the nonorthogonal and orthogonal diabatic representations, and to calculate the coupling matrices between adiabatic states and to generate points for plots of the elements of these matrices.

It is interesting to note that the elements of the transformation matrix $\mathbf{C}(R)$ are quite smoothly varying functions of R. This behavior might have been expected since the method of symmetric orthogonalization is, in a certain sense, a gentle procedure which produces a minimum change in the basis set. At small values of R, however, the difficulty of orthogonalization increases and rather large amounts of the nonorthogonal basis functions are added and subtracted to maintain orthogonality. As the two atoms approach each other, the off-diagonal elements of the overlap matrix become large, some of the basis functions become almost linearly dependent, and one of the eigenvalues of the overlap matrix becomes very small. Thus, the norm of $\mathbf{C}$ becomes very large.

Adiabatic Potential Curves and Electronic Eigenfunctions. Diagonalization of the Hamiltonian matrix in the symmetrically orthogonalized diabatic basis yields the adiabatic potential energy curves $H_{ii}^a (R)$ according to eq 24. We recall from eq 22 that the matrix $\mathbf{A}$ is defined in terms of the unitary matrix $\mathbf{U}$ which diagonalizes the electronic Hamiltonian in the symmetrically orthogonalized diabatic basis. Therefore, the columns of the matrix $\mathbf{U}$ are the eigenvectors of the matrix $\mathbf{H}^s$, and since the negative of an eigenvector is still an eigenvector with the same eigenvalue, a problem arises in establishing the sign to be given to these eigenvectors. To calculate the coupling matrices defined in eq 26 and 27 we must take derivatives of the elements of the matrix $\mathbf{U}$ and therefore we must establish a sign convention which yields smoothly varying functions of R. In the case of avoided crossings as considered here, the character of the eigenvectors changes rapidly over very small distances and the relative contributions of the components change rapidly also.

To overcome this difficulty we have adopted the following procedure. At large internuclear distances, beyond the position of the last crossing of ionic and covalent curves, the character of each adiabatic curve is unambiguous and corresponds to a configuration chosen as one of the original basis functions. We start the calculation of $\mathbf{U}$ at some value $R = R_n$ where the sign of each column is determined and proceed stepwise to smaller values $R_{n-1}, R_{n-2},$

etc. At each point after the first, the calculated elements of column i of the matrix $\mathbf{U}$ are compared to the values at the previous point by computing the two quantities

$$\lambda_\pm = \sum_{k=1}^N [U_{ki}(R_n) \pm U_{ki}(R_{n-1})]^2 \qquad (36)$$

for each column of $\mathbf{U}$. If the minimum of these two quantities is equal to λ_-, then the sign of column i is left unchanged while if the minimum is equal to λ_+, the sign of column i is changed to its negative. Thus, the decision for the sign of the eigenvectors is based on a smoothness criterion involving all the components of the vector at each value of R.

This procedure was carried out with step size $R_n - R_{n-1} = 0.1a_0$. It yields continuous, although sometimes sharply varying, functions. We checked that the results obtained are independent of step size.

Coupling Matrices in the Adiabatic Representation. Note that $\mathbf{A}$ is a function only of R (not of $\vec{R}$) so that the partial derivative operator $\vec{p}$ reduces to an ordinary derivative with respect to R in eq 26b and 27. Defining

$$\mathbf{M} = \frac{1}{2\mu} \mathbf{U}^\dagger \mathbf{C}^{-1} \frac{d\mathbf{A}}{dR} \qquad (37)$$

$$\mathbf{M}_1 = \frac{1}{2\mu} \mathbf{U}^\dagger \mathbf{C}^{-1} \left(\frac{d\mathbf{C}}{dR}\right) \mathbf{U} \qquad (38)$$

$$\mathbf{M}_2 = \frac{1}{2\mu} \mathbf{U}^\dagger \frac{d\mathbf{U}}{dR} \qquad (39)$$

and using eq 22 we may write

$$\frac{1}{2\mu} \mathbf{U}\mathbf{C}^{-1}(\vec{p}\mathbf{A}) = -i\mathbf{M}\hat{e}_R = -i(\mathbf{M}_1 + \mathbf{M}_2)\hat{e}_R \qquad (40)$$

where $\hat{e}_R$ is a unit vector in the direction of $\vec{R}$. Similarly we define the matrices

$$\mathbf{N} = \frac{1}{2\mu} \mathbf{U}^\dagger \mathbf{C}^{-1} d^2\mathbf{A}/dR^2 \qquad (41)$$

$$\mathbf{N}_1 = \frac{1}{2\mu} \mathbf{U}^\dagger \mathbf{C}^{-1}(d^2\mathbf{C}/dR^2)\mathbf{U} \qquad (42)$$

$$\mathbf{N}_2 = \frac{1}{2\mu} \mathbf{U}^\dagger d^2\mathbf{U}/dR^2 \qquad (43)$$

so that

$$\frac{1}{2\mu} \mathbf{U}^\dagger \mathbf{C}^{-1}(p^2\mathbf{A}) = -\mathbf{N} = -(\mathbf{N}_1 + 4\mu\mathbf{M}_1\mathbf{M}_2 + \mathbf{N}_2) \qquad (44)$$

From the above definitions, we see that the matrices $\mathbf{M}_1$ and $\mathbf{N}_1$ represent contributions to the coupling matrices which arise primarily from the orthogonalization procedure while the matrices $\mathbf{M}_2$ and $\mathbf{N}_2$ represent contributions which arise from the diagonalization procedure. We may thus separate the effects of the two procedures and analyze the relative contribution of each to the total coupling matrices.

The curve fits to $\mathbf{H}^n(R)$, $V_p(R)$, and $\mathbf{C}(R)$ are used to generate $\mathbf{A}$, $\mathbf{C}$, and $\mathbf{U}$ at four equally spaced points $10^{-3} a_0$ apart. Then the required first and second derivatives of $\mathbf{A}$, $\mathbf{C}$, and $\mathbf{U}$ are calculated using a four-point difference formula.

V. Results and Discussion

Nonorthogonal Diabatic Basis. The calculated Hamiltonian matrix elements in the nonorthogonal diabatic representation for the $^1\Sigma^+$ valence-bond states are shown in Fig-
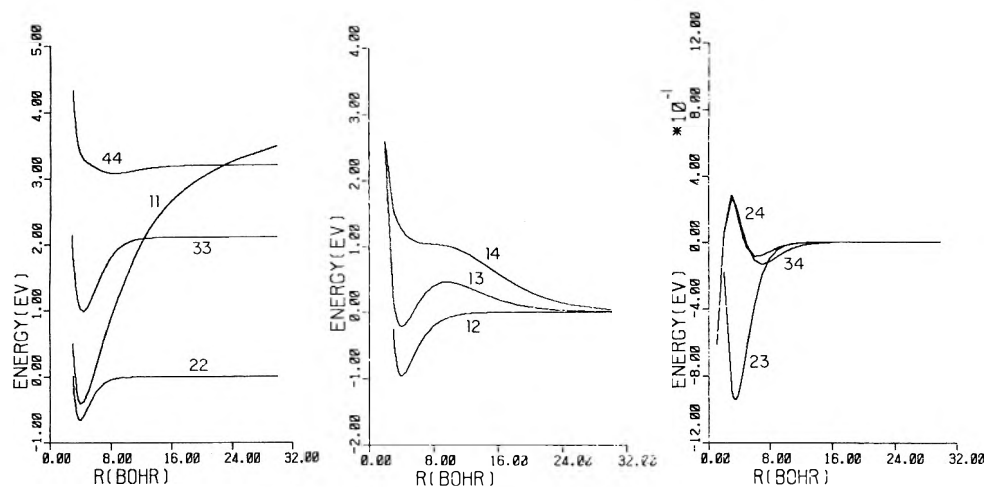
Figure 1. The matrix elements H_{ij}^n for the $^1\Sigma^+$ states of NaH in the nonorthogonal diabatic basis as functions of the internuclear distance R. Each curve is labeled by the pair of indices ij. The curve corresponding to H_{11}^n includes the polarization correction of eq 35. The notation on the right-most ordinate means that each number along the ordinate should be multiplied by 10^{-1}.
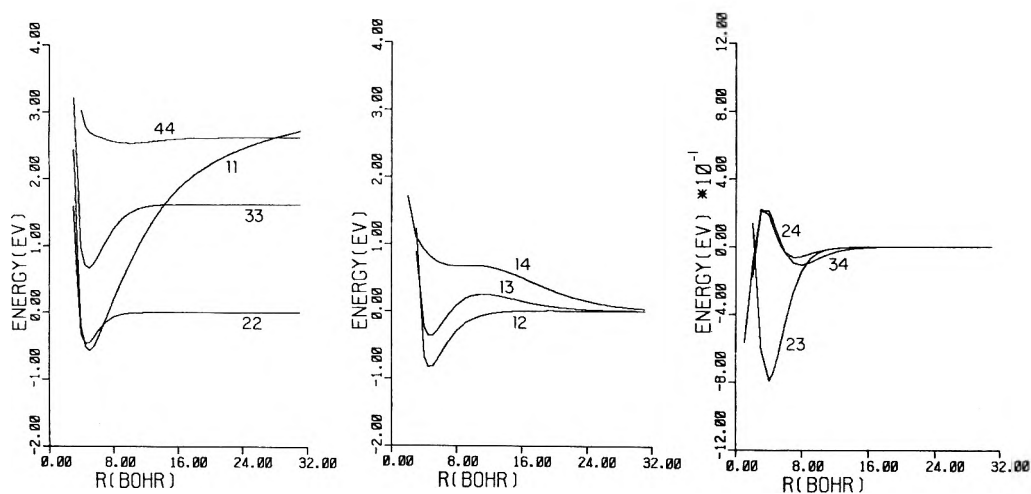
Figure 2. Same as Figure 1 except for KH.
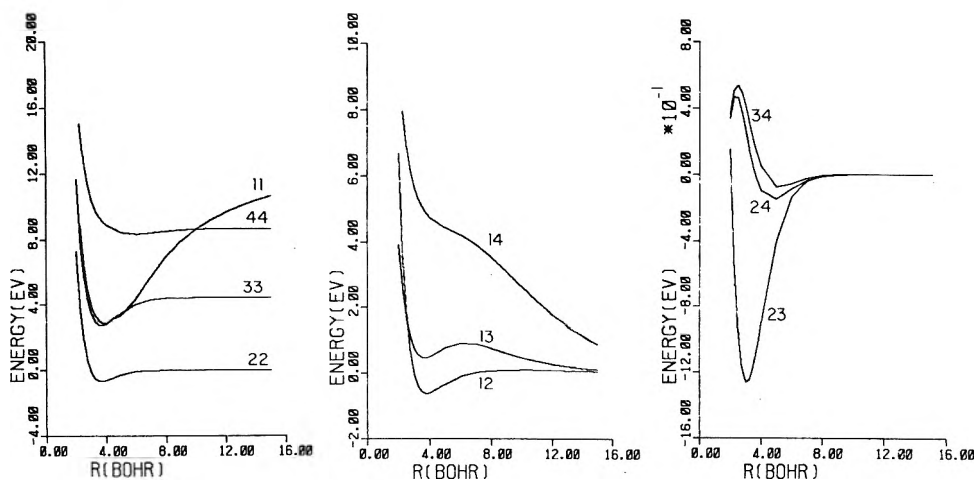
Figure 3. Same as Figure 1 except for MgH⁺.

ure 1 for NaH, Figure 2 for KH, and Figure 3 for MgH⁺. The curves corresponding to the matrix elements H_{11}^n in each case include the polarization potential correction of eq 35 and the reader should henceforth assume this polarization potential is present.

We note first of all the occurrence of curve crossings be-

tween the ionic curve H_{11}^n and the covalent curves. It is particularly interesting that no crossing occurs for NaH between H_{11}^n and the lowest covalent curve H_{22}^n. In earlier treatments of the problem it was assumed that a crossing would occur at a large value of R (7.7 a_0 by Bates and Boyd[3] and 7.55 a_0 by Grice and Herschbach[4]) where H_{22}^n was assumed to be essentially constant and where H_{11}^n was assumed to be well represented by the sum of a coulomb potential and a polarization potential. However, Figure 1 shows that the above assumption fails for our calculations and no crossing occurs because our calculated H_{11}^n is sufficiently less attractive than previous workers assumed. This same effect is true for KH where the crossing of the ionic curve with the lowest covalent curve is found at smaller R values than those assumed by Bates and Boyd[3] and by Grice and Herschbach.[4] There is no crossing between the ionic and lowest covalent states for MgH^+ either, but in this case the absence of the crossing is due to the higher ionization potential of Mg^+ and no crossing was expected.

We next note the large separation in distance between the attractive regions of the ionic curve H_{11}^n and the covalent curve H_{33}^n for NaH and KH. Configuration interaction including these two states yields the qualitative features of the adiabatic $A^1\Sigma^+$ state potential curve with the abnormally broad, flat minimum which leads to the well-known spectroscopic anomalies[31,32] in these states. It is easy to see here that this effect is due to the fact that the ionic curve H_{11}^n is the second lowest curve in this region and that its attractive region occurs at abnormally large distances, i.e., around $R = 9$ a_0. The effect is missing for MgH^+ since the two curves H_{11}^n H_{33}^n essentially coincide near their minima so no extended well region is expected for the A state. The A state for MgH^+ has been observed to be normal spectroscopically.[33]

The similarity of the off-diagonal Hamiltonian matrix elements for all three molecules is striking. We note in particular the long-range nature of the matrix elements H_{12}^n, H_{13}^n, and especially H_{14}^n which are the interactions of the ionic state with the covalent states. The matrix elements H_{23}^n, H_{24}^n, and H_{34}^n between covalent states are of shorter range. It is interesting that the matrix element H_{24}^n between the ns $^1\Sigma^+$ and n^*s $^1\Sigma^+$ is very similar to the matrix element H_{34}^n between the np $^1\Sigma^+$ and n^*s $^1\Sigma^+$ states while the matrix element H_{23}^n between the ns $^1\Sigma^+$ and np $^1\Sigma^+$ states is quite different.

The Hamiltonian matrix elements for the $^3\Sigma^+$ valence bond states are shown in Figure 4 for NaH, Figure 5 for KH, and Figure 6 for MgH^+. All diagonal matrix elements correspond to covalent configurations for this symmetry. Although not shown on the figures, curve crossings occur between the matrix element H_{11}^n and the two higher matrix elements H_{22}^n and H_{33}^n at small values of R. These crossings will produce rather large coupling matrices in these regions which will be discussed below.

The off-diagonal matrix elements are again very similar from one molecule to another. The matrix elements H_{13}^n and H_{23}^n between the n^*s $^3\Sigma^+$ state and the ns $^3\Sigma^+$ and np $^3\Sigma^+$ states, respectively, are again similar to each other while the element H_{12}^n between the ns $^3\Sigma^+$ and np $^3\Sigma^+$ states is quite different.

Orthogonal Diabatic Basis. The Hamiltonian matrix elements in the orthogonal diabatic representation for the $^1\Sigma^+$ states are shown in Figure 7 for NaH, Figure 8 for KH, and Figure A1[34] for MgH^+. Comparing these curves with the curves in the nonorthogonal representation we note a num-
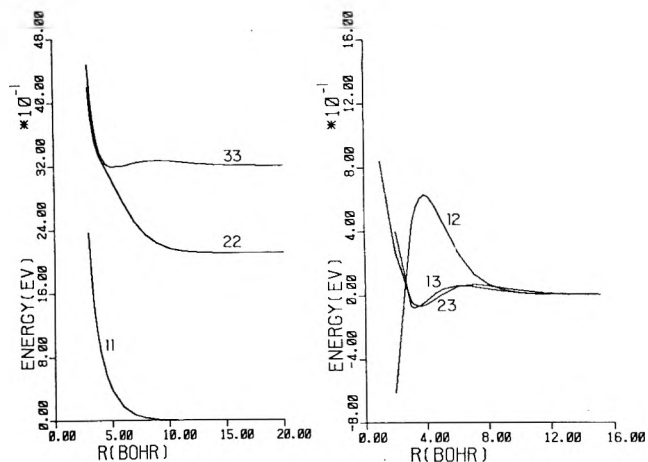
Figure 4. The matrix elements H_{ij}^n for the $^3\Sigma^+$ states of NaH in the nonorthogonal diabatic basis as functions of internuclear distance R. Each curve is labeled by the pair of indices ij.
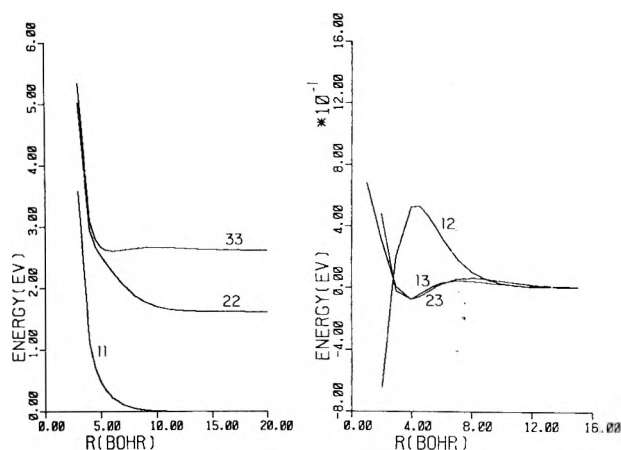
Figure 5. Same as Figure 4 except for KH.
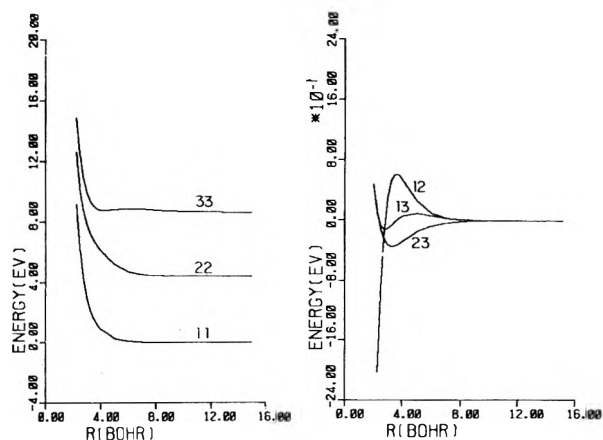
Figure 6. Same as Figure 4 except for MgH^+.

ber of differences. The attractive wells for the $3^1\Sigma^+$ and $4^1\Sigma^+$ states of NaH and KH are not as deep as they were in the nonorthogonal basis and the well for the $2^1\Sigma^+$ state has completely disappeared. The $2^1\Sigma^+$ and $3^1\Sigma^+$ states of MgH^+ have wells which are not quite as deep as in the nonorthogonal basis while the $4^1\Sigma^+$ state has a slightly deeper well than in the nonorthogonal basis. The curve corresponding to the ionic configuration H_{11}^s (R) has shifted position relative to the other diagonal elements thereby
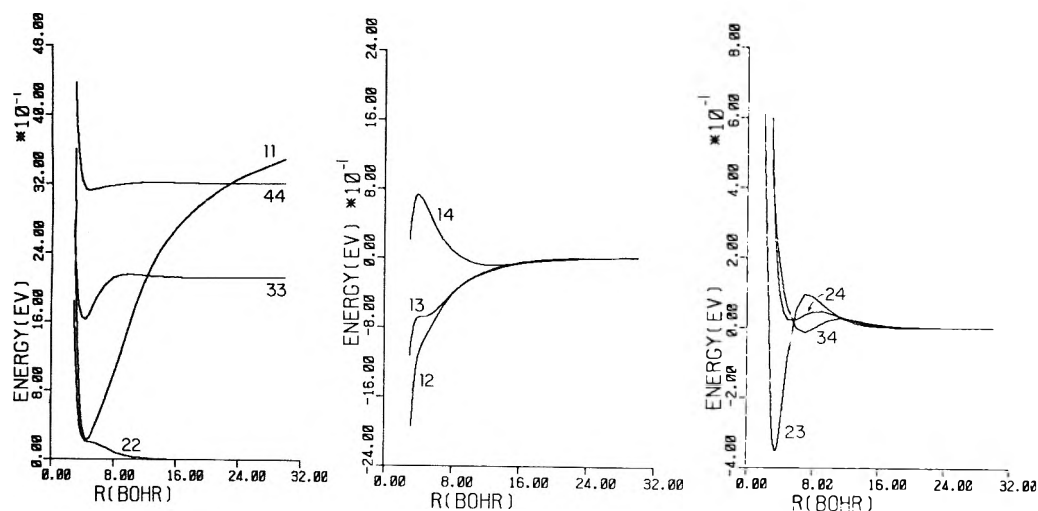
Figure 7. The matrix elements $H_{ij}{}^s$ for the $^1\Sigma^+$ states of NaH in the symmetrically orthogonalized diabatic basis as functions of internuclear distance R. Each curve is labeled by the pair of indices ij.
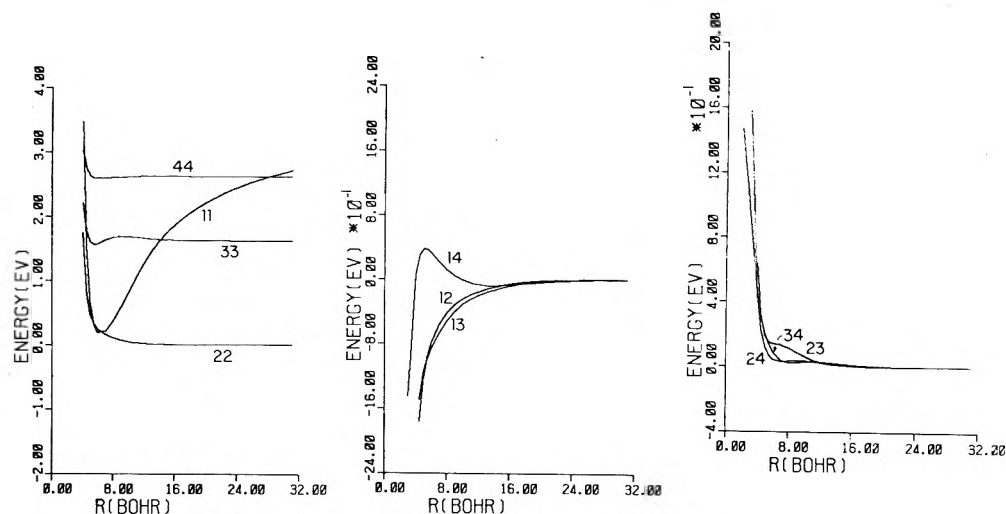
Figure 8. Same as Figure 7 except for KH.

changing the positions of the crossing points and in fact introducing new crossing points. New crossing points at small R values appear for all three molecules; in the case of NaH, where there was no crossing between the $1^1\Sigma^+$ and $2^1\Sigma^+$ potential curves in the nonorthogonal basis, there are now two crossings between $R = 4$ a_0 and $R = 5$ a_0. In the case of MgH$^+$, the ionic curve no longer so closely resembles the potential curve of the $3^1\Sigma^+$ state near its minimum.

The off-diagonal Hamiltonian matrix elements have also changed considerably. Nevertheless, the corresponding matrix elements are still remarkably similar from molecule to molecule, the most notable exception being the matrix element $H_{23}{}^s$ of KH which is somewhat different from the same matrix element for NaH or MgH$^+$. It is interesting that the matrix elements $H_{12}{}^s$, $H_{13}{}^s$, and $H_{14}{}^s$ between the ionic configuration and the covalent configurations are not of as long a range as they were in the nonorthogonal representation.

Mulliken,[31] neglecting overlap, has reported a calculation for the diabatic matrix element between the lowest covalent state and the ionic state in LiH. His result, as a function of R, has the same qualitative shape as the matrix elements $H_{12}{}^s(R)$ reported here. His function varies from -1.5 eV at $R = 2.0$ a_0 to -0.1 eV at $R = 5$ a_0 while the

functions reported here vary from -11.6 to 0.9 eV for NaH, from -21.6 to -1.2 eV for KH, and from -5.0 to -1.0 eV for MgH$^+$ over the same interval.

The Hamiltonian matrix elements for the $^3\Sigma^+$ states in the symmetrically orthogonalized representation are shown in Figure 9 for NaH, Figure 10 for KH, and Figure A2[34] for MgH$^+$. The most interesting difference between the two representations is the introduction of additional curve crossings of the diagonal matrix elements at small values of R. These crossings will show up in the coupling matrices discussed below. The off-diagonal matrix elements have changed shape but the similarity noticed in the nonorthogonal representation between the elements $H_{13}{}^n$ and $H_{23}{}^n$ remains for $H_{13}{}^s$ and $H_{23}{}^s$ while the element $H_{12}{}^s$ has a different character.

The shapes of these matrix elements as functions of R depend on the particular method of orthogonalization chosen. Since we are free to multiply our orthogonalizing matrix by an arbitrary unitary matrix as discussed above, it is possible to produce matrix elements in an orthogonal diabatic representation with widely varying characteristics. We have carried out the calculation for canonical orthogonalization[8] and have found qualitative and quantitative differences in all the matrix elements. For example, for NaH
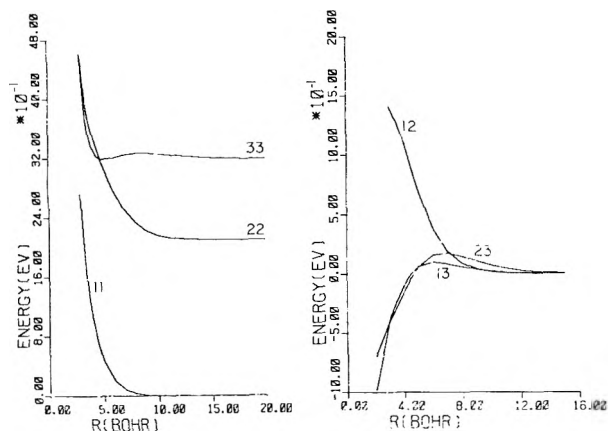
Figure 9. The matrix elements H_{ij}s for the $^3\Sigma^+$ states of NaH in the symmetrically orthogonalized diabatic basis as functions of internuclear distance R. Each curve is labeled by the pair of indices ij.
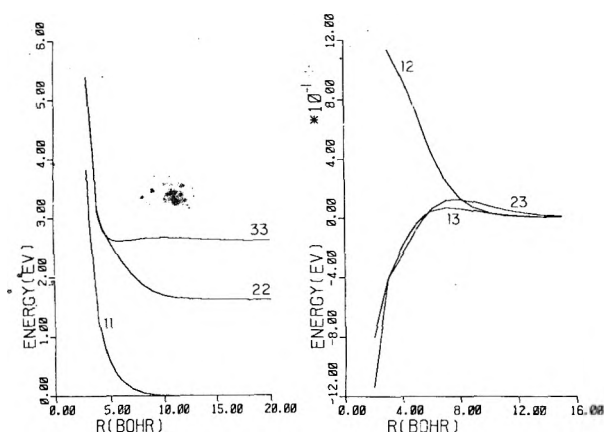
Figure 10. Same as Figure 9 except for KH.

Figure 11. The adiabatic potential curves for NaH. All nine curves calculated in this work are shown plus the experimentally determined RKR curves for the $X^1\Sigma^+$ and $A^1\Sigma^+$ states.

Figure 12. Same as Figure 11 except for KH.

the matrix element H_{12} at 5 a_0 is -0.903 eV for symmetric orthogonalization and 0.392 eV for canonical orthogonalization, the matrix element H_{13} at 12 a_0 is -0.176 and -0.410 eV, respectively, and the matrix element H_{14} at 20 a_0 is -0.035 and 0.034 eV, respectively.

As discussed by O'Malley,[35] however, some diabatic representations have particular physical significance. In the work presented here, the original nonorthogonal valence bond molecular basis has particular significance in terms of the bonding models which have been used previously to discuss the interaction of ionic and covalent configurations in the hydrides considered here. Symmetric orthogonalization was then chosen because it gives an orthogonal basis which differs from the physically motivated basis as little as possible.

The Adiabatic Potential Curves and Electronic Eigenfunctions. We present now the results for the adiabatic potential curves. The results are shown for NaH in Figure 11, for KH in Figure 12, and for MgH$^+$ in Figure 13.

We recall that the parameter γ in the polarization potential was adjusted in such a way that the experimental value of the dissociation energy of the A$^1\Sigma^+$ states was not exceeded. Comparing the A$^1\Sigma^+$ states obtained in this way with the experimentally determined RKR potential curves which are discussed in ref 30 and shown in Figures 11–13, we see that our procedure for determining γ yields adiabatic A$^1\Sigma^+$ potential energy curves which have the correct shape but which are shifted to larger values of R especially in the cases of KH and MgH$^+$.

It should be noted that the C$^1\Sigma^+$ states calculated here have no real physical significance since the ionic curve in the nonorthogonal basis will have another avoided crossing with the next higher covalent state of the same symmetry above the highest one considered here. The main reason for considering four $^1\Sigma^+$ states is that the addition of the fourth $^1\Sigma^+$ molecular basis function produces a fundamental difference in the calculated B$^1\Sigma^+$ state. In a three-state calculation omitting the $4^1\Sigma^+$ nonorthogonal diabatic state, the B$^1\Sigma^+$ state dissociates to the ionic configuration while in the four-state calculation it dissociates correctly to the M(n^*s) + H(1s) atomic state. At values of R less than the position of the avoided crossing, the B$^1\Sigma^+$ in the three-state calculation has very little character of a molecular bound state. In the four-state calculation, however, a large amount of binding energy is added and the state resembles
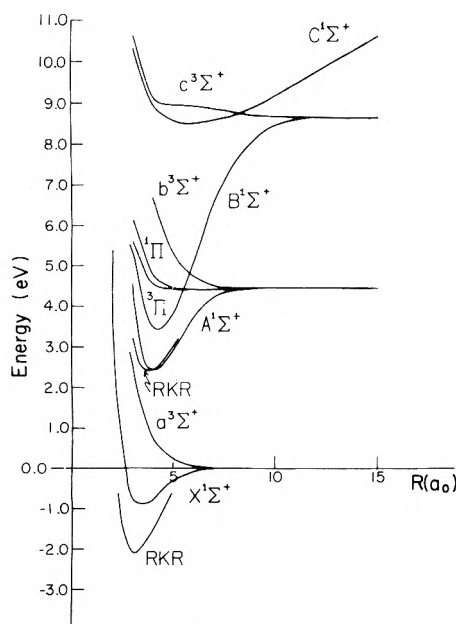
Figure 13. Same as Figure 11 except for MgH+.

TABLE IV: Squares $|U_{ij}|^2$ of the Coefficients for the Expansion of the Adiabatic $^1\Sigma^+$ Wave Function in Terms of the Orthogonal Diabatic Basis Functions Near the Equilibrium Internuclear Distances of the Ground States

		Diabatic			
Adiabatic		Ionic	ns	np	$(n + 1)$s
NaH	$X^1\Sigma^+$	0.487	0.426	0.066	0.021
$R = 4.0\ a_0$	$A^1\Sigma^+$	0.259	0.549	0.157	0.035
	$B^1\Sigma^+$	0.188	0.020	0.777	0.014
	$C^1\Sigma^+$	0.066	0.004	0.000	0.930
KH	$X^1\Sigma^+$	0.523	0.375	0.089	0.013
$R = 5.0\ a_0$	$A^1\Sigma^+$	0.089	0.474	0.429	0.008
	$B^1\Sigma^+$	0.029	0.032	0.151	0.788
	$C^1\Sigma^+$	0.359	0.120	0.331	0.191
MgH+	$X^1\Sigma^+$	0.098	0.811	0.091	0.000
$R = 3.5\ a_0$	$A^1\Sigma^+$	0.770	0.120	0.010	0.100
	$B^1\Sigma^+$	0.031	0.064	0.896	0.008
	$C^1\Sigma^+$	0.101	0.005	0.003	0.891

the $A^1\Sigma^+$ state below it. Thus, the addition of the fourth molecular basis state to the calculation has given physical meaning to the $B^1\Sigma^+$ states.

At this point, it is interesting to examine the nature of the bonding $^1\Sigma^+$ molecular states. In Table IV we give the squares of the coefficients for the expansion of the adiabatic wave functions in terms of the symmetrically orthogonalized diabatic basis functions near $R = R_e$ for the ground state of the three molecules. Since symmetric orthogonalization has been used, these basis functions resemble the original nonorthogonal basis functions and we have labeled them as ionic, ns, np, and n^*s according to the configurations to which they correspond in the limit of infinite separation.

Consider first the behavior of the eigenfunctions at large R. The $X^1\Sigma$ state changes character from covalent to ionic near $R = 7\ a_0$ for NaH and near $R = 8\ a_0$ for KH. The $A^1\Sigma^+$ state changes from covalent to ionic near $R = 12\ a_0$ for NaH and near $R = 15\ a_0$ for KH. The $B^1\Sigma^+$ state changes from covalent to ionic near $R = 23\ a_0$ for NaH and $R = 28\ a_0$ for KH. The $C^1\Sigma^+$ states change from ionic to covalent at the same places that the $B^1\Sigma^+$ states change from covalent to ionic but the covalent state comes in with a negative sign.

The ground state of MgH+ is somewhat different from those of NaH and KH. This difference is due to the higher ionization potential of Mg+ which prevents the ionic curve from descending low enough to interact in the same way with the lowest covalent state. There is, however, a change in character in the state at values of R less than $R = R_e$. The excited states exhibit characteristics similar to those of NaH and KH. The $A^1\Sigma^+$ state changes from covalent to ionic near $R = 6\ a_0$, the $B^1\Sigma^+$ state changes from covalent to ionic near $R = 10\ a_0$, and the $C^1\Sigma^-$ state changes from ionic to covalent at the same point with the covalent state coming in with a negative sign as it did in NaH and KH.

A very interesting result of these calculations is the fact that the triplet states also exhibit changes of character due to avoided crossings even though there is no simple physical explanation in terms of interactions with an ionic state since there is no ionic configuration in this case. The be-

havior of the triplet states for NaH and MgH+ are qualitatively the same while KH is quite different. In fact, the $b^3\Sigma^+$ and $c^3\Sigma^+$ states for KH approach the behavior of a step function model. The change in character in these states takes place near $R = 5.5\ a_0$ over an interval of less than 0.1 a_0, and we shall find in the next section that the coupling matrices in this region are quite large and very narrow.

Near the equilibrium position, we see that the $X^1\Sigma^+$ states of NaH and KH are a mixture of the ionic and ns covalent states with the large component ionic as expected. The $X^1\Sigma^+$ state of MgH+, however, is almost entirely covalent as we might have expected since we have seen that no curve crossing between the ionic and ns covalent states occurs in this case.

The $A^1\Sigma^+$ state for NaH is a mixture of the ionic state and the ns and np covalent states and is predominantly covalent. For KH the $A^1\Sigma^+$ state has a similar mixture of ionic and covalent states but has much less ionic character. The $A^1\Sigma^+$ state of MgH+ is predominantly ionic.

The $B^1\Sigma^+$ states of NaH and MgH+ are similar to each other having the character of the np configuration, while the same state for KH is dominated by the n^*s state with a small component of np.

The nature of these states may be compared to the results of Melius et al.[36] for the excited states of LiH. They found that the $A^1\Sigma^+$ state has significant sp-hybrid character while the $B^1\Sigma^+$ state is essentially s-like in character. From the discussion above we see that our results for KH are in agreement with this picture of the molecular bonding but the results for NaH and MgH+ are not in agreement. In other words, there appears to be more hybridization in LiH and KH than in NaH and MgH+. In the former two cases the ionic configuration and the bonding sp-hybrid covalent configuration lead to the lowest two adiabatic potential curves and the n^*s covalent configuration is lower in energy than the antibonding sp-hybrid covalent configuration. Although this effect is less important for NaH and MgH+, we have performed additional calculations using only three molecular basis functions for NaH which show that the $B^1\Sigma^+$ adiabatic potential energy curve is still appreciably

TABLE V: Calculated and Experimental Equilibrium Distances R_e (in a_0) and Dissociation Energies D_e (in eV)

	$X^1\Sigma^+$				$A^1\Sigma^+$			
	R_e (expt)	R_e (calcd)	$D_e{}''$ (expt)	$D_e{}''$ (calcd)	R_e (expt)	R_e (calcd)	$D_e{}'$ (expt)	$D_e{}'$ (calcd)
NaH	3.572	4.121	2.05	1.085	6.064	6.115	1.33	1.303
KH	4.055	4.882	1.87	0.995	6.959	7.505	1.12	1.142
MgH⁺	3.116	3.439	2.1	0.989	3.792	4.175	2.0	2.111

lowered near $R = R_e$ by addition of the fourth molecular basis function for NaH.

For small values of R, many changes occur in the character of the $^1\Sigma^+$ states for all three molecules. These changes are due to the presence of avoided crossings at small R and give rise to large coupling matrices in these regions as we shall see below. However, these avoided crossings may only be artifacts of the model used here and it is not clear whether they have any physical significance.

In Table V we present a comparison of experimental and calculated dissociation energies and equilibrium positions for the $X^1\Sigma^+$ and $A^1\Sigma^+$ states of the three molecules. The sources of the experimental values are explained in ref 30. From that table we see that we have been able to obtain almost all of the dissociation energy D_e' for the $A^1\Sigma^+$ states by the adjustment of the polarization potential but that the equilibrium position is shifted to larger R in each case. For the $X^1\Sigma^+$ states, about 53% of the dissociation energy has been obtained for NaH, 54% for KH, and 43% for MgH⁺. The equilibrium positions for the $X^1\Sigma^+$ states are again too large.

It is interesting for comparison with Table V to note that Cade and Huo[37] made an extended basis Hartree–Fock calculation for the $X^1\Sigma^+$ state of NaH and obtained $D_e{}'' = 0.936$ eV and $R_e = 3.616$ a_0. Szasz and McGinn[38] using the same model Hamiltonian as used in this work with their Phillips–Kleinman effective potential have reported values for R_e and D_e for the $X^1\Sigma^+$ states of NaH and KH. Using a trial wave function which is a linear combination of a covalent wave function and an ionic wave function both with adjustable parameters, they determined variationally the values $R_e = 3.77$ a_0 and $D_e{}'' = 1.21$ eV for NaH and $R_e = 4.235$ a_0 and $D_e{}'' = 0.916$ eV for KH. Adding a correlation factor to their wave function, they found $R_e = 3.78$ a_0 and $D_e{}'' = 1.463$ eV for NaH and $R_e = 4.21$ a_0 and $D_e{}'' = 1.230$ eV for KH.

In a valence bond calculation using a fixed minimum basis set of atomic orbitals which are optimized for the atoms and using complete configuration mixing, Heil, O'Neil, and Schaeffer[39] have found for the Cl_2 molecule that they obtain an equilibrium separation which is 18% larger than the experimental value and a dissociation energy which is only 29% of the experimental value. They attribute their poor results to the lack of flexibility within the molecular environment of the atomic orbitals in the valence bond model. The same effect has been pointed out previously by Harris and Michels[40] for the F_2 molecule.

In the work presented here, we have also used a valence bond model with a small (although larger than minimum basis set) set of fixed atomic orbitals which are optimized for the atoms but we have allowed only partial configuration mixing. It is clear that when only a few fixed atomic

orbitals are included in the basis set and these orbitals are optimized for the atomic states rather than at small R, there will be a systematic error yielding relatively more accurate, i.e., lower, energies at larger R than at small R. This effectively shifts the calculated value of R_e toward larger R. We conclude that the poor values for R_e and D_e obtained here are due in large part to the inflexibility of our atomic orbitals, to the fact that they are optimized at large R, and to the fact that our orbital basis is not large enough rather than to a lack of other configurations which could be found using our orbital basis.

In Figure 14, we compare the ground state potential curve for NaH obtained by Cade and Huo[37] with the adiabatic states calculated here and with a set of adiabatic states calculated by Lewis, McNamara, and Michels.[41] The latter authors have performed a configuration mixing calculation in which only the valence electrons are promoted in excited configurations, i.e., they used the frozen core approximation. This approximation is similar physically to the effective potential formalism used in the present work but their choice of configurations differs from that used in the present work. The calculations of Lewis et al. are limited to $R > 4$ a_0. From the figure we see that Lewis, McNamara, and Michels have obtained a larger and more accurate binding energy for the ground state than we have but that the binding energy we have obtained is larger than that obtained by Cade and Huo. The $A^1\Sigma^+$ potential curve obtained by Lewis, McNamara, and Michels has a completely incorrect shape compared to the RKR curve. Their Π states, however, are probably better than the ones calculated here since we have included no configuration mixing for these states. Nevertheless, we see from Figure 14 that the Π state curves obtained here have essentially the same shape as those obtained by Lewis, McNamara, and Michels and that their curves are lower in energy by only a few tenths of an electron volt. Part of the difference in the two $b^3\Sigma^+$ states is due to the presence of an avoided crossing in our calculation between the two highest $^3\Sigma^+$ states. This feature does not appear in the adiabatic potential curves of Lewis, McNamara, and Michels.

Comparison with other Work and Examination of the Curve Crossings. In the Introduction we indicated that the separation $\Delta W(R_c)$ between the adiabatic potential curves at the position $R = R_c$ of a crossing of two diabatic curves is important in the LZS model. Under the assumption that the system is described by a linear combination of two diabatic wave functions i and j, this separation is given by

$$\Delta W(R_c) = 2\left| H_{ij} - H_{ii}S_{ij} \right|/(1 - S_{ij}^2) \qquad (45)$$

where all quantities are to be evaluated at $R = R_c$. In eq 45 H_{ii} is the value of the two diagonal Hamiltonian matrix elements which cross at $R = R_c$ in the diabatic basis and H_{ij} is the matrix element between the two states which cross each other. The overlap between the two states is S_{ij}. In the nonorthogonal diabatic basis, eq 45 becomes

$$\Delta W(R_c{}^n) = 2\left| H_{ij}{}^n - H_{ii}{}^n S_{ij} \right|/(1 - S_{ij}^2) \qquad (46)$$

where the superscript n on R_c refers to the value of R_c in the nonorthogonal diabatic basis. In the symmetrically orthogonalized basis, eq 45 reduces to

$$\Delta W(R_c{}^s) = \left| 2H_{ij}{}^s \right| \qquad (47)$$

where $H_{ij}{}^s$ is the matrix element between the two states in the symmetrically orthogonalized basis evaluated at the
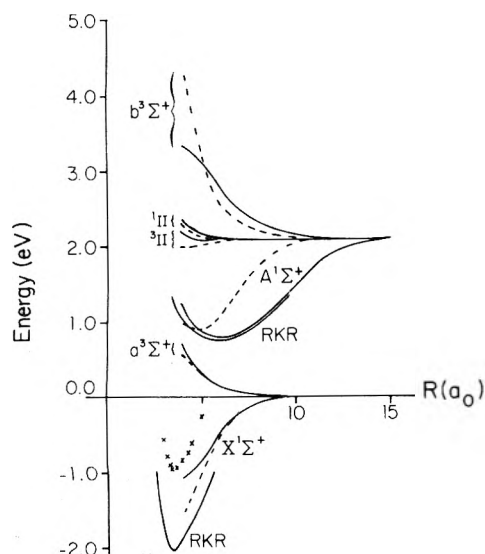
Figure 14. The adiabatic potential curves for NaH. The six dashed curves were calculated by Lewis, McNamara, and Michels and in each case the corresponding curve as calculated in the present work is shown for comparison. The X's are the results of Cade and Huo for the X$^1\Sigma^+$ state and the RKR curves are for the X$^1\Sigma^+$ and A$^1\Sigma^+$ states.

position $R_c{}^s$ of the crossing of the symmetrically orthogonalized diabatic potential curves. As mentioned previously, $R_c{}^s$ is not equal to $R_c{}^n$.

Using eq 46, the quantity ΔW has been calculated for the large R crossings for NaH and KH by Bates and Boyd[3] and the work has recently been repeated in modified fashion by Grice and Herschbach[4] for the crossing with the lowest covalent state for the same two molecules. The quantity ΔW has also been obtained for many other systems and the results have been tabulated by Olson, Smith, and Bauer.[42] It should be noted, however, that the values for H_{ij} listed in that tabulation are just half the values of ΔW given by Bates and Boyd. Thus Olson et al. assumed that Bates and Boyd were using an orthogonal representation which in fact they were not using.

Using the assumed $V_p(R)$ and the analytic forms which we have fit to our Hamiltonian matrix $H^n(R)$ and to the transformation $C(R)$, we have calculated the quantity ΔW from eq 46 for the nonorthogonal basis at the same values of R as were used by Bates and Boyd and by Grice and Herschbach. No crossings actually occur at these points in our model, but the calculations were performed to compare treatments. Since $H_{ii}{}^n(R_c) \neq H_{jj}{}^n(R_c)$ in our model, eq 46 is not really applicable to the present calculations at these R values; it is applied correctly at the positions of the crossings of the present model below. However, to compare our results to those of previous workers for the ionic–covalent curve crossings, we set $H_{ii}{}^n$ in eq 46 equal to the asymptotic energy of the appropriate nonorthogonal diabatic covalent potential curve as they did. This is called procedure B in Table VI and the comparison of the results of procedure B with previous estimates of ΔW is essentially a comparison of calculated values of $H_{ij}{}^n$ and S_{ij} for $i \neq j$. In addition, to illustrate the sensitivity of eq 46 to this choice we also used the equation with $H_{ii}{}^n$ equal to the appropriate nonorthogonal diabatic covalent potential curve of the present work evaluated at $R = R_c$. These results are labeled procedure A in Table VI. Comparison of procedure A with procedure B shows that the results differ by 0.3–10%. Next

we compare procedure B to the results of previous workers.

We give also in Table VI the three quantities P_1, P_2, P_3 which are defined as follows. P_1 is

$$P_1 = \Delta W_1 / \Delta W_2 \qquad (48)$$

where ΔW_1 is the value of ΔW calculated in the nonorthogonal representation in this work by procedure B and ΔW_2 is the value due to either Bates and Boyd or Grice and Herschbach. P_2 is

$$P_2 = \phi_1 / \phi_2 \qquad (49)$$

where ϕ_1 is the value of the pseudowave function used in this work evaluated at $x = R_c$ and ϕ_2 is the value of the coulomb approximation function used by Bates and Boyd. P_3 is

$$P_3 = \rho_1 / \rho_2 \qquad (50)$$

where ρ_1 is the probability density of finding an electron the distance $x = R_c$ from the proton as calculated from Goddard's GF function used in this work and ρ_2 is the same quantity calculated from either the Löwdin function used by Bates and Boyd or from the function used by Grice and Herschbach.

Considering first the crossings for the states dissociating to Na(3s) and K(4s), we see that the value for ΔW obtained here in the nonorthogonal basis is in good agreement with the value obtained by Bates and Boyd while the value given by Grice and Herschbach is much larger than the other two. These last authors attribute the difference between their results and those of Bates and Boyd to the difference in the H$^-$ functions used. Detailed comparison of functions used for H$^-$, however, shows that the value of the probability density ρ corresponding to their H$^-$ function is comparable to the ρ corresponding to the Löwdin function used by Bates and Boyd and actually smaller than the ρ for the GF function used here in the region from 7 to 9 a_0. On this basis alone, one would expect Grice and Herschbach to obtain a smaller value of ΔW. It is interesting to note that Grice and Herschbach used Whittaker functions for the alkali wave functions. The only difference for large x between these functions and the coulomb approximation functions used by Bates and Boyd is the normalization constant which appears in the equation used by Bates and Boyd but not in the equation used by Grice and Herschbach. Comparison with a numerical Hartree–Fock wave function for K (see above) shows that this constant leads to radial wave functions which are accurately normalized in the asymptotic region for the ground s state and it is interesting to note that for Na(3s) it has the value 0.543 and for K(4s) it has the value 0.537. Multiplying the values of ΔW due to Grice and Herschbach by these values we find $\Delta W = 1.54 \times 0.543 = 0.836$ eV for Na(3s) and $\Delta W = 1.06 \times 0.537 = 0.569$ eV for K(4s). These results are in much better agreement with the present results and the results obtained by Bates and Boyd. Therefore, it seems as though a great deal of the difference in the results is due to the lack of normalization of the alkali functions used by Grice and Herschbach.

We see from the table that we obtain better agreement, in general, with previous work when we evaluate $H_{ii}{}^n$ at the asymptotic energies since this was the assumption made in the previous studies. Our results on the whole agree fairly well with those of Bates and Boyd but the differences seem to have no correlation with the differences in the wave

TABLE VI: Comparison of the Energy Separation $\Delta W(R_c)$ in Electron Volts with Previously Calculated Values at the Positions R_c (in bohrs) of Previously Determined Avoided Crossings

State[a]	R_c	ΔW Previous work	ΔW This work A[b]	ΔW This work B[c]	P_1[d]	P_2[e]	P_3[f]	P_2P_3
Na(3s)	7.7	0.585 (BB)[g]	0.520	0.573	0.98	0.99	3.2	3.1
Na(3s)	7.55	1.54 (GH)	0.564	0.627	0.41		3.3	
Na(3p)	12.6	0.320 (BB)	0.278	0.286	0.89	0.38	9.7	0.37
Na(4s)	22.9	4.35×10^{-2} (BB)	7.90×10^{-2}	7.88×10^{-2}	1.81	0.39	79.0	31.0
K(4s)	8.8	0.495 (BB)	0.455	0.492	0.99	0.83	4.0	3.3
K(4s)	8.8	1.06 (GH)	0.455	0.492	0.46		3.5	
K(4p)	14.3	0.242 (BB)	0.235	0.233	0.96	0.32	12.0	3.8
K(5s)	27.7	1.90×10^{-2} (BB)	3.18×10^{-2}	3.19×10^{-2}	1.68	0.35	23.0	8.1

[a] The state which crosses the ionic state at $R = R_c$. [b] Obtained with H_{ii}^n equal to the appropriate nonorthogonal diabatic covalent matrix element. [c] Obtained with H_{ii}^n equal to the asymptote of the covalent state. [d] Equation 48. [e] Equation 49. [f] Equation 50. [g] BB denotes Bates and Boyd; GH denotes Grice and Herschbach.

functions used. One might naively expect, since the crossings occur at large R, that the difference in ΔW would have contributions from the differences in the atomic wave functions of the electron transferred in a given transition between two diabatic states so that $P_1 \simeq P_2P_3$. However, the values given in the table show that this is not even approximately true.

As mentioned above, no actual curve crossings occur in our model at the positions listed in Table VI. Again using the analytic forms for the matrices $H^n(R)$ and $C(R)$ and the polarization potential $V_p(R)$ we have determined all of the curve·crossings which occur for all three molecules in both *the nonorthogonal diabatic and the orthogonal diabatic* representations. The positions R_c of these crossings are given in Tables VII-IX. We notice first of all that the total number of crossings is not constant from one representation to the other. Especially interesting is the fact that no crossing occurs between the $1^1\Sigma^+$ and $2^1\Sigma^+$ states for NaH in the nonorthogonal basis but two crossings occur in the orthogonal basis. It is also interesting that for all three molecules the orthogonalization process introduces new crossings at small values of R between the ionic and covalent states as well as crossings between the covalent states. For those crossings which occur in both representations the position of the crossing is not constant. Some of these positions may shift as much as 1 a_0 or even 2 a_0 for small values of R_c while the ones occurring at larger values of R_c tend to shift by only a few tenths of 1 a_0.

We shall see below that, although the results in the adiabatic representation are independent of the method of orthogonalization, the curve crossings which occur in the symmetrically orthogonalized diabatic basis are of fundamental importance in determining the character of the coupling matrices between adiabatic electronic states. The large R crossing points for $^1\Sigma^+$ states have an obvious physical interpretation in terms of interactions between the ionic and covalent configurations. The small R crossings for the $^1\Sigma^+$ states and all the crossings for $^3\Sigma^+$ states have no *such obvious interpretation and may just be artifacts of the* original nonorthogonal basis chosen or of the model Hamiltonian assumed. Further work with larger basis sets is required to better understand the $^1\Sigma^+$ and $^3\Sigma^+$ manifolds at small R.

Since the LZS model places a great deal of importance on the quantity ΔW at the points $R = R_c$, we have calculated these quantities from our analytic forms for all crossings given in the tables and the values obtained are listed in Tables VII-IX. For the nonorthogonal diabatic representation we have used eq 46 and for the symmetrically orthogonalized diabatic basis we have used eq 47.

It will be recalled that the quantity ΔW given by eq 46 for a nonorthogonal basis and eq 47 for an orthogonal basis is the energetic separation between the two adiabatic potential curves at the position of an avoided crossing under the assumption that the system is described in terms of a two-state basis. Here we are dealing with a four-state system ($^1\Sigma^+$ manifold) and a three-state system ($^3\Sigma^+$ manifold) and it is not true that the values of ΔW obtained from eq 46 or 47 will be equal to the actual separation between *the adiabatic potential curves. We have therefore deter-* mined the actual separation $\Delta W'$ between these curves at the positions of the avoided crossings using the curves obtained from our analytic forms. These values are also listed in the tables for comparison with ΔW.

If a particular avoided crossing is adequately described in terms of two of the present diabatic states, then ΔW and $\Delta W'$ will be approximately equal. From the results in Tables VII-IX we see that in general for the large R crossings the two quantities are approximately equal while for small R crossings some of the values are about equal but the majority are not. Thus, it would seem that the large R crossings may indeed be treated in terms of a two-state model in *the present diabatic basis but the small R crossing in gen-* eral may not.

The Coupling Matrices in the Adiabatic Representation. Next we present results for the matrices M and N and analyze their characteristics in terms of the relative contributions of the matrices M_1, M_2, N_1, and N_2.

The properties of M and N are determined by the derivatives of the matrix elements of the two matrices C and U according to eq 37–44. We recall that the matrix C is the transformation from the nonorthogonal to the orthogonal diabatic basis and that the matrix elements of C are fairly slowly varying functions of R. Therefore, we expect to find that the matrix elements of M_1 and N_1 are fairly small. The *matrix U is the transformation which diagonalizes the elec-* tronic Hamiltonian in the orthogonal diabatic basis and the matrix elements of U as functions of R change very rapidly in certain regions corresponding to the change in character of the adiabatic states in the regions of avoided crossings. We expect therefore that the elements of M_2 and N_2 will be somewhat larger than those of M_1 and N_1 and that the elements of M_2 will have peaks in the regions where the avoided crossings occur in the symmetrically orthogonalized di-

TABLE VII: Curve Crossing Positions R_c (in bohrs) for NaH States for Both the Nonorthogonal and Orthogonal Diabatic Bases and the Separation (in eV) between Adiabatic Potentials at R_c where ΔW is from Eq 46 or 47 and $\Delta W'$ is Measured from the Calculated Curves

j	$i = 2$			$i = 3$			$i = 4$		
	R_c	ΔW	$\Delta W'$	R_c	ΔW	$\Delta W'$	P_c	ΔW	$\Delta W'$
$^1\Sigma^+$ nonorthogonal									
1				12.45	0.296	0.319	23.02	7.81×10^{-2}	7.93×10^{-2}
$^1\Sigma^+$ orthogonal									
1	4.28	2.10	2.14	3.22	1.84	1.62	2.83	0.132	2.53
1	4.86	1.86	1.82	12.32	0.332	0.329	23.09	7.88×10^{-2}	7.89×10^{-2}
2				2.49	0.314	3.46	2.13	5.34	1.56
$^3\Sigma^+$ nonorthogonal									
1	1.83	4.18	1.72	1.67	2.72	4.44			
$^3\Sigma^+$ orthogonal									
1	1.86	4.34	1.75	1.77	2.70	3.81			
2				2.59	0.954	1.68			
2				4.82	6.44×10^{-2}	0.220			

TABLE VIII: Curve Crossing Positions R_c (in bohrs) for KH States for Both the Nonorthogonal and Orthogonal Diabatic Bases and the Separation (in eV) between Adiabatic Potentials at R_c where ΔW is from Eq 46 or 47 and $\Delta W'$ is Measured from the Calculated Curves

j	$i = 2$			$i = 3$			$i = 4$		
	R_c	ΔW	$\Delta W'$	R_c	ΔW	$\Delta W'$	R_c	ΔW	$\Delta W'$
$^1\Sigma^+$ nonorthogonal									
1	4.33	2.12	2.09	2.31	1.75	1.69	1.57	2.31	27.3
1	6.77	1.08	1.04	14.31	0.234	0.239	28.00	3.12×10^{-2}	3.19×10^{-2}
$^1\Sigma^+$ orthogonal									
1	5.68	1.88	1.55	4.43	3.12	1.64	4.12	0.254	2.82
1	6.67	1.25	1.08	14.50	0.228	0.225	28.16	3.12×10^{-2}	3.12×10^{-2}
2				3.79	1.64	2.17	3.49	1.60	1.59
$^3\Sigma^+$ nonorthogonal									
1	1.96	3.92	1.28	1.84	2.49	4.40			
$^3\Sigma^+$ orthogonal									
1	1.98	4.06	1.30	1.93	2.52	3.94			
2				3.67	0.506	0.786			
2				4.71	0.198	0.343			

TABLE IX: Curve Crossing Positrons R_c (in bohrs) for MgH⁺ States for Both the Nonorthogonal and Orthogonal Diabatic Bases and the Separation (in eV) between Adiabatic Potentials at R_c where ΔW is from Eq 46 or 47 and $\Delta W'$ is Measured from the Calculated Curves

j	$i = 2$			$i = 3$			$i = 4$		
	R_c	ΔW	$\Delta W'$	R_c	ΔW	$\Delta W'$	R_c	ΔW	$\Delta W'$
$^1\Sigma^+$ nonorthogonal									
1				4.10	2.18	1.09	9.99	0.521	0.635
1				5.53	1.60	1.22			
$^1\Sigma^+$ orthogonal									
1				3.56	1.02	0.667	2.20	1.90	2.97
1				5.89	1.42	1.31	9.73	0.626	0.642
$^3\Sigma^+$ nonorthogonal									
1	1.73	18.6	5.71	1.59	4.37	21.7			
$^3\Sigma^+$ orthogonal									
1	1.74	20.4	15.6	1.94	2.08	6.27			
2				2.64	0.374	2.15			

abatic basis while the elements of N_2 will go through a change in sign at these points.

The results of the calculations of the coupling matrices M and N are shown in Figures 15–22 and A3–A6[34] where we have plotted the matrix elements as functions of internuclear distance. We have plotted the elements of the ma-
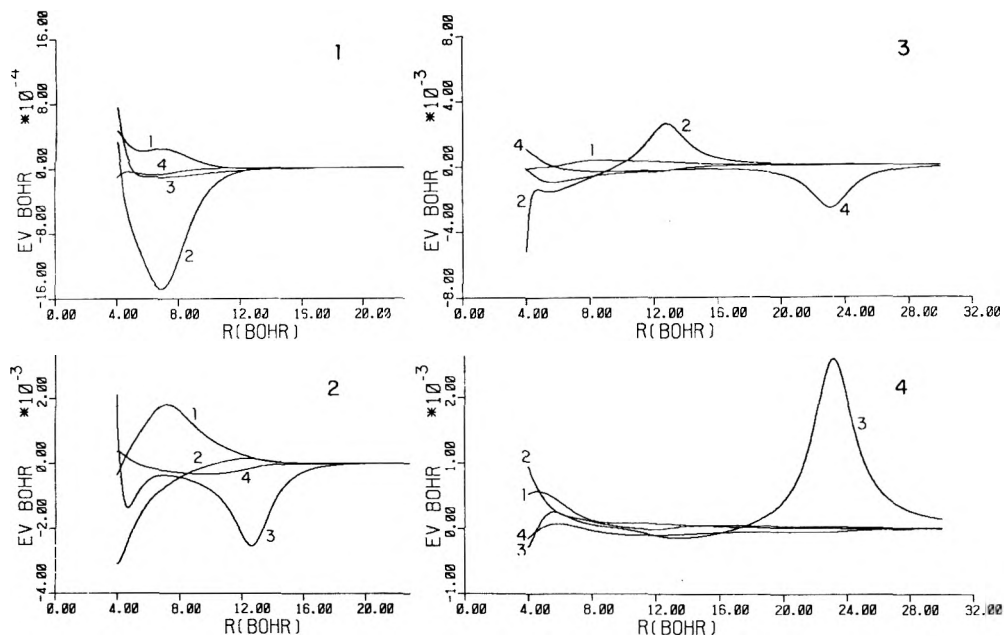
Figure 15. The coupling matrix elements M_{ij} for the $^1\Sigma^+$ states of NaH as functions of internuclear distance R. Each of the four subfigures corresponds to one column j and each curve is labeled by the row index i.
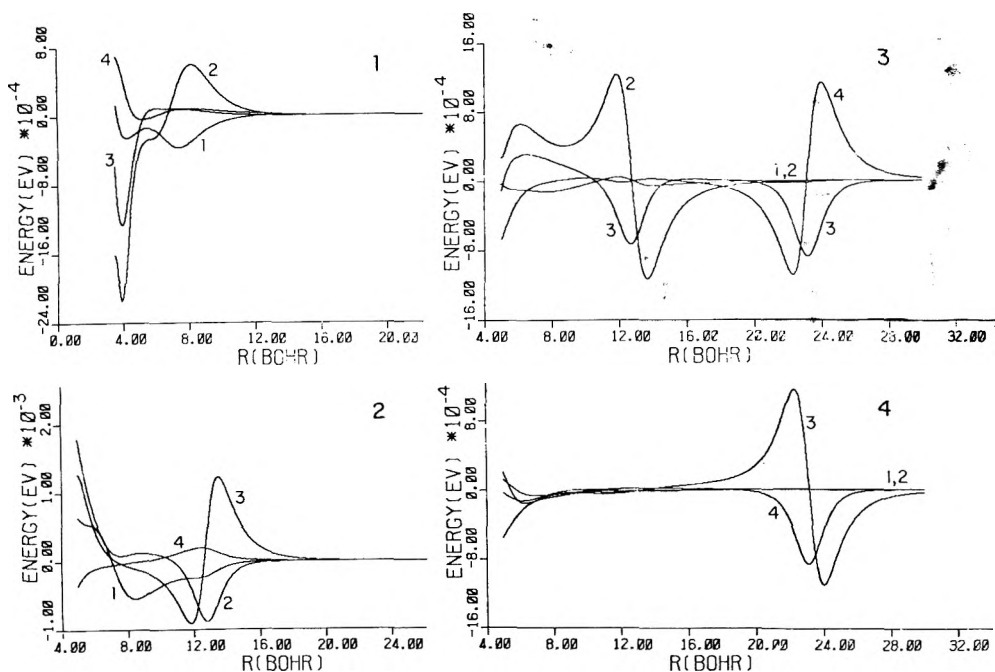
Figure 16. Same as Figure 15 except the coupling matrix elements N_{ij} for the $^1\Sigma^+$ states of NaH are shown.

trices column by column and the number of each curve refers to the component of the column being plotted for that particular curve.

Recalling the ordering convention for the adiabatic states, i.e., lowest energy first at each value of R (see above), we see for example that curve 2 of column 1 is the interaction between the $X^1\Sigma^+$ state and the $A^1\Sigma^+$ state, curve 3 of column 1 is the interaction between $X^1\Sigma^+$ state and the $B^1\Sigma^+$ state, curve 4 of column 1 is the interaction between the $X^1\Sigma^+$ state and the $C^1\Sigma^+$ state, etc.

For the $^1\Sigma^+$ states, it was necessary to make two graphs for each matrix: one for large values of R, in general greater than about 4 a_0, and one for small values of R. The results

for large R are shown in Figures 15–18 and A3 and A4;[34] the results at small R are given in ref 30. For the $^3\Sigma^+$ states the results are shown in Figures 19–22 and A5 and A6.[34]

Comparing the matrix M with the matrix M_2 shows that qualitatively the major contributor to the matrix M is the matrix M_2 and that the matrix M_1 adds only a small amount. However the contributions from M_1 are important.

The elements of the matrix N_1 are in general quite small at large values of R and have significant size only at small R where the matrix $C(R)$ has large derivatives. The product matrix $4\mu M_1 M_2$ is also small and therefore the main contribution to the matrix N comes from the matrix N_2.
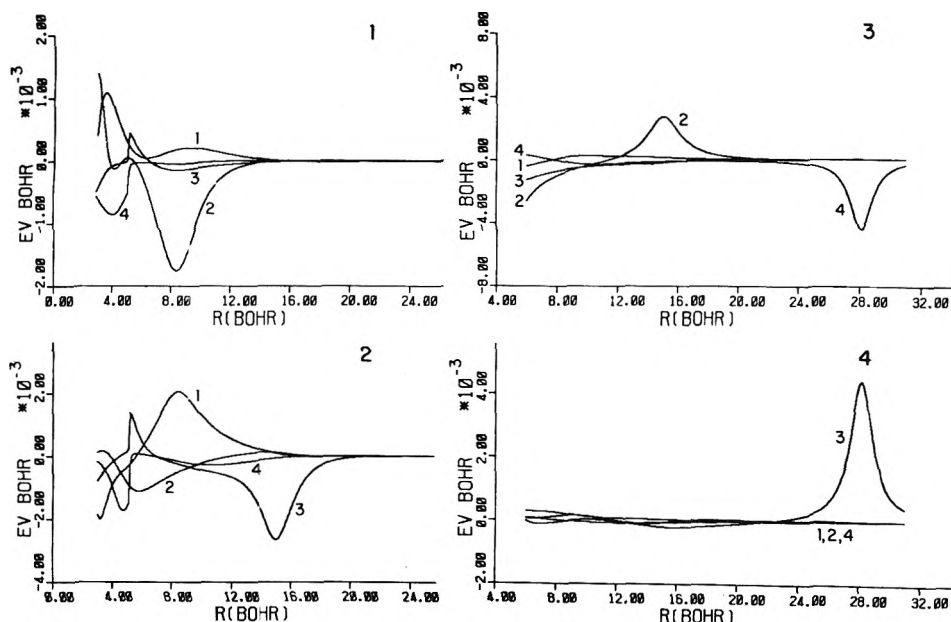
Figure 17. Same as Figure 15 except the coupling matrix elements M_{ij} for the $^1\Sigma^+$ states of KH are shown.
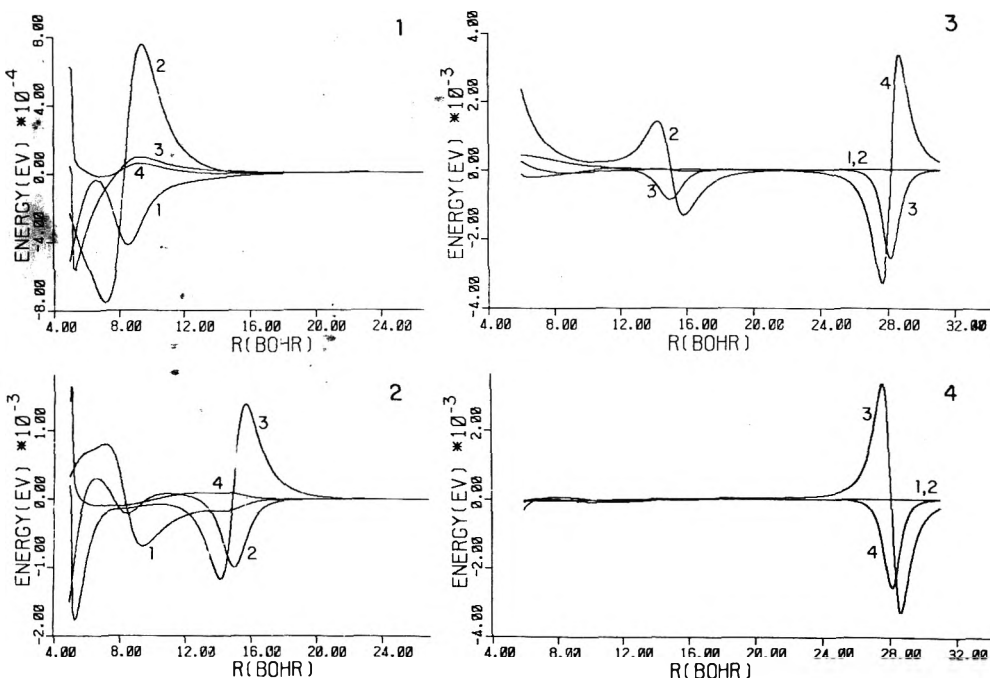
Figure 18. Same as Figure 15 except the coupling matrix elements N_{ij} for the $^1\Sigma^+$ states of KH are shown.

From eq 43 we see that N_2 is related to the derivatives of the matrix U which diagonalizes the matrix H^s so that properties of both the matrix M and the matrix N are mainly related to the diagonalization of H^s rather than to the orthogonalization of the basis functions.

We discuss first the results for the $^1\Sigma^+$ states at large values of R. For the matrix M shown in Figure 15 for NaH, Figure 17 for KH, and Figure A3[34] for MgH$^+$, the most prominent feature is the existence of broad peaks in certain matrix elements. For NaH, the matrix elements M_{21} and M_{12} peak near 7 a_0 and the position of this peak correlates with the change in character of the $X^1\Sigma^+$ wave function which appears as a crossing of elements 1 and 2 of column 1 of the matrix A. The matrix elements M_{32} and M_{23} peak near 13 a_0 and this position correlates with the change in

character of the $A^1\Sigma^+$ wave function which appears as a crossing of elements 1 and 3 of column 2 of the matrix A. The matrix elements M_{43} and M_{34} peak near 23 a_0 and this position correlates with the change in character of the $B^1\Sigma^+$ wave function which appears as a crossing of elements 1 and 4 of column 3 of the matrix A. Similar correlations may be made for KH and MgH$^+$. The same may be done for the triplet states for all three molecules.

The fact that the matrix elements of M which couple different adiabatic electronic states are large over a very wide range of R values raises serious questions concerning the Landau–Zener–Stueckelberg treatment of the curve crossing problem. This model assumes that transitions from one adiabatic curve to another take place only at the positions of avoided crossings and that coupling between these states
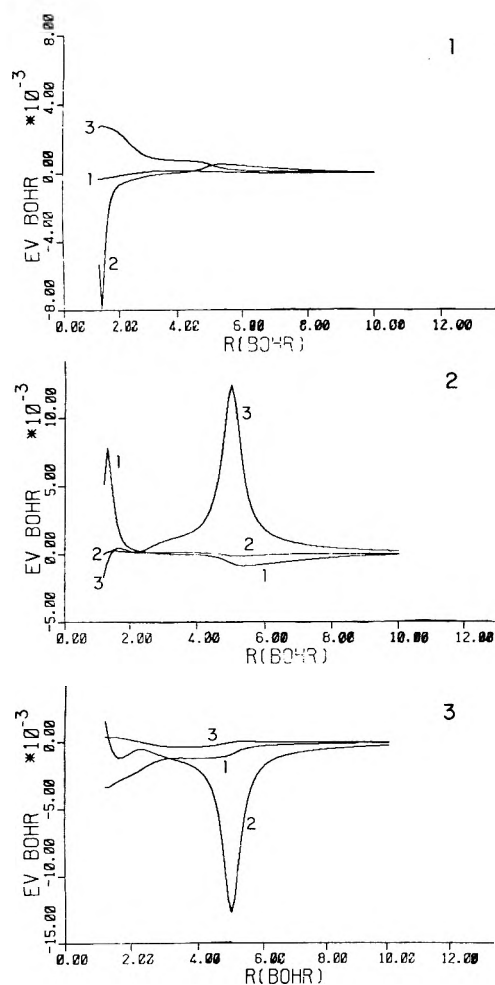
Figure 19. Same as Figure 15 except the coupling matrix elements M_{ij} for the $^3\Sigma^+$ states of NaH are shown.

Figure 20. Same as Figure 15 except the coupling matrix elements N_{ij} for the $^3\Sigma^+$ states of NaH are shown.

at other values of R is negligible. From our results, however, we see that the coupling elements of the matrix **M** are significant over large regions as wide as 10–12 a_0 in some cases.

We may compare the sizes and shapes of our matrix elements for **M** to those calculated by Oppenheimer[43] in the London model[44] for KI for the avoided crossing between ionic and covalent configurations which occurs near $R = 21$ a_0 in that system. Oppenheimer obtains a very sharply peaked coupling matrix element near $R = 21$ a_0 over a region of width about 2 a_0. Dividing through by twice the reduced mass of the KI molecule to convert to the same units as presented here, we find that the peak has a maximum value of about 5.1×10^{-3} eV bohr. We compare this value to our coupling matrix element M_{34} for the avoided crossing near $R = 28$ a_0 for KH which is large over a region of width about 8 a_0 and has a maximum value of about 4.3×10^{-3} eV bohr. Thus the adiabatic states in KI change character over a much smaller range of R values than do those for KH while the size of the coupling matrix is about the same in the two cases.

We turn now to the results for the matrix **N** for the $^1\Sigma^+$ states shown for large values of R in Figure 16 for NaH, in Figure 18 for KH, and in Figure A4[34] for MgH⁺. We note first of all that at the positions where the off-diagonal elements of the matrix **M** go through maxima as described above the corresponding elements of the matrix **N** go

through zero. This relation might have been expected since the matrix **M** is given in terms of the first derivative of the matrix **A** as defined in eq 37 and the matrix **N** is given in terms of the second derivative of the matrix **A** as defined in eq 41.

Another feature of the results is the existence of peaks in the diagonal elements of **N** at the positions of zeroes of corresponding off-diagonal elements. For example, for the $^1\Sigma^+$ state of NaH shown in Figure 16 the elements N_{33} and N_{44} both have peaks at the zeroes of the elements N_{34} and N_{43}. In the adiabatic approximation described by Wolniewicz[45] and Hirschfelder and Meath[6] the diagonal elements of all coupling matrices are added to the potential energy curve $W_k(R)$. From eq 27, 40, and 44 we see that in the adiabatic representation the matrix G^a is given by

$$G^a = A^\dagger G^n A - i4\mu A^\dagger F^n A \cdot M \hat{e}_R - N \qquad (51)$$

From the figures, we see that the peaks in the diagonal elements of **N** are always negative and that therefore these matrix elements will make positive contributions to the adiabatic potential energy curves. These contributions are on the order of 10^{-3} eV for the $^1\Sigma^+$ states.

The coupling matrices for the $^3\Sigma^+$ states are shown for NaH in Figures 19 and 20, for KH in Figures 21 and 22, and for MgH⁺ in Figures A5 and A6.[34] The matrix elements for
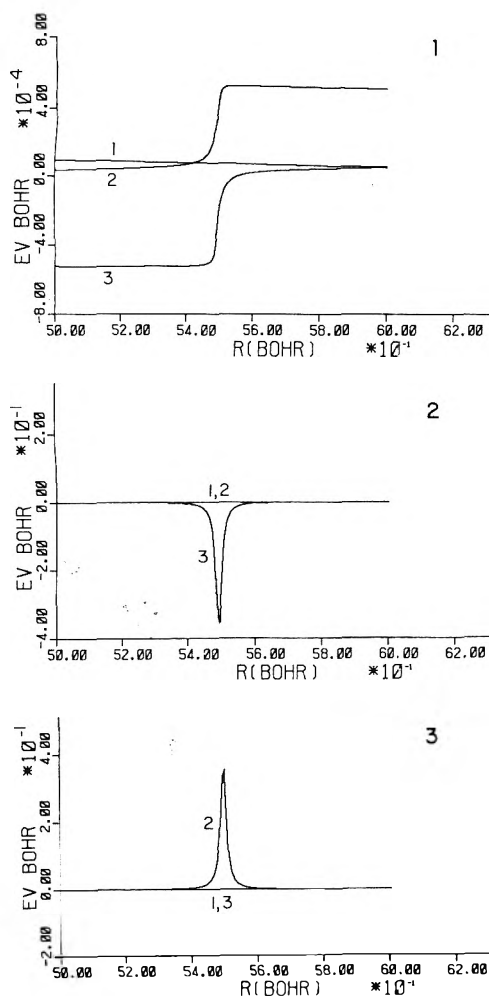
Figure 21. Same as Figure 15 except the coupling matrices M_{ij} for the $^3\Sigma^+$ states of KH are shown.

Figure 22. Same as Figure 15 except the coupling matrices N_{ij} for the $^3\Sigma^+$ states of KH are shown.

NaH and MgH$^+$ are quite similar while those for KH are somewhat different. The differences for KH are due to the rapid change in character of the b$^3\Sigma^+$ and c$^3\Sigma^+$ states in a very narrow region near $R = 5.5 \ a_0$ which we have mentioned above. To show clearly the nature of the matrix elements for KH in this region we have restricted the range of R values included in Figures 21 and 22.

The most prominent feature of the coupling matrices for the $^3\Sigma^+$ states is the existence of peaks in the elements M_{12}, M_{21}, M_{23}, and M_{32} which in turn lead to corresponding variations in the elements of the matrix **N**. We note that the matrix elements M_{23} and M_{32} for NaH are of the same sign and about the same order of magnitude as the corresponding elements for MgH$^+$ and that they extend over a fairly wide range of R values, about 5 a_0 fo. NaH and about 2 a_0 for MgH$^+$. For KH, however, the corresponding elements are of opposite sign, are an order of magnitude larger, and are much narrower, extending over a range of only about 0.1 a_0. We have mentioned above that the change in character of the adiabatic states for KH in this region of R approaches the behavior of a step function and the corresponding coupling matrix elements approach the behavior of a delta function.

Note the very large matrix elements N_{23}, N_{32}, N_{22}, and N_{33} for the KH $^3\Sigma^+$ states shown in Figure 22 near $R = 5.5$ a_0. These matrix elements have magnitudes as large as 20 eV. As discussed above for the $^1\Sigma^+$ states, the diagonal ele-

ments N_{22} and N_{33} are included in the adiabatic effective internuclear potential energy curves in the adiabatic approximation of Wolniewicz and Hirschfelder and Meath. These potential curves would therefore have very narrow positive peaks of height 20 eV near $R = 5.5$ a_0. This approximation gives an upper bound to the true electronic eigenvalues.[6] It is not clear in this case whether the upper bound thus obtained would be a good one.

Evans, Cohen, and Lane[46] have applied the London model[44] to the curve crossing problem for the excited triplet states of He$_2$, and although the crossing in that system is of a different type from the ones considered here, we may compare the coupling matrix elements obtained by those authors with the ones obtained here. Dividing the maximum value of their peak by twice the reduced mass of He$_2$, we find that their matrix element has a maximum value of about 2.0 $\times$ 10^{-3} eV bohr at $R = 3$ a_0 with a width of about 2 a_0. This value may be compared with the M_{32} element for NaH which has a maximum of about 13 $\times$ 10^{-3} eV bohr near $R = 5$ a_0 with a width of about 2 a_0.

At small values of R the matrix elements are much larger and vary more rapidly over very short intervals. However, an accurate treatment of the dynamics at small R may require more complete calculations than the present ones. As mentioned above, our original nonorthogonal valence bond basis set was chosen to describe the physics of the problem

at large values of R and the atomic orbitals are not allowed to adjust as the atoms approach each other. We know that our potential curves are not as accurate at small R as at large R and the behavior of the coupling matrices at small R may therefore be only an artifact of our model. However, the qualitative features of our results do indicate that an accurate treatment of the small R region would be interesting.

The effect of large coupling matrices at small values of R on the cross section obtained in a scattering calculation is not clear until the actual calculations are performed. At thermal energies they will probably not be important since they occur in the region beneath the high repulsive wall of adiabatic potential energy curves. Furthermore, they will contribute only to the lowest partial waves since the centrifugal barrier at higher angular momenta will prevent the atoms from approaching the region where the coupling is large. The coupling matrix elements at large R, however, will provide large contributions to the quenching since the cross section is approximately proportional to the square of the distance at which the transition occurs and thus because many more partial waves will contribute. Therefore, even though the coupling matrices at small R are much larger than those at large R, it is expected that they will not contribute as much to the quenching cross section.

We emphasize at this point that the results presented here are independent of the method of orthogonalization used. For example, suppose we orthogonalize the nonorthogonal diabatic basis by multiplication by the matrix $\mathbf{CX}$ where $\mathbf{X}$ is an arbitrary unitary matrix so that

$$\phi^\circ = \phi^n \mathbf{CX} \tag{52}$$

Equation 52 is consistent with our general form of orthogonalization as discussed above (see eq 22). The Hamiltonian matrix in this representation is given by

$$\mathbf{H}^\circ = \mathbf{X}^\dagger \mathbf{H}^s \mathbf{X} \tag{53}$$

and the adiabatic Hamiltonian matrix is given by

$$\mathbf{H}^a = (\mathbf{X}^\dagger \mathbf{U}^\dagger)^\dagger \mathbf{H}^\circ \mathbf{X}^\dagger \mathbf{U} \tag{54}$$

where the unitary matrix $\mathbf{U}$ is defined by eq 24. Therefore, the unitary matrix which diagonalizes $\mathbf{H}^\circ$ is the product matrix $\mathbf{X}^\dagger \mathbf{U}$ and the matrix $\mathbf{A}^\circ$ which transforms from the nonorthogonal to the adiabatic representation is given by

$$\mathbf{A}^\circ = \mathbf{CXX}^\dagger \mathbf{U} = \mathbf{A} \tag{55}$$

Thus, the transformation $\mathbf{A}$ and hence also its derivatives are independent of the method of orthogonalization. Likewise for the matrix $\mathbf{M}^\circ$ in this representation, we have

$$\mathbf{M}^\circ = \frac{1}{2\mu}(\mathbf{X}^\dagger \mathbf{U})^\dagger (\mathbf{CX})^{-1} \, d\mathbf{A}^\circ/dR = \mathbf{M} \tag{56}$$

so that the matrix $\mathbf{M}$ and by a similar argument the matrix $\mathbf{N}$ are also independent of the method of orthogonalization.

As we have seen, the character of the elements of the matrix $\mathbf{A}$ as functions of R is chiefly determined by the character of the elements of the matrix $\mathbf{U}$. The character of these elements is in turn determined by the positions of the curve crossings of the diagonal elements of the symmetrically orthogonalized diabatic electronic Hamiltonian matrix $\mathbf{H}^s$. Therefore, since the matrix $\mathbf{A}$ is independent of the method of orthogonalization, the positions of the curve crossings in the symmetrically orthogonalized diabatic rep-

resentation are of fundamental importance in determining the nature of the coupling between adiabatic states.

It will be noticed from the figures that the matrix $\mathbf{M}$ is not skew symmetric which may be seen from the fact that the diagonal elements are not zero and the peaks corresponding to transposed elements are shifted slightly with respect to each other and are of different absolute magnitude. However the matrix $\mathbf{M}_2$ is skew symmetric which follows from the fact that the matrix $\mathbf{U}$ is unitary. We have in fact

$$d(\mathbf{U}^\dagger \mathbf{U})/dR = 0 = (d\mathbf{U}^\dagger/dR)\mathbf{U} + \mathbf{U}^\dagger(d\mathbf{U}/dR) \tag{57}$$

so that

$$\mathbf{U}^\dagger(d\mathbf{U}/dR) = -(d\mathbf{U}^\dagger/dR)\mathbf{U} = -(\mathbf{U}^\dagger(d\mathbf{U}/dR))^\dagger \tag{58}$$

and therefore from eq 39 we have

$$\mathbf{M}_2 = -\mathbf{M}_2{}^\dagger \tag{59}$$

We recall from eq 26b and 40 that one of the coupling matrices in the adiabatic representation which appears in the coupled differential equations for the nuclear motion, eq 21, is given by

$$\vec{\mathbf{F}}^a = \mathbf{A}^\dagger \vec{\mathbf{F}}^n \mathbf{A} - i\mathbf{M}\hat{e}_R \tag{60}$$

Since the adiabatic representation is real and orthogonal for the Σ states, the matrix $\vec{\mathbf{F}}^a$ for the Σ states is skew symmetric. Therefore, since $\mathbf{M}_2$ is also skew symmetric, the diagonal elements of the matrix $\mathbf{M}_2$ must be equal to the negatives of the corresponding diagonal elements of the radial component of the matrix $\mathbf{A}^\dagger \vec{\mathbf{F}}^n \mathbf{A}$.

With these results, we see from eq 51 and 60 that the coupling matrices $\vec{\mathbf{F}}^a$ and $\mathbf{G}^a$ in the adiabatic representation are also independent of the method of orthogonalization although of course they do depend on the initial nonorthogonal basis assumed. We recall furthermore that we have not calculated the matrices $\vec{\mathbf{F}}^n$ and $\mathbf{G}^n$ so that we have only obtained a portion of the total coupling matrices, i.e., the part corresponding to the matrices $\mathbf{M}$ and $\mathbf{N}$. We have also noted that the matrix $\mathbf{M}$ is not skew symmetric while the matrix $\vec{\mathbf{F}}^a$ must be skew symmetric. One method of avoiding this problem is to note that the matrix $\vec{\mathbf{F}}^a$ may also be written

$$\vec{\mathbf{F}}^a = \mathbf{U}^\dagger \vec{\mathbf{F}}^s \mathbf{U} - i\mathbf{M}_2 \hat{e}_R \tag{61}$$

We could neglect the first term of eq 61 instead of neglecting the first term of eq 60 and use the skew symmetric matrix $\mathbf{M}_2$ as an approximation for the coupling matrix $\vec{\mathbf{F}}^a$. However, the matrix $\mathbf{M}_2$ is not independent of the method of orthogonalization since for the orthogonalization according to eq 52 we have

$$\mathbf{M}_2{}^\circ = \frac{1}{2\mu}(\mathbf{X}^\dagger \mathbf{U})^\dagger d(\mathbf{X}^\dagger \mathbf{U})/dR \tag{62a}$$

$$= \mathbf{M}_2 + \frac{1}{2\mu}\mathbf{U}^\dagger \mathbf{X}(d\mathbf{X}^\dagger/dR)\mathbf{U} \tag{62b}$$

To avoid this difficulty we suggest the following procedure. We may write the identity

$$\mathbf{M} = \mathbf{M}_3 + \mathbf{M}_4 \tag{63}$$

where $\mathbf{M}_3$ is the skew symmetric matrix

$$\mathbf{M}_3 = \frac{1}{2}(\mathbf{M} - \mathbf{M}^\dagger) \tag{64}$$

and M_4 is the symmetric matrix

$$M_4 = \frac{1}{2}(M + M^\dagger) = \frac{1}{2}(M_1 + M_1^\dagger) \qquad (65)$$

where the contribution of M_2 to the matrix M_4 is cancelled since M_2 is skew symmetric. We may now neglect the matrix M_4 which is small since the matrix elements of M_1 are in general small. Then our approximation for the matrix $\bar{F}^a$ would be the skew symmetric matrix M_3 defined by eq 64 which is independent of the method of orthogonalization since the matrix M is.

Similarly, for the matrix G^a, which must appear as a symmetric matrix in the coupled differential equations for the nuclear motion, we form the identity

$$N = N_3 + N_4 \qquad (66)$$

where

$$N_3 = \frac{1}{2}(N - N^\dagger) \qquad (67)$$

and

$$N_4 = \frac{1}{2}(N + N^\dagger) \qquad (68)$$

and use the symmetric matrix N_4 as an approximation for the matrix G^a.

The above method for approximating the coupling matrices between adiabatic electronic states has the double advantage that the matrices used are independent of the method of orthogonalization and they also contain a contribution from the orthogonalization which generally has been ignored[47] in the literature.

We have of course still not obtained the total coupling between the electronic adiabatic states since we have not calculated the quantities $\bar{F}^n$ and G^n and it is not clear what the relative importance of these matrices will be compared to the matrices M and N. Tully has suggested[48] that "in low energy collision processes of interest to chemists, significant nonadiabatic behavior is invariably associated with a distinct and relatively sudden change of electronic configuration." Such behavior is described entirely by the second term of eq 60 and Tully and Preston have used this argument to justify neglecting the first term of eq 60 in applications.[48,49] It is possible in the case of a complete electronic basis set to define a diabatic basis such that the coupling matrices $\bar{F}^d$ and G^d are identically zero so that all coupling between adiabatic states arises from derivatives of the unitary matrix which diagonalizes the electronic Hamiltonian H^d in that representation. However, such a representation[50] corresponds to electronic functions which are not allowed to vary as functions of the internuclear distance.[30,51,52] It is expected, therefore, that such a representation will give a very poor description of the molecule except in the limit of a very large basis set.

In the work presented here we have chosen a small basis set which is motivated by the physical properties of the molecules being considered and which we feel is large enough to include the properties of interest. Some indication of this is given in the discussion of adiabatic potential curves and bonding. Symmetric orthogonalization was then chosen to preserve this physical meaning in the orthogonal basis. This physical meaning will be important as a guide to making chemically motivated approximations[48,49] in treating the dynamics.

It is surely possible to use another method of orthogonalization such that the matrix $\bar{F}^a$ may be written

$$\bar{F}^a = \bar{F}^d - iM_2{}^d \hat{e}_R \qquad (69)$$

where the matrix $\bar{F}^d$ makes a smaller contribution to the coupling than does the matrix $\bar{F}^s$ in the case of symmetric orthogonalization. The matrix $M_2{}^d$ would then give a better description of the coupling than the matrix M_3 defined in eq 64. However, until the matrix $\bar{F}^n$ is calculated, it is not clear what method of orthogonalization yields the smallest matrix $\bar{F}^d$ nor is it clear how much of the physical meaning is retained in the basis set for other methods of orthogonalization. The matrix $\bar{F}^n$ can be calculated several ways.[53] One easy way is to make a numerical approximation to the derivative of eq 6. Then it reduces to a difference of overlap integrals. Thus if δ is small enough

$$\bar{F}^n(R) \simeq -\frac{i}{2\mu\delta}[\langle \phi^n(R) | \phi^n(R + \delta) \rangle - S]$$

Once the matrix $\bar{F}^n$ has been calculated there is no need for approximation and just as in the treatment proposed here all methods of orthogonalization would be equivalent. We note, however, that the matrix $\bar{F}^n$ does not generally become the matrix of null vectors in the large R limit[54] and new complications arise in the nuclear motion problem which do not arise using the present treatment. Previous workers have suggested some methods for overcoming these difficulties[53-55] and such methods must be considered if the effect of $\bar{F}^n$ on the scattering is not negligible.

Added Note. The large positive corrections to the potential energy curves from the diagonal coupling terms near an avoided crossing (discussed above) are very interesting. A positive diagonal coupling term peaking at about 0.06 eV near an avoided crossing was observed previously for the E,F state of H_2.[56] Andresen and Nielsen observed very large positive coupling terms ("of the order of the potential depth" but with "an extremely narrow range") near an avoided crossing for some other excited states of H_2.[57]

VI. Summary

We have calculated potential energy curves and a major part of the coupling matrix elements in the adiabatic representation and more than one diabatic representation for several singlet and triplet states of NaH, KH, and MgH$^+$. We have discussed these results and compared them to each other and to previous work. For the latter comparison we emphasized the differences in wave functions used. The present calculations illustrate the functional forms of the coupling matrix elements as functions of internuclear distance more clearly than previous work.

Supplementary Material Available. Figures containing matrix elements $H_{ij}{}^a$, M_{ij}, and N_{ij} for the $^1\Sigma^+$ and $^3\Sigma^+$ states of MgH$^+$ as functions of internuclear distance will appear following these pages in the microfilm edition of this volume of the journal. Photocopies of the supplementary material from this paper only or microfiche (105 × 148 mm, 24× reduction, negatives) containing all of the supplementary material for this issue may be obtained from the Business Office, Books and Journal Division, American Chemical Society, 1155 16th St., N.W., Washington, D.C. 20036. Remit check or money order for $4.00 for photocopy or $2.50 for microfiche, referring to code number JPC-75-2745.

References and Notes

(1) (a) This article is based on the Ph.D. thesis of one of the authors (R.W.N.). This work was supported in part by the National Science Foundation. (b) Alfred P. Sloan Research Fellow.

(2) L. Landau, Z. Phys. Sovjet., 2, 46 (1932); C. Zener, Proc. Roy. Soc. London, Ser. A, 137, 696 (1932); E. C. G. Stueckelberg, Helv. Phys. Acta, 5, 369 (1932); W. R. Thorson, J. B. Delos, and S. A. Boorstein, Phys. Rev. A, 4, 1052 (1971); J. B. Delos and W. R. Thorson, Phys. Rev. A, 6, 728 (1972).

(3) D. R. Bates and T. J. M. Boyd, Proc. Phys. Soc. London, Ser. A, 69, 910 (1956).

(4) R. Grice and D. R. Herschbach, Mol. Phys., 27, 159 (1974).

(5) Except where stated otherwise we use hartree atomic units where $m = e = \hbar = a_0 = 1$; the unit of energy is the hartree (1 hartree $= 4.360 \times 10^{-18}$ J $= 27.21$ eV) and the unit of length is the bohr (1 $a_0 = 5.292 \times 10^{-11}$ m). We also use the approximation $\mu_e \simeq m$.

(6) J. O. Hirschfelder and W. J. Meath, Adv. Chem. Phys., 12, 3 (1967).

(7) C. J. Ballhausen and A. E. Hansen, Annu. Rev. Phys. Chem., 23, 15 (1972).

(8) P. O. Lowdin, Adv. Quantum Chem., 5, 185 (1970).

(9) L. R. Kahn and W. A. Goddard, J. Chem. Phys., 56, 2685 (1972).

(10) H. Hellmann, Acta Physicochim. URSS, 1, 913 (1935); H. Hellmann, J. Chem. Phys., 3, 61 (1935).

(11) P. Gombas, Z. Phys., 94, 473 (1935); 118, 164 (1941).

(12) J. D. Weeks, A. Hazi, and S. A. Rice, Adv. Chem. Phys., 16, 283 (1969); J. N. Bardsley, Case Stud. At. Phys., 4, 299 (1974).

(13) D. G. Truhlar, J. Comput. Phys., 10, 123 (1972).

(14) L. Szasz and G. McGinn, J. Chem. Phys., 42, 2363 (1965).

(15) G. A. Hart and P. L. Goodfriend, J. Chem. Phys., 53, 448 (1970).

(16) W. H. E. Schwarz, Theor. Chim. Acta, 11, 377 (1968).

(17) W. H. E. Schwarz, Acta Phys. Acad. Sci. Hung., 27, 391 (1969).

(18) W. H. E. Schwarz, J. Chem. Phys., 54, 1842 (1971).

(19) All experimental atomic energies, except for H⁻, in this article are taken from the standard tables [C. E. Moore, Natl. Bur. Stand. Circ., No. 467 (1949)]. Since we are neglecting spin–orbit coupling, the P state energies are weighted averages of the observed $^2P_{1/2}$ and $^2P_{3/2}$ components. The H⁻ energy is taken from C. L. Pekeris, Phys. Rev., 126, 1470 (1962).

(20) J. C. Philips and L. Kleinman, Phys. Rev., 116, 287 (1959).

(21) L. Szasz and G. McGinn, J. Chem. Phys., 47, 3495 (1967).

(22) J. Callaway and P. Laghos, Phys. Rev., 187, 192 (1969).

(23) H. F. Schaefer, III, "The Electronic Structure of Atoms and Molecules", Addison-Wesley, Reading, Mass., 1972, p 57.

(24) W. A. Goddard, J. Chem. Phys., 48, 1008 (1968).

(25) C. Froese, Can. J. Phys., 41, 1895 (1963).

(26) D. R. Bates and A. Damgaard, Phil. Trans. R. Soc., Ser. A, 242, 101 (1949).

(27) H. F. Schaeffer, III, J. Chem. Phys., 52, 6241 (1970). The authors are grateful to Dr. K. C. Kulander for providing a copy of this program.

(28) A. Dalgarno, Adv. Phys., 11, 281 (1962).

(29) D. W. Marquardt, J. Soc. Ind. Appl. Math., 11, 431 (1963).

(30) R. W. Numrich, Ph.D. Thesis, University of Minnesota, Minneapolis, Minn., 1974.

(31) R. S. Mulliken, Phys. Rev., 50, 1028 (1936).

(32) A. G. Gaydon, "Dissociation Energies", 3rd ed, Chapman and Hall, London, 1968, p 102.

(33) M. E. Pillow, Proc. Phys. Soc. London, Ser. A, 62, 237 (1949).

(34) Figures A1 through A6 will appear following this article in the microfilm edition of this volume of the journal. See paragraph at end of text regarding supplementary material.

(35) T. F. O'Malley, Adv. At. Mol. Phys., 7, 223 (1971).

(36) C. F. Melius, W. A. Goddard, and L. R. Kahn, J. Chem. Phys., 56, 3342 (1972); C. F. Melius and W. A. Goddard, ibid., 56, 3348 (1972).

(37) P. E. Cade and W. M. Huo, J. Chem. Phys., 47, 649 (1967).

(38) L. Szasz and G. McGinn, J. Chem. Phys., 48, 2997 (1968).

(39) T. G. Heil, S. V. O'Neil, and H. F. Schaeffer, III, Chem. Phys. Lett., 5, 253 (1970).

(40) F. E. Harris and H. H. Michels, Int. J. Quantum Chem., Symp., 1, 329 (1967).

(41) E. L. Lewis, L. F. McNamara, and H. H. Michels, Phys. Rev. A, 3, 1939 (1971).

(42) R. E. Olson, F. T. Smith, and E. Bauer, Appl. Opt., 10, 1848 (1971).

(43) M. Oppenheimer, J. Chem. Phys., 57, 3899 (1972).

(44) F. London, Z. Phys., 74, 143 (1932); R. S. Berry, J. Chem. Phys., 27, 1288 (1957).

(45) L. Wolniewicz, J. Chem. Phys., 45, 515 (1966).

(46) S. A. Evans, J. S. Cohen, and N. F. Lane, Phys. Rev. A, 4, 2235 (1971).

(47) M. J. Redmon and D. A. Micha, Int. J. Quantum Chem., Symp., 8, 253 (1974).

(48) J. C. Tully, J. Chem. Phys., 59, 5122 (1973).

(49) R. K. Preston and J. C. Tully, J. Chem. Phys., 54, 4297 (1971); J. C. Tully, ibid., 60, 3042 (1974).

(50) F. T. Smith, Phys. Rev., 179, 111 (1969).

(51) B. Andresen and S. E. Nielsen, Mol. Phys., 21, 523 (1971).

(52) H. Gabriel and K. Taulbjerg, Phys. Rev. A, 10, 741 (1974).

(53) See, e.g., J. C. Browne, Adv. At. Mol. Phys., 7, 47 (1971), and references therein.

(54) See, e.g., D. W. Jepsen and J. O. Hirschfelder, J. Chem. Phys., 32, 1323 (1960); W. R. Thorson, ibid., 42, 3878 (1965); D. R. Bates and D. Sprevak, J. Phys. B, 4, L47 (1971); J. C. Y. Chen, V. H. Ponce, and K. M. Watson, ibid., 6, 965 (1973); V. Sether Raman, W. R. Thorson, and C. F. Lebeda, Phys. Rev. A, 8, 1316 (1973), and references therein.

(55) C. F. Melius and W. A. Goddard, III, Chem. Phys. Lett., 15, 524 (1972).

(56) S. Kolos and L. Wolniewicz, J. Chem. Phys., 50, 3228 (1969); W. Kolos, Adv. Quantum Chem., 5, 99 (1970).

(57) S. E. Nielsen, private communication. See also B. Andresen, Thesis, University of Copenhagen, Copenhagen, 1974, ref 51, and B. Andresen and S. E. Nielsen, Mol. Phys., submitted for publication.

High-Resolution Electron Paramagnetic Resonance Study of Deuteration in Toluene Anion Radical

Suzanne Kowalski, Roger V. Lloyd,[1] and David E. Wood*

Department of Chemistry, University of Connecticut, Storrs, Connecticut 06268   (Received June 13, 1975)

The individual ring proton hfs in ortho and meta monodeuterated toluene anion radical have been resolved by preparation with 2/1 THF/DME solvent and potassium at −90°C. The presence of deuterium does cause relatively large changes in the remaining proton hfs but the assignment of Bolton and Carrington (meta > ortho) is proven correct.

The EPR spectrum of the toluene anion radical was completely analyzed by Bolton and Carrington,[2] who assigned the 5.12-G hyperfine splittings (hfs) to the ortho protons, and the 5.45-G hfs to the meta protons, on the basis of the decrease in the total width of the spectrum upon deutera-

tion at the ortho position. Since it has been found more recently that deuteration has a large perturbing effect upon the hfs of the benzene anion radical[3] because of vibronic interactions,[4] we decided to reinvestigate the spectra of toluene anions deuterated at both the ortho and the meta posi-

tions with sufficient resolution to obtain the individual hfs of the remaining ring protons. Our assignments are shown for 1–3. We estimate the hyperfine splittings (hfs) to be ac-

CH$_3$ 0.77   CH$_3$ 0.78   CH$_3$ 0.82

5.17   5.27 D   5.02   5.37
5.49   5.40 0.78   5.66   0.82
                  5.67
0.48   0.52   0.53   D

1   2   3
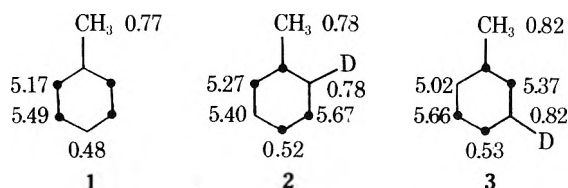
curate to within ±0.02 G. Thus the original assignment of the hfs in 1 was fortuitously correct, because assignment by overall difference using meta deuterated toluene would have given the opposite (incorrect) result.

Monodeuterated toluenes were prepared by the Grignard reaction from the appropriate bromotoluene and D$_2$O, and each contained ~12% nondeuterated toluene. EPR samples were prepared from the reaction at low temperatures of $\simeq 10^{-4}$ M solutions of the toluene in 2/1 THF/DME with a potassium mirror under high vacuum conditions. The second-derivative EPR spectra were fitted by computer simulations with line widths of 0.10 G and which included the presence of the nondeuterated toluene. The parameters obtained are shown above. The spectrum of 3 at −85°C (the highest temperature studied because of line broadening) showed an additional partially resolved splitting of 0.06 G from the potassium counterion. Although this is much smaller than the 0.7-G potassium splitting recently observed in a room-temperature spectrum of 1,[5] it is completely consistent with previous low-temperature studies,[6] and with the positive temperature dependence observed for the cation hfs in the EPR spectra of other ion-pair systems.[7-9] An internally consistent assignment based on making the smallest possible changes in the hfs of both deuterated species simultaneously upon deuteration of 1 would give the parameters as shown. A treatment based on molecular orbital theory and comparison with the results for benzene-1-d leads to the same conclusion. In benzene anion the degeneracy of the symmetric (S) and antisymmet-

ric (A) antibonding orbitals is lifted by the substitution of one deuterium for hydrogen, so that in the benzene-1-d anion radical the A state is slightly more stable than the S state, and one nodal plane of the A state is along the C–D bond.[9,10] If we assume that deuterium has the same effect in the toluene anion we would have the A state stabilized to give increased spin density at the positions shown above (dark circles). This would result in increase methyl and para proton hfs in both deuterated radicals relative to the unsubstituted toluene anion, which is in fact observed. In order to assign the three ring proton splittings in each deuterated radical we used the criteria that the proton hfs will be increased from the value in the nondeutrated radical at positions with dark circles and decreased elsewhere. Both initial assignments in the toluene anion radical were then considered. The only assignments which are consistent for all three radicals are those given above.

In conclusion, this study shows that in systems such as the toluene anion radical where vibronic interactions are important,[10] deuteration can have a profound influence, and the results of such deuteration must be treated with caution.

References and Notes

(1) American Chemical Society, Petroleum Research Fund Postdoctoral Fellow.
(2) J. R. Bolton and A. Carrington, *Mol. Phys.*, **4**, 497 (1961).
(3) R. G. Lawler, J. R. Bolton, G. K. Fraenkel, and T. H. Brown, *J. Am. Chem. Soc.*, **86**, 520 (1964).
(4) D. Purins and M. Karplus, *J. Chem. Phys.*, **62**, 320 (1975).
(5) M. A. Komarynski and S. I. Weissman, *J. Am. Chem. Soc.*, **97**, 1589 (1975).
(6) G. L. Malinoski, Jr., W. H. Bruning, and R. G. Griffin, *J. Am. Chem. Soc.*, **92**, 2665 (1970).
(7) P. Graceffa and T. R. Tuttle, Jr., *J. Chem. Phys.*, **50**, 1908 (1969).
(8) E. de Boer and E. L. Mackor, *J. Am. Chem. Soc.*, **86**, 1513 (1964).
(9) E. de Boer and J. P. Colpa, *J. Phys. Chem.*, **71**, 21 (1967).
(10) A. M. Ihrig, P. R. Jones, I. N. Jung, R. V. Lloyd, J. L. Marshall, and D. E. Wood, *J. Am. Chem. Soc.*, **97**, 4477 (1975), and references therein.

Diffusion in Mixed Solvents. II. The Heat of Mixing Parameter[a]

P. A. Carapellucci[1b]

Jet Propulsion Laboratory, California Institute of Technology, Pasadena, California 91103 *(Received July 24, 1975)*

Publication costs assisted by the Jet Propulsion Laboratory/NASA

Anomalous diffusion properties of iodine and reactants of various chemical reactions in binary solvents are often observed. Correlation of second-order rate constants for many reactions involving electron transfer between organic molecules, solvated electron reactions, iodine diffusion coefficients, and triplet state electron transfer reactions has been made with the heat of mixing parameter (HMP) for the aqueous binary solvent systems. The aqueous binary solvents studied are those containing methanol or ethanol (type I solvent); 1-propanol or *tert*-butyl alcohol (type II solvent); or sucrose or glycerol (type III solvent). A plot of the HMP vs. the diffusion parameter for each reaction yields superimposable curves for these reactions in a particular solvent mixture over the entire solvent mixture range, irrespective of the value of the reaction's rate constant or diffusion coefficient in water. The HMP is either $\Delta H^M/X_1 X_2$ or $(\partial \Delta H^M/\partial n_2)/X_2$, where the subscript 2 refers to water, depending on the relative solubilities of the diffusing species in the components of the solvent system. The diffusion parameter, against which HMP is plotted, is $k\epsilon\eta/(k\epsilon\eta)_w$, where k refers to the second-order rate constant or diffusion coefficient, ϵ the dielectric constant, and η the viscosity; w refers to those values in water. Thermal diffusion is considered important to the explanation of these correlations, and to the theory of diffusion and kinetics in general.

Introduction

In recent years, interest has been revived in mixed solvent interactions. Theoretical models have been proposed and various experimental methods have been used to elucidate the nature of the interactions. Many chemical reactions have been studied in such solvent systems because certain mixtures facilitated the various reactions, some systems are used as viscosity increasing agents to study "diffusion controlled" reactions, and because the area of mixed solvents is a fertile and relatively unexplored field.

Those systems using water as one of the cosolvents have received most of the attention due to the widespread occurrence of such systems in nature and the many anomalies attributed to water structures.[2-6] Anomalous peaks as a function of solvent composition in heats and entropies of activation of fluorescence[2] and Stern–Volmer quenching constants[7] in various aqueous alcoholic solutions have been reported. Similar behavior has also been found for energies, heats, and entropies of activation for chemical reactions in similar solvent mixtures.[4-6]

In a previous communication[8] it was shown that the heat of mixing parameter (HMP), $\Delta H^M/X_1 X_2$, where X_1 and X_2 represent the mole fractions of the components of an aqueous binary solvent, is a way of predicting the solvent composition at which the maxima and minima occur in the enthalpy and entropy of activation values for several reactions and the fluorescence of indole. It was further shown that anomalies in reaction rate constants[9] and diffusion coefficients[9,10] as a function of solvent composition could also be correlated with the HMP.[8] This communication will further support the importance of HMP in diffusion processes involving aqueous solutions and possibly for mixed solvents in general.

Results and Discussion

With respect to the heat of mixing, there are three fundamentally different types of aqueous binary solvents containing alcoholic functional groups. Type I contains those

where ΔH^M is either positive or negative over the total composition range. Type II contains those where ΔH^M is positive over some parts of the composition range, and negative over the remainder. Type III contains those where the alcoholic functional component is polyfunctional or a solid such that the other reacting or diffusing species in solution are insoluble or very slightly soluble in the alcoholic component compared to the aqueous component. Commonly used examples of alcoholic functional components in aqueous binary solvents are: type I, methanol and ethanol;[11] type II, 1-propanol,[11] 2-propanol,[11] and *tert*-butyl alcohol;[12] type III, sucrose and glycerol.[8] Correlations of diffusion data with heat of mixing parameters will be presented for all three types of aqueous solvent systems. For the diffusion systems considered here, the solvent properties of the individual solvent components are similar for types I and II solvent systems. Consequently, the reactants in a diffusion process are likely to see the binary solvent as a "homogeneous continuum" with respect to solubility. For type III, however, preferential solubility will be in the water for the reaction systems to be discussed in this communication.

The complicated physical behavior of aqueous solutions of molecules containing alcoholic functional groups has often been acknowledged.[2] One method of approaching the problem is to attempt to theoretically delineate the interactions at a molecular level. Another approach is to observe the effects of the solvent mixtures on diffusion properties of other molecules in solution and to proceed from there to delineate the molecular level interactions. The approach taken here is the latter. Several chemical reactions studied in aqueous solvent mixtures revealed that their rate constants over the entire solvent composition range could be correlated with thermodynamic properties of the solvent.[8] The heat of mixing rather than the excess free energy or excess entropy was found to correlate with rate constants and diffusion coefficients.[8] These correlations will be extended in the context of solvents of types I, II, and III.

For the following diffusion processes, data will be correlated. The superscript on the reaction number designates the reference of origin of the data.

$$e_{sol}^- + NO_3^- \rightarrow \qquad (1)^9$$

$$e_{sol}^- + C_6H_5NO_2 \rightarrow \qquad (2)^9$$

diffusion coefficient of iodine $\qquad (3)^{10}$

$$CH_3(C_6H_5)CO\cdot^- + (C_6H_5)_2CO \rightarrow CH_3(C_6H_5)CO +$$
$$(C_6H_5)_2CO\cdot^- \quad (4)^{13,14}$$

$$CH_3CHO\cdot^- + (C_6H_5)_2CO \rightarrow CH_3CHO + (C_6H_5)_2CO\cdot^-$$
$$(5)^{13}$$

$$CH_3C(C_6H_5)O\cdot^- + C_6H_5NO_2 \rightarrow CH_3(C_6H_5)CO +$$
$$C_6H_5NO_2\cdot^- \quad (6)^{13}$$

$$CH_3CHO\cdot^- + C_6H_5NO_2 \rightarrow CH_3CHO + C_6H_5NO_2\cdot^-$$
$$(7)^{13}$$
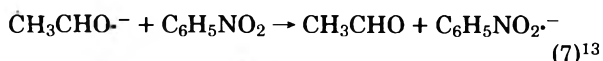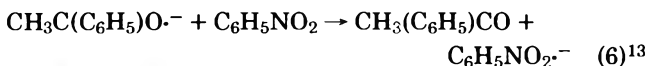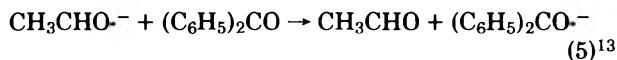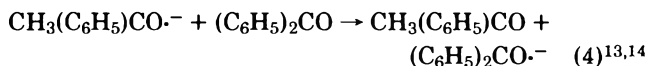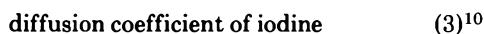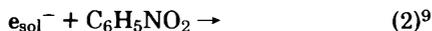
The encounter limited reaction of the triplet state of zinc uroporphyrin

$$T + Fe(CN)_6^{3-} \rightarrow ZnUP\cdot^+ + Fe(CN)_6^{4-} \quad (8)^{8,15}$$
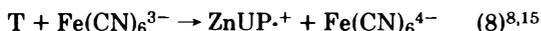
(where T and ZnUP·$^+$ are respectively the triplet state and monocation radical of zinc uroporphyrin).

$$H^+ + (bromocresol\ green)^{2-} \rightarrow (HBG)^- \quad (9)^{16}$$

Type I Solvents. Aqueous ethanol and methanol are the type I solvents used for these reactions. Figures 1 and 2 represent the HMP vs. diffusion parameter $[k\eta\epsilon/(k\eta\epsilon)_w$ or $D\eta\epsilon/(D\eta\epsilon)_w$ where k and D refer to second-order rate constants and diffusion coefficients, respectively, ϵ and η are dielectric constant and viscosity, and subscript w refers to those quantities in water] for reactions 1–7 in aqueous ethanol solutions. Data for all reactions represent solvent compositions from pure water to pure ethanol. According to the original papers from which these data were obtained, the data could not be correlated over the whole solvent composition range. Neither the diffusion parameters nor the rate constants or diffusion coefficients follow the reciprocal viscosity or reciprocal dielectric constant behavior, nor do they follow the Debye diffusion equations for ionic species. Figures 1 and 2 show two important correlations. First, the diffusion parameter can be plotted on *one axis* even though the initial values for the diffusion property in water are quite different for different reactions: for (1) 8.75×10^9 M^{-1} sec^{-1}; (2) 5.84×10^{-5} cm^2 sec^{-1}; (3) 2.25×10^{-5} cm^2 sec^{-1}; (4) 7.45×10^8 M^{-1} sec^{-1}; (5) 1.11×10^9 M^{-1} sec^{-1}; (6) 2.90×10^9 M^{-1} sec^{-1}; (7) 3.30×10^9 M^{-1} sec^{-1}. Second, the HMP intercept when the diffusion parameter is zero is the *same* for all seven diffusion related events; this feature will be discussed later in this communication.

Reaction 4 was also measured in aqueous methanol. It, like aqueous ethanol, has exothermic ΔH^M values at the temperatures used for these studies, 21°C. Figure 3 represents these data.

Type II Solvents. Type II solvents are represented by aqueous 1-propanol. At $t = 21$°C, ΔH^M values are exothermic for alcohol mole fractions $0 < X_1 < 0.41$ and endothermic $0.41 < X_1 < 1$;[11,19] reaction 4 in this solvent system is represented in Figure 4. The three diffusion parameter points with the HMP < 0 are from solutions with $X_1 < 0.41$, while those with HMP > 0 result from $X_1 > 0.41$. *This indicates that the diffusion parameter is decreased in an environment where ΔH^M is endothermic and in-*

creased when ΔH^M is exothermic. This agrees with the conclusion stated[8] for the iodine diffusion coefficient in a series of aqueous and nonaqueous binary solvent systems.

Type III Solvents. Type III solvents pose a special problem, but eventually they may be more simple to handle theoretically than either type I or II. Before the HMP plots for reactions 4, 8, and 9 in type III solvents are displayed, required definitions and a preliminary conceptual model will be presented. This will aid in the understanding of a fundamental difference in the HMP plots for reactions 1–9 between solvent types I and II, and type III.

It was previously mentioned that for type III solvents, preferential solubility of the measured diffusing species (for reactions 1–9) will be in the water. *The usual connotation of a biphasic solvent mixture must not be invoked here. In case of type III, the usual nomenclature of solute for sucrose or glycerol and solvent for water leads to unnecessary complications. It is best that they be considered as components of the aqueous solvent. The additional species whose diffusion properties are measured in the solvent then become the solutes.*

A Model. A very simplified conceptual model is based on the well-known fact that heat is evolved or absorbed when two liquids having substantial intermolecular forces are mixed. It follows then that the motion of a third species would demix the solvent ahead of it only to have the solvent remix in its wake.[8,20] Several factors influence diffusion properties in fluid solutions. There are, of course, energies, heats, and entropies associated with both the demixing and remixing processes. Viscosity is a macroscopic quantity which is indicative of the relative strengths of the solution intermolecular forces once they are formed. The dielectric constant is a measure of polarizability and must be considered since intermolecular interactions affect the charge distribution within the dynamic solvent system. Also, most of the data available are for diffusion processes which involve either charged or highly polarizable species. *The solubility of the diffusing species in the individual solvent components is important. That property can determine the classification of a mixed solvent as type I, II, or III for a particular diffusion process.* Every diffusing species in solution is solvated. The degree of which the first solvation layer has the same composition as the bulk solvent depends primarily on the relative degree to which the diffusing species is soluble in each of the components of the solvent, and on any special cohesive properties of the solvent itself. Diffusion is dynamic. Intersolvent interaction formation is dynamic. It is thus logical that molecular participation in solvation layers of the diffusing species is dynamic also, depending on solubility, cohesive solvent properties, solvent Brownian motion, and local and bulk temperatures.

As the diffusing species moves, the local temperature is higher or lower than the bulk (isothermal) temperature according to exothermicity or endothermicity of the heat of mixing. This local temperature change also causes a local volume change which is related to the volume of mixing. The local temperature change can result in a local solvation of the diffusing species which is different from that existing at "isothermal" conditions. The complicated behavior of solution diffusion phenomena renders more complete definition of this model unwarranted at this time. It is preferred that sufficient data be correlated so that the model can be experimentally and theoretically defined.

HMP Plots in Types I and II Solvents. The most strik-
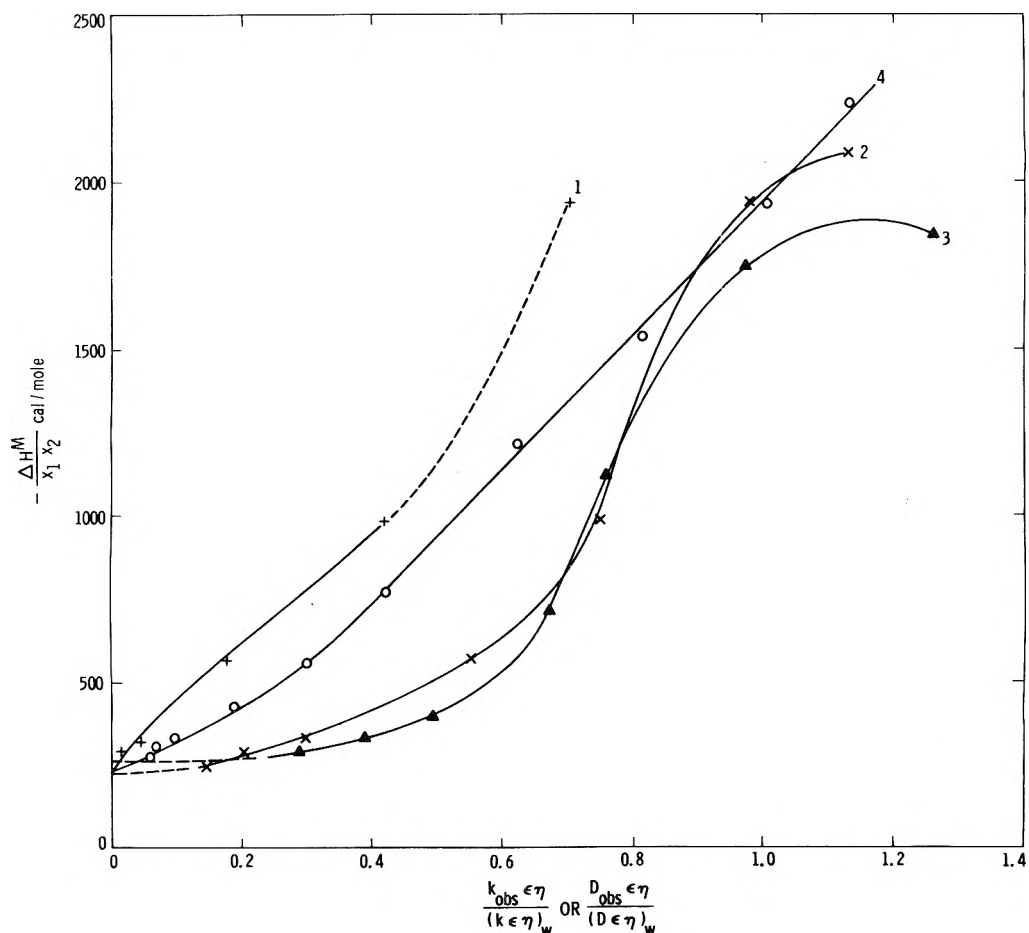
Figure 1. The HMP plot for reactions 1–4 (solvent ethanol–water): reaction 1, rate constants (ref 9), dielectric constants (ref 17, p 161), viscosity (ref 9), HMP (calculated from ref 11), $t = 25°C$; reaction 2, diffusion coefficients (ref 9), rest of data legend is same as for reaction 1; reaction 3, diffusion coefficients of I_2 (ref 10), rest of data legend is same as for reaction 1; reaction 4, rate constants (ref 13 and 14), dielectric constants (calculated from ref 17, p 161 and ref 18, pp 1–49), viscosity (ref 19, Vol. 5, p 21), HMP (calculated from ref 11 and ref 19, Vol. 5, p 159) $t = 21°C$.
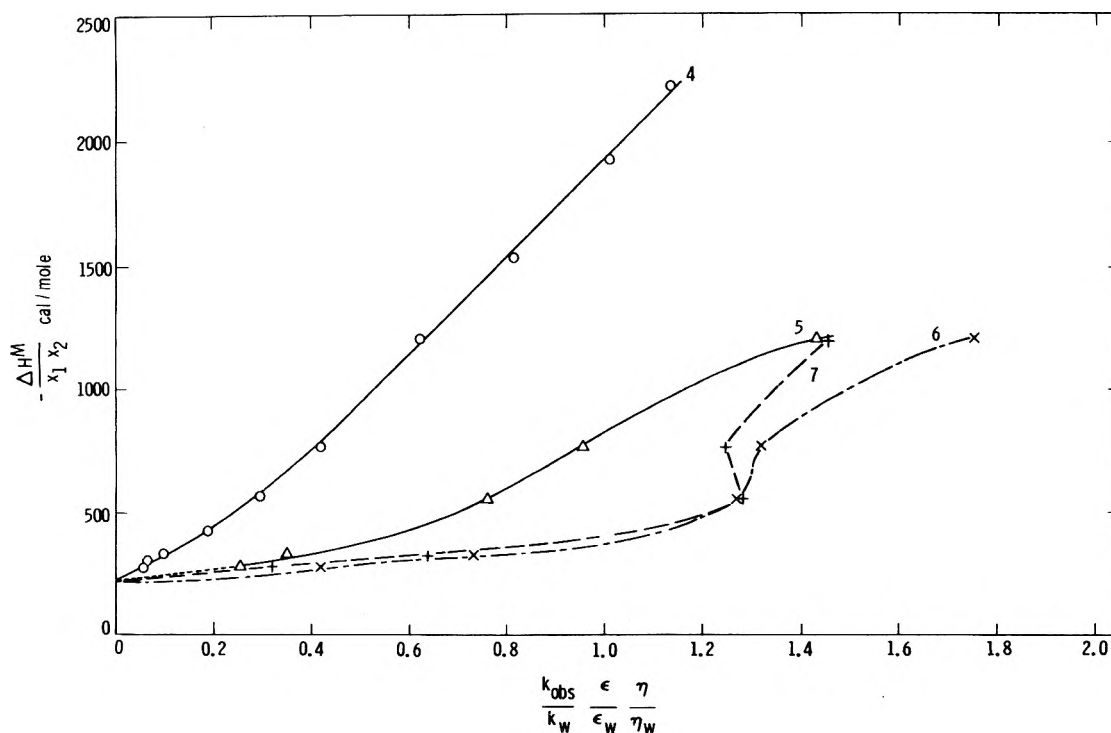
Figure 2. The HMP plot for reactions 4–7 (solvent ethanol–water): reaction 4 (see Figure 1 for data references, the graph is repeated here for comparison purposes); reactions 5–7, rate constants (ref 13), rest of data legend is same as for reaction 4 (Figure 1).
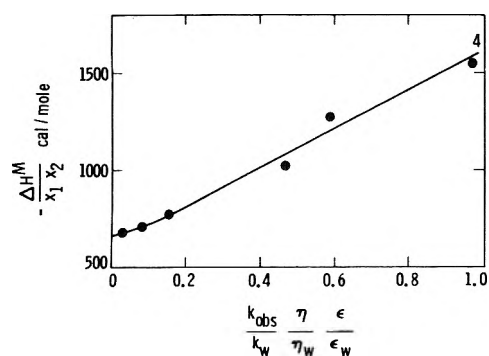
Figure 3. The HMP plot for reaction 4 (solvent methanol–water): rate constants (ref 14), dielectric constant (calculated from ref 18, pp 1–49 and ref 17, p 161), viscosity (calculated from ref 19, Vol. 5, p 22), HMP (calculated from ref 19, Vol. 5, p 159 and ref 11), $t = 21°C$.

Figure 5. A plot of $\partial \Delta H^M / \partial T$ vs. mole fraction of methanol: calculated from ref 19, Vol. 5, p 159 and ref 11, $t = 25°C$. Paucity of data suggests that the data points be smoothed.

Figure 4. The HMP plot for reaction 4 (solvent 1-propanol–water): rate constants (ref 14), dielectric constant (calculated from ref 17, p 161), viscosity (calculated from ref 19, Vol. 5, p 23), HMP (calculated from ref 19, Vol. 5, p 160), $t = 21°C$.

ing common feature about Figures 1–4 is that of the intercept point. For each of the aqueous alcoholic solvents, ethanol (Figures 1 and 2), methanol (Figure 3), and 1-propanol (Figure 4) the HMP plot intercept value is that value for the HMP when $\partial \Delta H^M / \Delta T = 0$, for $0 < X_1 < 1$, at the experimental isothermal temperature. Figure 5 represents $\partial \Delta H^M / \partial T$ vs. mole fraction of methanol. A diffusion parameter of zero is a limiting condition in solution. A direct interpretation is that local temperature changes are required for diffusion to occur, thereby supporting the view that thermal diffusion[20,21] and "ordinary diffusion" cannot be treated as separate subjects.[8]

The shapes of the HMP plots vary from linear to S-shaped to nonmonotonic behavior (Figures 1–4). Many variables can determine the shape of this plot: the obvious ones are (1) encounter vs. nonencounter limited reactions, (2) relative solubilities and activities of the diffusing species in the components of the solvent at various X_1, and (3) the effect of local temperature changes on item 2.

HMP Plots in Type III Solvents. Type III solvents are those in which the diffusing species are primarily soluble in only one of the solvent components. Examples considered here are aqueous sucrose and glycerol. Aqueous sucrose is a more suitable example and was used[8] to illustrate that for these solvents, the HMP is expressed as $(\partial \Delta H^M / \partial n_2)/X_2$;
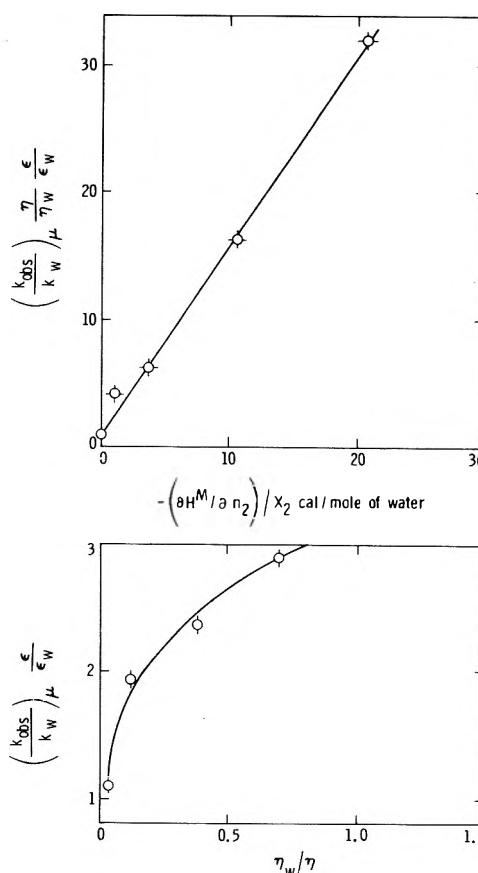
Figure 6. (Upper) The HMP plot for reaction 8 (solvents sucrose–water) (ref 8), dielectric constant (ref 17, p 161), viscosity (ref 22, p j-248), HMP (calculated from ref 23), $t = 25 \pm 1°C$. (Lower) The reciprocal viscosity plot of rate constants for reaction 8.

Figure 6 illustrates reaction 8. Figure 7 illustrates HMP plots for reactions 4 and 9 in aqueous glycerol solutions for $0 \le X_1 \le 0.50$. The same basic model applies for all three types of solvents. Type III, however, in its extreme case is simpler. Since the diffusing species are only soluble in the water, the partial molal function is that which is important. Figure 6 shows that the HMP plot in aqueous sucrose for the encounter limited reaction 8[15] is linear.[8] Figure 7 shows that similar plots in aqueous glycerol for reactions 4 and 9 are superimposible but S-shaped. Here as in types I and II solvents the HMP plots show the same noteworthy fea-
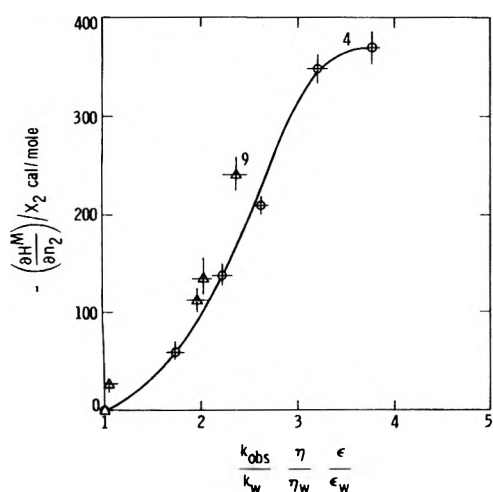
Figure 7. The HMP plot for reactions 4 and 9 (solvent glycerol–water): Reaction 4 (circles), rate constants (ref 14), dielectric constants (calculated from ref 24, p 318), viscosity (calculated from ref 24, p 279, HMP (calculated from ref 19, Vol. 5, p 157), $t = 21°C$; reaction 9 (triangles), rate constants (ref 16), dielectric constants and viscosity from above references, HMP (calculated from ref 19, Vol. 5, p 157), $t = 25°C$.

Figure 8. The reciprocal viscosity plot of the rate constants for reactions 4 and 9 (solvent glycerol–water): reaction 4, circles; reaction 9, triangles. See legend of Figure 7.

tures. Even though the reaction rates in water for (4), 7.45 $\times 10^8 M^{-1}$ sec^{-1}, and (9), 5.77 $\times 10^{10} M^{-1}$ sec^{-1}, are different by orders of magnitude, the HMP plots are superimposable. Reciprocal viscosity plots of the rate constants in aqueous glycerol (Figure 8) and aqueous sucrose (Figure 6 lower) are nonlinear, further illustrating a previous argument that the linearity or nonlinearity of such plots does not constitute a necessary and sufficient condition for the classification of encounter limited reactions.[8]

General Discussion. One of the primary interests in this work is the development of an understanding of the methods by which solvents influence diffusion phenomena and reaction rates. The approach here has been to use systems where the solvents were not an integrated part of the reaction. Moderate successes with the correlations of HMP and the diffusion parameter are indicated. Correlations of reaction rates and thermodynamic quantities have been done before.[25,26] Other attempts to explain reaction rates in mixed solvents for complicated reactions have also involved partial molal quantities of thermodynamic functions.[27] The maxima in the enthalpy and entropy of activation of the fluorescence of indole in aqueous alcohol solvents coincides with the maxima in the $\Delta H^M/X_1X_2$ function vs. X_1.[2] The maxima and minima in the activation parameters for several reactions,[4–7] including reactions 4–7, exhibit extrema at low X_1 also.[13] It is possible that the activation parameters reflect a temperature change in the HMP and is not in the first approximation a property of the reaction being studied. It is recognized that the quantities called the HMP, $\Delta H^M/X_1X_2$ and $\partial\Delta H^M/\partial n_2/X_2$, are not mathematically identical. It is further recognized that the solvation of the reacting species is different in the two solvent types. The observation that the diffusion parameter approaches zero at the composition where $\partial\Delta H^M/\partial T = 0$ for the aqueous methanol, ethanol, and 1-propanol solvents is noteworthy since the behavior of the heat of mixing is different for these solvents. The Stern–Volmer constants for the quenching of anthracene fluorescence by bromide ion in aqueous *tert*-butyl alcohol at 26°C[7] was also found to similarly correlate with a type II HMP plot. This whole correlation is based on a comparison with diffusion con-

stants in water, consequently the correlations are not directly applicable to pure solvent values. Work in progress and also a literature survey of rate constants for diffusion processes in pure solvents appear to indicate a dependence on solvent thermal conductivity, a thermal process.
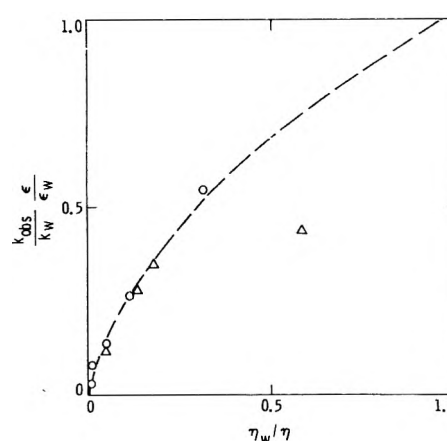
Experimental Section

The rate constant data for the oxidation of the triplet state of zinc uroporphyrin (reaction 8) was obtained using a low-intensity repetitive flash photolysis apparatus. The photomultiplier output was computer averaged with a Fabritek 1072 averager. The apparatus was similar to that already described;[15] the analytical monochromator, however, had a 2-Å band pass.

References and Notes

(1) (a) Presented in part at the Fifth International Congress of Radiation Research, July, 1974, Seattle, Wash. This paper presents the results of one phase of research carried out at the Jet Propulsion Laboratory, California Institute of Technology, under Contract No. NAS 7-100, sponsored by NASA. (b) NAS–NRC Senior Resident Research Associate 1973–1975 at the Jet Propulsion Laboratory.
(2) R. Lumry and S. Rajender, *Biopolymers*, **9**, 1125 (1970).
(3) T. Matsui, L. G. Hepler, and E. M. Woolley, *Can. J. Chem.*, **52**, 1910 (1974).
(4) J. G. Martin and R. E. Robertson, *J. Am. Chem. Soc.*, **88**, 5353 (1966).
(5) J. F. G. Engbersen and J. B. F. N. Engberts, *J. Am. Chem. Soc.*, **96**, 1231 (1974).
(6) L. Menninga and J. B. F. N. Engberts, *J. Phys. Chem.*, **77**, 1271 (1973).
(7) C. A. G. Brooks, K. M. C. Davis, and M. J. Blandamer, *J. Solution Chem.*, **3**, 247 (1974).
(8) P. A. Carapellucci, *J. Am. Chem. Soc.*, **97**, 1278 (1975).
(9) F. Barat, L. Gilles, B. Hickel, and B. Lesigne, *J. Phys. Chem.*, **77**, 1711 (1973).
(10) K. Nakanishi and T. Ozasa, *J. Phys. Chem.*, **74**, 2956 (1970).
(11) R. F. Lama and B. C. Y. Lu, *J. Chem. Eng. Data.*, **10**, 216 (1965).
(12) J. Kenttamaa, E. Tommila, and M. Martti, *Ann. Acad. Sci. Fenn., Ser. A2*, **93**, 3 (1959).
(13) O. I. Micic and B. Cercek, *J. Phys. Chem.*, **78**, 285 (1974).
(14) B. Cercek, private communication.
(15) P. A. Carapellucci and D. Mauzerall, *Ann. N.Y. Acad. Sci.*, **244**, 214 (1975).
(16) P. Warrick, Jr., J. J. Auborn, and E. M. Eyring, *J. Phys. Chem.*, **76**, 1184 (1972).
(17) H. S. Harned and B. B. Owen, "The Physical Chemistry of Electrolytic Solutions", 3rd ed, Reinhold, New York, N.Y., 1958.
(18) L. Meites, Ed., "Handbook of Analytical Chemistry", 1st ed, McGraw-Hill, New York, N.Y., 1963.
(19) "International Critical Tables", McGraw-Hill, New York, N.Y., 1929.
(20) J. N. Agar, *Adv. Electrochem. Electrochem. Eng.*, **3**, 31 (1963).
(21) H. J. V. Tyrrell, "Diffusion and Heat Flow in Liquids", Butterworths, London, 1961.
(22) H. A. Sober, Ed., "Handbook of Biochemistry", Chemical Rubber Co., Cleveland, Ohio, 1968.

(23) J. B. Taylor and J. S. Rowlinson, *Trans. Faraday Soc.*, **51**, 183 (1955).
(24) C. S. Miner and N. N. Dalton, Ed., "Glycerol", Reinhold, New York, N.Y., 1953.
(25) E. M. Arnett, "Physico-Chemical Processes in Mixed Aqueous Solvents," F. Franks, Ed., Heineman Educational Books, London, 1967, p

105.
(26) E. Grunwald and A. Effio, *J. Am. Chem. Soc.*, **96**, 423 (1974).
(27) T. F. Fagley, G. A. Von Bodungen, J. J. Rathmell, and J. D. Hutchinson, *J. Phys. Chem.*, **71**, 1374 (1967); T. F. Fagley, J. S. Bullock, and D. W. Dycus, *ibid.*, **74**, 1840 (1970).

Formation of Radical Cations of Methoxylated Benzenes by Reaction with OH Radicals, Tl^{2+}, Ag^{2+}, and $SO_4 \cdot^-$ in Aqueous Solution. An Optical and Conductometric Pulse Radiolysis and in situ Radiolysis Electron Spin Resonance Study

P. O'Neill, S. Steenken,* and D. Schulte-Frohlinde

Institut für Strahlenchemie im Max-Planck-Institut für Kohlenforschung, D-433 Mülheim a.d. Ruhr, Germany (Received June 16, 1975)

The reactions of anisole, 1,2-, 1,3-, and 1,4-dimethoxybenzene and 1,2,3-, 1,2,4-, and 1,3,5-trimethoxybenzene with Tl^{2+}, Ag^{2+}, $SO_4 \cdot^-$, and OH, respectively, were investigated in aqueous solution using optical and conductometric pulse radiolysis and in situ radiolysis ESR for detection. Tl^{2+} and Ag^{2+} were produced by reaction of OH with Tl^+ and Ag^+, respectively. $SO_4 \cdot^-$ was generated by reaction of e_{aq}^- with persulfate. Tl^{2+}, Ag^{2+}, and $SO_4 \cdot^-$ react with the methoxylated benzenes by electron transfer to yield radical cations and Tl^+, Ag^+, and SO_4^{2-}, respectively. In the absence of cyclohexadienyl radicals the radical cations decay by second-order kinetics with rate constants ranging from $<4 \times 10^3$ to $1 \times 10^9 M^{-1} sec^{-1}$ depending on the positions of the methoxy groups relative to each other. OH radicals react with the methoxylated benzenes by addition to the aromatic ring with diffusion-controlled rates. Depending on conditions, the hydroxycyclohexadienyl radicals thus formed subsequently undergo three different types of reaction: (a) bimolecular decay (k values ranging from 8×10^8 to $2 \times 10^9 M^{-1} sec^{-1}$); (b) reaction with protons to yield radical cations (k values from 2×10^8 to $1.4 \times 10^9 M^{-1} sec^{-1}$); and (c) reaction with radical cations (k values from 8.6×10^8 to $3.5 \times 10^9 M^{-1} sec^{-1}$). The assignment of the optical absorption spectra of the radical cations and the determination of the respective extinction coefficients is based on a combination of optical and conductivity data. The radical cation yield obtained at pH 1 by reaction of protons with the OH adducts of the substrates amounts to >90% in the case of anisole, 1,3-dimethoxybenzene, and 1,3,5-trimethoxybenzene.

Introduction

One-electron oxidation of benzene derivatives to yield radical cations has been accomplished in nonaqueous systems[1] using electrolytic methods,[2] oxidation in strong acids,[1,3-6] reaction with metal ions,[7,8] and in aqueous solution in the presence of metal ions using radiolytic procedures.[9] Radical cations have also been postulated[10-15] as intermediates in reactions involving the sulfate radical anion, $SO_4 \cdot^-$. Very recently, from product studies[14,16] and a pulse radiolysis investigation[17] of reactions of OH radicals with aromatics, data were presented indicating that radical cations may also be important in aromatic hydroxylation. As yet, however, no direct proof for the intermediate existence of radical cations in OH reactions with aromatics has been presented and the mechanism of their formation is still controversial. Hamilton[14] suggested a direct electron transfer from the aromatic to the OH radical,[18] however, other workers[16,17] favor addition of the OH radical to the ring followed by an acid-catalyzed dehydration step. The concept of formation of hydroxycyclohexadienyl radicals by OH addition to the ring is in agreement with data obtained by pulse radiolysis[19] and ESR.[20,21]

This paper describes the reactions of OH radicals with anisole, 1,2-, 1,3-, and 1,4-dimethoxybenzene (DMB) and 1,2,3-, 1,2,4-, and 1,3,5-trimethoxybenzene (TMB) and the subsequent reactions of the intermediates. The above compounds were thought to be particularly suitable for investigating the mechanism of radical cation formation because of the expected stabilizing effect of electron-donating groups on radical cations. Since Tl^{2+}, Ag^{2+}, and $SO_4 \cdot^-$ have been shown[9] to mediate in the production of radical cations, the reactions of the former species with the substrates were also investigated in order to provide supplementary information.

Experimental Section

1,4-Dimethoxybenzene (Merck) was recrystallized twice from methanol prior to use. 1,2- and 1,3-dimethoxybenzene (Fluka) were fractionally distilled under an atmosphere of nitrogen. Anisole (Merck), 1,2,3- (Fluka), 1,2,4- (Merck), and 1,3,5- (Fluka) trimethoxybenzene, thallium(I) sulfate (Merck), silver nitrate (Merck), and potassium persulfate (Merck) were of the highest purity available and were used without further purification. In the pulse radiolysis experi-

ments the water used was triply distilled under nitrogen, from alkaline permanganate, from acid dichromate, and finally from a quartz vessel.

The 3-MeV van de Graaff accelerator and the ancillaries used for optical and conductivity measurements have previously been described.[22,23] With the conductivity detection system, measurements were limited to $3.8 < pH < 11$. Solutions were irradiated at $20 \pm 2°C$ with electron pulses of 1-μsec duration. The pH of the solutions was adjusted using perchloric acid. Dosimetry was carried out using the modified Fricke solution (10^{-2} M ferrous sulfate in 0.8 N sulfuric acid). Doses were in the range 0.5–1 krad. The optical density values used to plot the spectra have all been normalized to 3 krads and refer to a 1-cm path length.

The in situ radiolysis ESR experiments were performed at ~5°C using the method described by Eiben and Fessenden.[24] Magnetic field measurements were made with a field-tracking NMR unit and frequency counter. The g factors were determined from simultaneous measurements of field and microwave frequency taking account of the magnetic field difference between the ESR cell and NMR probe positions. The coupling constants and g factors are estimated to be accurate to 50 mG and 2×10^{-5}, respectively.

Results and Discussion

I. Formation of Radical Cations by Tl^{2+}, Ag^{2+}, and $SO_4{}^-$. On pulse irradiation of 10^{-3} M Tl_2SO_4 solutions saturated with N_2O at pH 4 and containing 10^{-4} M of anisole, 1,2-, 1,3-, or 1,4-dimethoxybenzene (DMB), or 1,2,3-, 1,2,4-, or 1,3,5-trimethoxybenzene (TMB), respectively, transient absorptions were observed at $\lambda > 400$ nm which were not present in the absence of the aromatics and which were different from the transients observed on OH attack on the aromatics in the absence of Tl^+. Under the experimental conditions the OH radicals formed during the electron pulse preferentially react with Tl^+ to yield[25,26] Tl^{2+} ($k = 10^{10}$ M^{-1} sec^{-1}). The decay of the absorption of Tl^{2+} was found to parallel the formation of the transients at $\lambda > 400$ nm.

In the case of 1,4-DMB, the absorption spectrum of the transient formed by reaction with Tl^{2+} is very similar to that previously assigned to the radical cation in concentrated sulfuric acid[6,27] or in acetonitrile.[28] Using the in situ radiolysis ESR method,[24] spectra were obtained from 1,4-DMB solutions that were assigned[9] to the cis and trans isomers of the radical cation of 1,4-DMB, the trans/cis ratio being 1.12:1 at 5°C. This assignment is confirmed by the fact that the coupling constants and g factors of the isomers are almost identical with those measured in concentrated sulfuric acid[6] or aluminum chloride–nitromethane solvent.[29]

ESR spectra were also obtained by in-situ irradiation of N_2O-saturated 10^{-3} M Tl_2SO_4 solutions containing 10^{-4} M of the substrates listed in Table I. In the case of 1,3,5-TMB only very weak lines were observed that could not be unambiguously assigned. The spectrum observed from 1,2,4-TMB could not be fully analyzed due to strong overlap of lines from isomeric species. However, on the basis of the apparent g factor of the spectrum it may be assigned to the radical cation of 1,2,4-TMB. With the remaining substances the ESR spectra could be identified consistently as due to the radical cations of the respective substrates. In contrast to the case of 1,4-DMB, the spectra obtained from 1,2- and 1,3-DMB and from 1,2,3-TMB showed no evidence

for the existence of more than one isomer. In the case of 1,4-DMB, the assignment of the coupling constants to specific ring positions is based on MO calculations.[6] For 1,2- and 1,3-DMB, the assignment of the coupling constants to ring protons is based on a comparison with the coupling constants of radical cations from isomeric dimethoxybenzoic acids. This is possible since substitution of a ring proton by a carboxyl group exerts only a small influence on the coupling constants of the remaining protons.[30] The ESR spectrum of the radical cation of 1,2-DMB is shown in Figure 1.

The spectrum of the species formed from anisole by reaction with Tl^{2+} is characterized by three equivalent and five nonequivalent protons. Since attempts to produce the radical cation of anisole in the system nitromethane–boron trifluoride resulted in the production of the radical cation of 4,4'-dimethoxybiphenyl,[5] the possibility that the species observed might be dimeric should be considered. The radical cation of 4,4'-dimethoxybiphenyl can be excluded on the basis of a comparison of the experimentally observed coupling constants with those previously measured[5] for this species. A cyclohexadienyl radical, formed by reaction of an anisole radical cation with anisole
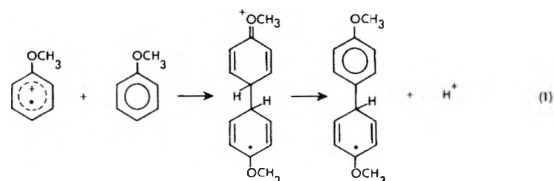
can be ruled out since cyclohexadienyl radicals of this type are characterized[31] by methylene proton couplings larger than 30 G and by equivalent meta protons, provided the cyclohexadienyl part of the molecule is symmetric. It is therefore suggested that the experimentally observed species is the monomeric radical cation, the nonequivalence of the ortho and meta protons, respectively, being caused by hindered rotation of the benzene ring about the C–O bond, due to considerable C–O double bond character. The g factor is in agreement with this assignment. Supporting evidence is derived from the observation by pulse radiolysis that the absorption spectrum and the formation kinetics of the transient from anisole are independent of anisole concentration.

On the basis of the observations obtained from ESR, the absorptions measured optically at $\lambda > 400$ nm are assigned to the radical cations of the substrates. The reactions occurring in the Tl^+ system at pH 4 may thus be formulated as shown in eq 2 and 3. Thus Tl^+ mediates as a catalyst in

$$Tl^+ + OH \rightarrow Tl^{2+} + OH^- \qquad (2)$$

$$Tl^{2+} + \text{substrate} \rightarrow Tl^+ + [\text{substrate}]\cdot^+ \qquad (3)$$
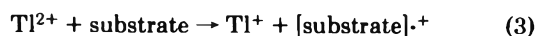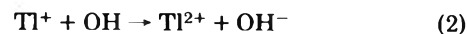
the electron transfer between the substrates and OH radicals. Tl^{2+} can be replaced by Ag^{2+} (Table II) produced[32,33] by oxidation of Ag^+ by the OH radical.

The decay rates of the radical cations were measured at $\lambda > 400$ nm in the Tl^+ system at pH 4. The radical cations were found to decay by second-order kinetics. The rate constants and the spectral characteristics are presented in Table II. The radical cations of anisole, 1,3-DMB, and 1,3,5-TMB decay with considerably faster rates than those of 1,2- and 1,4-DMB and 1,2,3- and 1,2,4-TMB. In agreement with these kinetic results, the stationary concentration of the radical cations of anisole and 1,3-DMB was

TABLE I: Coupling Constants (in Gauss) and g Factors of Radical Cations

Structure	Methyl protons				Ring protons					g	Notes
	$a_1{}^a$	a_2	a_3	a_4	a_2	a_3	a_4	a_5	a_6		
	4.83 (3)				4.52	0.21	9.97	1.00	5.51	2.00351	b
	3.33 (3)	3.33 (3)			0.16	4.89	4.89	0.16		2.00374	
	2.95 (3)		2.95 (3)		<0.05		10.53	2.10	10.53	2.00354	
	3.41 (3)			3.41 (3)	1.59	2.92		1.59	2.92	2.00388	
	3.45 (3)			3.45 (3)	1.49	2.99		1.49	2.99	2.00365	In conc H_2SO_4 (ref 6)
	3.24 (3)			3.24 (3)	2.61	2.61		1.88	1.88	2.00388	
	3.33 (3)			3.33 (3)	2.68	2.68		1.81	1.81	2.00365	In conc H_2SO_4 (ref 6)
	2.03 (3)	5.16 (3)	2.03 (3)				0.47	6.26	0.47	2.00398	

a Indexes refer to ring positions. b The assignment of the coupling constants to individual ortho and meta protons, respectively, is as yet arbitrary.
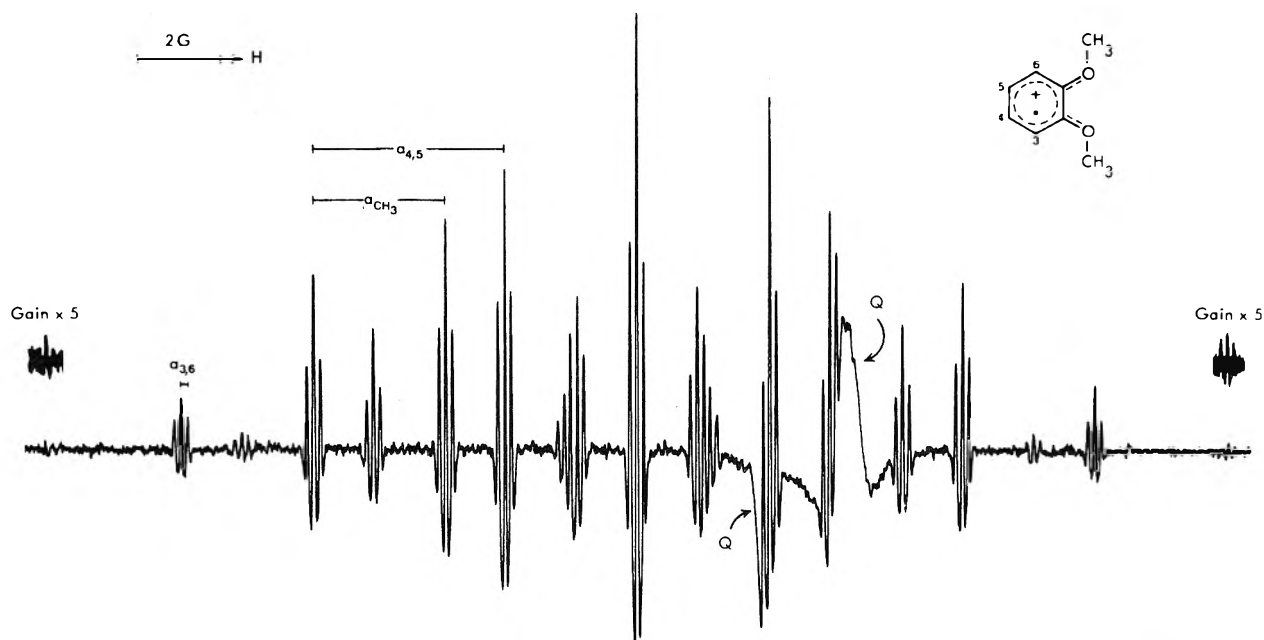
Figure 1. Second-derivative ESR spectrum obtained on radiolysis of a N_2O saturated 10^{-3} M Tl_2SO_4 solution containing 10^{-4} M 1,2-DMB at pH 3 and about 5°C. The indexes of the coupling parameters "a" refer to ring positions. Q designates the quartz signal.

found by ESR to be considerably lower than that of 1,2- and 1,4-DMB and 1,2,3- and 1,2,4-DMB, respectively. The difference in the lifetimes between anisole and 1,3-DMB and 1,3,5-TMB on the one hand and 1,2- and 1,4-DMB and

1,2,3- and 1,2,4-TMB on the other probably reflects differences in thermodynamic stability of the radical cations. Such differences can be predicted on the basis of elementary MO considerations. The low signal-to-noise ratio ob-

TABLE II: Spectral Characteristics and Rate Constants^a for Formation and Decay of Radical Cations

Substrate	Radical cation		$k(\mathrm{Tl^{2+}}$ + substrate), M^{-1} sec^{-1}	$k(\mathrm{SO_4}^{\cdot-}$ + substrate), M^{-1} sec^{-1}	$k(\mathrm{Ag^{2+}}$ + substrate), M^{-1} sec^{-1}	$2k$(decay), M^{-1} sec^{-1} in Tl$^+$ system
	λ_{max}, nm	ϵ, M^{-1} cm^{-1}				
Anisole	280	7240	5.0×10^8	4.9×10^9	3.8×10^7	1.0×10^9
	430	3800				
1,2-DMB	290	9300	6.0×10^8	5.0×10^9	6.0×10^7	7.4×10^6
	400	2830				
1,3-DMB	<280					
	460	4000	8.0×10^8	7.0×10^9	6.3×10^7	6.0×10^8
	430^b	3550				
1,4-DMB	300	13000				
	430	9040	6.5×10^8	7.2×10^9	4.6×10^7	$<4 \times 10^3$
	460	9540				
1,2,3-TMB	290	12591	3.2×10^8	$\sim6-8 \times 10^9$	2.5×10^7	9.4×10^6
	410-420	2800				
1,2,4-TMB	300	11000				
	410	6890	6.8×10^8	7.8×10^9	7.0×10^7	4.7×10^7
	450	8860				
1,3,5-TMB	<280					
	540^b	4150	7.0×10^8	1.8×10^9	5.6×10^7	5.4×10^8
	580	5710				

^{a} The error in the k values is $\pm10\%$. ^{b} Shoulder.

served by ESR in the case of 1,3,5-TMB is suggested to be due to the combined effect of the short lifetime and of the large number of lines expected for the radical cation.

Radical cations were also obtained by irradiating argon saturated 10^{-3} M solutions of persulfate containing 10^{-4} M substrate. At pH ≥4, persulfate scavenges[34,35] the electrons to produce $SO_4\cdot^-$ ($k \sim 7 \times 10^9$ M^{-1} sec^{-1}) but not the OH radicals which react with the substrates to yield the corresponding hydroxycyclohexadienyl radicals. The sulfate radical anion subsequently reacts with the methoxylated benzene to yield the radical cation, e.g.

$$SO_4\cdot^- + DMB \rightarrow SO_4{}^{2-} + (DMB)\cdot^+ \qquad (4)$$
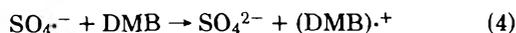
The rate constants k_4 were determined by observing the rate of formation of the optical absorption ($\lambda > 400$ nm) of the radical cations. The rate constants are presented in Table II. Since the rate of formation of the radical cations depended on substrate concentration and since it was approximately diffusion controlled, it is suggested that $SO_4\cdot^-$ reacts by direct electron transfer rather than by intermediate addition to the ring as proposed by Norman[10,36] and considered by Walling[15] using toluene and/or phenylacetic acid as substrates. This conclusion is in agreement with the experimental observation that in the reaction of $SO_4\cdot^-$ with the substrates the radical cation yield was independent of substrate structure. The same behavior was shown with Tl^{2+} and Ag^{2+}, but not with OH (see below). The absence of $SO_4\cdot^-$ adducts of aromatics is also in agreement with ESR results obtained by Fessenden.[31]

In the persulfate system, the lifetimes of the radical cations, monitored optically, were considerably shorter than those measured in the Tl$^+$ or Ag$^+$ systems. This was reflected also by the lower stationary concentration of the radical cations as observed by ESR. Since in the $S_2O_8{}^{2-}$ system, hydroxycyclohexadienyl radicals are formed together with radical cations, the radical cation concentration may be reduced by a fast reaction between radical cations and hydroxycyclohexadienyl radicals. This concept was tested by adding benzene ($\geq10^{-3}$ M) to a N$_2$O saturated

solution containing 10^{-3} M Tl$^+$ and 10^{-4} M 1,2-DMB at pH 4. In this solution a competition exists between Tl$^+$ and benzene for OH radicals resulting in the production of Tl^{2+} and hydroxycyclohexadienyl radicals of benzene and in a corresponding reduction of the radical cation yield. Formation of the radical cation of benzene from the OH adduct of benzene can be excluded under these conditions.[16] Similarly, Tl^{2+} was found not to react with benzene. If the hydroxycyclohexadienyl radicals of benzene react with the radical cation formed by reaction of Tl^{2+} with 1,2-DMB, an enhanced rate of decay of the radical cation should be observed. An increased rate of decay was in fact observed experimentally from which a rate constant of 1×10^9 M^{-1} sec^{-1} was obtained for the reaction of the hydroxycyclohexadienyl radical of benzene with the radical cation of 1,2-DMB. Analogous reactions are suggested to occur between hydroxycyclohexadienyl radicals and radical cations derived from the other substrates. Their rate constants, determined by pulse irradiating argon saturated 10^{-3} M persulfate solutions containing 10^{-4} M substrates at pH 5 and using optical detection, are presented in Table III. The rate constants are of the same order of magnitude as that of the reaction of the OH adduct of benzene with the 1,2-DMB radical cation.

II. Formation of Radical Cations from Hydroxycyclohexadienyl Radicals. Irradiations were performed in the pH range 1-7 using 10^{-4} M substrate and saturating with N$_2$O (pH >2.5) and argon (pH <2.5). The rate of addition of OH radicals to aromatic systems generally exceeds that of H abstraction from substituents by about two orders of magnitude.[19] It is therefore assumed that in the case of the substrates studied the OH radicals similarly react by addition to the ring to form hydroxycyclohexadienyl radicals.

The optical absorption spectra of the OH adducts were measured in N$_2$O saturated 10^{-4} M substrate solutions at pH 6-7. The spectra are similar to those of other[19,37] hydroxycyclohexadienyls and for the adduct of anisole the spectrum is in agreement with that[19,37] previously reported. The extinction coefficients were calculated by as-

TABLE III: Spectral Characteristics and Rate Constants[a] for Formation and Decay of OH Adducts

Substrate	OH adduct λ_{max}, nm	OH adduct ϵ, M^{-1} cm^{-1}	k(OH + substrate), M^{-1} sec^{-1}	$2k$(OH adduct), M^{-1} sec^{-1}	k(OH adduct + radical cation), M^{-1} sec^{-1}	k(OH adduct + H$^+$,[b] M^{-1} sec^{-1}
Anisole	320	4050	5.4×10^9	8.0×10^8	1.6×10^9	1.3×10^9
1,2-DMB	310	3870	5.2×10^9	1.5×10^9	2.7×10^9	6.4×10^8
1,3-DMB	330	6020	7.2×10^9	2.0×10^9	2.5×10^9	6.1×10^8
1,4-DMB	300[c]	7000	7.0×10^9	1.0×10^9	2.3×10^9	2.0×10^8
1,2,3-TMB	325	3390	8.0×10^9	9.8×10^8	3.5×10^9	1.2×10^9
	350	3420				
1,2,4-TMB	310	5730	8.1×10^9	1.1×10^9	1.5×10^9	1.4×10^9
1,3,5-TMB	340	7500	8.1×10^9	2.3×10^9	8.6×10^8	9.6×10^8

[a] The error in the k values is $\pm 10\%$. [b] k values are equal to $K_B k_C$ from eq 6. [c] An additional absorption maximum at λ 420 nm was observed and, as yet, is unassigned.

suming G(OH) = 5.5 and neglecting the contribution from H adducts. Since G(H) = 0.5, this procedure is justified, provided the extinction coefficients of the H adducts are similar to those of the OH adducts.[38]

In order to verify the latter assumption the absorption spectra of the H adducts were determined at pH 2 using 10^{-4} M substrate containing 10^{-2} M tert-butyl alcohol which scavenges the OH radicals. Under these conditions the electrons react with H$^+$ to yield H atoms, thus increasing G(H) to 3.2. The absorption spectra and the extinction coefficients of the H adducts were found to be similar to those of the OH adducts. In N$_2$O-saturated solutions at pH 6–7, the contribution of the optical absorption of the H adducts to that of the hydroxycyclohexadienyl radicals therefore amounts to less than 10%. The rate constants for formation and decay of the H adducts of the substrates are approximately 3–4 $\times$ 10^9 and 2 $\times$ 10^9 M^{-1} sec^{-1}, respectively.

The optical absorption spectrum of the hydroxycyclohexadienyl radical, produced in an irradiated aqueous solution of 10^{-4} M 1,2-DMB saturated with N$_2$O at pH 6.5, is shown in Figure 2. The spectrum has been corrected at λ <300 nm for removal of the substrate by assuming that G(-1,2-DMB) = G(OH) + G(H) = 6 in N$_2$O saturated aqueous solution. The spectral characteristics and the second-order rate constants for formation and decay of the OH adducts of the substrates are presented in Table III.

On lowering the pH to approximately 4, absorptions were observed at λ >400 nm that were absent in neutral solutions. These absorptions "grew in" while the absorptions due to the OH adducts decayed with an increased rate as compared to the situation at pH 7. From the similarity of the optical absorption spectra at λ >400 nm with those observed in the Tl$^+$, Ag$^+$, or S$_2$O$_8^{2-}$ systems, it is concluded that radical cations of the methoxylated benzenes are formed. This was confirmed using the in situ ESR method. The steady-state concentration of the radical cations was, however, lower than that in the Tl$^+$ or Ag$^+$ systems. The optical absorption spectra measured after 5 and 80 μsec, respectively, in irradiated 1,4-DMB and 1,3,5-TMB solutions are presented in Figure 3. In the case of 1,3-DMB and 1,2,3 and 1,3,5-TMB the absorption spectra of the radical cations and those of the OH adducts are sufficiently separated to compare the rate of decay of the OH adducts with the rate of formation of the radical cations. These rates were found to be identical (Figure 4b,c).

In the pH range 3–6, the pseudo-first-order rate of formation of the radical cations was found to be linearly de-
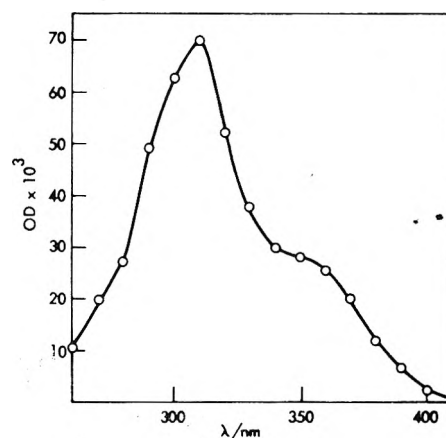
Figure 2. Optical absorption spectrum of the OH adduct of 1,2-DMB measured in an irradiated 10^{-4} M solution saturated with N$_2$O at pH 6.5.

pendent on H$^+$ concentration and independent of substrate concentration. Below pH 3 the rate of formation of the radical cations became independent of H$^+$ concentration but dependent on substrate concentration. Below pH 2, the rate constants measured for formation of the radical cations were similar to those measured for OH attack on the aromatic. The rate constants for the reaction of H$^+$ with the OH adducts are presented in Table III. The observed rate constants are suggested to be the product of the first-order rate constant k_C and the equilibrium constant K, which refers to the protonation equilibrium B of eq 6.

Conductivity measurements were performed in the pH range 4–7 using N$_2$O saturated solutions containing 10^{-4} M methoxylated benzenes. Between pH 4 and 6, after the pulse a decrease of conductivity was observed. The rate of decrease was the same as the rate of formation of the radical cations observed optically (Figure 4a,c). The decrease was followed by return of conductivity. By measurements using long observation times, the conductivity was found to return to the original value prior to the pulse (Figure 4d).

In order to explain the decrease of conductivity, it is assumed that H$^+$ (μ = 34 $\times$ 10^{-4} V^{-1} cm^{-1} sec^{-1}) is replaced by the radical cation. Assuming a mobility for the radical cation of 4 $\times$ 10^{-4} V^{-1} cm^{-1} sec^{-1}, G(radical cation) was estimated from the maximum removal of conductivity. The extinction coefficients of the radical cations in Table II were calculated by combining G(radical cation) measured by conductivity and G(radical cation)ϵ obtained optically. The dependences on pH of G(radical cation) expressed as a

P. O'Neill, S. Steenken, and D. Schulte-Frohlinde
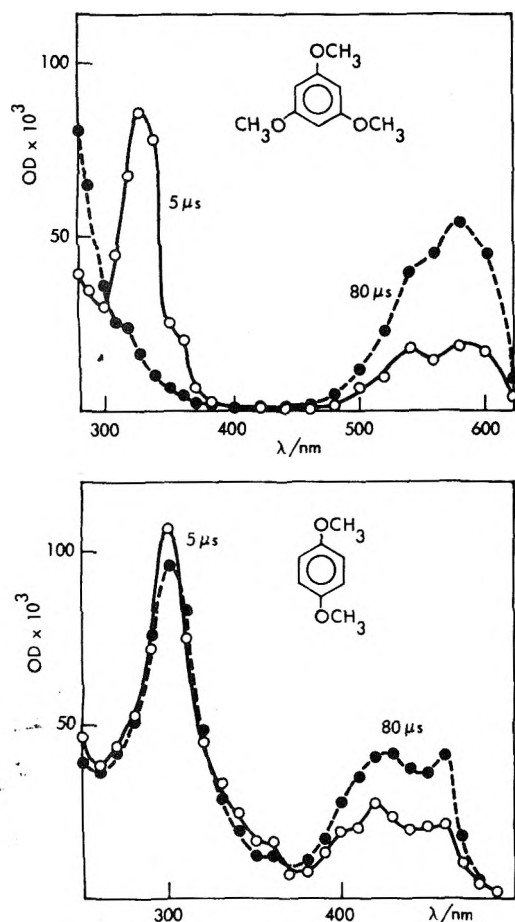
Figure 3. Optical absorption spectra measured in 10^{-4} M solutions saturated with N_2O at pH 4 after 5 and 80 μsec for 1,4-DMB and 1,3,5-TMB.
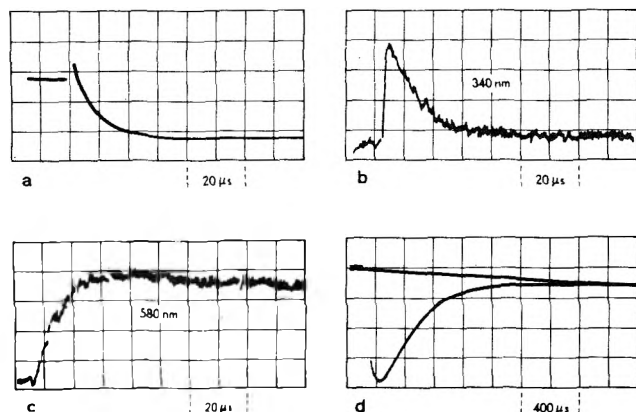
Figure 4. Changes observed in the conductivity and optical absorption signals on pulse irradiation of N_2O saturated 10^{-4} M solutions of 1,3,5-TMB and 1,3-DMB. Dose 0.5 krads: (a–c) 1,3,5-TMB pH 4.1, (a) conductivity, (b and c) optical absorption; (d) 1,3-DMB pH 5.2, conductivity.

percentage of G(OH) are shown in Figure 5. Qualitatively similar dependences were obtained by ESR. The agreement of the dependences determined optically and by conductivity and the kinetic observations are further confirmation of the assignment of the absorptions at $\lambda > 400$ nm to radical cations. At pH 1 the yield of radical cations from anisole, 1,3-DMB, and 1,3,5-TMB is $>90\%$ of G(OH) whereas for the other methoxylated benzenes the yields are between 45
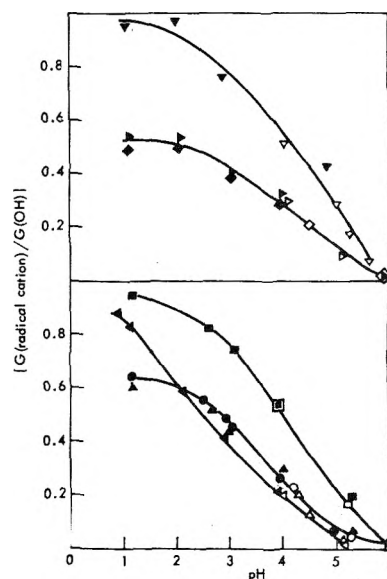
Figure 5. The dependence of G(radical cation) on pH in the optical (full symbols) and the conductivity (open symbols) experiments: (▼) 1,3,5-TMB; (▶) 1,2,4-TMB; (♦) 1,2,3-TMB; (■) 1,3-DMB; (●) 1,4-DMB; (▲) 1,2-DMB; (◀) anisole.

and 65% of G(OH). An explanation for the difference in behavior between the two groups of compounds will be given in terms of specific addition of OH to ring positions.[39]

From the return of conductivity it is concluded that H^+ is regenerated. The rate of return of conductivity was found to be identical with the rate of decay of the radical cations. The rates were found to depend on pH. At pH 4 the rates followed second-order kinetics and were similar to the rates of decay of the OH adducts, whereas between pH 4 and 5 the rates of return of conductivity and of radical cation decay tended toward first order and were different from the decay rates of the OH adducts.

At fixed pH the yields of the radical cations were found to vary with dose per pulse. The experimentally observed dependence of radical cation yield on dose rate (0.4–2.2 krads/pulse) at pH 4 could be quantitatively analyzed in terms of competition between OH adducts and H^+ for OH adducts. The following equation was found to be obeyed:

$$\frac{1}{(OD)_{RC}} = \frac{1}{C} + k'\frac{[dose]}{[H^+]} \qquad (5)$$

where C and k' are constants and $(OD)_{RC}$ is the normalized optical density measured at the absorption maxima of the radical cations.

The following mechanism is proposed to explain the experimental observations. 1,4-DMB is used as the example but the mechanism also applies for the other methoxylated benzenes.
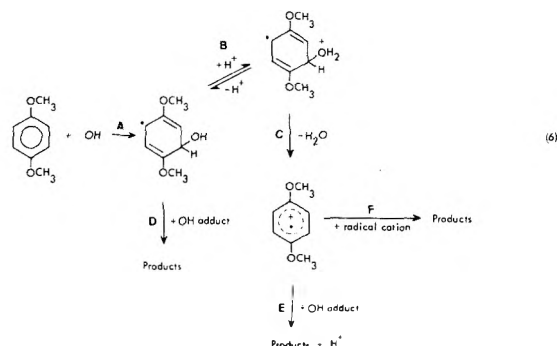
The initial attack of OH radicals, step A, is by addition to the aromatic system producing hydroxycyclohexadienyl radicals which were observed optically. The formation of radical cations from hydroxycyclohexadienyls is suggested to proceed through a protonated intermediate which is in equilibrium with the OH adduct. This is represented by steps B and C which account for $\geq 97\%$ of the radical cations produced. Thus a direct electron transfer, as suggested by Hamilton,[14] does not seem to occur between OH radicals and the aromatic. In support of this is the fact that the rate of formation of the radical cation at pH >3 is independent of the substrate concentration. Step B followed by step C is proposed to account for the dependence of the yield and the rate of formation of the radical cation on H^+ concentration. At pH <3 the rate of formation becomes independent of H^+ concentration but dependent on substrate concentration since $k_A[\text{aromatic}] < k_B[H^+]$, i.e., at pH <3 the OH addition reaction becomes rate determining and not the reaction with protons. Nonlinear dependences have previously been reported[17] for the acid-catalyzed elimination reaction from hydroxycyclohexadienyl radicals of methylated benzenes; these dependences were interpreted in terms of a reaction scheme including radical cation formation from OH adducts by a pH independent reaction. From the low yields of radical cations ($\leq 3\%$) in the methoxylated benzene systems at pH values ≥ 6 it is concluded that a pH independent process can play only a minor role ($\leq 3\%$).

The competition between steps B and D is proposed to explain the dependence of the yield of radical cation on dose per pulse since the rates of radical–radical reactions (step D) are dose rate dependent. In order to explain the enhanced rate of decay of the radical cations in the presence of uncharged radicals, e.g., cyclohexadienyl radicals, step E is introduced. The first-order decay of the radical cation at pH ≥ 5 occurs since the concentration of OH adducts, under these conditions, is approximately an order of magnitude higher than that of the radical cations whereas the second-order decay rates observed at pH ~ 4 result from the concentrations of the OH adducts and the radical cations being approximately equal. The return of the conductivity to that existing before the pulse can best be rationalized in terms of H^+ production by step E. Electron transfer from hydroxycyclohexadienyl radicals to radical cations may result in a carbonium ion which will immediately hydrolyze to yield H^+:

(7)
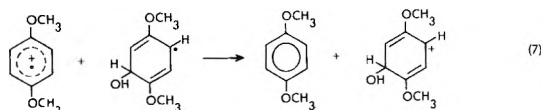
H^+ may also be derived from a dimerization product, e.g.

(8)
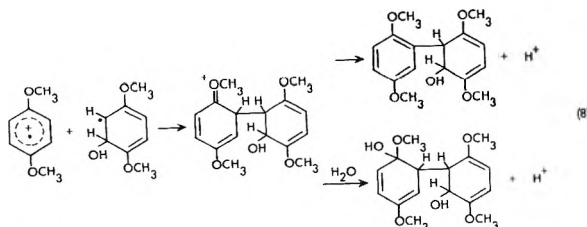
A cleavage of the radical cation to produce H^+ and an uncharged radical, as recently suggested[16,17] for the radical cations of methylated benzenes, is unlikely for methoxylat-

ed benzenes. Such a process should lead to a pH-independent first-order return of conductivity and a corresponding first-order decay of the optical absorption; this was not experimentally observed.

From the experimental observations that in the absence of uncharged radicals the radical cations decay according to a second-order rate law (step F), it is concluded that the rate of hydrolysis (reserve C) is less than the bimolecular decay of the radical cations. Therefore, a very fast reversible hydration as suggested by Walling[15,16] for radical cations from benzene, toluene, phenylacetic acid, and phenyl-substituted alcohols does not occur in the methoxylated benzene systems.

References and Notes

(1) For a review see G. Vincow, "Radical Ions", E. T. Kaiser and L. Kevan, Ed., Interscience, New York, N.Y., 1968, p 151.
(2) A. Ronlan, J. Coleman, O. Hammerich, and V. D. Parker, *J. Am. Chem. Soc.*, **96**, 845 (1974).
(3) P. D. Sullivan and N. A. Brette, *J. Phys. Chem.*, **79**, 474 (1975).
(4) W. F. Forbes and P. D. Sullivan, *J. Am. Chem. Soc.*, **88**, 2862 (1966).
(5) D. L. Allara, B. C. Gilbert, and R. O. C. Norman, *Chem. Commun.*, 319 (1965).
(6) W. F. Forbes and P. D. Sullivan, *Can. J. Chem.*, **44**, 1501 (1966).
(7) E. I. Heiba, R. M. Dessau, and W. J. Koehl, *J. Am. Chem. Soc.*, **91**, 6830 (1969).
(8) I. H. Elson and J. K. Kochi, *J. Am. Chem. Soc.*, **95**, 5060 (1973).
(9) P. O'Neill, S. Steenken, and D. Schulte-Frohlinde, *Angew. Chem.*, **87**, 417 (1975); *Angew. Chem., Int. Ed. Engl.*, **14**, 430 (1975).
(10) R. O. C. Norman, P. M. Storey, and P. R. West, *J. Chem. Soc. B*, 1087 (1970).
(11) D. H. Hey, G. H. Jones, and M. J. Perkins, *J. Chem. Soc., Perkin Trans. 1*, 118 (1972).
(12) A. Ledwith, P. J. Russell, and L. H. Sutcliffe, *Chem. Commun.*, 964 (1971); *Proc. R. Soc. London, Ser. A*, **332**, 151 (1973); *J. Chem. Soc., Perkin Trans. 2*, 630 (1973).
(13) A. Ledwith and P. J. Russell, *Chem. Commun.*, 291, 959 (1974).
(14) M. E. Snook and G. A. Hamilton, *J. Am. Chem. Soc.*, **96**, 860 (1974).
(15) C. Walling and D. M. Camaioni, *J. Am. Chem. Soc.*, **97**, 1603 (1975).
(16) C. Walling and R. A. Johnson, *J. Am. Chem. Soc.*, **97**, 363 (1975).
(17) K. Sehested, H. Corfitzen, H. C. Christensen, and E. J. Hart, *J. Phys. Chem.*, **79**, 310 (1975).
(18) O$^-$, the conjugate base of OH, has recently been suggested to react by direct electron transfer with phenolate and aniline (P. Neta and R. H. Schuler, *J. Am. Chem. Soc.*, **97**, 912 (1975)).
(19) L. M. Dorfman and G. E. Adams, *Natl. Stand. Ref. Data Ser., Natl. Bur. Stand.*, No. 46 (1973).
(20) W. T. Dixon and R. O. C. Norman, *J. Chem. Soc.*, 4857 (1964).
(21) C. R. E. Jefcoate and R. O. C. Norman, *J. Chem. Soc. B*, 48 (1968).
(22) N. Getoff and F. Schwörer, *Radiat. Res.*, **41**, 1 (1970).
(23) H. G. Klever, Ph.D. Thesis, Ruhr-Universität Bochum, 1974.
(24) K. Eiben and R. W. Fessenden, *J. Phys. Chem.*, **75**, 1186 (1971).
(25) H. A. Schwarz, D. Comstock, J. K. Yandell, and R. W. Dodson, *J. Phys. Chem.*, **78**, 488 (1974).
(26) P. O'Neill and D. Schulte-Frohlinde, *Chem. Commun.*, 387 (1975).
(27) H. Yamada and K. Kimura, *J. Chem. Phys.*, **51**, 5733 (1969).
(28) K. Kawai, N. Yamamoto, and H. Tsubomura, *Bull. Chem. Soc. Jpn.*, **42**, 369 (1969).
(29) W. F. Forbes, P. D. Sullivan, and H. M. Wang, *J. Am. Chem. Soc.*, **89**, 2705 (1967).
(30) S. Steenken and P. O'Neill, to be submitted for publication.
(31) H. Zemel and R. W. Fessenden, *J. Phys. Chem.*, **79**, 1419 (1975).
(32) J. Pukies, W. Roebke, and A. Henglein, *Ber. Bunsenges. Phys. Chem.*, **72**, 842 (1968).
(33) J. H. Baxendale, E. M. Fielden, and J. P. Keene, "Pulse Radiolysis", M. Ebert, J. P. Keene, and A. J. Swallow, Ed., Academic Press, London, 1965, p 207.
(34) W. Roebke, M. Renz, and A. Henglein, *Int. J. Radiat. Phys. Chem.*, **1**, 29 (1969).
(35) E. Hayon, A. Treinin, and J. Wilf, *J. Am. Chem. Soc.*, **94**, 47 (1972).
(36) R. O. C. Norman and P. M. Storey, *J. Chem. Soc. B*, 1099 (1970).
(37) P. Neta and L. M. Dorfman, *Adv. Chem. Ser.*, No. 81, 222 (1968).
(38) This seems to be the case quite generally, cf. ref 19 for a review.
(39) S. Steenken, P. O'Neill, and D. Schulte-Frohlinde, to be submitted for publication.

Effect of Temperature on Optical Basicity in the Sodium Oxide–Boric Oxide Glass System

J. A. Duffy* and R. J. Grant

Department of Chemistry, University of Aberdeen, Aberdeen AB9 2UE, Scotland (Received June 19, 1975)

Glasses in the Na_2O–B_2O_3 system, whose compositions ranged from 0 to 33% Na_2O, were heated gradually from ambient temperature to 500–600°C, and the spectral changes of the Pb^{2+} probe indicator ion were recorded. The frequency shift of the $^1S_0 \rightarrow {}^3P_1$ absorption band revealed only a slight decrease in (apparent) optical basicity up to around the glass transition temperature, but at higher temperatures the fall in optical basicity occurred at a much greater rate. Similar effects were noted in the oscillator strength which decreased sharply, and in the band width which increased. The results are interpreted in terms of the occurrence of some degree of disruption of the glass network, above T_g, with the conversion of bridging oxides to nonbridging (and simultaneous conversion of boron atoms from fourfold to threefold coordination). Microscopic optical basicities, λ, are assigned to the individual oxides, and although the bulk optical basicity, Λ, of the glass probably remains unchanged, the distribution of λ values in the glass changes as the network disrupts thereby allowing the Pb^{2+} probe ion to enter sites of locally higher optical basicity than the bulk Λ value of the glass.

The basicity of a glass can be envisaged in terms of the ability of the constituent oxygens to donate negative charge to an (acidic) indicator such as a probe metal ion added in trace quantity. Probe ions which are especially suitable for this purpose are $d^{10}s^2$ metal ions such as Pb^{2+}. The large frequency shifts in the s–p spectra of these ions on being transferred from the "free" (gaseous) state to the glass may be regarded as a measure of the donation of negative charge to the probe ion.[1-3] For most glasses the absorption by Pb^{2+} occurs in the accessible region of the uv (i.e., below ca. 50000 cm^{-1}) and arises through the transition $^1S_0 \rightarrow {}^3P_1$.[1] The frequency shift, $\nu_f - \nu_{glass}$ (where ν_f and ν_{glass} are the $^1S_0 \rightarrow {}^3P_1$ frequencies of Pb^{2+} "free" and in the glass, respectively) can be compared with the shift $\nu_f - \nu_{O^{2-}}$ (where $\nu_{O^{2-}}$ is the frequency for Pb^{2+} in CaO). The latter shift represents the extent of electron donation to Pb^{2+} in an "ionic" oxide, where we would expect the donation to be at a maximum, and the ratio of the electron donation in the glass to that in "ionic" oxide medium can be expressed as $(\nu_f - \nu_{glass})/(\nu_f - \nu_{oxide})$. This ratio is known as the *optical basicity*, Λ, of the glass,[4] and ideally it lies between zero and unity. For the Pb^{2+} probe ion, ν_f is 61700 cm^{-1}, ν_{oxide} is 29700 cm^{-1},[4] and thus

$$\Lambda_{Pb(II)} = (61700 - \nu_{glass})/31000 \qquad (1)$$

Although optical basicity is an experimentally determined quantity, it is now possible, in principle, to predict its value for any oxide medium through calculations which consider the effects of the constituent cations (Na^+, B^{3+}, etc.) upon the electron donor properties of the oxide.[5] The calculations require a knowledge of the number of cations (relative to the total number of oxides), their oxidation numbers, and their basicity moderating parameters (which are related simply to electronegativity), and they give not only basicities of "bulk" media, but also the basicites of individual oxides (see later).

Inorganic glasses are convenient media for investigating effects and trends brought about by changes in basicity, and indeed such investigations are necessary if a proper understanding of the role of basicity in glass chemistry is to

be achieved. Several workers have investigated the effect of glass composition on the spectrum of Pb^{2+} and other $d^{10}s^2$ ion.[1,6-8] Particularly suitable for studying effects brought about by gradual increases in basicity are the alkali oxide–boric oxide systems, and the spectroscopic trends of $d^{10}s^2$ ions indicate the drastic effect of alkali oxide on the structure of the glass in providing sites of various optical basicities for the probe ion.[4,9,10]

The structure of a borate glass (or any other network glass), however, is also bound to be affected by *temperature*, especially in the range beyond the glass transition temperature, T_g. The present work was undertaken to investigate whether structural changes brought about by temperature would be reflected in the response of the Pb^{2+} probe. The glass system chosen was Na_2O–B_2O_3, uv spectra being obtained for Pb^{2+} in host glasses at temperatures up to 500–600°C.

Results

The absorption band of Pb^{2+} which is used for measuring optical basicity (due to the transition $^1S_0 \rightarrow {}^3P_1$) always appears on the lower energy side of the more intensely absorbing $^1S_0 \rightarrow {}^1P_1$ band, the maximum of which is beyond the uv transparency of the glass. In the present study, it is observed that for all Na_2O compositions of the borate glasses, increase in temperature brings about some degree of change in the $^1S_0 \rightarrow {}^3P_1$ absorption band, the maximum moving to lower frequencies. For the high alkali glasses (25 and 33% Na_2O) the frequency shifts are quite small even up to 500°C; at these higher temperatures, the effect of band broadening and the decrease in absorbance result in the absorption band merging as a shoulder to the more intense, spin allowed band, and it is not possible to estimate ν_{max} very accurately for the 25 and 33% Na_2O glasses. The deleterious effects of temperature were found to be far less pronounced in the spectra of the glasses having a Na_2O content of 18% and below, making these glasses much more suitable for study. For these lower alkali glasses, it was observed that although the spectral changes are quite small up to ca. 300°C, they are much more profound for tempera-

tures greater than 300–400°C. Figure 1 shows the changes for a 7.8% Na_2O glass, for example, and it can be seen that as well as the decrease in ν_{max}, there is also a fall in the optical density. These changes resemble quite strikingly those observed in the spectrum of Pb^{2+} in the $Na_2O-B_2O_3$ glass system when the Na_2O content is increased at ambient temperature (this can be seen for example when Figure 4, ref 7 is compared with Figure 1 in the present paper).

From the frequencies can be obtained, through eq 1, the (apparent) optical basicities, $\Lambda_{Pb(II)}$, of each glass at the temperatures for which the spectra were run. The changes in $\Lambda_{Pb(II)}$ with temperature are shown in Figure 2. The greater extent to which the very low alkali glasses respond to the higher temperatures results (see Figure 3) in the remarkable situation at 500°C where the basicity of the $Na_2O-B_2O_3$ system remains virtually unchanged for alkali oxide contents over the range 0–18%!

For the low alkali glasses, the plots in Figure 2 would suggest that, for each glass, two straight lines could be drawn reasonably through the points, one corresponding to the trend for lower temperatures and the other for higher temperatures. The temperature at which the faster trend takes over from the slower (the point of intersection of the two lines) is found, except in the case of vitreous B_2O_3, to be close to the glass transition temperature determined by differential thermal analysis (see Table I). The pattern of behavior for the optical density of the $^1S_0 \rightarrow {}^3P_1$ band with increasing temperature is similar to that for the frequency (see Figure 4), and the transition temperatures obtained are included in Table I. (For B_2O_3, the agreement with T_g is now much better.)

Discussion

Trend in Observed Basicity. The results in Figure 2 which summarize the effect of temperature on $\Lambda_{Pb(II)}$ are probably open to more than one interpretation, but we regard the trend observed for temperatures above T_g as arising through profound changes occurring in the covalent structure of the glass.

In the alkali oxide–boric oxide glass system, the results of Bray and co-workers have shown that each alkali oxide serves to convert two boron atoms from three to four coordination (or nearly so),[11] and addition of alkali oxide does not, on the whole, result in the conversion of the bridging oxides into nonbridging oxides (cf. the situation in alkali oxide–SiO_2 glass systems).[21] When the glass is heated, however, there is increasing vibration of the boron and oxygen atoms, and with the transition from solid to liquid it is necessary to envisage large-scale disruption of the network with the conversion of bridging oxides to nonbridging. The liquid can be regarded in terms of a dynamic system involving the breaking and remaking of boron–oxygen bonds, and this situation will also obtain, though to a decreasing extent, as the temperature is lowered to T_g. Thus, in our experiments where the glass is heated from ambient temperature upward, T_g can be regarded as marking the onset of equilibria such as:

(2)

Figure 1. Uv absorption spectra of Pb^{2+} in sodium borate glass (7.8% Na_2O) at various temperatures (°C).

Figure 2. Changes in $\Lambda_{Pb(II)}$ with temperature observed for glasses in the $Na_2O-B_2O_3$ system.

Nonbridging oxides are much more basic than bridging (see later), and if they are produced in a site in which the other oxides undergo no change, then the basicity of the site is increased. Since Pb^{2+} ions seem to have a slight preference for more highly basic sites in the alkali borate glass systems,[4,9,10] it is to be expected that they will tend to move into these new sites. With the production of more of these sites (with increasing temperature), so more Pb^{2+} ions will signal a lower $^1S_0 \rightarrow {}^3P_1$ frequency and the maximum of the absorption band envelope undergoes the observed red shift.

It should also be noted that production of the more high-

Figure 3. Observed trend in optical basicity, $\Lambda_{Pb(II)}$, with temperature in the $Na_2O-B_2O_3$ glass system.

Figure 4. Changes in the extinction coefficient of the $^1S_0 \rightarrow {}^3P_1$ band with temperature in the $Na_2O-B_2O_3$ glass system. (The graphs are labeled according to the mole percent Na_2O content of the glass.)

TABLE I: Glass Transition Temperatures of Sodium Borate Glasses Obtained from Differential Thermal Analysis and from Uv Spectra

| Glass, mol % Na_2O | Glass transition temp, °C | | |
| | | uv spectroscopy | |
	DTA	frequency shift	absorbance change
0	256	315	265
7.8	320	330	315
13.2	362	355	380
16.0	405	420	410
18.0	433	425	445

ly basic oxides would be expected to result in a red shift of the uv absorption edge of the undoped glass because of the reduced tightening of the electron shells of the oxide as it undergoes the change from bridging to nonbridging. (The impairment of uv transparency with increasing alkali content is well known for glasses generally, see, for example, ref 12.) This red shift is in fact observed as the temperature of the undoped borate glass is raised, thus strongly supporting the existence of equilibria of the type suggested above.

In terms of the optical basicity concept, the production of the sites of greater basicity does not necessarily require there to be any change in the "bulk" basicity of the glass. This can be illustrated by referring to the *microscopic optical basicities* of the individual oxides. In a series where all the oxides are equivalent, for example, MgO or Li_2SO_4, it is possible to assign to each oxide a microscopic optical basicity value, λ,[22] which is the same as that of the bulk medium. However, in media containing different oxides, for example, a glass with both bridging and nonbridging oxides, the λ values will be different from the bulk Λ value of the

medium. Microscopic optical basicities can be calculated in a similar manner to bulk Λ values (see Appendix), and values of λ for oxides in an alkali borate glass are given in Table II. It should be noted that λ depends not only on whether the oxide is briding or nonbridging but also on the coordination number of the boron. In the alkali borate glass system, the oxides will have λ values of 0.42 (for B(3)–O–B(3) oxides) and 0.50 (for B(3)–O–B(4) oxides). Any oxides that bridge two four-coordinate borons will have a λ value of 0.57, although such oxides need not be generated until 30% alkali oxide and not, incidently, 16.7% (cf. ref 13). With the rupture of a B(3)–O– B(4) bridge, as in the equilibrium given above, the production of the nonbridging oxide, with $\lambda = 0.71$, occurs simultaneously with the production of *three* B(3)–O–B(3) oxides from B(3)–O–B(4) oxides. The total decrease in basicity suffered by these three oxides from 0.50 to 0.42 balances (exactly if more accurately expressed λ values were used) the increase in the λ value of the single oxide which changes from bridging to nonbridging. Thus, oxides of greater (and smaller) optical basicity are generated and there is no overall increase in the bulk optical basicity of the glass.

Absorption Band Intensity. It can be seen from Figure 1 that increasing the temperature of the glass causes not only a decrease in ν_{max} but simultaneously a decrease in optical density. This behavior was observed for all the glasses, and when the absorbance of the band was plotted against $\Lambda_{Pb(II)}$ for each glass, it was found that the points lay close to a straight line. The graphs revealed that the optical density of the $^1S_0 \rightarrow {}^3P_1$ band was halved when $\Lambda_{Pb(II)}$ increased by approximately 0.05 unit.

Since the band envelope also undergoes some broadening (see later) it is necessary to regard the absorption in terms of the oscillator strength, f, rather than in terms of absorbance, since the latter is concerned only with the peak height. With λ in cm^{-1} and the extinction coefficient, ϵ, in M^{-1} cm^{-1}, f is given by[14]

$$f = 4.315 \times 10^{-9} \int \epsilon \, d\nu$$

TABLE II: Microscopic Optical Basicity, λ, of Oxide in Various Borate Groups

Type of oxide	Boron coordination	λ^a
Nonbridging	Threefold	$1 - 0.864 \times \dfrac{1}{3} = 0.71$
Nonbridging	Fourfold	$1 - 0.864 \times \dfrac{1}{4} = 0.78$
Bridging	Both threefold	$1 - 0.864 \times \dfrac{2}{3} = 0.42$
Bridging	Both fourfold	$1 - 0.864 \times \dfrac{1}{2} = 0.57$
Bridging	One threefold One fourfold	$1 - 0.864 \times \dfrac{7}{12} = 0.50$

^{a} λ is calculated from eq 4.

Estimating the absorption area due to the transition $^1S_0 \rightarrow$ $^3P_1$ is not straightforward for a number of reasons: first, the background spectrum of the glass itself varies with temperature, although it is possible to correct for this by subtracting the spectrum of the undoped glass (with the same path length); second, the edge of the $^1S_0 \rightarrow$ $^1P_1$ band extends over such a limited range of frequency that only an approximate estimate of its absorption in the frequency range of the $^1S_0 \rightarrow$ $^3P_1$ band can be made (see Figure 1, for example); third, between the $^1S_0 \rightarrow$ $^3P_1$ and $^1S_0 \rightarrow$ $^1P_1$ transition there is the Laporte forbidden, spin forbidden transition $^1S_0 \rightarrow$ $^3P_2$, and although its absorption is comparatively small, the transition is vibronic and therefore expected to increase in intensity with temperature. It was found that spectral data for which these difficulties are least were those determined in B_2O_3 glass. Using these data, absorption areas were measured and hence values of the oscillator strength for the $^1S_0 \rightarrow$ $^3P_1$ transition were obtained at different temperatures. The correlation with the optical basicity signalled by the Pb^{2+} ion (at these temperatures) is shown in Figure 5, and it can be seen that increasing $\Lambda_{Pb(II)}$ is accompanied by a decrease in the oscillator strength. The fall in extinction coefficient (as shown in Figure 4) is therefore only partly due to band broadening effects.

The decrease in the overall band absorption with rising $\Lambda_{Pb(II)}$ is fully in accord with the nature of the $^1S_0 \rightarrow$ $^3P_1$ transition. The transition is formally spin forbidden, but gains its intensity from the spin allowed $^1S_0 \rightarrow$ $^1P_1$ transition by virtue of its enormous spin–orbit coupling constant, ζ_{6p} ($\zeta_{6p} = 12390$ cm^{-1} for the free Pb^{2+} ion). The oscillator strength depends upon the magnitude of the spin–orbit coupling constant, and since this is known to decrease with increasing covalency between a metal ion and its surroundings,[15] the decrease in absorption that accompanies increasing optical basicity means that there is an increase in the degree of covalency in the Pb^{2+}–oxide interaction. This is exactly in accord with the interpretation of optical basicity in terms of a Lewis acid–base interaction.

Absorption Band Width. Disruption of the glass network above T_g to produce nonbridging oxides in addition to bridging oxides already in the glass leads to an increased range of microscopic optical basicity. For the scheme envisaged earlier in this discussion (eq 2), in a low alkali glass, where there are oxides bridging two three-coordinated bo-
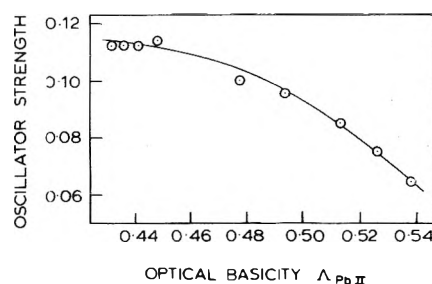
Figure 5. Plot of oscillator strength, f, for the $^1S_0 \rightarrow$ $^3P_1$ transition of Pb^{2+} vs. $\Lambda_{Pb(II)}$ signaled in vitreous B_2O_3.

rons or one three- and one four-coordinated boron, we go from a range (see Table II) of 0.42–0.50 (i.e., 0.08 unit) to the much wider range 0.42–0.71 (i.e., 0.29 unit), on account of the formation of a nonbridging oxide. As the temperature is increased above T_g, the latter range becomes increasingly important, and the number of different sites available for the Pb^{2+} ions is therefore increased. On the basis of this model we should expect a broadening of the band envelope and a reduction in the extinction coefficient in addition to that brought about by the change in oscillator strength (see above). Even if nonbridging oxides do already exist in the glass at ambient temperature then at temperatures above T_g there is an increase in the number of oxides having basicity values corresponding to the limits of the range, and this would also lead to the same effect in the spectrum of the probe ion.

Thus as a general principle, broadening of the absorption band envelope is expected to be slight at temperatures up to T_g but to occur to a much greater extent for temperatures above T_g. This was the pattern of behavior observed experimentally, and, for example, may be perceived from careful examination of Figure 1. Spectral changes for Pb^{2+} occurring in glasses where the Na_2O content is zero indicate that the principle also extends to vitreous B_2O_3 (and must, in the production of nonbridging oxides, presumably involve the formation of twofold coordinate boron). Figure 6, constructed using somewhat superior spectral data for this glass (see previously), shows clearly the marked changes occurring at temperatures greater than T_g. (For this diagram, the band width was calculated by dividing the band area by the band height for the $^1S_0 \rightarrow$ $^3P_1$ absorption envelope at the different temperatures.)

Changes Occurring below T_g. The arguments given in the previous sections would seem to account satisfactorily for the observed trends, namely, the frequency shift, the fall in absorption, and also band broadening of the Pb^{2+} ion. As far as the less pronounced spectral changes occurring below T_g are concerned, although it is possible that these would fit the configurational coordinate model which has been shown[19] to be appropriate for Pb^{2+} in $CaO–P_2O_5$ glass (in the range from ambient temperature to liquid nitrogen temperature, where the $^1S_0 \rightarrow$ $^3P_1$ frequency similarly undergoes a slight blue shift), it is difficult to suggest what *mechanism* is responsible. The explanation for the behavior above T_g does not imply any increase in the bulk optical basicity of the glass, but it is possible that a slight increase in basicity does come about as a result of minute changes in the basicity moderating parameters of the cations brought about by temperature;[23] a slight increase in the basicity moderating parameters would give rise, through eq 1 and 3, to a blue shift in the $^1S_0 \rightarrow$ $^3P_1$ frequency. An alternative explanation for the behavior below
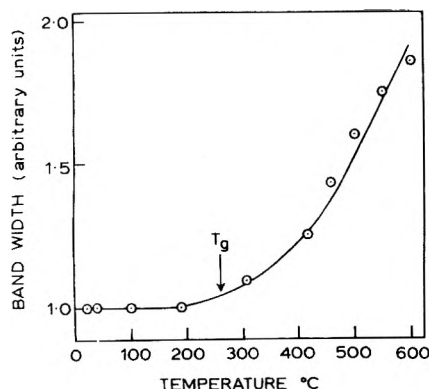
Figure 6. Effect of temperature on the width of the $^1S_0 \to {}^3P_1$ band of Pb^{2+} in vitreous B_2O_3.

T_g is that expansion effects in the glass may allow the Pb^{2+} probe ion to move slightly within the glass framework and thereby to alter its coordination sphere. This would be expected to be most easily achieved in vitreous B_2O_3 which has a ribbon structure (or boroxyl groups),[16] and indeed the effect of temperature was slightly more pronounced for B_2O_3 (Figure 2). This mechanism would imply that the spectrum of the probe ion would depend upon the thermal history of the glass, and the small discrepancies reported in the literature suggest that annealing effects might be important.[4,7,9,17]

Experimental Section

Preparation of the glasses and their doping was carried out in the usual manner.[4] The sodium oxide content of the glasses was determined by dissolving the glass in water and titrating with standard hydrochloric acid. Glass transition temperatures were measured using a Du Pont 900 differential thermal analyzer.

For obtaining the spectra of the glasses at elevated temperatures a special heater was constructed consisting of a platinum gauze approximately 8 × 20 mm the supports of which slot into two brass bushes and are held by grub screws; the bushes are mounted on a platform which can be tilted between vertical and horizontal. The heater is energized from a low-voltage transformer (rated at 3 V, 50 A) which is connected to the main supply via a variable transformer. For mounting the glass sample, the heater is tilted horizontally, energized so that the glass melts thereby sticking to the gauze, then vitrified simply by allowing it to cool. To record the spectrum of the glass, it is necessary to mask the light beam using an apperture of 3–4 mm, the reference beam being similarly attenuated. The glass was brought to the required temperature by setting the variable transformer on a previously calibrated scale obtained by recording the temperature of a similar glass with a thermocouple. After obtaining spectra at the higher temperatures, the glass was allowed to cool to ensure that the path length had not changed owing to any softening of the glass. Although the original, ambient temperature spectrum was always obtained, the experiments were not designed with the intention of investigating any possible hysteresis which may occur in these glasses.

It is worth pointing out that the heater described above was also found to be suitable for mounting molten salts, and the uv and visible spectra of sulfates, fluorides, etc. were readily obtained. Compared with the conventional type of furnace that is used in spectrophotometers, the

present apparatus has the advantage that the molten salt is not required to come into contact with any container material other than the platinum of the gauze, and it is therefore suitable for the more corrosive melts.

Appendix

The equation which allows the Λ value of an oxide medium to be predicted (given in ref 5) can be rearranged to yield

$$\Lambda = 1 - \left| \frac{z_A r_A}{2}\left(1 - \frac{1}{\gamma_A}\right) + \frac{z_B r_B}{2}\left(1 - \frac{1}{\gamma_B}\right) + \ldots \right| \quad (3)$$

z_A, z_B, $\ldots$ are the oxidation numbers and $r_A, r_B, \ldots$ are the ratio, with respect to the total number of oxides, of the cations A, B, $\ldots$, and γ_A, γ_B are the basicity moderating parameters (γ for boron is 2.36[5]).

In calculating the microscopic optical basicity of a single oxide, Λ is replaced by λ, and for a borate glass in which the effect of cations other than B^{3+} can be neglected, λ is given by

$$\lambda = 1 - \frac{3r_B}{2}\left(1 - \frac{1}{2.36}\right) = 1 - 0.864 r_B \quad (4)$$

r_B will obviously depend upon whether the boron is three-coordinate or four-coordinate and also upon whether the oxide is bridging or nonbridging. Using eq 4, values of λ are calculated for individual oxides in borate glasses (see Table II). Strictly, these values hold only in the lithium borate system (since only Li has a γ value of unity), but since the λ values are used in the present context only for comparison purposes within the sodium borate system, it is not necessary to make the small correction which arises through the difference in the γ values between Na and Li. Also for present purposes, the effects of partial neutralization within BO_3 or BO_4 units (which eq 4 does not consider) can be neglected, although the significance of these effects will be discussed in a future publication.

References and Notes

(1) J. A. Duffy and M. D. Ingram, *J. Chem. Phys.*, **52**, 3752 (1970).
(2) J. A. Duffy and M. D. Ingram, *J. Chem. Phys.*, **54**, 443 (1971).
(3) J. A. Duffy and M. D. Ingram, *Inorg. Chim. Acta*, **7**, 594 (1973).
(4) J. A. Duffy and M. D. Ingram, *J. Am. Chem. Soc.*, **93**, 6448 (1971).
(5) J. A. Duffy and M. D. Ingram, *J. Inorg. Nucl. Chem.*, **37**, 1203 (1975).
(6) A. K. Ghosh, *J. Chem. Phys.*, **42**, 2623 (1965).
(7) A. Paul, *Phys. Chem. Glasses*, **11**, 46 (1970).
(8) R. Reisfeld and L. Boehm, *J. Non-Crystalline Solids*, **17**, 209 (1975).
(9) A. J. Easteal and D. J. Udy, *Phys. Chem. Glasses*, **14**, 107 (1973).
(10) J. A. Duffy and M. D. Ingram, *Phys. Chem. Glasses*, in press.
(11) P. J. Bray and J. G. O'Keefe, *Phys. Chem. Glasses*, **4**, 37 (1963).
(12) E. H. Sigel, *J. Phys. Chem. Solids*, **32**, 2373 (1971).
(13) T. Abe, *J. Am. Ceram. Soc.*, **35**, 284 (1952); H. Rawson, "Inorganic Glass Forming Systems", Academic Press, London, 1967, p 113.
(14) C. K. Jørgensen, "Absorption Spectra and Chemical Bonding in Complexes", Pergamon Press, London, 1962, p 92.
(15) Reference 14, p 186.
(16) G. M. Bartenev, "The Structure and Mechanical Properties of Inorganic Glasses", Wolters-Noordhoff, Groningen, 1970, p 66.
(17) A. J. Easteal, private communication.
(18) G. P. Smith, D. W. James, and C. R. Boston, *J. Chem. Phys.*, **42**, 2249 (1965).
(19) S. Parke and R. S. Webb, *J. Phys. Chem. Solids*, **34**, 85 (1973).
(20) J. A. Duffy, unpublished results.
(21) The bridging and nonbridging oxygens are referred to as "oxides" to conform with the principles of coordination chemistry. Boron has a formal oxidation number of $+3$ and oxygen -2, but the existence of free B^{3+} and O^{2-} ions is in no way implied.
(22) It should be noted that λ is not the same as $\lambda_1, \lambda_2, \ldots$ as used by Easteal[9] (see Appendix).
(23) Data relating to the effect of temperature on basicity moderating parameters are very sparse. From frequency shifts observed for Pb^{2+} in molten chlorides,[18] it would appear that the effect is very small, e.g., in the LiCl–KCl (41% KCl) melt, rising from 440 to 640°C results in an increase of only 1.8% in optical basicity.[4] Furthermore, it has been observed that subjecting borate glasses to liquid nitrogen temperature has little effect on the $^1S_0 \to {}^3P_1$ frequency.[20]

Excited State Reactivity of Aza Aromatics. IV. Fluorescence Properties and Acid–Base Equilibria of Naphthylpyridylethylenes

Gianna Favaro, Fausto Masetti, Ugo Mazzucato, *

Istituto di Chimica Fisica, Università di Perugia, 06100 Perugia, Italy

and Pietro Bortolus

Laboratorio di Fotochimica e Radiazioni d'Alta Energia del C.N.R., 40126 Bologna, Italy (Received February 3, 1975; Revised Manuscript Received September 15, 1975)

Publication costs assisted by the Consiglio Nazionale delle Ricerche (Roma)

Fluorescence properties (quantum yields and lifetimes) have been measured for the six isomeric 1-naphthyl-2-pyridylethylenes and their conjugate acids. The basicity in the first excited singlet state, determined by fluorimetric titration, increases strongly with respect to the ground state. Kinetic parameters for the protolytic equilibration in the excited state have been evaluated from fluorescence–pH curves and fluorescence lifetimes.

Introduction

It has often been observed that the basicity of aza aromatics having low lying π,π^* singlet states strongly increases on excitation. For some azastilbenes[1] and azaphenanthrenes[2] direct fluorimetric titration and pK^* calculation by the Förster cycle have been performed; the results obtained by the two methods were found to be in good agreement.

Thus, a study of the basicity of styrylpyridines in the first excited singlet state gave an important contribution to the understanding of the mechanism of trans → cis photoisomerization of these compounds.[3]

The present paper reports the results of an investigation of the acid–base equilibria of the six isomeric trans naphthylpyridylethylenes (NPE's) in the first excited singlet state together with information on fluorescence quantum yields and lifetimes of free bases and their conjugate acids.

The results obtained show that the NPE's are also stronger bases in the first excited singlet state than in the ground state. The pK^* values are similar for all the isomers, whereas fluorescence quantum yields and lifetimes depend on the relative positions of pyridyl and naphthyl groups and on protonation.

Experimental Section

The compounds studied are the six isomeric trans 1(α,β)-naphthyl-2(2-,3-,4-)-pyridylethylenes prepared by standard procedures,[4] referred to as NPE, preceded by a greek letter and a number indicating the isomeric position of the naphthyl and pyridyl groups with respect to the ethylenic bond.

NPE
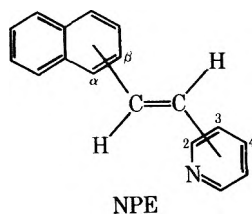
Ground state and excited state ionization constants were determined at room temperature (ca. 22°C), in 90/10 (v/v)

water–ethanol mixtures by spectrophotometric and fluorimetric titration, respectively.

A Sargent PXB pH meter with glass electrode was employed. The highest pH values were corrected for alkaline error.

Absorption spectra were registered by a Unicam SP500 spectrophotometer. Solute concentrations of the order of 10^{-5} M in Britton buffers ($\mu = 0.1$), 40-mm path length cells were used for absorptiometric titrations.

Fluorescence measurements were performed on a Hitachi Perkin-Elmer MPF-3 fluorescence spectrophotometer, with an accessory for spectrum correction, using rhodamine B as a quantum counter.

For the fluorimetric titrations, solute concentrations were of the order of 5×10^{-6} M. Britton buffers[5] were used up to pH 12 and NaOH solutions for higher pH values. The ionic strength was kept constant ($\mu = 1$) by adding Na_2SO_4, which has negligible quenching power on fluorescence.[1] Fluorescence intensity vs. pH plots were obtained by following the fluorescence decrease of the conjugate acid and/ or the emission increase of the free base with increasing pH. When both types of measurements were feasible, the fluorimetric titration curves for the basic and acidic forms were reciprocal to one another.

The excited state basicity constants for the equilibrium

$$NPE^* + H_2O \overset{\vec{k}}{\underset{\vec{k}}{\rightleftharpoons}} NPEH^{+*} + OH^- \tag{1}$$
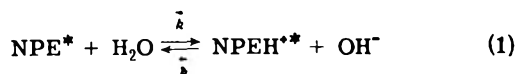
were obtained by application of steady-state kinetics[6] leading to the equation

$$1/(I_b^0/I_b - 1) = (1/\vec{k}\tau_b) + (\vec{k}\tau_a/\vec{k}\tau_b)a_{OH^-} \tag{2}$$

where I_b^0/I_b is the intensity ratio (approximated to the quantum yield ratio) of the emission of a solution where 100% base exists and of solutions where NPE* is partially equilibrated. τ_a and τ_b are the experimental lifetimes of the acidic and neutral forms, respectively. Thus, a plot of $1/(I_b^0/I_b - 1)$ vs. the OH$^-$ activity yields a straight line[1] of slope $(\tau_a/\tau_b)(\vec{k}/\vec{k}) = (\tau_a/\tau_b)(K^*/K_w)$, where K^* is the dissociation constant of the excited NPEH$^+$ and K_w that of water.

Only for one of the six isomers (α,2-NPE) was the fluorimetric titration not performed, because of the too low percentage of equilibrated acid in the excited state and the high ϕ_b/ϕ_a ratio: the first factor does not allow base titration to be performed and both factors make acid titration difficult, as the intense long-wavelength tail of the base emission masks the weak emission from the conjugate acid.

Apparent pK^*'s were reduced (-0.3) to thermodynamic values by the approximate formula for the activity coefficients.[7] The reported values are a mean of data obtained in two or three runs, with a reproducibility of ± 0.1 pK units.

All the pK^*'s were also calculated by the Förster cycle,[6] using the formula

$$\mathrm{p}K^* = \mathrm{p}K - \frac{0.625}{T}\,\Delta\bar{\nu} \qquad (3)$$

where $\Delta\bar{\nu}$ (in centimeter^{-1}) is the difference in the 0–0 frequencies for the base and its conjugate acid. Both the average of absorption and fluorescence maxima and the intersection of the two normalized spectra were used to measure $\Delta\bar{\nu}$. The 0–0 frequencies and pK^* values reported in Table I are the averages of the values obtained by the two procedures. Accurate band onsets were not obtained because of the low solubility of NPE's in water, which did not allow absorption spectra at high concentrations to be recorded.

Fluorescence quantum yields were determined relative to 2-(1-naphthyl)-5-phenyl-1,3,4-oxadiazole (α-NPD) in cyclohexane solution and to quinine sulfate in H_2SO_4 1 N solution as standards[8] for the bases (pH 8) and the acids (pH 2), respectively; 50/50 (v/v) water–ethanol solutions were employed in order to exclude emission from the acidic form at pH 8, which strongly depends on the alcohol content of the solutions.[5,9] On the other hand, measurements in alkaline solutions (pH > pK^*) were found to be unsuitable because of inconstancy of their absorbance. Solute absorbance was in the range 0.1–0.15. The ϕ values reported were averaged from at least three integrated spectra, the reproducibility being within 5%.

The fluorescence lifetimes were measured in 50/50 (v/v) water–ethanol by the pulse sampling technique, using an apparatus with a resolution time of about 1 nsec, described elsewhere.[10] The reported values were averaged from three independent runs, with a reproducibility within 15–20%.

Different ethanol percentages, as used in the fluorimetric titration (10%), were found to have no effect on τ_a; the experimental check on τ_b was not feasible due to the low solubility of the NPE's in alkaline solution.

Results and Discussion

Naphthylpyridylethylenes in aqueous solutions show a long wavelength absorption maximum in the range 320–330 nm, which becomes broader and shifts toward the red on protonation (320–390 nm). Fluorescence spectra show a similar shift, the emission of the bases being in the range 390–420 nm and those of the acids in the 495–540-nm region. Solvent[11] and protonation effects on the spectra concur to indicate that the lowest singlet state originates from π,π^* excitation. The solvent relaxation red shift of fluorescence is much greater and more sensitive to structural effects for the acidic than for the basic forms. In particular, for both 3-pyridyl derivatives, whose lifetime is longer than for the other isomers, this shift is about 11000 cm^{-1} for the protonated forms and about 5500 cm^{-1} for the bases. Solvent effects appear more important for β-naphthyl derivatives.

TABLE I: Assumed 0–0 Frequencies (10^3 cm^{-1}) for Neutral ($\bar{\nu}_b$) and Protonated ($\bar{\nu}_a$) Forms and Basicity in the Ground and Excited States of Naphthylpyridylethylenes in 90/10 (v/v) Water–Ethanol

Isomer	$\bar{\nu}_b$	$\bar{\nu}_a$	pK	pK^* (calcd)	pK^* (fluor)	$\%^a$ (pH 8)
α, 2-NPE	26.88	23.61	4.40	11.4		5
α, 3-NPE	27.37	23.81	4.60	12.1$_5$	13.1	26
α, 4-NPE	26.70	22.66	5.20	13.7	12.6	15
β, 2-NPE	27.98	24.27	4.63	12.5	12.8	31
β, 3-NPE	28.31	24.92	4.72	11.3	12.4	23
β, 4-NPE	27.65	23.76	5.23	13.3$_5$	13.0	44

^{a} The percentage of acidic molecules equilibrated in the excited state was directly obtained by the constant intensity ratio $\phi_a/\phi_a{}^0$, or $1 - \phi_b/\phi_b{}^0$, measured between pK and pK^*.

TABLE II: Fluorescence Quantum Yields of Naphthylpyridylethylenes in Neutral (ϕ_b) and Cationic (ϕ_a) Forms

Compd	ϕ_b	ϕ_a
α, 2-NPE	0.022	0.008
α, 3-NPE	0.19	0.06
α, 4-NPE	0.015	0.01
β, 2-NPE	0.063	0.034
β, 3-NPE	0.40	0.07
β, 4-NPE	0.047	0.09
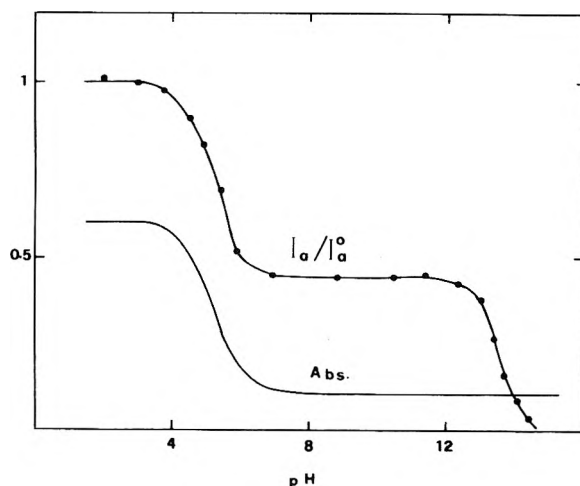
Figure 1. Absorptiometric and fluorimetric titration curves of β,4-NPE. Full points refer to the experimental measurements on the band of the protonated form at 510 nm (corrected for the small contribution of the base); excitation at the isosbestic point, 335 nm.

Ground state pK values, reported in Table I, are practically unaffected by the position of the naphthyl group. More significant effects are due to the position of the heteroatom, which results in more basic pK values for the para-substituted pyridines. Slightly lower pK values for ortho-substituted pyridines than for 3-pyridyl isomers are probably due to some steric effect.

The spectral shifts on protonation and the different trends of absorptiometric and fluorimetric titrations clearly indicate a difference in prototropic reactivity of the ground state and the lowest excited singlet state. While ab-

TABLE III: Fluorescence Lifetimes[a] and Kinetic Parameters for the Hydrolytic Equilibrium of Excited Naphthylpyridylethylenes

Compd	$\tau_b(\tau_b{}^0)$, 10^{-9} sec	$\tau_a(\tau_a{}^0)$, 10^{-9} sec	$\vec{k} = 1/(\text{intercept} \cdot \tau_b)$, 10^8 sec^{-1}	$\overleftarrow{k} = \text{slope}/(\text{intercept} \cdot \tau_a)$, 10^9 M^{-1} sec^{-1}
α, 2-NPE	0.9(41)	1.1(137)		
α, 3-NPE	1.4(7.4)	1.8(30)	2.5	0.89
α, 4-NPE	~0.8(53)	1.0(100)	2.2	2.9
β, 2-NPE	1.1(17.5)	1.4(41)	2.3$_5$	2.0
β, 3-NPE	3.8(9.5)	1.6(23)	0.8	1.5
β, 4-NPE	0.9(19)	1.3(14.5)	9.7	4.7

[a] Natural lifetimes, τ^0, in parentheses.

sorption vs. pH curves show only one inflection point, corresponding to the ground state pK, a second inflection point, corresponding to the excited state pK^*, appears on the fluorescence vs. pH curves. The example reported in Figure 1 for β,4-NPE shows that both intensity changes occur in a small pH range. Considering the second inflection, this fact indicates that the prototropic equilibrium is attained within the lifetime of the excited state. The pK^* values reported in Table I show a large increase of basicity (7 to 8 pK units) in the S$_1$ state for all isomers. The nitrogen position effect seems different than in the ground state, even if the lower precision in the pK^* measurements does not allow us to arrive at definitive conclusions. The pK^* values calculated by the Förster cycle can be considered to be in a satisfactory agreement with the experimental ones, taking into account the uncertainty in the 0–0 frequencies (Table I) used for the calculations.

The percentages of molecules which attain the prototropic equilibrium within the singlet lifetime, measured at pH 8 and 10% ethanol, are also reported in Table I. These values are higher for β- than for α-naphthyl derivatives.

The fluorescence quantum yields are reported in Table II. It is interesting to note that, as already found for styrylpyridines (StP's)[3] and dipyridylethylenes,[12] the ϕ values of the neutral molecules are about one order of magnitude greater when the heteroatom is in the meta position with respect to the ethylenic bridge, compared to the other isomers. Even in the protonated forms, the ϕ values of 3-pyridyl derivatives are relatively high, but the differences are less marked in this case. As the behavior of the 3-pyridyl isomers resembles that of the parent hydrocarbons (α- and β-styrylnaphthalenes),[13] it could be inferred that interaction between $^1\pi,\pi^*$ and ^{1}n,π^* states should be inefficient when the nitrogen is in the meta position. This behavior is similar to that observed for 3-StP. Higher yields were generally found for the bases than for the conjugate acids, a trend which is the opposite of that observed for other azastilbenes.[3] However, radiationless deactivation of the cations through n,π^* nonfluorescing states[3] should not be operative in this case.

Fluorescence decay lifetimes are reported in Table III. These values are also higher for 3-pyridyl derivatives but less than are the yields. This indicates a shorter radiative lifetime ($\tau^0 = \tau/\phi$) for these isomers (less than 10 nsec for the free bases) which are particularly resistent to radiationless deactivations. A general increase of τ was observed on protonation, with the exception of β,3-NPE. Slightly higher values were found for β- than for α-naphthyl derivatives. $\tau_b{}^0/\tau_a{}^0$ ratios are less than unity (with the exception of β,4-NPE) and smaller than τ_b/τ_a ratios. All this experimental

information, however, should be considered with caution as the measured lifetimes are generally very short and some trends can be masked by experimental error.

There is no apparent correlation between the fluorescence yields and lifetimes, thus the fluorescence rate constant $k_F = 1/\tau^0$ is dependent on the nitrogen positional isomerism. Comparison with τ and ϕ values in aprotic polar and nonpolar solvents[11] confirms the importance of structure in the decay processes. In the absence of important solvent–solute interactions (chemical reaction or change in configuration of the emitting state), the radiative lifetime τ^0 should be independent of the nature of the solvent, which would only influence the relative energies of the different levels. This constancy is not completely verified for NPE's in n-hexane,[11] acetonitrile,[11] and water–ethanol as solvents, since the reported values ($\tau_b{}^0$ in Table III) approximately approach those in n-hexane for α derivatives, but are closer to those in acetonitrile for β isomers. This indicates that, probably, the solvent affects the nature of the emitting state to a different extent for different isomers, by enhancing or decreasing the mixing of the fluorescent π,π^* state with the nonfluorescent n,π^* one.

Compared to styrylpyridines, NPE's have longer lifetimes in the neutral form allowing the acid–base equilibration in the excited state to be observed, whatever the nitrogen position. For StP's the lifetimes of the bases were too short to be experimentally measured and the equilibration in the excited state was detectable only for 3-StP.[1] A longer lifetime for the base clearly increases the percentage of molecules attaining the prototropic equilibrium (1) in the excited state. In fact, higher acid percentages were generally found for NPE's than for 3-StP and its 4' derivatives in the pH range 6–10, between pK and pK^*.[1] The equilibration percentages obviously depend not only on the base lifetime but also on the rate parameters for the hydrolytic process and thus on the basicity of the excited state. The kinetic constants $\vec{k}$ and $\overleftarrow{k}$ for reaction 1 were calculated following eq 2, from the plots $1/(I_b{}^0/I_b - 1)$ vs. a_{OH^-}, using the experimental τ values (third and fourth columns in Table III). Contrary to that observed for 3-StP's and for other compounds, where $\vec{k}$ depends only slightly on substituents and $\overleftarrow{k}$ approaches the diffusional value (6 × 10^9 M^{-1} sec^{-1}), for NPE's both rate parameters are affected to some extent by the position of the naphthyl and pyridyl groups. Only for β,4-NPE does $\overleftarrow{k}$ approach the diffusional value while lower values were found for the other isomers. Moreover, it should be noted that $\overleftarrow{k}$ is particularly high for such a reaction which leads to two charged species and thus should be characterized by a large negative activation entropy. The high value of $\overleftarrow{k}$ obviously corresponds to an high

pK^* value for these molecules. Apart from the possible implication of steric factors, these anomalies can be probably explained by considering the experimental error in the lifetime ratio, mainly in those cases where the lifetime is near, or less than, 1 nsec. For acridine, which is characterized by longer lifetimes, most reliable values were found (k = 8.4 × 10^6 sec^{-1}, $\overline{k}$ = 1.8 × $10^{10} M^{-1} \text{ sec}^{-1}$, p$K^*$ = 10.6).[14]

Owing to the high pK^* and the consequent high OH^- concentrations used for the fluorimetric titration, the implication of excited acidic molecules which react without diffusing should also be taken into account. The modified treatment,[6] based on the evaluation of the volume of diffusion around the excited $NPEH^+$, should however not introduce important changes considering also the low τ_a values of NPE's. Furthermore, it would lead to experimental pK^* values in less agreement with the calculated ones. Therefore, we think that the approximate pK^* values in Table I still represent a reliable measure of the basicity of NPE's in the S_1 state.

The high rate parameters found for β,4-NPE indicate that for this isomer the relaxation time of the prototropic equilibrium (1) is shorter than the mean lifetime of the excited species to a greater extent than for the other isomers, as expected from the high percentage of equilibration with the proton. This offers a particularly favorable situation to study the effect of pH on both fluorescence and photoisomerization quantum yields, as done for 3-StP in less favorable conditions.[3] This study, which is in progress in this laboratory, should give interesting information on the excited state responsible for photoreaction in protic medium.

References and Notes

(1) G. Favaro, U. Mazzucato, and F. Masetti, *J. Phys. Chem.*, **77**, 601 (1973).

(2) (a) M. Nakamizc, *Spectrochim. Acta*, **22**, 2039 (1966); (b) G. Favaro, F. Masetti, and U. Mazzucato, *Spectrochim. Acta, Part A*, **27**, 915 (1971); (c) E. Vander Donckt, R. Dramaix, J. Nasielski, and C. Vogels, *Trans. Faraday Soc.*, **65**, 3258 (1969); (d) G. Gennari, G. Cauzzo, and G. Galiazzo, *Gazz. Chim. Ital.*, **104**, 535 (1974).

(3) G. Bartocci, P. Bortolus, and U. Mazzucato, *J. Phys. Chem.*, **77**, 605 (1973).

(4) G. Galiazzo, P. Bortolus, and F. Masetti, *J. Chem. Soc., Perkin Trans. 2*, in press.

(5) See, e.g., H. T. S. Britton, "Hydrogen Ions", Vol. 1, Chapman and Hall, London, 1955, p 365.

(6) A. Weller, *Prog. React. Kinet.*, **1**, 187 (1961), and references therein; E. Vander Donckt, *ibid.*, **5**, 273 (1970).

(7) G. Beggiato, G. Favaro, and U. Mazzucato, *J. Heterocyclic Chem.*, **7**, 583 (1970).

(8) J. B. Birks, "Photophysics of Aromatic Molecules", Wiley-Interscience, London, 1970, pp 120, 124.

(9) U. Mazzucato, F. Masetti, and G. Favaro, *Gazz. Chim. Ital.*, in press.

(10) F. Masetti and U. Mazzucato, *Ann. Chim. (Italy)*, **62**, 519 (1972).

(11) F. Masetti et al., manuscript in preparation.

(12) D. G. Whitten and M. T. McCall, *J. Am. Chem. Soc.*, **91**, 5097 (1969).

(13) P. Bortolus and G. Gallazzo, *J. Photochem.*, **2**, 361 (1974).

(14) A. Weller, *Z. Electrochem.*, **61**, 956 (1957).

PHYSICAL PHENOMENA

spectroscopy,
thermodynamics,
reaction kinetics,
and other areas
of experimental
and theoretical
physical chemistry
are covered
completely in

THE JOURNAL OF PHYSICAL CHEMISTRY

The biweekly JOURNAL OF PHYSICAL CHEMISTRY includes over 25 papers an issue
of original research by many of the world's leading physical chemists. Articles, commu-
nications, and symposia cover new concepts, techniques, and interpretations. A "must"

for those working in the field or interested
in it, the JOURNAL OF PHYSICAL
CHEMISTRY is essential for keeping
current on this fast moving discipline.
Complete and mail the coupon now to
start your subscription to this important
publication.